PREDICTION OF DELAMINATION
IN
GLASS FIBRE REINFORCED COMPOSITE MATERIALS
USING
ELASTO-PLASTIC MODELLING

A thesis submitted by

Ayad Arab Ghaidan KAKEI, M Eng.

For the award of

Doctor of Philosophy

2019

ABSTRACT

Glass Fibre reinforced composite (GFRC) has been used for numerous structural applications in Aerospace, Chemical, Automotive and Civil infrastructure fields over a hundred of years. Due to this reason, understanding the intricate fracture behaviour of GFRC materials is crucial and essential for designing critical structural components.

Voids and micro-cracks are considered as imperfections in Glass Fibre Reinforced composites. Much research has been undertaken on approaches to calculate and evaluate the effects of the imperfections on mechanical properties. However, it is an established fact that the micro-mechanical approach alone is not sufficient to understand a complete damage accumulation process during delamination. The damage mechanism which largely affects the performance of GFRC structures is commonly known as "delamination". Since the delamination is invisible, and hard to detect with ordinary non-destructive evaluation methods, therefore it is considered as a hidden killer which can cause catastrophic failure without any prior warnings. Due to this reason, research work on delamination modelling, damage detection and self-healing materials have been the highly placed research topics for more than five decades. Unfortunately there are a number of unresolved problems in delamination damage modelling and prediction, and few grey areas regarding application of Structural Health Monitoring systems to monitor delamination damages. This thesis has proposed to study the insight into the cause of delamination damage and its propagation mechanisms, by analytical modelling and experimental verifications.

Within this research project, extension of the work by Tsukrov and Kachanov (2000) – "An innovative Elasto-plastic model" has been undertaken to evaluate, investigate and model the onset and propagation of delamination damages. Mode I, Mode II as well as Mixed Mode I/II delamination damage analysis has been utilised to study the proposed model predictions for GFRC structures for both in-plane and out-of-plane load applications.

The proposed model has been validated using the Double Cantilever Beam (DCB), End Notch Flexure configurations (ENF) and Cracked Lap Shear (CLS) experiments on 0/90-glass woven cloth specimens. For the validation process, the

procedures stipulated by ASTM standards were employed. It was observed that there were significant discrepancies between calculated fracture energies using standard procedures and the proposed model. Interestingly these observations have revealed some inconsistencies associated with the standard method for strain measurements that majorly controls the fracture energy calculations. This research project has demonstrated and evidently proven the accuracy of the proposed model predictions using the strain measured with embedded Fibre Bragg Grating (FBG) sensors, located inside the sample in proximity of the crack tip. The extended use of FBG strain measurement has created a breakthrough in Structural Health Monitoring (SHM) of composite structures. Non-availability of a suitable damage prediction model is an issue for accurate damage monitoring process. The proposed model has also demonstrated the potential for its integration with Structural Health Monitoring (SHM) systems. Additionally, Thermoplastic Stress Analysis (TSA) has been employed to monitor delamination. The potential for integration of FBG sensors and TSA techniques has been experimentally demonstrated during this project and, it is another breakthrough in SHM field as a result of this research.

In addition to analytical model, a detailed Finite Element model was also created on ABAQUS commercial software. The cohesive elements with state variables (SDV) and UMAT codes were used for FEA simulations. Interestingly, the FEA results have shown an excellent correlation with the experimental results.

Finally, this thesis has evidently proved the validity of the proposed model and integration of model with SHM system based on FBG sensors and TSA techniques. The outcomes of the thesis have provided a novel and innovative damage prediction model and a breakthrough technology for SHM systems.

Certification of Thesis

This Thesis is entirely the work of (**Ayad Arab Ghaidan KAKEI**) except where otherwise acknowledged. The work is original and has not previously been submitted for any other award, except where acknowledged.

Principal Supervisor: _____

Associate Supervisor: _____

Student and supervisors signatures of endorsement are held at USQ

Acknowledgements

I would like to thank God for his never-ending grace, mercy, and provision during what ended up being one of the toughest times of my life.

I would like to express my deepest gratitude and thanks to my principal supervisor, **Dr Jayantha Epaarachchi**, who has the attitude and the substance of a genius. He continually and convincingly conveyed a spirit of adventure in regard to research and an excitement in regard to instructions. Without his guidance, insight and persistent help this work would not have been possible. I would like to thank my associate supervisor **Dr Mainul Islam** for his advice and valuable comments and suggestions those were essential in improving of this research.

I would like to thank **Professor Jinsong Leng**, Adjunct professor in the centre for smart materials and structures, Harbin Institute of Technology. In addition I would like to thank **N. Rajic**, Defence Science and Technology Group, Australia for providing some important devices. I am extremely grateful for their assistances and suggestions throughout my project.

My deepest gratitude goes to my parents for unending support in making this research possible.

I would like to thank my wife for being by my side all these years and for all have done. I am thankful to the fate because I have lovely wife in my life and it feels so awesome to have such loving wife. In addition I would like to express my love to my daughters ***Lana*** and ***Nadine***.

My acknowledgment to my sponsor ***Iraqi Government***, and special thanks to the ***Iraqi Cultural Attaché*** office (Canberra) for all the supports during the period of the study.

Associated Publications

Journal and Chapter of book

Kakei, A, Epaarachchi, J, Kahandawa, G & Leng, J 2016, 'Development of Fracture and Damage Modeling Concepts for Composite Materials', in J Epaarachchi & G Kahandawa (eds), *Structural Health Monitoring Technologies and Next-Generation Smart Composite Structures*, CRC Press USA, Ch 9, pp. 339-64.

Kakei, A, Epaarachchi, JA, Islam, M, Leng, J & Rajic, N 2016, 'Detection and Characterization of Delamination Damage Propagation in Woven Glass Fibre Reinforced Polymer Composite using Thermoelastic Response Mapping', *Composite Structures*, vol. 153, pp. 442-50. (IF: 3.858, SNIP: 2.033).

Kakei, AA, Islam, M, Leng, J & Epaarachchi, JA 2018, 'Use Of An Elasto-Plastic Model and Strain Measurements of Embedded Fibre Bragg Grating Sensors to Detect Mode I Delamination Crack Propagation in Woven Cloth (0/90) Composite Materials', *Structural Health Monitoring*, vol. 17, no. 2, pp. 363-78. (IF: 3.798, SNIP: 1.862).

Kakei, A, Islam, M, Leng, J & Epaarachchi, JA 'Evaluation of Onset and Propagation of Mode II Delamination Crack in Glass Fibre Reinforced Composite Materials using Elasto-Plastic Model'. It is ready to submit to *Structural Health Monitoring*. (IF: 3.798, SNIP: 1.862)

Kakei, A & Epaarachchi, JA 2018, 'Use Of Fibre Bragg Grating Sensors for Monitoring Delamination Damage Propagation in Glass-Fibre Reinforced Composite Structures', *Frontiers of Optoelectronics*, vol. 11, no. 1, pp. 60-8. (SNIP: 0.784)

Kakei, A, Islam, M, Leng, J & Epaarachchi, JA 2018, 'Evaluation of Delamination Crack Tip in Woven Fibre Glass Reinforced Polymer Composite using FBG Sensor Spectra and Thermoelastic Response', *Measurement Journal of the International Measurement Confederation (IMEKO)*, Vol 122, pp. 178-185 (IF: 2.359 and SNIP: 1.630),

Kakei, A, Islam, M, Leng, J & Epaarachchi, JA 'Monitoring Delamination Crack Tip in Fibre Reinforced Polymer (FRP) Composite Components using Fibre Bragg

Grating (FBG) and Thermal Stress Mapping Techniques'. It is ready to submit to *IEEE Sensors* (IF: 2.617, SNIP: 1.555).

Kakei, A, Islam, M, Leng, J & Epaarachchi, JA 'An Investigation Mixed Mode Delamination Propagation Use Elasto-Plastic Model in Fibre Reinforced Polymer'. It is ready to submit to *Composite A* (IF: 4.920, SNIP: 2.105).

Refereed Conference Proceedings

Ayad Kakei, Jayantha A Epaarachchi, Nick Rajic, Jinsong Leng, Mainul Islam, Gayan Kahandawa (2015). Integrated FBG Sensor Responses and Full Field Thermo-elastic Stress Approach to Monitor Damage Accumulation in Glass Fibre Reinforced Composite Plates. *Proceeding of the 10th international workshop on structural health monitoring* (IWSHM2017). Stanford, CA, USA1-3 September 2015.

Ayad Kakei, J. A. Epaarachchi, Mainul Islam, J Leng (2016). Elasto-plastic analysis of a delamination damage propagation in a 0/90 Woven Cloth Composite beam. *Proceeding of 10th Asian-Australasian Conference on Composite Materials (ACCM-10)*, Busan, South Korea.

Ayad Kakei, J.A. Epaarachchi, Mainul Islam, J. Leng, Anura P. Rathnayake, N.K. Hettiarachchi (2017). Evaluation of Thermo-Elastic Stress Analysis (TSA) and Digital Image Correlation (DIC) Techniques for Detection of Delamination Crack Propagation of Glass Epoxy Composite Plate under Uni-Axial Cyclic Loading. Proceeding of the *21st International Conference on Composite Materials (ICCM21)*, Xi'an, 20-25th August 2017.

Ayad Kakei, Jayantha Epaarachchi, Mainul Islam, Zhang Zhichun, Jinsong Leng (2017). An Investigation of the Performances of Embedded Buckypapers within A 0/90 WC Glass Fibre Reinforced Composite Specimen with a Delamination, Under Tensile Loading. Proceeding of the *11th international workshop on Structural Health Monitoring (IWSHM2017)*. Stanford, CA, USA12-14 September 2017.

Jayantha .A. Epaarachchi, **Ayad Kakei** (2017). Use of FBG Sensors for Monitoring Mode I Delamination Damage Propagation. Proceeding of the *9th*

Australasian Congress on Applied Mechanics (ACAM9) 27 - 29 November 2017, UNSW, Sydney, Australia.

Ayad Kakei, Jayantha A Epaarachchi (2017). Monitoring delamination crack in fibre reinforced polymer (FRP) composite components using Fibre Bragg Grating (FBG) sensors and Thermal Stress Mapping Techniques. Proceeding of the *9th Australasian Congress on Applied Mechanics (ACAM9) 27 - 29 November 2017*, UNSW, Sydney, Australia.

Ayad Kakei, Jayantha Epaarachchi (2018). Monitoring Tip of Embedded Mixed Mode Delamination Crack Propagation Using TSA Technique. Proceeding of the *11th Asian-Australasian Conference on Composite Materials (ACCM-11*), Cairns, 29th July – 1st August, 2018, Australia.

Table of Contents

List of Figures

List of Tables

Abbreviations

AEs	Acoustic Emissions
ASTM	American Society for Testing and Materials
CAI	Compression After Impact
CBT	Correction Beam Theory
CCM	Compliance Calibration Method
CFRP	Carbon Fibre Reinforced Polymer
CLPT	Classical Laminated Plate Theory
CLS	Cracked Lap Shear
CMC	Ceramic Matrix Composite
CZM	Cohesive Zone Model
DBT	Direct Beam Theory
DCB	Double Cantilever Beam
DCOD	Delaminated Growth Crack Opening Displacement
DFT	Discrete Fourier Transformation
DI	Distortion Index
DIC	Digital Image Correlation
DOF	Degree of Freedom
DSTO	Defence Science Technology Organisation
EEVM	Eigen Function Expansion Variational Method
ELS	End Loaded Split
ENF	End Notched Flexure
EPFM	Elastic-Plastic Fracture Mechanics
ESL	Equivalent Single Layer
FBG Sensor	Fibre Bragg Grating sensor
FEA	Finite Element Analysis
FPZ	Fracture Process Zone
FRP	Fibre Reinforced Polymer
FSDT	First-order Shear Deformation Theory
FWHM	Full-Width Half-Maximum
GFRC	Glass Fibre Reinforced Composite
GFRP	Glass Fibre Reinforced Polymer
GSCM	Generalized Self-Consistent Method

IR Camera	infrared camera
LEFM	Linear Elastic Fracture Mechanics
LW	Layer Wise
MMB	Mixed Mode Bending
MMC	Metal Matrix Composite
NDE	Non Destructive Evaluation
NDT	Non-Destructive test
PAUT	Phased Arrayed Ultrasonic Techniques
PMC	Polymer Matrix Composite
PS-FBG	Phase-Shifted Fibre Bragg Grating
PWR	Peak Wavelength Ratio
RVE	Representative Volume Element
SDVN	Solution Dependent State Variables
SEM	Scanning Electron Microscope
SERR	Strain Energy Release Rate
SHM	Structure Health Monitoring
SIF	Stress Intensity Factors
TSA	Thermoelastic Stress Analysis
UMAT	User Material Defined Subroutine
VCCT	Virtual crack closure technique
VUMAT	User Material Subroutine For Implicit Analysis
WC	Woven Roving Fabrics Composite
XFEM	Extended Finite Element Method

List of Symbols

E_d	Delamination growth parameter
ΔN	Fatigue cycling
ΔT	Temperature increases
1/R	The curvature
a	A half length of crack
C_p	Thermoelastic constant
C_p	The specific heat at constant pressure
dU	Change in elastically stored energy
dW	Change in Work done
E	Young's modulus of the materials
e_e	Elastic energy due to structural changes/ or dissipated from delamination crack)
E_{ep}	Young modulus of epoxy (matrix)
e_s	Elastic energy per unit length of composite beam
E_x	Young modulus (x-axis)
E_y	Young modulus (y-axis)
G	Energy release rate or fracture energy
G_I	Mode I fracture energy
G_{IC}	Critical Mode I fracture energy
G_{II}	Mode II fracture energy
G_{IIC}	Critical Mode II fracture energy
G_{III}	Mode III fracture energy
G_{IIIC}	Critical Mode III fracture energy
G_{shear}	Total fracture energy ($G_{II}+G_{III}$)
G_T	Total fracture energy (G_I+G_{II})
G_{xy}	Young modulus (xy-axis)
h	Half thickness of the specimen
K_{ef}	Penalty stiffness of cohesive elements
K_I	Mode I stress intensity factor
K_{II}	Mode II stress intensity factor
Λ	The grating period

λ_B	The Bragg wavelength
M	Total moment (M_u+M_b)
M_b	Bending moment of bottom section
M_u	Bending moment of upper section
n_{eff}	The effective refractive index
P	Applied loading
T_0	Average temperature of the solid
T_0	Average temperature
U	Elastic energy
ux, uy,& uz	Displacements between upper and lower crack surface
v	Passion ratio
W	Work done
x, y, z	Local Cartesian coordinate
y	The direction of neutral axis of the beam section
γ	The free surface energy per unit area associated increment area
$\Delta\sigma$	The variation of the first stress
ε(y)	Strain
ε_{max}	Maximum strain measured in the surface of composite specimen
ε_{Yepoxy}	Yield strain of epoxy
λ	Linear thermal expansion coefficient
ρ	The mass density
σ(y)	Stress
σ_x	Elastic stress field around a crack tip, x-axis
σ_y	Elastic stress field around a crack tip, y-axis
σ_Y	Yield stress
τ_{xy}	Elastic shear stress around a crack tip
μ	Delamination location through thickness ratio

Chapter 1: INTRODUCTION

1.1: Background

Composite Materials are formed by combination of two or more materials. The newly formed composite materials have improved mechanical properties and are more resistant to environmental conditions. There are many types of composite materials according to their applications. Laminated composite material shown in Figure ***1-1*** is one of the common types of composite materials which utilises high-strength fibres in a resin matrix. In a Laminated composite, the fibres and matrix are combined to make a single ply. This is formed by stacking plies and laying different fibres oriented in an arranged manner. The laminate are then cured under high temperature and pressure. The directional properties of fibre are different along the two orthogonal directions. The composite laminate structures can be modelled as orthotropic materials. Anisotropic behaviour results due to an angle ply orientations. A composite laminate with different orientation plies can be treated as layered anisotropic medium.

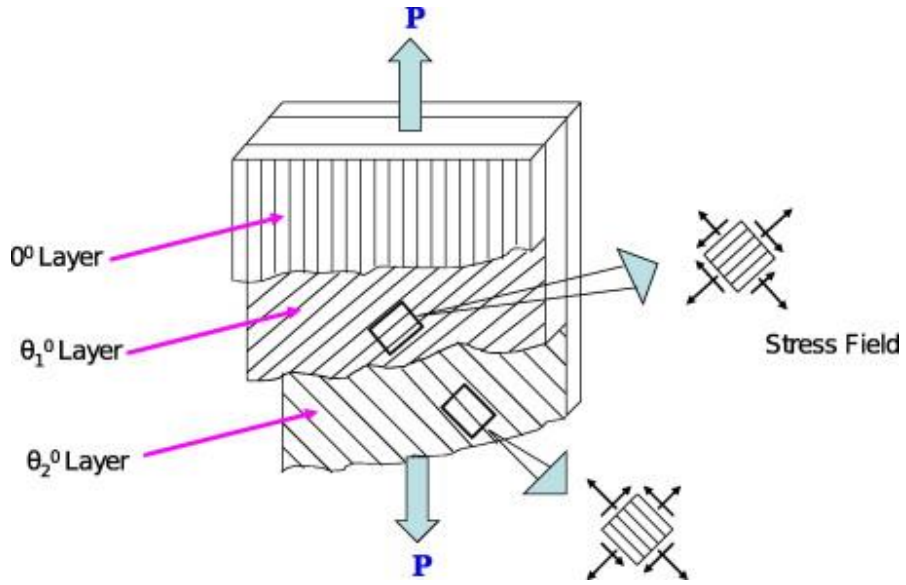

Figure 1-1 Off-axis laminate loaded in axial tension (Singh & Talreja 2010)

Glass Fibre Reinforced Composite (GFRC) are widely used as plate and shell structures in the Aerospace, Chemical, Automotive and Civil infrastructure field due to their high strength to weight ratio. Although GFRC's show excellent performance in many application, however they suffer from some imperfections in structure due to embedded cracks. The embedded cracks in fibre reinforced composite laminate may vary from micro-cracks to inherent flaws. The complete

rupture of the laminate occurs when the crack propagation reaches the interface under increased loading. The common cracks observed in the reinforced composite laminate are transverse cracks, along the fibres in constituent laminate, and perpendicular to the interfaces. This type of cracking is common to all layered structures along with longitudinal cracking and delamination. Delamination between plies is one of most common Mode of failure of composite structures. Delamination is a type of crack that forms between neighbouring plies because of the weak inter-laminar strength between the fibre and the matrix.

Delamination can happen during different life stages of composite structures. It may occur during manufacturing, transport and in-service. During manufacturing process, while curing, it may set-in due to the contraction of the matrix (resin). In addition delamination may also arise under various circumstances, such as due to low velocity impact, fatigue, buckling, due to discontinuities in structures of composites. Such discontinuities give rise to inter-laminar stress between adjacent plies. Some of these causes are shown in Figure ***1-2***.

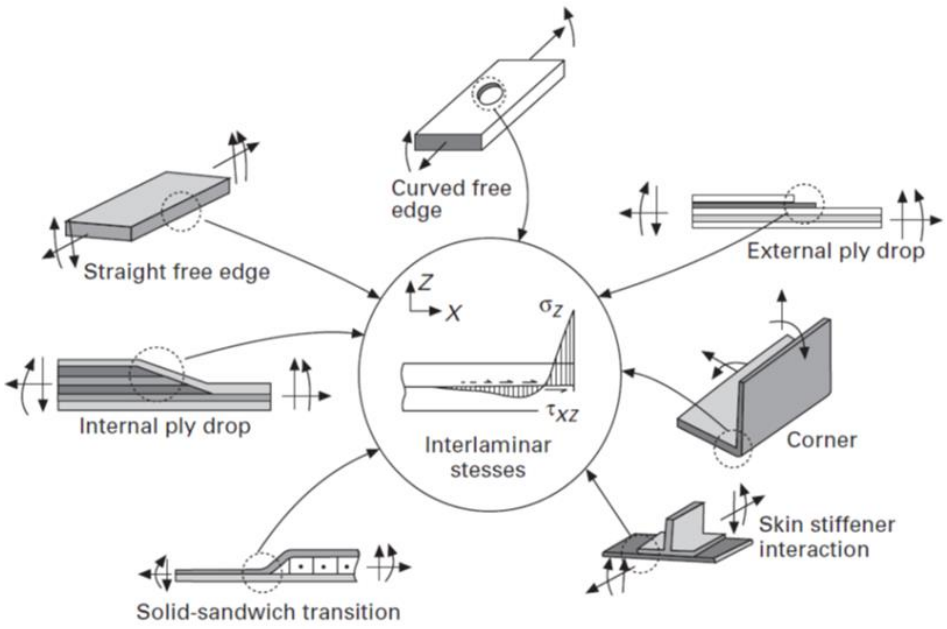

Figure 1-2 Sources of delamination at geometric and material discontinuities(Sridharan 2008)

Delamination is a diffused type of damage in composite materials. Unlike metallic structures, GRFC structure exhibit stress-concentration regions such as voids and local delamination. The loss of adhesion between two plies of laminate is an example of local stress concentration. The local stress concentrations affect the

mechanical behaviour of the composite. The deterioration trends in composites such as transverse cracking, de-bonding, and delamination are quite different to that commonly observed in metallic materials. For this reasons, it is advised to monitor composite structures regularly. Above mentioned issues were the reason for the development of Structure Health Monitoring (SHM) technique for composite structures (Chang 2003; KakeiEpaarachchiKahandawa, et al. 2016; Zhou & Sim 2002).

The propagation of delamination damage in composite structure depends on several parameters such as the geometrical and mechanical properties of the composite structures or on the nature of the delamination crack damages (Mode I or Mode II or mixed Mode I/II) or on the external applied loadings (Nassar & Casavant 2008). The spread of delamination depends on the direction of applied loading at the tip of the delamination crack such as opening (Mode I) or shearing (Mode II) or tearing (Mode III). Delamination damage can be defined on the basis of extent of the crack through the matrix (epoxy) between the two plies. It means that delamination cracks develop in the weakest part of the composite structure. Pure epoxy shows large plastic deformation under tensile loadings as shown in Figure ***1-3***. Large plastic deformation indicates elastic-plastic deformation at the delamination crack tip. Embedding few small sensors in composite structures can provide useful information to understand stability of delamination damage.

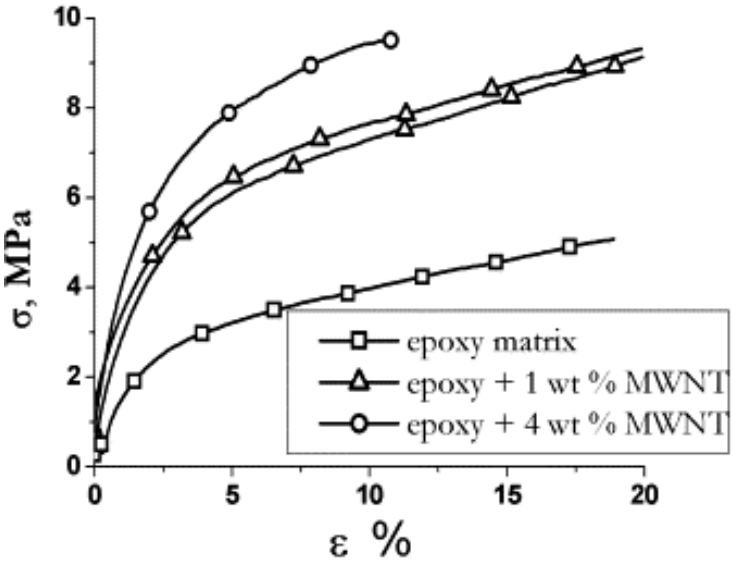

Figure 1-3 Tensile test stress–strain curves of the resin and its composites (Allaoui et al. 2002)

Previously, when a component of composite structure showed a crack, it was either changed or repaired. This approach is expensive and could be avoided if sufficient information is available to analyse the causes of failure.

As mention above, composite structures can have many different types of damages. Monitoring of composite structures is required for damage detection, if they are to be used in critical applications. Damage detection technologies employ vibration and damping methods (Adams et al. 1978). However, due to the complexities of composite structures, there are insufficient offline Non-Destructive test (NDT) methods. Due to limitations with NDT methods, online structural Health Monitoring (SHM) systems are more favoured. SHM system can be defined as the process of implementing the damage detection and characterization strategy for engineering structures. Addressing damage in composite structures needs efficient, robust and accurate SHM system.

Since, it is difficult to predict and detect damage based on surface analysis tests due to the intricate behaviour of the layered composite. Therefore use of bonding FBG sensors and bonding strain gauge on the surface of composite specimens is not helpful. To overcome this limitation, for detection and prediction of delamination damage in composite structures, sensors can be embedded in the host composite materials. Since the embedded sensor cannot be easily replaced, it must possess sufficient durability. The Fibre Bragg Grating (FBG) sensor is one of the most suitable sensors for embedment in composite structures. FBG senor has the ability to measure the strain and temperature at its attached location. This sensor can be embedded in the composite structure during manufacturing and does not affect the mechanical properties of the materials. Furthermore, FBG sensor is also non-conductive therefore it is free from other electromagnetic noises.

The strain concentration at the tip of delamination crack causes the distortion of reflected FBG spectra. This phenomenon is called “chirp” and can be used as a qualitative information of the damage. Prediction of initiation and propagation of delamination damage using FBG sensor requires a robust analytical process which is a remaining challenge in FBG sensor based SHM systems.

The prediction of life i.e. the damage accumulation is also not well understood due to anisotropic nature of the GFRC material. The mechanism of “delamination” the

silent killer of the GFRC components also remains an unresolved research question. Therefore it is appropriate to develop a model based on micro-cracks theory for predicting delamination damage onset and propagation, considering damage mechanism inside GFRC and integrating it with strain variation which measured by embedded FBG sensor. The research work in this thesis is used measured elasto-plastic strain at the tip of delamination crack using an embedded FBG sensor for predicting delamination damage propagation. This method provides accurate information for prediction of delamination crack stability. Further, this information will assist with development of a maintenance strategy for composite structures thereby leading to reduced wear and tear/ replacement cost.

1.2: Research motivation of the project

GFRC is used in many advanced engineering applications such as aerospace, civil infrastructure and automotive structural components. To date, and still continuing, a lot of research has been conducted on damage modelling and lifetime predictions of laminated composites. Unfortunately, there are still many unanswered questions regarding damage modelling. There are different types of damage characteristics such as transverse cracks, longitudinal cracks, delamination and environmental conditions which may affect damage accumulation in the laminated composite materials. As such a logical investigation of damage behaviour is vital to understanding unexplored area of progressive damage accumulation of GFRC materials to avoid catastrophic failures. The delamination is considered the most dangerous cause for catastrophic failure of composite components among many other factors identified for failure of laminated composites. Due to this reason many micro-mechanical damage models have been proposed to investigate the effect of micro-cracks and delamination. These Models have predicted stiffness reduction in GFRC as a key parameter for life prediction. Further research is therefore required to understand, investigate and develop analytically and verify experimentally the effect of delamination onset and propagation on GFRC.

1.3: Objective of the research

The main objective of this study is to develop an accurate damage model to predict damage onset and propagation which has ability to integrate with standard

Structural Health Monitoring system. An Elasto-plastic damage model, integrated with Fibre Bragg Grating (FBG) sensors will be proposed. A validation of proposed damage model will be confirmed with experimental results and Finite Element analysis (FEA) using cohesive elements to simulate delamination damage with User subroutine Umat of State Damage variables (SDVn) available in ABAQUS commercial FEA software. The specific objectives of the study are as follows:

1. In-depth understanding of delamination process and mechanism of glass reinforced/epoxy composite.
2. Development of an accurate mathematical model to predict delamination process.
3. Model verification through experimental investigation of the model for prediction using embedded Fibre Optics Sensor and TSA stress field mapping techniques.
4. Development of an analytical (FEA) method using ABAQUS cohesive elements and state damage variables to simulate delamination process.
5. Development of a procedure for integration of embedded fibre optic sensor output with mathematical model prediction for development of standard health monitoring system.

1.4: Focus and scope of the research

The study focused on understanding and investigating delamination damage propagation in GFR composite under different loading types. The study involves experimental investigation and analytical modelling. The experimental program is planned for GFR composite under different damage Modes (Mode I, Mode II, and Mixed Mode I/II) and a SHM will be incorporated to monitor delamination damage propagation. The experimental results will be used to correlate the elasto-plastic developed model and finite element predictions. The scope of this study is summarised below:

1. The Elasto-plastic model was developed (extended model from Tsukrov and Kachanov (Tsukrov & Kachanov 2000)) predict onset of a delamination damage and propagation in GFR composite. The elasto-plastic strain at the tip of delamination crack was calculated to confirm the Elasto-plastic model predictions. In addition Finite element analysis (cohesive element) using commercial FEA software ABAQUS was employed to understand the local bending at the tip of

delamination crack and prediction of delamination damage using user subroutine Umat (State Damage variables SDVn).

2. The monitoring of delamination damage in GFR composite was investigated. For this purpose, two health monitoring techniques, namely embedded FBG sensor, and thermoselastic stress analysis (TSA) were employed for examining delamination damage propagation. A FBG sensor (5mm grating length) was embedded for measuring strain at delamination crack tip and the TSA system used a FLIR A325 commercial micro-bolometer camera, to record strain map of the sample surface due to delamination damage.

3. The Elasto-plastic model prediction has utilised energy method (energy release rate). The delamination damages were evaluated and investigated for a number of case studies. Different damage Modes such as Mode I, Mode II and mixed Mode I/II damage were studied.

4. The status of embedded damage in GFRC was described using numerical model based on embedded FBG sensor strain measurements.

1.5: Outline of the thesis

This thesis consists of six main chapters including this introduction, and presents the scope, objective and findings of the research project.

Chapter 2 presents the general background information on GFR composite. It also includes a critical review of the literature regarding the previous research on the damage modelling in GFR composite. In addition, delamination damages and delamination damage process have been briefly reviewed and advanced delamination damage detection technologies are reported.

Chapter 3 establishes an Elasto-plastic mathematical model to evaluate Fracture energy (G), uses FEA based on CZM to develop an improved understanding of initiation and propagation of delamination, and provides a numerical model for evaluating the effects of embedded delamination on the mechanical properties and effect of increased stress in sub-layer of Glass Fibre Reinforced Polymer (GFRP).

Chapter 4 investigates and analyses the experimental and simulation methods to characterize the mechanical properties of GFRP composite and explains materials properties, utilising Thermoelastic Stress Analysis (TSA), and FBG sensor to

develop an improved understanding of the propagation of delamination under quasi-static and dynamic loading.

Chapter 5 uses previously established Elasto-plastic model to evaluate delamination damage in 0/90 GFRP. The strain reading at the crack tip is measured using an embedded FBG sensor and crack propagation is monitored using Thermoelastic Stress Analysis (TSA). This chapter discusses different case studies for delamination damage Modes such as Mode I, Mode II and axial loading mixed Mode I/II. The numerical model that extended from Tsukrov and Kachanov (Tsukrov & Kachanov 2000) has also been discussed.

Chapter 6 presents the conclusion that summarizes the main findings of the study and suggests recommendations for future work.

Chapter 2: REVIEW OF RELATED LITERATURE

Associated publication: Kakei, A, Epaarachchi, J, Kahandawa, G & Leng, J 2016, 'Development of Fracture and Damage Modelling Concepts for Composite Materials', in J Epaarachchi & G Kahandawa (Eds), Structural Health Monitoring Technologies and Next-Generation Smart Composite Structures, CRC Press USA, ch 9, pp. 339-64.

2.1: Introduction

The word composite means 'made up of distinct parts or substances'. A composite material consists of two or more distinct constituent materials which are bound together to form an integral unit. The composite material properties differ from its constituent materials. The concept of combining materials to produce a material with improved properties has been explored for thousands of years. The composite materials (composites) are classified into two main groups. The first group composites are known as "Filled materials". This material is formed by filling up basic or matrix material with some particles to improve its properties. The second group of composite materials (subject of study in this thesis) involves composites that are called "Reinforced materials". Within this type of composite one of the constituents forms a continuous phase, called the matrix and the others acts as fibre reinforcement, which is generally much stronger and stiffer than the matrix (Vasiliev & morozov 2011).

The matrix that holds the reinforcements in an orderly pattern can be polymer, ceramic or metal as shown in Figure ***2-1***. Composite materials are classified as Polymer Matrix Composite (PMC), Ceramic Matrix Composite (CMC), or Metal Matrix Composite (MMC). Polymer matrix composites (PMCs) are made up of a variety of short or continuous fibres bound together in a polymer matrix. Unlike a Ceramic matrix composite (CMC), in which the reinforcement is used to increase the fracture toughness, the reinforcement in a PMC provides high strength and stiffness. The role of the matrix is not only to bond the fibres together, to protect the fibres but also to resist transfer of shear stress between them.

Reinforced Composites, with long or short fibres are often used in large structures such as ships, pressure tanks, aircrafts, and wind turbine wings. The fibres in the fibre-reinforced epoxy materials, provide the resistance to the tensile and compressive stresses. The common polymer composites based on polymer matrix

are Glass Fibre Reinforced Polymer (GFRP) and Carbon Fibre Reinforced Polymer (CFRP). The fibre reinforced polymer composites (FRPs) are increasingly being considered as a substitute for traditional materials in civil engineering field, namely concrete and steel. FRP composites are lightweight, no-corrosive, exhibit high specific strength and stiffness, are easily constructible, and can be tailored to meet different performance requirements. Due to these reasons, FRP composites are utilised in new construction and for rehabilitation of structures, such as for reinforcement in concrete, bridge decks, modular structures, formwork, for strengthening and seismic upgrade (Masuelli 2013).

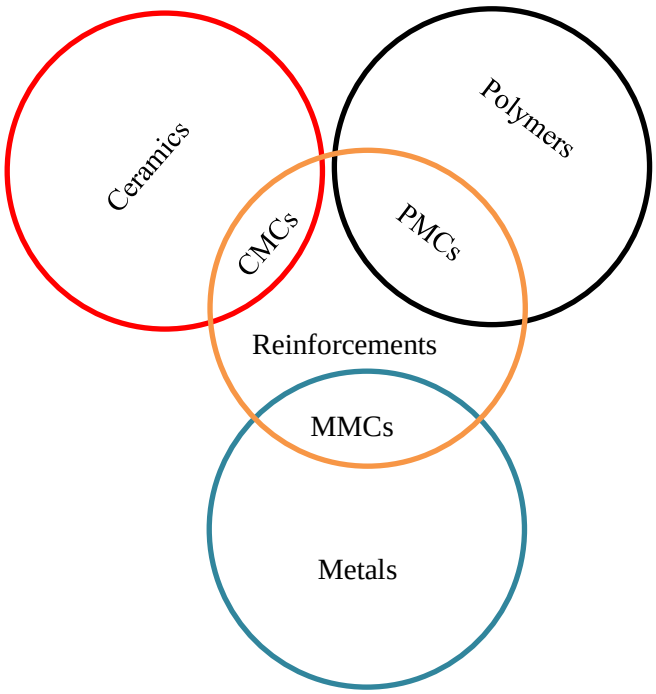

Figure 2-1 The Family of Composite materials

Presence of fibres of glass and carbon in polymer, improves its mechanical properties such as stiffness and strength. The different properties of fibres such as size, type, volume fraction, density and orientation of fibres have a significant effect on the performance of the fibre reinforced polymer composites (FRPs)

The laminated structure often consists of two constituent materials. One constituent material provides continuous phase, and is called matrix while the other is called fibre and provides reinforcement as shown in Figure ***2-2***. As shown there are different types of matrix in laminated composite structures such as ceramic, metal, or polymer. Polymer matrix is usually cheaper and easy to manufacture, therefore

the majority of composite structures are polymer matrix, such as epoxy matrix. Glass Fibre Reinforced Polymer (GFRP) and Carbon Fibre Reinforced Polymer (CFRP) are the examples of widely used polymer reinforced composite materials. The polymer resin comes in two parts, resin and hardener. The ratio of hardener and resin affect the properties of laminated composite.

Fibres are responsible for increasing the strength in fibre reinforced composites. The effective strength depends on size, type, density and orientation of fibres in the matrix. There are different types of fibres used in engineering applications. Glass fibre and carbon fibre are the most common types. Glass fibres are low in strength compared to carbon fibres, but due to its low cost and simple manufacturing process, it is popular for low-end applications such as vehicle body parts, aircrafts, and boats. In comparison, Carbon fibres have high strength. The tensile modulus in carbon fibre compares well to that in ferrous materials, as shown in Table ***2-1***. Since the strength to weight ratio is higher, due to its light weight property, carbon fibre has replaced the metallic materials in aircraft industry.

Laminated composite structures are damage susceptible and involve certain distinct damage Modes, such as interfacial de-bonding (Figure ***2-3***) transverse cracking (Figure ***2-4***), delamination (Figure ***2-5***) and fibre breakage. Damage and imperfections in composite structures, due to geometric discontinuity can cause stress concentration. Due to its anisotropic and brittle behaviours, the laminated composites are more sensitive to geometric discontinuity than metallic materials. Cavities or inclusions are a common imperfection detected in laminated structures. These cavity or inclusion may lead to delamination. Delamination is geometric discontinuity in resin (cohesive) area between two neighbour layers in a laminate composite. Delamination occurs at the interface between the two neighbours lamina. Delamination is not easily detectable and can lead to sudden failures.

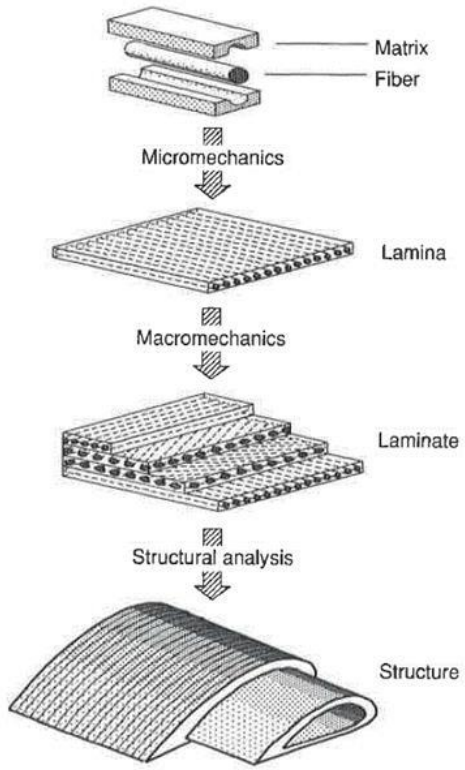

Figure 2-2 Levels of consideration and the corresponding types of analysis for composite materials (Kollár & Springer 2003)

Table 2-1General Physical properties of GFRC compared with steel and Aluminium (Ma et al. 2012)

Types	**Density ($g/cm^{3)}$**	**Thermal Coefficient $10^{-6}/K$**	**Tensile Strength MPa**	**Modulus of Elasticity GPa**	**Fracture Strain %**
Steel	7.9	11.7	483-690	200	6-12
Aluminium	2.7	24	310	68.9	12
GFRC	1.3-2.1	6.0-10.0	483-1600	35-51	1.2-3.1
CFRC	1.3-1.4	9.0-0.0	600-3690	120-580	0.5-1.7

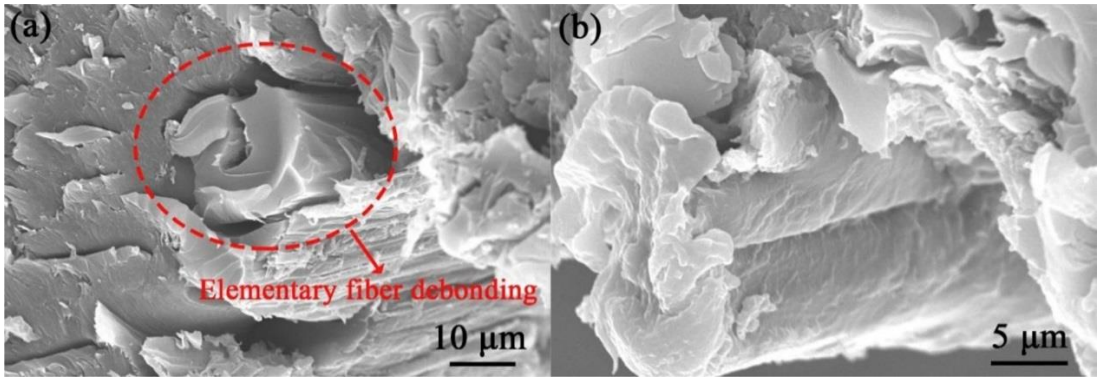

Figure 2-3 SEM photographs of sisal fibres fractured by single fibre pull-out tests: (a) elementary fibre debonding and (b) elementary fibre pull-out (L=0.332mm) (Li, Li & Zhou 2017)

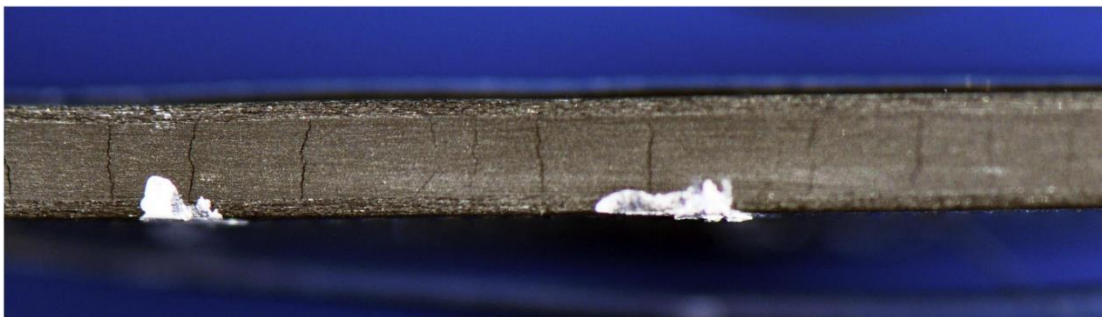

Figure 2-4 Transverse crack damage propagation in prepreg HexPly AS4/8852 (the edge images for specimen $[0_2/90_4]_s$) (Hu, H. et al. 2016))

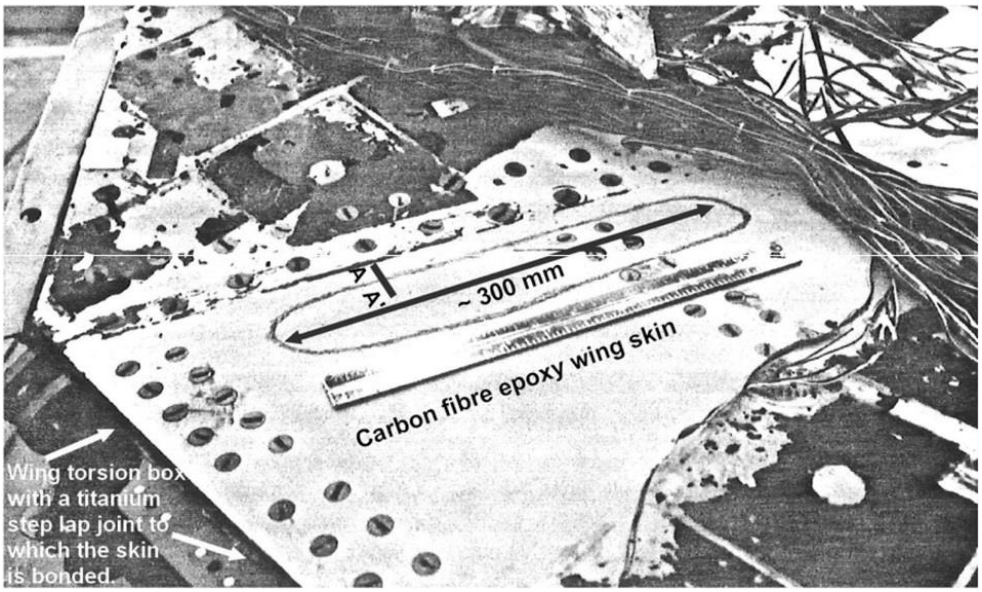

Figure 2-5 Large delamination in the composite seen in an early 'F/A-18' fatigue test at 1633 simulated flight hours (Jones et al. 2017)

2.2: Damage behaviour in composite structures

2.2.1: Introduction

The damage behaviour under static and dynamic loading in composite is quite different to metallic materials. The fracture in metal commonly starts with single cracks. While in the laminated composite structures when the static or dynamic loading is applied several damage Modes appear. Generally the first failure Mode is called inter-laminar cracks or matrix cracking in off-axis plies (Rebière, Maâtallah & Gamby 2001). The crack density increases with increasing static and dynamic cyclic loads.

2.2.2: Transverse crack

The first damage observed in composite materials under applied load is transverse cracking. It occurs in the transverse direction of laminated composite. This crack causes inter-laminar stress concentration at the crack tips. Increase in this stress can cause more damage between layers at interface of plies. This type of crack may encourage development of other cracks which are parallel to applied load such as delamination and longitudinal cracks (Rebière & Gamby 2008). Thereby transverse matrix cracks can be classified as a Mode of failure.

In laminated composite structures, a thin, brittle layer (epoxy) is bonded between tougher substrate layers (fibres). A thin layer is susceptible to cracking under applied stress. Due to the lamina constrained by adjacent lamina the crack propagation in laminate becomes difficult. This retarding is called constraining effect (Barbero 2011). These effects constrain propagation of inherent microdefects into fully developed crack and further hides the appearance of multiple cracks, to indicate major loss of stiffness and strength in the lamina (Barbero & Cortes 2010). These effects can be reduced by increasing the thickness of ply-off layers with respect to 0^o adjacent plies but this way may increase possibility of delamination. Kelly (Kelly 1994) pointed out that for a quasi-isotropic laminate (0/±45/90) the constraining effects decrease on 0^0 layer when thickness in 45^o layer increases, which permits further delamination. Furthermore the strain for crack initiation decreases with increase of thickness of the transverse ply. Mall and Portner (Mall & Portner 1992) viewed that if the number of transverse plies is increased the strain for crack initiation in the cross-ply laminates reach a value equal to the strength of transvers lamina. When constraining parameter $\lambda = t_0 / t_{90}$ increase, the number of 0

ply become greater, therefore the 0 plies carry most of tensile loading and the initiation of the three different damage Modes is delayed. In addition the strain energy release rate associated with damaging composites is decreased (Rebière & Gamby 2008). So it can be expected that the thickness of transverse ply overcome the constraining effects of longitudinal plies. (Zhang, Fan & Herrmann 1999) research was regarding the constraining effect on the ply cracking and its induced delamination in laminated composite materials.

2.2.3: Delamination damage

Delamination is caused by separation of fibre layers. A local or transverse crack delamination starts from a transverse matrix crack. Where transverse cracks terminate, delamination may originate at the interface. This delamination grows normal to the transverse crack from which it originates. Local delamination starts at matrix ply cracks due to a high inter-laminar stress concentration at the crack tips (Zhang, Fan & Herrmann 1999).

Delamination usually develops from transverse cracking damage. Once transverse crack reaches the interface between plies it is arrested. Thereafter, the delamination starts from transverse cracks tips in the region between neighbouring plies with increasing applied load. Presences of delamination cracking in composite structures makes it unsuitable for use (O'brieb 1987). This cracks appears just before ultimate failure (stress), therefore it indicates later stages of damage. The experimental work observed that, at the last stage of damage, the transverse cracking stopped but longitudinal cracking continued with delamination growth. Energy release rates vary very slowly with the longitudinal crack density (Rebière & Gamby 2008).

There are many different types of delamination depending on applied loading and delamination location in the composite structures. Uni-axial compressed loading causes buckling delamination (Juhász & Szekrényes 2017). Buckling delamination length has a significant influence on the buckling Mode shape of the composite materials as shown in Figure ***2-6***. Fortunately buckling delamination can be detected easily. Many studies have been published to show the effect of artificial delamination shapes on the buckling delamination propagation in E-glass/epoxy composites. Liu and Zhang (Liu & Zheng 2013) studied the effect of through-the-width multiple delamination of symmetric and asymmetrical composite laminates

on the buckling and post buckling loads. The studies show that asymmetry decreases the local buckling load and initial delamination loading. The effects of through-the-width strip, circular and peanut shaped delaminations, triangle and inverted triangle patterned delaminations through the thickness direction have been investigated experimentally by (Aslan & Daricik 2016). According to results, the multiple large delaminations significantly affect the compressive and flexural strength and critical buckling load but tensile strength is less influenced by multiple delaminations. Another type of delamination is free-edge delamination. Free-edge delamination initiates at the free edges of the structure. It initiates along the load free edges and propagate normal to the load direction. Edge delamination originates from the load-free edge of a composite plate (Zhang, Fan & Herrmann 1999; Zhang & P. Herrmann 1999). This type of delamination as shown in Figure ***2-7***, can be observed in simple tension tests of uniform rectangular cross section specimen. Normally, free-edge delamination appears from transverse matrix cracking, and experimental results have proven free-edge delamination onset of a specimen under tension (Guillamet et al. 2014). Edge delamination tests have been performed on several specimens with various lay-ups and loaded under inter-laminar shear, tension and compression (Lagunegrand et al. 2006). The tests have exhibited that layer thickness has significant influence on delamination onset stress. Local delamination grows uniformly from the tips of angle-ply matrix cracks under tensile loadings (Kashtalyan & Soutis 2002) and compressive loadings (Kim & Kedward 1999) or from impact loading (Kim & Sham 2000) or from voids (void appears in the composite during the manufacturing process or by nucleation from volatiles during processing (Kardos, Duduković & Dave 1986), see Figure ***2-8***) (Lambert et al. 2012).

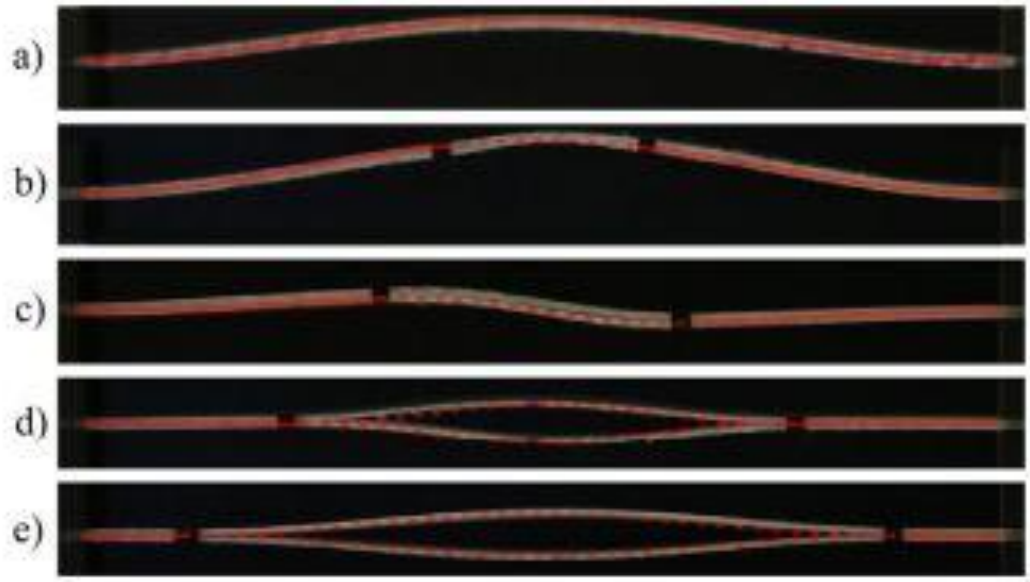

Figure 2-6 The Mode shapes obtained from the experiment and from the simulation: (a) d = 0 mm (b) d = 40 mm (c) d =65 mm (d) d = 100 mm (e) d = 150 mm, where d is the length of embedded delamination(Juhász & Szekrényes 2017)

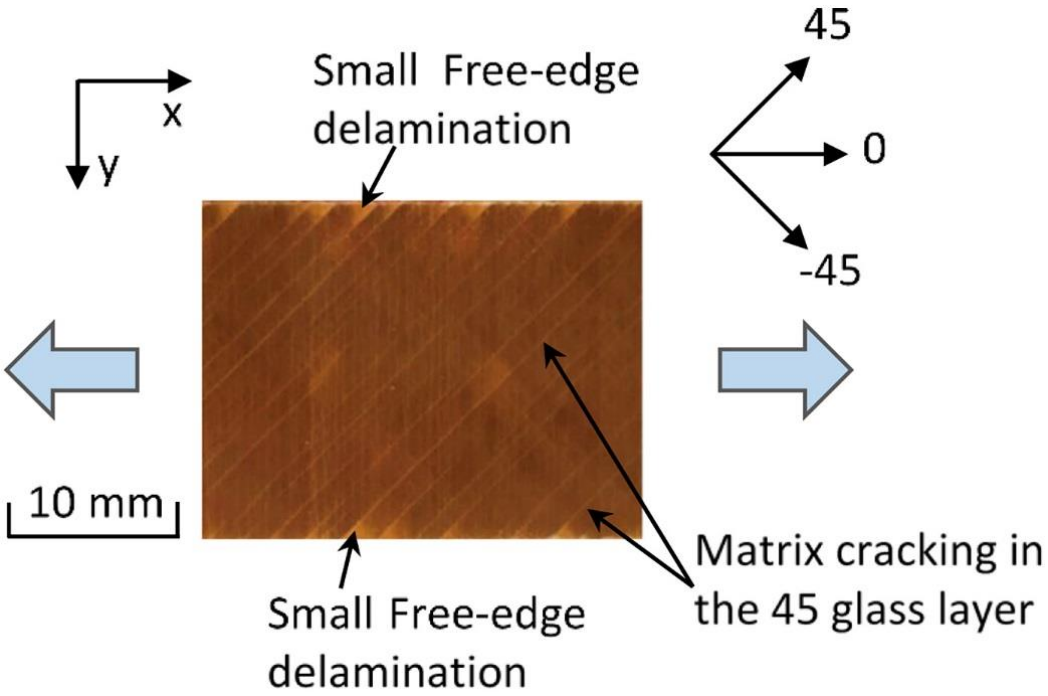

Figure 2-7 Photograph from the top of the $[45_G/90_G/-45_G/0_G/0_C/45_C/90_C/-45_C]_s$ orientation-dispersed quasi-isotropic hybrid laminate just before final failure showing small free-edge delamination(Jalalvand, Fotouhi & Wisnom)

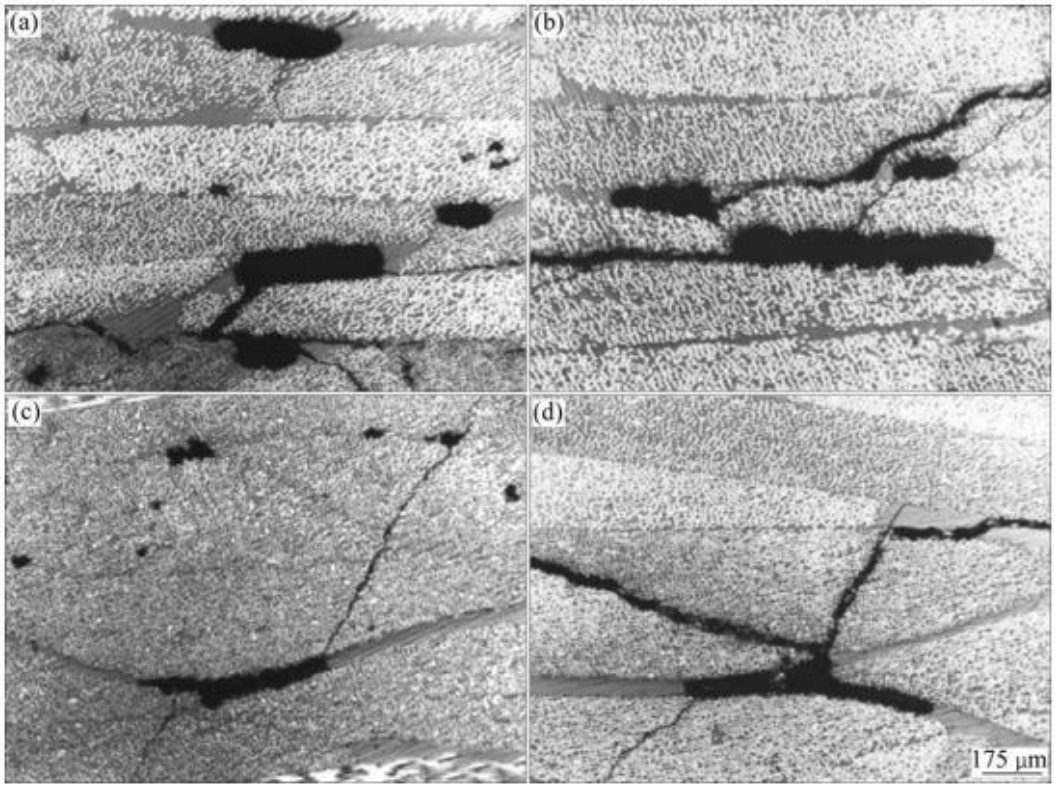

Figure 2-8 Micrographs of tested specimen with different void contents showing cracks emanating from voids for different composite specimens(Zhu et al. 2009)

Transverse cracks and delamination cause reductions in elastic properties of laminate structures. The reduction of stiffness depends on three parameters, namely crack density, relative delamination area and neighbouring lamina orientation angle θ. In addition the transverse cracking tip causes reduction in the shear modulus and Poisson's ratio of cross-ply and symmetric balance laminates (Kashtalyan & Soutis 2000). The reduction of axial stiffness in symmetric laminated with the central 90/0 layer strongly depends on the orientation of the adjacent ply group. Kashtalyan and Soutis (Kashtalyan & Soutis 2000) investigated the reduction of stiffness properties of Graphite/Epoxy as a function of constraining ply orientation angle θ with fixed length of delamination. The reduction of axial modulus occurs mainly due to transverse cracking and transverse crack tip delamination. Transverse cracking tip delamination has significant role in reduction of shear modulus with contribution of transverse cracking and splitting, as shown in Figure ***2-9***.

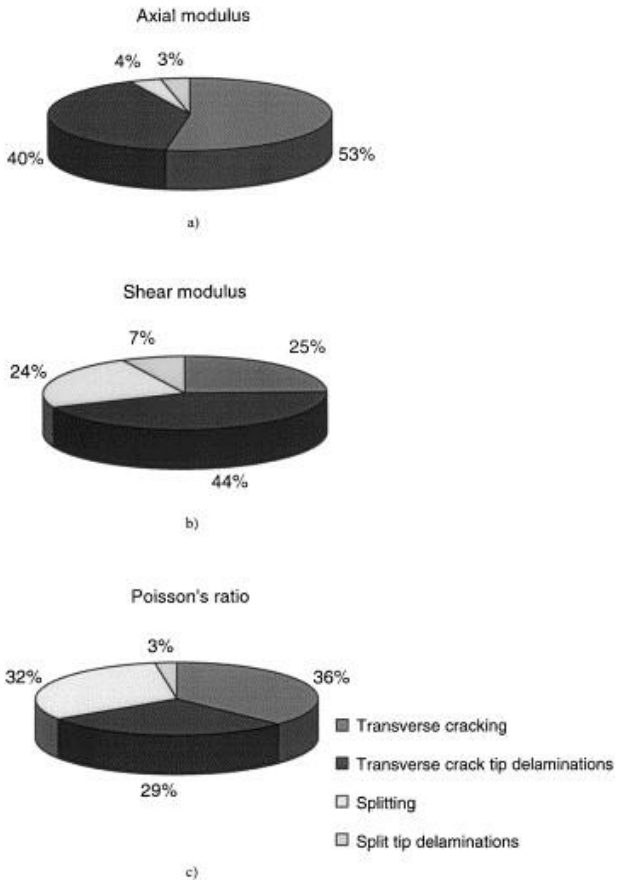

Figure 2-9 Comparisons of damage Mode contributions into the total reduction of the laminate elastic properties due to transverse cracking, splitting, transverse crack tip and split tip delaminations for a $[0_2/90_4]_s$ CFRP laminate: (a) axial modulus; (b) shear modulus; (c) Poisson's ratio (Kashtalyan & Soutis 2000).

2.2.4: Delamination damage approaches

There are two common approaches used to analyse the microcracks and delamination in composite structures: Stress Intensity Factors approach (SIF) and Strain Energy Release Rate approach (SERR). Although SIF approach is used for detecting delamination in composite materials but because of the difficulty of extracting the stress field ahead of delamination crack tip, an alternative way is to use the strain Energy Release Rate (SERR) as the driving force parameter for the delamination growth (Xiang et al. 2014).

Energy balance approach can be used with Linear Elastic Fracture Mechanics (LEFM) and the Elastic stress field (Stress Intensity Factor). The energy balance approach is based on the concept that the crack is extended when the energy release is adequate to overcome the resistance of material. This approach was proposed by Griffith (Griffith 1921) and then was followed by a more detailed treatment of the

energy release rate, *G*, as introduced by Irwin (George 1956). The energy release rate can be defined as the rate of change of potential energy with the crack area.

The delamination damage behaviour due to energy release rates has been examined extensively in many researches. Both Mode I and Mode II energy release rate are determined for examining delamination damage initiation and propagation. Understanding delamination onset and propagation mechanisms is crucial for understanding the resilience of failure tolerance design of laminated composites especially for textile reinforced materials (Kuhtz et al. 2017). There is important relation between G and the change in compliance (inverse of stiffness) of a cracked material. This relationship is a big reason for using Strain energy release rate (G) to simulate onset and propagation of cracks and delamination in laminated composite materials. The strain energy release rate has been used to predict initiation and propagation of cracks and delamination in composite structures. There are number of references in literatures regarding use of energy release rates for delamination or interface fracture. Delamination growth has been described by applying the classical energy release rate criteria by (Fraternali 1996). Energy release rates G_I and G_{II} are derived by using a global method For a cracked laminate subject to axial forces and bending moments (Luo & Tong 2012). Strain energy release rate (G_{IC}) and Mode-I delamination growth in carbon graphene/epoxy (CG-Ep) hybrid nanocomposites has been studied using the double cantilever beam (DCB) test under static loading by David et al (Hawkins & Haque 2015). The results show that significant enhancements in G_{IC} that graphene contribute in neat epoxy will also prominently enhance the resistance to delamination in graphene/epoxy (CG-Ep) samples. The energy release rate approach is applied to describe the delamination growth rate in a fibre metal laminate such as Glare by Alderliesten et al (Alderliesten, Schijve & Zwaag 2006). The work was performed to determine the relationship between the delamination growth rate and the calculated energy release rate. Liaojun et al (Yao et al. 2014) have discussed the use of the strain energy release rate (G) as a parameter to characterize fatigue delamination growth in composite materials. It has been proven, that it is incorrect to apply quasi-static results to normalize fatigue results because fatigue loading is significantly different and normalization of fatigue data with quasi-static SERR becomes meaningless. An equivalent energy release rate is proposed by Boyano et

al (Boyano et al. 2017) for The crack propagation performance of the End Notched Flexure with inserted roller (ENFR) test. The proposed method takes into account the interaction of the Mode I and Mode II for F593/T300 carbon/epoxy unidirectional composite. It was concluded that the equivalent method shows the stability of the crack propagation of the End Notched Flexure with inserted roller (ENFR) mixed Mode test. In addition all tests carried out under displacement control show stable crack propagation. Mode I and Mode II strain energy release rate in the delamination zone are accounted for using First-order Shear Deformation Theory (FSDT) by Saheed et al (Ojo et al. 2017) for machining operations, such as drilling of FRP laminates as shown in Figure ***2-10***. This method can be employed to general laminates subject to mixed Mode delamination initiation. The results show that the increase in ply thickness has significant effect on the shear deformation and prediction of the critical thrust force. The literature on strain energy release rate for predicting delamination damage, indicates that many improvement as well as evaluation of this method has been undertaken. First order shear laminate theory has been used by few researchers to evaluate opening crack delamination. Zhang et al (Zhang, Fan & Herrmann 1999) used first order shear laminate theory to investigate the constraining mechanisms of the constraining plies on the delamination growth. The result showed that ply groups of the 90 plies effect the stiffness and assist with stabilizing/reducing strain energy release rate. In addition, first order shear laminate theory was used by (Nairn & Hu 1992) to investigate the delaminated crack opening displacement in cryogenic fuel tank. They used five layers and three layers stress analysis models but they neglected the influences of the remote constraining layers. Unfortunately no research has been done regarding plastic deformation in the strain energy release rate criteria.

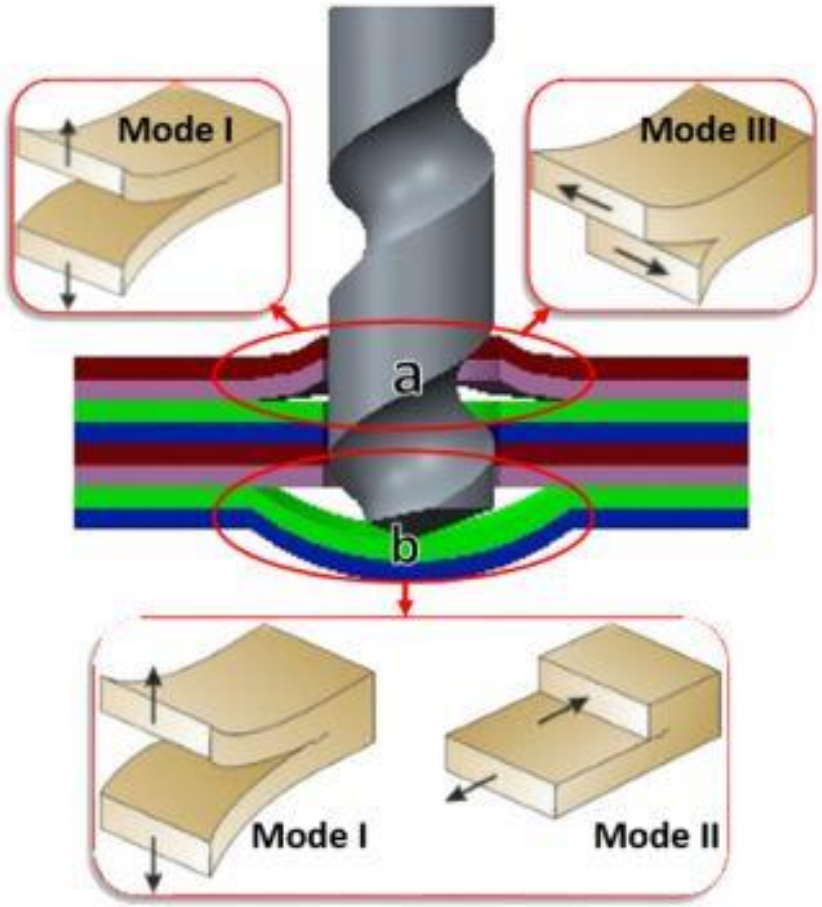

Figure 2-10 Delamination phenomena depicting different Modes during (a) peel-up and (b) push-out type(Ojo et al. 2017)

2.2.5: Finite element approach

There are a number of procedures available to evaluate the strain energy release rate (SERR) to predict delamination onset and propagation. Here three methods are discussed. First, Extended Finite Element Method (XFEM), Second, the Virtual crack closure technique (VCCT) and third process is Cohesive or damage zone models.

2.2.5.1: Extended finite element method (XFEM)

Extended Finite Element Method (XFEM) has been used to model delamination in composite structures. XFEM is especially designed to solve discontinuities in the materials. However XFEM was developed by Ted Belytschko in 1999 for remeshing finite element method for crack growth (Belytschko & Black 1999). Curiel Sosa and Karapurath (Curiel Sosa & Karapurath 2012) used XFEM to simulate delamination growth in metal laminate and Golewski et al (Golewski, Golewski & Sadowski 2012) have employed XFEM to simulate Mode II fracture

propagation in concrete with the additive material of siliceous fly-ash as shown in Figure ***2-11***. Using XFEM for modelling 2D crack showed good agreement with the experimental results. Therefore XFEM could be a likely technique for the failure analysis of composite structures. Grogan et al (Grogan, Leen & Ó Brádaigh) simulate prediction of delaminated growth crack opening displacement (DCOD) for quasi-isotropic laminate under thermal fatigue loading. The benefit of the proposed method can simulate both inter- and intralaminar crack growth in two and three-dimensional geometries. XFEM is suitable for microcrack initiation and propagation (intra-laminar failure), but XFEM does not has ability to simulate delamination growth between plies (inter-laminar failure). Therefore some works use combination of XFEM and cohesive element for modelling delamination in composite materials (Grogan, Ó Brádaigh & Leen 2015; Hu, X. F. et al. 2016; Wang et al. 2017; Yazdani, Rust & Wriggers 2016). Most theories used with finite element to predict failure in composite materials, differ significantly from the experimental observations. These numerical theories are mostly based on continuum approaches. In multiple cracks case the continuum damage is not sufficient to predict the failure. In addition in laminated composite structures when interface cracks (delamination) crosses a ply, the strain energy release rate does not meaningful trends because delamination geometry becomes three dimensions (O.O & J. N 1992), therefore it may be appropriate to look at trends of strain energy release as a function of delamination size.

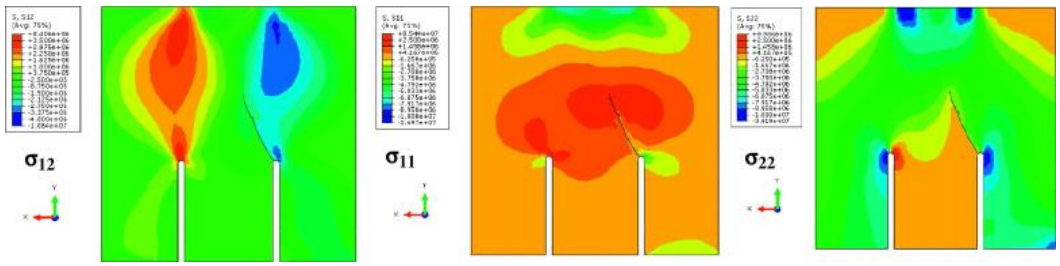

Figure 2-11 Principal stresses at second stage of crack development use XFEM (Golewski, Golewski & Sadowski 2012)

2.2.5.2: Virtual Crack Closure Technique (VCCT)

The VCCT, first suggested by Rybicki and Kanninen (Rybicki & Kanninen 1977) has also been used to predict delamination in laminated composite structures. This technique can be used under assumption of considering the delamination growth

process as a crack propagation phenomenon (Kachanov 1988). With this assumption, delamination can be assigned as a fracture process between laminated layers as inter-laminar damage. The composite structure behaviour in presence of inter-laminar damage and the conditions for the delamination growth initiation can be studied by using fracture mechanics principle. Thus, fracture mechanics concepts can be generally utilised for analysis of delaminated composite structures.

The VCCT is based on Irwin's crack assumption. The assumption suggests that when a tiny crack extends, the energy released in the process is equivalent to the work required to close the crack to its original length. The crack will propagate when the critical value of strain energy rate G_C is equal or less than the strain energy rate G. The three Modes (Mode I, Mode II and Mode III) are shown in Figure ***2-12***. Energy release G_I, G_{II}, and G_{III} respectively, can be calculated from nodal force and displacement achieved using finite element model (Ronald April 2002). Therefore the work "W" required to close the crack can be calculated in two analysis steps.

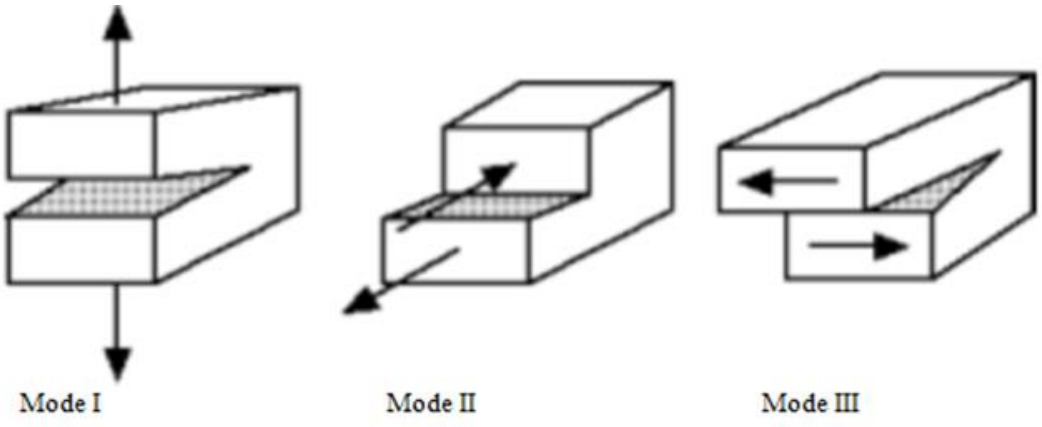

Figure 2-12 Fracture Modes (Ronald April 2002)

The main advantage of VCCT is that it uses strain energy to calculate fracture in materials and can evaluate strain energy release rate in one step but suffers from a disadvantage. The main drawback is that it assumes self- similar propagation, therefore only crack propagation can be predicted. Although VCCT has this drawback, but it has been used by many researchers to model delamination cracks and has provided good results. Two dimensional and three dimensional VCCT methods are used to calculate the distribution of strain energy release rate (SERR) along delamination front (Pereira & de Morais 2004; Pereira et al. 2004; Robinson,

Javidrad & Hitchings 1995; Schön et al. 2000; Shokrieh, Heidari-Rarani & Rahimi 2012). VCCT technique has been used for R-curve for DCB specimens (Shokrieh et al. 2012). The *p*-convergent partial discrete-layer elements with the virtual crack closure technique (VCCT) for the delamination analysis of laminated composite plates by Jae et al (Ahn & Woo 2015). The proposed work is incorporated with VCCT to estimate the energy release rate. Salpekar et al (Salpekar, O'Brien & Shivakumar 1996) have used the VCCT with two other techniques to calculate strain energy release (G) during delamination propagation in laminate composite structures. The virtual Crack Closure technique (VCCT) was used to calculate the distribution of G along delamination front at each delamination length. The elements behind and ahead of the delamination front are orthogonal. This requirement was unfulfilled because the finite element mesh configuration is dictated by the shape of the local delamination. Orthogonal requirement is the basic prerequisite to simulate delamination by VCCT, however Salpekar et al (Salpekar, O'Brien & Shivakumar 1996) regarded that the VCCT gives accurate G distribution front and the delamination though the finite element at the delamination front is not orthogonal. It means that the VCCT may be a robust technique for G calculation in delamination cases. The VCCT technique was developed to evaluate the strain energy release and delamination front. VCCT approach utilises fracture mechanics criteria especially when it combines with interface element (Xie & Biggers 2006). A mixed-Mode fracture criterion is used to predict delamination growth.

$$E_d = \left(\frac{G_I}{G_{IC}}\right)^{\alpha} + \left(\frac{G_{II}}{G_{IIC}}\right)^{\beta} + \left(\frac{G_{III}}{G_{IIIC}}\right)^{\gamma} \geq 1 \qquad (2.1)$$

where E_d is the delamination growth parameter. G_{IC}, G_{IIC}, and G_{IIIC} are the critical values corresponding to Mode I, mode II and Mode III loading, respectively. The exponents constant α, γ, and β were taken as suggested by Kutlu and Chang (Kutlu & Chang 1992). However simulation of delamination growth by VCCT has some difficulties. VCCT technique requires nodal variable and topological information from the nodes ahead and behind the crack tip in addition to its sensitivity to mesh size for calculating fracture parameters (R 2002). Therefore it is extremely difficult to calculate fracture parameters with progressive crack propagation.

2.2.5.3: Cohesive zone models

Cohesive approach as a numerical simulation has been used to simulate delamination in recent decades. This approach is based on the concept of the cohesive crack model. Cohesive damage region is developed near the crack front. The cohesive crack model presented by Dugdale (Dugdale 1960), introduced a concept that a thin plastic zone is generated in front of the notch in thin steel sheet. This concept was further expanded by Barenblatt (Barenblatt, G. I. 1962) who introduced cohesive forces in order to solve the equilibrium problem in elastic bodies with cracks. Hillerborg et al (Hillerborg, Modéer & Petersson 1976) has introduced the concept of tensile strength to allow for existing cracks growth and also to allow for initiation of new cracks. Cohesive zone methods have been used for analysing crack growth in concrete by Hillerborg et al (Hillerborg, Modéer & Petersson 1976). Cohesive damage zone model relate tractions to displacement jumps at an interface where crack may occur as shown in Figure ***3-13***. Therefore the damage is related to the maximum traction in the traction displacement jump equation. The traction-separation relation can be applied to the cohesive elements. The response of the cohesive elements is initially considered linear elastic with penalty stiffness of K_{eff} up to the maximum traction (T_{ult}) where damage initiates. Then, the stiffness of cohesive elements degrades following $K = (1 - D(\delta)) K_{eff}$. The traction reduces to zero and new crack surfaces are formed when the area under the traction-displacement jump equation equal to fracture toughness G_C. The use of cohesive elements can overcome some of the difficulties in numerical simulation of delamination damage, experienced with VCCT technique. Generally, cohesive element technique works within the framework of continuum damage mechanics.

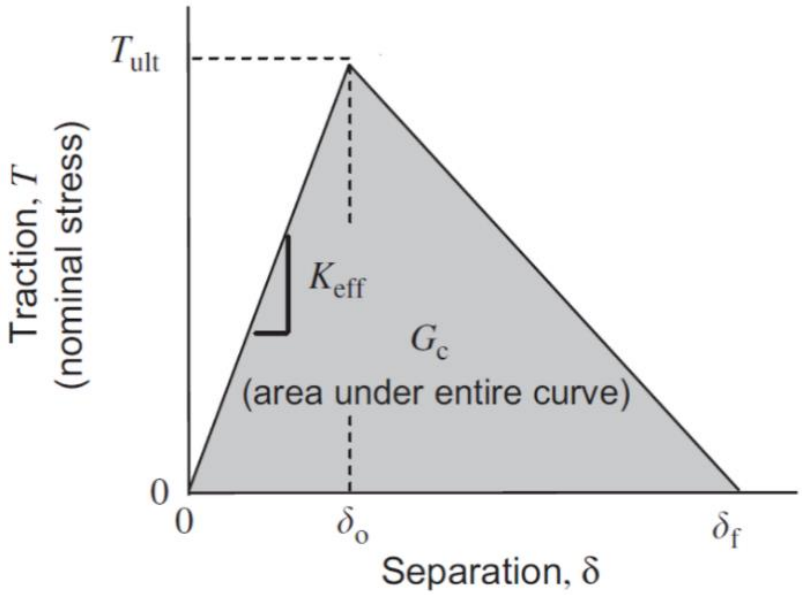

Figure 2-13 Cohesive parameters of typical bilinear traction-separation model(Chen, D & El-Hacha, R 2014)

In order to accurately account for the variation of fracture toughness as a function of Mode ratio in epoxy composites, the mixed-mode criterion has been proposed by Benzeggagh and Kenane (Benzeggagh & Kenane 1996). This criteria is stated as a function of the Mode I, Mode II, and Mode III fracture toughness:

$$E_d = \frac{G_T}{G_C} \geq 1 \tag{2.2}$$

Where G_T is equal to $G_I + G_{II} + G_{III}$ and G_C is equal to

$$G_C = G_{IC} + (G_{IIC} + G_{IC}) \left(\frac{G_I + G_{shear}}{G_T}\right)^{\eta} \tag{2.3}$$

Where$G_{shear} = G_{II} + G_{III}$, and η parameter obtained from Mixed Mode Bending (MMB) tests at different Mode ratios.

Shape and parameters of Cohesive Zone model (CZM) significantly affect the accuracy of finite element modelling of delamination damage propagation in composite materials. Various shapes of traction-separation laws in CZM are presented to provide acceptable results for delamination growth. Figure ***2-14*** shows the common forms of these traction-separation laws. Geubelle and Baylor (Geubelle & Baylor 1998) employed a bilinear CZM to simulate the initiation and propagation of transverse matrix cracks and delamination fronts in thin composite plates subjected to low-velocity impact. A bilinear cohesive zone damage model based on interface finite element modelling has been used by De Moura and de

Morais (de Moura & de Morais 2008) for analyses of End Notched Flexure (ENF) and End Loaded Split (ELS) test. A cohesive beam model for inter-laminar fracture in Mode II is proposed with bilinear cohesive law for finite element analyses by De Morais (de Morais 2011). Bilinear and linear- exponential traction separation model is used with or without considering the initial fracture for the damage process zone during the Mode II delamination damage propagation. In the most of the above mentioned researches the bilinear CZM may give acceptable results for delamination propagation, provided fracture process zone in the region of the delamination crack tip is small (Heidari-Rarani & Ghasemi 2017). In addition the bilinear CZM is suitable for simulating delamination damage when the macroscopic mechanical behaviour of interface in the material system has provided no plastic deformation in the matrix (Chandra et al. 2002). The trapezoidal form of the traction-separation law (Figure ***2-14***(c)) has been suggested by Tvergaard and Hutchinson (Tvergaard & Hutchinson 1992) to examine crack growth resistant in elasto-plastic materials. The ductile interface material can be accurately represented by a trapezoidal CZM law due to its ductility. The shape of CZMs have significant impact on the delamination damage propagation, however if the interface layer is not highly ductile, the interface layer behaviour can still be correctly modelled by any CZM shape law (Fernandes & Campilho 2016). In consideration, of matrix plasticity, micro-cracking and bridging zone in the wake of crack, trapezoidal and trilinear are employed to consider damage mechanisms in the simulation of delamination growth. The trilinear CZM shown in Figure ***2-14*** (d) consists of an initial linear elastic undamaged region and a bilinear softening law. In fact, each branch of linear softening damage process represents a different fracture mechanism in laminated composites such as plasticity, quasi-brittle matrix cracking and fibre bridging. A three-linear CZM obtained from the superposition of two bilinear by (Heidari-Rarani, Shokrieh & Camanho 2013) has been shown that it is possible to obtain an R-curve response and long process zones by superimposing two different bilinear traction-separation laws.

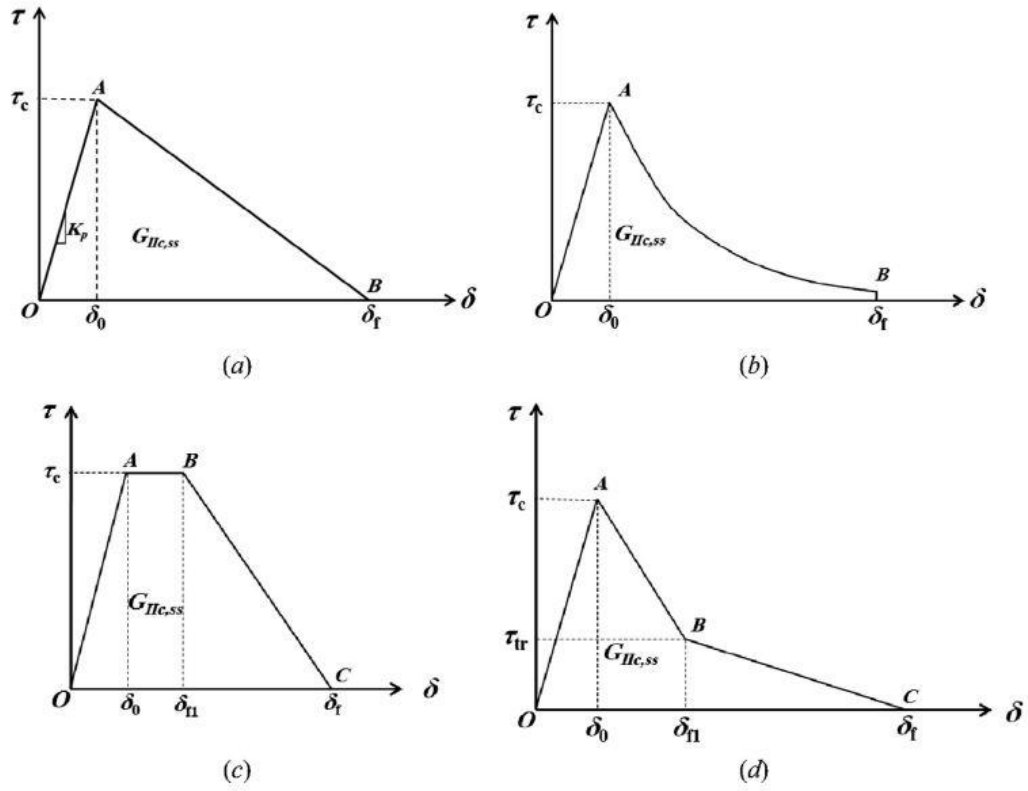

Figure 2-14 Different forms of traction-separation laws: (a) Bilinear form, (b) linear-exponential form, (c) trapezoidal form, and (d) trilinear form (Heidari-Rarani & Ghasemi 2017)

Bilinear and linear-exponential traction-separation forms are common forms used in commercial finite element package ABAQUS. Other traction-separation laws can be used to define the cohesive zone behaviour in ABAQUS through input of tabular data that relates damage variables to displacement. The bilinear is preferred due to its simplicity (it only needs three independent parameters, i.e., steady-state fracture toughness, interface strength and penalty stiffness, to fully describe the fracture process) and due to its relative accuracy in the prediction of delamination growth in composites with small fracture process zone (FPZ) or small-scale bridging. However, some researchers have determined that the traditional bilinear cohesive zone model (CZM) cannot capture the fracture behaviour of laminated composites in the presence of large-scale fibre bridging. In order to overcome this problem, researchers have built appropriate user subroutine to simulate actual damage process. A user subroutine with the superimposed cohesive laws was employed in ABAQUS user element by (Heidari-Rarani, Shokrieh & Camanho 2013). In this user subroutine, two parallel groups of two-parameter CZMs were defined. The proposed method shows good correlation with experimental results

for the R-curve results. Konstantinos et al (Anyfantis & Tsouvalis 2011) have proposed model to consider the existence of a bridging zone and of a cohesive zone in front of the physical crack tip for unidirectional glass/epoxy End Notch Flexure (ENF) coupons. For this purpose two traction– separation models were employed for the representation of the fracture process zone (FPZ) developing during the delamination propagation process.

The advantages of CZM is its simplicity, unification of crack initiation and progression within one model (Heidari-Rarani & Ghasemi 2017). Cohesive zone model has been employed to simulate and evaluate delamination damage crack propagation in different composite structures. Due to the flexibility of cohesive element, Mohamed et al (Mohamed et al. 2017) used two cohesive laws for prediction of delamination propagation for z-pin and unpinned reinforced laminated composite. The results show that user-defined cohesive element is capable of describing both the resin-rich interface layer and the large scale bridging mechanism of the pins. A string-based cohesive zone model (CZM) for inter-laminar delamination is developed by Zhang et al (Zhang, Gao & Yu 2017). This cohesive zone model is validated through a series of simulation results. Zero thickness cohesive element approach using both the bilinear and exponential cohesive laws is employed by Tabiei and Zhang (Tabiei & Zhang 2017). The bilinear law shows more definitive behaviour in case of cyclic loading than exponential. Choice of right cohesive stiffness, element size and bilinear cohesive law can decrease the computational time, limited due to artificial compliance. Zou and Lee (Zou & Lee 2017) have proposed method to include both friction and enhanced interfacial shear strength in a cohesive element. The proposed Mode is employed to simulate delamination damage in specimens with cut and dropped plies and its prediction are in coherence with available experimental data. Panettieri et al (Panettieri, Fanteria & Danzi 2016) investigated the effect of cohesive element parameters (the inter-facial strengths and the cohesive mesh size) in CAI impact test for propagation of delamination damage after impact. The study showed that the cohesive element parameters affect accuracy and the computational cost. Cohesive Zone modelling (CZM) technique has been used to determine position of the crack tip during propagation of Mode I delamination in the glass/epoxy composite specimens by Saeedifar et al (Saeedifar et al. 2015). Due to poor

performance of CZM method, a modified CZM of the inter-laminar fracture toughness is proposed to calculate the delamination damage propagation. Modified CZM method shows better performance to detect initiation delamination damage stage in the laminated composite structures. In the proposed model a fracture toughness function which reflects the variation of fibre bridging traction is considered instead of constant fracture toughness. Both the DCB and MMB test are used to examine the proposed model. The result gives evidence of the effectiveness (viscosity coefficient and the variation of fibre bridging tractions) of the proposed model.

2.3: Measurement of Fracture Toughness

There are three fracture Modes in composite structures. Each Mode need fracture toughness property. Energy method has been adapted to measure fracture toughness property in this research. A standard specific method Double cantilever beam (DCB) will be used to measure the fracture energy G_I for Mode I. End-notched flexure (ENF) standard will be used to evaluate fracture energy G_{II} for Mode II. Mode III corresponds to less commonly test inter-laminar "scissoring" shear loading. Finally the mixed fracture energy for Mode I/II will be evaluated by mixed Mode delamination using Cracked Lap Shear (CLS) test.

2.3.1: DCB Test (Mode I delamination test)

The DCB test is designed for determination of composite Mode I inter-laminar fracture toughness (G_{IC}). The DCB specimens usually consist of composite specimen with insert at mid-plane (Figure ***2-15***) to serve as starter crack. Load is applied through the metal hinges bonded to the end of the specimen. The crack length is measured along the specimen edges. G_{IC} is computed by measuring crack length, applied loading, and load-point deflection. DCB test is popular method to characterize Mode I delamination damage of composite structures. This test was initially described in the ASTM standard (ASTM1990) and has been developed more recently in British standard (BSI2001) and the international standard (ISO2009). ASTM D 5528-13 Standard (International 1994) employed shear corrected beam theory to evaluate crack initiation in metallic materials. The data analysis method is usually based on linear beam theory. However, the DCB specimen test is suitable for limiting deflection to the geometrically linear range.

Basically there are two different LEFM methods, namely the area and compliance method to record fracture data. There is good agreement between fracture values with the area and compliance methods (Hashemi, Kinloch & Williams 1989). However this relationship is poor with values obtained from the "load" and "displacement" methods based on simple beam theory (Nageswara Rao & Acharya 1995). These inconsistencies are due to several factors, like errors in crack length and displacement measurements, shear correction (Yoshihara & Satoh 2009), large displacement correction (Williams 1987) and fibre bridging effect. It is observed that none of these possible errors are significant enough to eliminate the discrepancies and correct the analytical method. Another source of error in DCB simple beam analysis is the belief that the beams are built-in cantilevers (i.e., the slope and deflection are zero at the crack tip of the DCB specimen).

Different geometrical parameters such as initial length, width and thickness may affect the R-curve in DCB specimens. It means that, R-curve is a geometry-dependent property (Tamuzs, Tarasovs & Vilks 2001). Shokrieh et al (Shokrieh, Salamat-talab & Heidari-Rarani 2014) investigated the effect of initial delamination length on Mode I bridging law of unidirectional E-glass/epoxy double cantilever beam (DCB) specimens using digital image processing method. They concluded that the shape of bridging law and energy dissipation in bridging zone is slightly affected by change in crack length. Sou et al (Suo, Bao & Fan 1992) showed that specimen size and geometry do not influence on the steady state toughness of a slender DCB. The effect of thickness and initial delamination crack on the R-curve behaviour of unidirectional E-glass/epoxy DCB specimen is evaluated by Shokrieh et al (Shokrieh, Heidari-Rarani & Ayatollahi 2012). The result shows that the R-curve shape does not change within a specific range of initial crack length to thickness ratios (i.e., $8.5 < a_0/2h < 19$). This is because there is no change in initiation and propagation of delamination toughness and length of bridging zone. The effect of stacking sequence on R-curve behaviour E-glass/epoxy DCB laminates with 0°//0° has been studied by Shokrieh et al. (Shokrieh & Heidari-Rarani 2011). The experiments show that the stacking sequence has significant effect on initiation and propagation of delamination toughness, however effect on the bridging length could not be proved. Another work is by Shokrieh et al. (Shokrieh, Salamat-talab & Heidari-Rarani 2016) for

investigating the effect of interface fibre angle on the R-curve behaviour of double cantilever beam (DCB) specimens made of E-glass/epoxy under Mode I loading. Results indicate, that the interface angle has significant impact on the steady-state inter-laminar fracture toughness as well as the bridging zone length. Due to good penetration of two adjacent layers of the delamination interface for CB specimens with 0°//0° interface, lowest initiation inter-laminar fracture toughness and the greatest bridging zone length were able to be recorded.

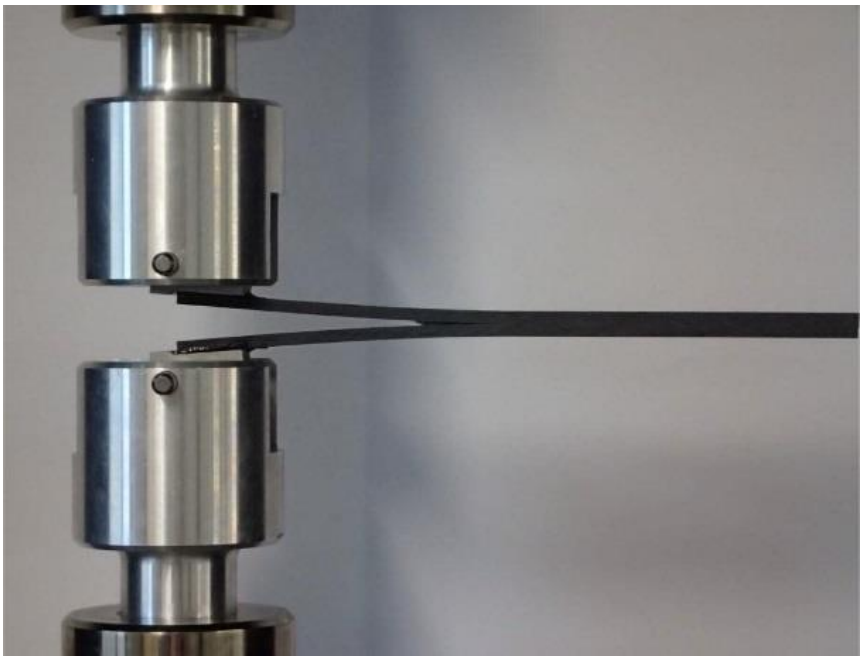

Figure 2-15 DCB test specimen under testing on the test machine (Bin Mohamed Rehan et al. 2017)

2.3.2: End Notched Flexure ENF test (Mode II)

The ENF test, shown in Figure ***2-16*** is one of the widely accepted test for characterizing Mode II inter-laminar fracture toughness. For Mode II testing, the three-point End Notched Flexure (ENF) test was standardized as ASTM D 7905 in 2014 (International 2014). This test is designed to measure the inter-laminar fracture toughness under in-plane shear deformation Mode. In ENF test, the load is applied at the centre. The specimen is rested on the two outer rollers. The total span between outer roller to the mid of the span is L/2. An artificial delamination crack is inserted in the mid-plane at specimen end. The end notched flexure (ENF) test is a suitable method for measuring the Mode II delamination toughness (Davies, Blackman & Brunner 1998).

ENF tests conducted by many researchers demonstrate that several factors contributed towards critical strain energy release rate for crack growth. First factor states that instability of ENF test leads to determination of initiation value but not resistance curves. Carlsson et al. (Carlsson, J.W. Gillespie & Pipes 1986) proposed a simple design for sizing the ENF specimen to minimize geometric nonlinear response and to avoid nonlinear material behaviour or flexural failure. The large thickness to length geometry is required for tough resin systems to reduce inter-laminar shear effect (M'Membe et al. 2016). Second, the issue of friction contributions was raised and this lead to question whether Mode II data is to be regarded as apparent value with no significance as materials data (O'Brien 1998). The influence of friction in the 3ENF has been investigated numerically by Carlsson et al.(Carlsson, J.W. Gillespie & Pipes 1986). The results show that the influence on G_{IIc} values would be less than 5% for most cases for friction coefficient range 0 to 0.5. Nevertheless, the 3ENF specimen appeared satisfactory.

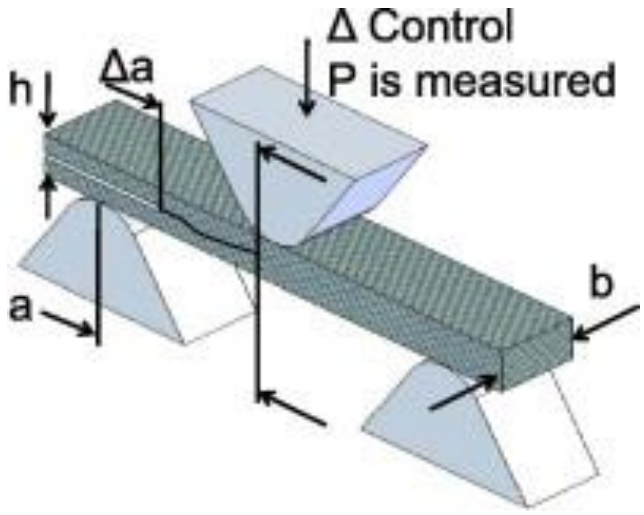

Figure 2-16 ENF test set up and determined parameters (Pankow et al. 2011)

2.3.3: Cracked lap Shear Mixed Mode (I/II)

In actual composite structures, delamination is subject to a combination of loading Modes and, thus, the fracture toughness corresponding to mixed-Mode delamination growth is required. Here, therefore, focus is on Mixed Mode (Mode I and II) testing, for which standardized tests exist. A cracked lap shear (CLS) specimen in mixed Mode condition is one of the specimens that have been widely used for characterizing fracture toughness and studying fracture behaviour of adhesively bonded joints as shown in Figure ***2-17***. It can also be used to simulate

delamination of composite laminate and skin-flange deboning (used in engineering structures).

Brussat et al, (1977) (Brussat, Chiu & Mostovoy 1977b) proposed the Cracked Lap Shear (CLS) specimen to investigate the mixed Mode fracture behaviour of shear loaded adhesive joints. The cracked lap shear (CLS) has been extended to investigate adhesive joint deboning (Cheuk & Tong 2002; Li et al. 2015; Moya-Sanz, Ivañez & Garcia-Castillo 2017; Rhee 1993; Ribeiro et al. 2016) and delamination damage in composites (Rhee 1994). However the mixed Mode cracked lap shear (CLS) test is originally developed for testing adhesively bonded metallic joints. In CLS test, the applied loading (P) and dc/da in equation (2.4) can be substituted directly to calculate the inter-laminar fracture toughness, $G_{I/II}$. Alternatively, the expression of Russell and street (Russell & Street 1985) can be used to calculate $G_{I/II}$;

$$G_{I/II} = \frac{P^2}{2b^2}\left[\frac{1}{(Eh)_2} - \frac{1}{(Eh)_1}\right] \tag{2.4}$$

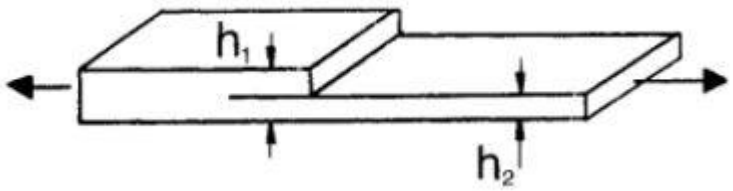

Figure 2-17 CLS specimen for mixed Mode inter-laminar fracture tests

Where the subscripts 1 and 2 refer to the sections indicated in Figure ***2-17***. Beam theory gives value $G_I/G_{I/II}$=0.205 for unidirectional specimens with delamination placed at the mid- plane(Brussat, Chiu & Mostovoy 1977a). The large rotation at tip of crack and complex analysis for the crack tap shear (CLS) can be considered a significate disadvantage, leading to its limited use (Szekrényes 2006).

2.4: Structural Health Monitoring concepts for identification of damage growth

2.4.1: Introduction

The process of systematizing condition assessment of structures by observing and interpreting their in-serving response is called Structural Health Monitoring (SHM). It can be estimated that SHM is a new and improved approach to allow

Non Destructive Evaluation (NDE). The diagnosis of SHM system involves the integration of sensors, possibly smart materials, data transmission, computational power, and processing ability inside the structures (Daniel 2010). SHM can measure damage as change in material properties. Long term, the output of this process is systematic and consistent updated information regarding the ability of the structure to perform and expected aging and degradation due to operational environment. The SHM process involves regular observation of the system with different equipment, such as IR camera (thermography) and FBG sensors. These technologies have been extensively enhanced for use in laminated composite structures over last few years (Kahandawa & Hafizi 2012).

The improvement in safety strongly motivates, development of a SHM system, due to unsatisfactory maintenance. Over last few years a number of accidents related to delamination in composite structures could have been avoided. Delamination damage propagation caused the loss of upper rudder of Concorde G-BOFA (Figure ***2-18***) during a flight from Christchurch, NZ, to Sydney, Australia on 18 April 1989. It is considered that the incident happened when the delamination damage spread over a large area of the rudder which had progressively reduced the stiffness of the surface until it was inadequate to withstand the in-flight stresses.

Figure 2-18 Losing upper rudder of upper rudder of Concorde G-BOFA due to delamination damage. The photograph was taken at Sydney by Ken Watson, at that time a Qantas Engineer (http://www.concordesst.com/latestnews_02_1.html)

Many non-destructive techniques have been developed over past decades for detection and the propagation of delamination in composites. Acoustic emission (Lagunegrand et al. 2006; Saeedifar et al. 2015), thermography (Colombo & Vergani 2014), lamb wave(Chiu, Rose & Nadarajah 2017) and full field non-contact optical methods (Haj-Ali & Elhajjar 2014; Haj-Ali et al. 2008; Johnson 2014) are some of the major technologies in place at the moment. Examination of damages in Glass/Epoxy composite using infrared imaging techniques for detecting crack propagation, and subsequent delamination in composite materials has always been a challenge due to complex temperature variations caused by the heating methods. Many researchers have put in significant effort to overcome these challenges. In a recent study (Ghadermazi et al. 2015) used Discrete Fourier Transformation (DFT) to process the *"Step Heating"* thermography data to obtain phase images which are more accurate to quantitatively characterize the defect depth and dimensions in composites. Another recent work of (Meola et al. 2015) has used *lock-in* thermography and Phased Arrayed Ultrasonic Techniques (PAUT) for identification of both size and location of the delamination of an impact damage. The false signals were exuded using locked-thermographic module, which controls the frequency of the heating source. They concluded that the accuracy and the correlation of results from both testing have a high acceptance rate. In recent years a similar method to lock-in thermography & PAUT, "thermos-sonic" and infra-red (IR) thermography methods were used successfully for detecting delamination in polymer matrix laminates (Kuhn, Valot & Herve 2012). Although the thermographic method provides an excellent detection capability for delamination in composite, several false thermal signals makes it hard to quantify the extent of damage. This significant problem was extensively investigated and found that synchronization of applied cyclic loading with the infrared signal could successfully filter out spurious thermal signals (Johnson 2014).

2.4.2: Infrared thermography (IR Thermography)

Thermography is the investigation of the surface temperature of a body by infrared ray's detection via thermal-camera. This technique basically depends on modification of the surface temperature during thermal and mechanical loading applications. In past thermography technique was used in many isotropic material applications. Recently thermography technique has been extended to detect

damage and defects in composite structures. This technique has ability to detect damage Modes in composite structures successfully as much as in isotropic materials. This technique being of non-destructive nature, has been widely applied for quick inspection of large components (Colombo & Vergani 2014; Colombo, Vergani & Burman 2012).

Infrared thermography has both qualitative and quantitative analysis. Qualitatively, this technique can detect the damages of several different types of composite structures such as delamination, fibre-matrix debonding and defects. Thermoelastic Stress Analysis is an example of thermography-based quantitative analysis, This experimental process of stress measurement is based on the thermo-elastic effect (Greene, Patterson & Rowlands 2008).

The Thermoelastic effect was given a theoretical foundation by William Thomson (Lord Kelvin) in 1853. Thomson (Thomson 1853) presented a linear relationship between the temperature change of a solid and the change in the sum of principle stress for isotropic materials:

$$\frac{\Delta T}{T_0} = -K_0 \Delta\sigma \tag{2.5}$$

Where, T_0 is the average temperature of the solid, $K_0=\lambda/\rho\ C_p$ is the thermoelastic constant, λ is the linear thermal expansion coefficient, ρ the mass density, C_p the specific heat at constant pressure, and $\Delta\sigma = \Delta(\sigma_1+\sigma_2+\sigma_3)$ is the variation of the first stress invariant. This equation formulated for a homogeneous isotropic materials, has also been extended to orthotropic materials, by considering different thermoelastic constants in each direction, due to anisotropy (Colombo, Vergani & Burman 2012; Greene, Patterson & Rowlands 2008):

$$\rho C_p \frac{\Delta T}{T_0} = -(\alpha_{11}\Delta\sigma_{11} + \alpha_{22}\Delta\sigma_{22} + \alpha_{33}\Delta\sigma_{33}) = \alpha_{ii}\Delta\sigma_{ii} \tag{2.6}$$

Under tensile static load composite materials, same as other isotropic materials experience an initials decrease in surface temperature due to thermoelastic effect. The surface temperature decreases with increasing extension load. Temperature deviates linearly till a minimum and then it starts to increase as shown in Figure ***2-19***.

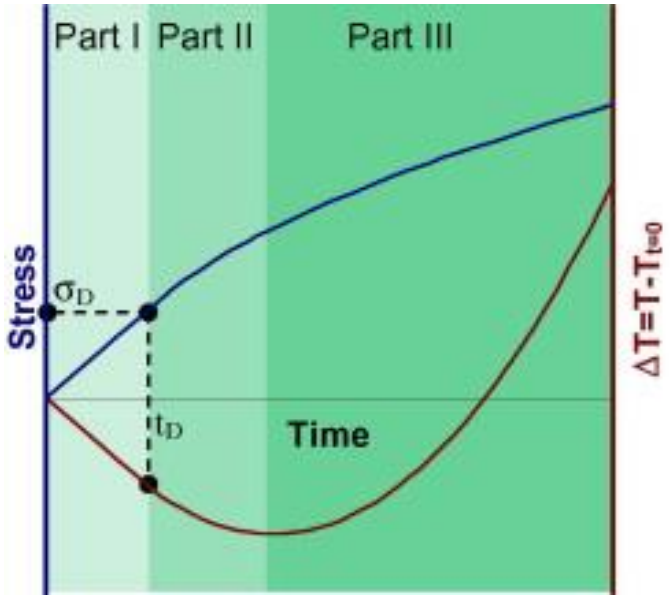

Figure 2-19 Schematic representation of the typical stress and temperature trends as a function of time, during a static tensile test (Colombo, Vergani & Burman 2012)

Application of thermography to dynamic loads can be taken into account, under assumption that the surface temperature changes can be accepted during cycling load. Depending on experimental observation, during fatigue the surface temperature of the loaded samples tends to reach a constant value (La Rosa & Risitano 2000). After initial thermal response, temperature increases (ΔT) during cycling (Δ*N*), thus the ratio $\Delta T/\Delta N$, is a typical feature of each tested material and it can be related to the applied stress as shown in Figure ***2-20***.

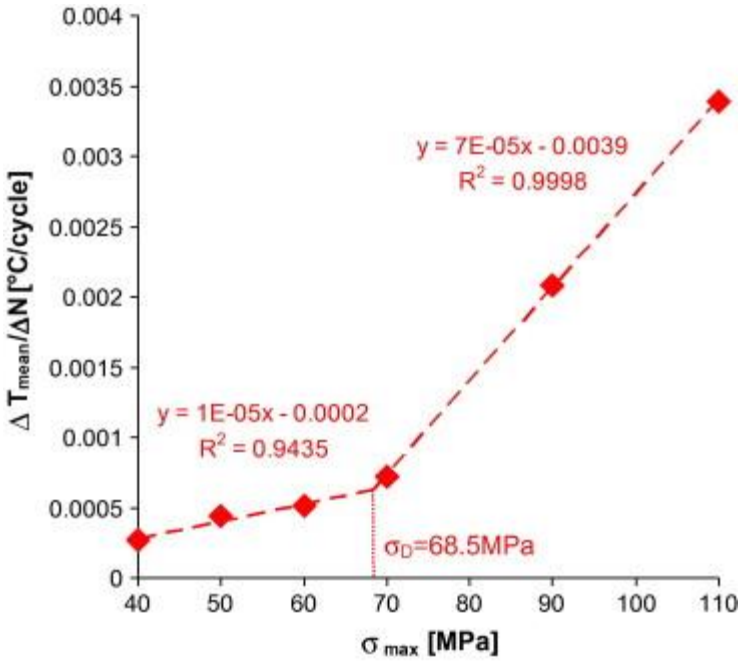

Figure 2-20 Schematic representation of the classic ΔT/ΔN trend with respect to the stress amplitude(Colombo, Vergani & Burman 2012)

Non-destructive TSA method has shown a capability to estimate damage in composite structures. Many recent studies have shown that the TSA based techniques are powerful tools for estimating damage in fibre reinforced polymeric materials. A study carried out on a damage in a single lap joint using TSA and correlated to microstructural analysis in carbon fibre/epoxy composite (Haj-Ali & Elhajjar 2014), has proved the ability of TSA method to capture early stages of damage in bonded joints. However, the investigation of the delamination by TSA is a relatively limited research field and extended studies are warranted to investigate robust techniques to use on a wider range of FRP materials.

The Non- interferometric techniques such as the grid method and digital image correlation (DIC) generally have less stringent requirements under experimental conditions. The DIC technology determines the deformation by comparing the grey intensity changes of the object surface before and after deformation (B. Pan et al. 2009). DIC techniques have been applied to detect deformation in homogeneous materials. and has been successfully extended to investigate the initiation and propagation of damage in composite materials (Crupi et al. 2015). Although DIC techniques have shown significant achievements in composite material field, unfortunately some limitations and errors still remain in the data processing algorithms. Furthermore DIC is not able to accurately measure strain near the cracks due to high strain concentration and considered as a nano-scale stress analysis method.

A recent advance in low-cost microbolometer technology has reduced the high capital cost of the traditional TSA system. Using these recent advances, a TSA system called MITE© was developed by Defence Science Technology Organisation (DSTO) of Commonwealth of Australia. The complete details can be found in (Nick Rajic & Rowlands 2013; Rajic N., Weinberg S. & D. 2007). The references details MITE© system's capabilities and has shown that the low-cost microbolometer device is affordable and better suited for in-service applications. The major advantage of the MITE© system is flexibility of usage in a wider range of applications such as civil, maritime and aerospace sectors because of its small

size, tolerance to shock and vibration and low power consumption compared to its *photon* counterpart.

2.4.3: Embedded FBG sensor and Strain measurements

Fibre Bragg grating (FBG) sensors have undergone a rapid development in the recent years. They are lightweight and have small physical dimensions, suitable for being embedded a structure. The main advantages of FBGs over other fibre sensor is its low cost, good linearity, wavelength multiplexing capacity, resistance to harsh environments and the transduction mechanism. FBG's are small and therefore they do not affect the properties of composites in which they are embedded in smart structures. These features allow engineer's to add functionality in composite structures for monitoring similar to nervous system in human body.

When light is made to pass through the grating, at a particular wavelength (Bragg wavelength), the light reflected by the varying zones of refractive indices will be in phase and amplified as shown in Figure ***2-21***.

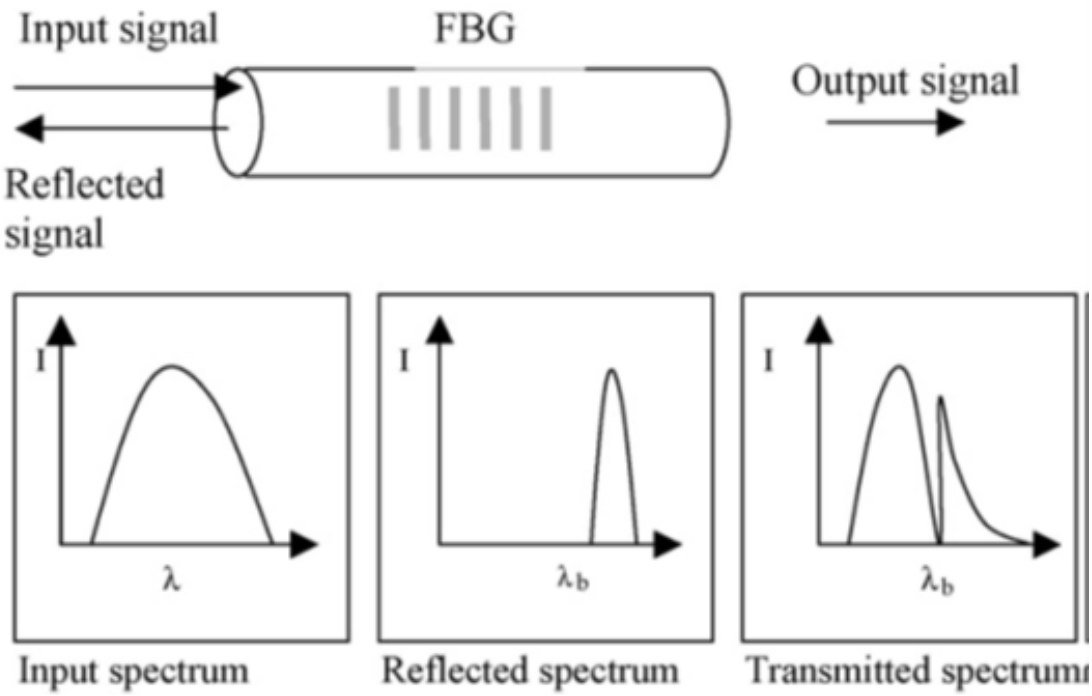

Figure 2-21 Transmission and reflection spectra from an FBG.

The Bragg wavelength is expressed as;

$$\lambda_B = 2n_{eff}\Lambda \qquad (2.7)$$

Where λ_B is the Bragg wavelength, n_{eff} is the effective refractive index of the FBG and Λ is the grating period.

Embedded FBG sensors in composite structures are used to evaluate stain changes and detect damages. FBG sensing technology for detection delamination growth is a growing practice. However delamination growth cannot be captured alone with FBGs, this is due to the non-homogenous strain field near the delamination. The non-uniform strain that results from delamination cracks causes the FBG's reflected spectral response to have multiple-peaks, with no single means of interpretation (Sorensen et al. 2007). Some researchers have used short gauge length sensors or bonding the sensors to the surface damage under static loading to overcome this difficulty. Most of the theoretical models depend on micromechanical approach. Micromechanical approach can be used to calculate delamination. VCCT approach and cohesive damage methods are widely used to calculate strain energy rate associated with delamination growth. Optical experiment methods used to detect delamination damage growth in composite structures are Infrared thermography and FBG sensors. Each model shows advantage and disadvantage to detect delamination growth.

Recent advances in fibre optic sensor technologies have provided great opportunities to develop techniques for characterising and detecting delamination initiation and propagation in composite materials (Alfredo, Antonio & Soller 2010; Ying et al. 2003). Much research work has been done for detecting internal damage in composite structures using Fibre Bragg Grating (FBG) sensors. Yashiro et al. (Yashiro et al. 2005) investigated the relationship between the multiple damage states of the laminate and the complicated reflection spectrum of the FBG sensor using a numerical model which could maps strain field around the damaged region. They concluded that the FBG sensor spectra significantly changes relative to the crack size. Sans et al. (Sans et al. 2012) used 8 mm long FBG sensor to locate the crack tip in a carbon/epoxy unidirectional sample which was subjected to mix mode fracture situation. It was found that with the FBG sensors an axial strain field measured within the grating can be used to determine the location of the crack tip. Okabe and Yashiro (Okabe & Yashiro 2012) analysed the reflected spectrum of embedded FBG sensors using a strain field simulated by layer-wise finite-element analysis using cohesive elements for damage extension in single holed CFRP

laminated plate under static and fatigue loading. Takeda et al. (Takeda, Okabe & Takeda 2002) studied the quantitative detection of delamination in CFRP cross-ply laminates under four-point bending test loading using the small-diameter FBG sensor. Then, Takeda et al.(Takeda et al. 2005) applied the small-diameter FBG sensors to the monitoring of delamination size in the CFRP laminates subjected to low-velocity impact. Sorensen et al.(Sorensen et al. 2007) used FBG strain data to characterise fibre bridging tractions during delamination using long FBG sensors embedded parallel to the delamination plane in DCB specimens. Stutz et al.(Stutz, Cugnoni & Botsis 2011) used an array of several short FBG sensors to measure the strain fields in the proximity of the delamination crack tip under monotonic and fatigue loadings. Kahandawa et al. (Kahandawa, Gayan C. et al. 2013; Kahandawa, G. C. et al. 2013) revealed a novel configuration of FBG sensors to acquire strain readings to overcome practical constraints and the engineering challenges associated with FBG-based SHM systems. Kakei et al.(Kakei et al. 1-3 september 2015) used FBG and Thermoelastic Stress Analysis (TSA) engagement techniques to detect and monitor accumulation damage in glass fibre reinforced composite under fatigue loading. Yu et al.(Yu et al. 2016) used a novel phase-shifted fibre Bragg grating (PS-FBG) system to identify the acoustic emissions (AEs) of damages in a CFRP cross-ply laminate. The system has shown a great potential for a practical SHM system for CFRP laminates because it considers advantages of the FBG sensor.

2.5: Summary

As shown GFR composites have been used in many different applications. These materials have shown significant potential for the development of new structures that has resistance to the impact of weathering and degradation in severe environments. The critical review of the literature has provided significant information on damage Modes in GFR composites and reasons for damage propagation. It has also given an indication on the damage behaviours in GFR composites. As explained above, there is no specific method for prediction and propagation damage modes in GFR composites due to its anisotropic behaviour. It is therefore; important that for effective and safe recommendations for utilization of composites, through knowledge of its damage behaviours is required. This information is important in order to avoid unexpected and sudden failures in GFR

composite members. Many damage models in GFR composites have been reviewed in this chapter, including theoretical and experimental methods. It is found that each model has different limitation regarding detection and prediction of damage Modes, in particular, delamination damage Mode. Theoretically, Cohesive elements show better results of simulation delamination damage, but to examine delamination crack, cohesive elements need to build accurate user subroutine Umat such as State Damage Variables (SDVn) for evaluating crack tip and local bending in cohesive element. Experimentally, embedded delamination damage crack cannot be easily seen visually. Prediction of delamination damage growth is not easy due to complexity of strain measurement at the delamination damage crack tip. Research model should investigate the delamination crack tip strain to predict propagation of delamination damage. On same note, strain mapping for damage accumulation may provide accurate information for embedded delamination damage situation.

Delamination damage mode is the most common failure modes of GFR composite. Several innovation techniques have been proposed to overcome the difficulty in detecting this damage. Recent advancement in fibre optic sensor technologies have provided a good opportunity to detect delamination damage in GFR composite. Embedded Fibre Bragg Grating (FBG) sensor was employed to detect delamination damage but it was used for detecting delamination in specific area. Research models could be based on micromechanical approach and measurement of strain at tip of delamination crack utilising embedded FBG sensor to assist with development of accurate model to predict and investigate delamination crack stability. Thermoelastic Stress Analysis (TSA) was used to detect delamination damage in composite. Unfortunately due to resin between layers of composite, it could not measure the change of strain and temperature exactly. In addition TSA technologies only provides the changes of the strain ($\Delta\varepsilon$) and changes of temperatures (ΔT) which cannot be used to calculate the strain at the tip of delamination damage. On the other hand, this technology may help to find the tip of delamination crack and with strain mapping. Engaging TSA with embedded FBG sensor may provide accurate delamination crack tip detection results for FBG sensor and the mathematical model. To author's best knowledge, there has been no studies conducted for investigating the elasto-plastic delamination crack tip strain

using FBG sensor to predict delamination crack growth and TSA technique in GFR composite. The above mentioned issues have been the main motivation of this study to develop accurate model for predicting and detecting delamination damage behaviour of GFR composite materials

Chapter 3: ELASTO-PLASTIC DAMAGE MODELLING FOR LAMINATED COMPOSITE MATERIALS

Associated publication:

Kakei, AA, Islam, M, Leng, J & Epaarachchi, JA 2018, 'Use of An Elasto-Plastic Model and Strain Measurements of Embedded Fibre Bragg Grating Sensors to Detect Mode I Delamination Crack Propagation in Woven Cloth (0/90) Composite Materials', *Structural Health Monitoring*, vol. 17, no. 2, pp. 363-78.

Kakei, A & Epaarachchi, JA 2018, 'Use of Fibre Bragg Grating Sensors For Monitoring Delamination Damage Propagation in Glass-Fibre Reinforced Composite Structures', *Frontiers of Optoelectronics*, vol. 11, no. 1, pp. 60-8.

3.1: Introduction

Modern understanding of the fracture behaviour of brittle materials like glass stems from the important research of Griffith (Griffith 1921). The Griffith theory of fracture, which depends of linear elastic fracture mechanics, has been applied widely to the fracture of glass and metals, and more recently to polymers. It is considered that propagation of a crack in a perfectly elastic material can be analysed at small elastic strains. Subsequent work has further shown that it can also be applied for situations involving localized plastic deformation (not for general yielding in the specimen) at the crack tip (Ward & Sweeney 2004).

Linear Elastic Fracture Mechanics can only deal with limited crack tip plasticity. The plastic zone must be small compared to the crack size. The cracked body as a whole should behave in an approximately elastic manner. In case of extended crack tip plasticity, the problem should be treated elasto-plastically. The concept of Elastic-Plastic Fracture Mechanics (EPFM) is complex, therefore it is not as well developed as Linear Elastic Fracture Mechanics (LEFM) (Michael, Jan & Russell 2004).

In CLPT, FSDT and higher order theories the stresses and strains of a laminated composite plate are depending on in-plane deflections of midplane and its curvatures. The classical laminated plate theory (CLPT) is found to be adequate for most applications where the thickness of the laminate is small. When the classical laminated plate theory is not applicable, a refined theory is used such as the first order shear deformation plate theory (FSDT) or higher order theories. The FSDT

yields a constant value of transverse shear strain through the thickness of the plate, and thus requires shear corrections factors. Despite the use of high order theories gives the increase accuracy and represents the true distribution of the strain through thickness, but the increase accuracy is outweighed by the increase in the number of unknown constants and increased accuracy with an increase in computational effort (Reddy JN. 2004). The classical plate theory (CLPT) is adequate for the analysis the thin plates, especially when the transverse deformation is negligible. Laminated composite plates used here are comparatively thin and therefore the shear deformation in thickness direction can be neglected. The classical laminate theory CLPT is based on the classical plate theory of Kirchhoff-Love, i.e., it neglects the shear deformation in the thickness direction of the laminate. As such in this study, CLPT is sufficient to calculate stress and strain at the delamination crack tip.

Using structural health monitoring techniques to detect internal damages and investigate composite structures has been developed in last few years. Many advanced technologies have been used such as optical sensors for that purpose. However, it is equally important to develop a model that can accommodate sensor input and the fracture mechanics. The sub-damages such as local delaminations, voids and imperfections during manufacturing are critical issues affecting the life time of composite structures. Unfortunately, damages modelling of laminated composite structures have been remaining as an unresolved problem for many years because of the properties of laminated composite are not continuous.

The sub-damage such as local delaminations and voids and imperfection productions in composite structure is critical issue. It is not easy to model these types of damages in laminated composite structures because the properties of laminated composite are not continuous. However, Tuskrov and Kachanov (2000) have presented model for discussing damage in anisotropic media which has an excellent potential to use in laminated composite materials. Unfortunately, the use of Tuskrov and Kachanov directly in laminated composite materials is prohibitive as properties of the layers of composite laminate changes layer by layer and therefore the properties of the materials through the thickness are not constant. Due to this reason Tuskrov and Kachanov theory needs to be extended to use with laminated composite materials. Therefore, in this chapter a modification of Tuskrov and Kachanov has been presented to simulate and evaluate stress

concentration in the damage lamina and calculate changing of strain due to sub-damage through the thickness.

All models in review have not considered exact delamination damage propagation and find failure. None of existing models can predict the damage because they do not consider nature of damage. In this chapter a model has been proposed to investigate delamination propagation in laminate composite structure using both embedded Fibre Bragg Grating (FBG) sensor strain measurement and Fracture energy. The model will provide an early warning about possible fractures in composite structures. This model is based on the elasto-plastic strain at the crack tip as the major input metric. The proposed model is based on the fracture mechanics of composite material, the prediction of the model can be considered as significantly higher levels of accuracy than the existing delamination damage models.

3.2: Fracture mechanics concepts

Many theories have been applied to explain and simulate fracture in materials. Griffith fracture theory considered that fracture produces a new surface area and suggested that for fracture to occur, the increase in energy required to produce the new surface must be balanced by a decrease in elastically stored energy. In general the growth of the crack depends on amount of work *dW* on the system by external forces and a change *dU* in the elastically stored energy *U*. the difference between these quantities, $-dU$, is the energy available for the formation of the new surface. The growth of a crack by a length da can be defined as:

$$\frac{dW}{da} - \frac{dU}{da} \geq \gamma \frac{dA}{da} \tag{3.1}$$

Where γ is the free surface energy per unit area of surface and *dA* is the associated increment of surface.

A crack in a solid consists of disjointed upper and lower faces. The join of the two crack faces forms the crack front. The two crack faces are usually assumed to lie in the same plane before deformation. When the cracked body is subjected to external loads (remotely or at the crack surfaces), the two crack faces move with respect to each other and these movements may be described by the differences in

displacements ux, uy, and uz between the upper and lower crack surfaces, where (x, y, z) is local Cartesian coordinate system entered at the crack front with the x-axis perpendicular to the crack front, the y-axis perpendicular to the crack plane, and the z-axis along the crack front see Figure ***3.1***. There are three independent movements corresponding to three fundamental fracture Modes as pointed out by Irwin (IRWIN 1957), which are schematically illustrated in Figure ***3.2***. These basic fracture Modes are usually called Mode I, Mode II, and Mode III, respectively, and any fracture Mode in a cracked body may be described by one of the three basic Modes, or their combinations (Michael, Jan & Russell 2004).

1. **Mode I (Opening Mode):** The two crack surfaces experience a jump only in uy, that is, they move away symmetrically with respect to the undeformed crack plane (xz-plane).
2. **Mode II (Sliding Mode):** The two crack surfaces experience a jump only in ux, that is, they slide against each other along directions perpendicular to the crack front but in the same undeformed plane.
3. **Mode III (Tearing Mode):** The two crack surfaces experience a jump only in uz, that is, they tear over each other in the directions parallel to the crack front but in the same undeformed plane.

3.2.1: Crack-tip stress field

Consider a crack in a homogeneous isotropic linear elastic infinite plate as shown in Figure ***3-1***(a). The crack lies on the y = 0 line and in the region x = ±a. This discontinuity with zero thickness and sharp ends is defined as a crack. A crack can also be explained as a limiting case of an elliptical hole with a major axis of 2a and minor axis approaching a zero value. Under external loading the crack faces at $\theta = \pm \pi$ in Figure ***3-1***(a) can displace relative to each other (Sridharan 2008). Figure ***3.1***(b) shows a crack in an infinite solid. The two- and three-dimensional stress states are also shown in Figure ***3-1***(b). Any complex deformation of the crack faces can be described by a combination of three fracture Modes, Mode-I, Mode-II, and Mode-III as shown in Figure ***3-2***.

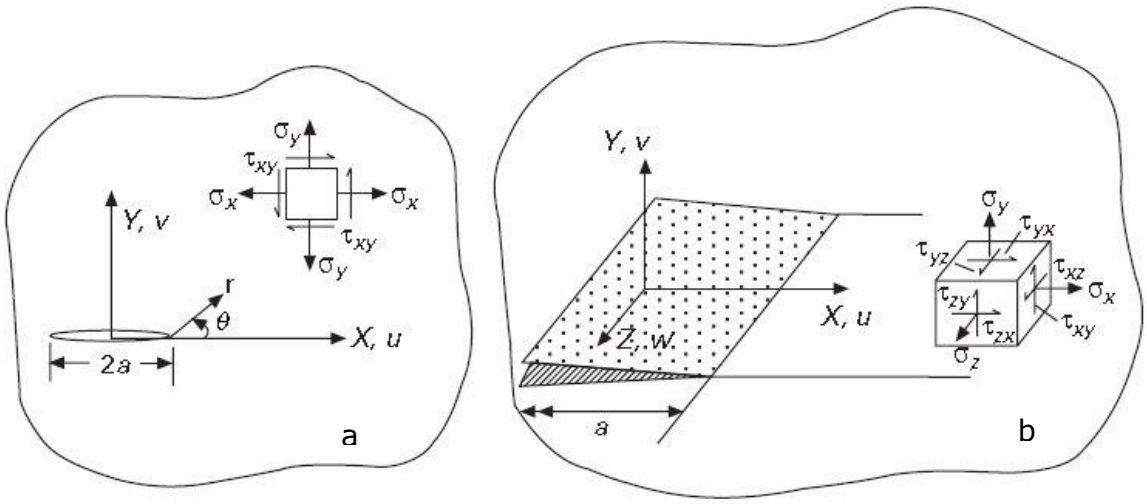

Figure 3-1Cracks in plates and solids (a) crack in a plate (two dimensions), (b) Crack in a solid (three dimensions)

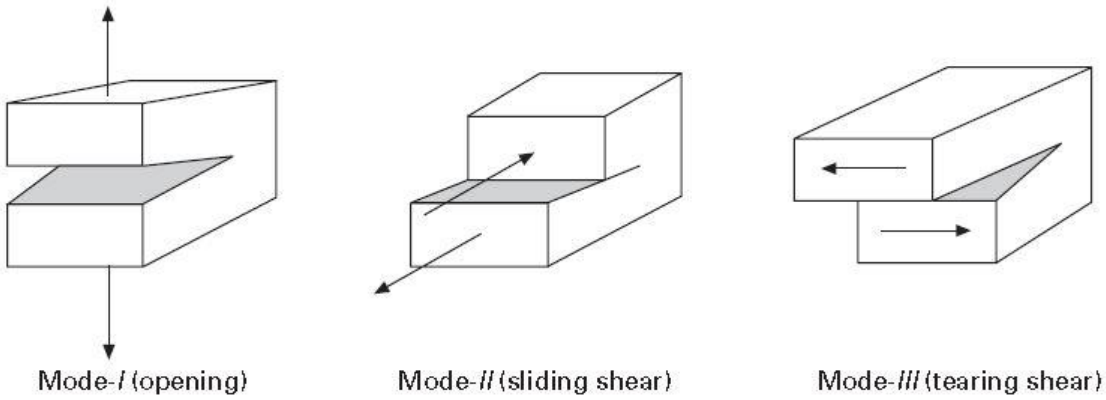

Figure 3-2 Three fracture Modes

The elastic stress field around a crack tip has been well characterized and documented by many researchers. The stress field in the immediate vicinity of the crack can be written as;

$$\sigma_x = \frac{K_I}{\sqrt{2\pi r}}\cos\left(\frac{\theta}{2}\right)\left[1-\sin\left(\frac{\theta}{2}\right)\sin\left(\frac{3\theta}{2}\right)\right]-\frac{K_{II}}{\sqrt{2\pi r}}sin\left(\frac{\theta}{2}\right)\left[2+cos\left(\frac{\theta}{2}\right)cos\left(\frac{3\theta}{2}\right)\right]$$

$$\sigma_y = \frac{K_I}{\sqrt{2\pi r}}\cos\left(\frac{\theta}{2}\right)\left[1+\sin\left(\frac{\theta}{2}\right)\sin\left(\frac{3\theta}{2}\right)\right]+\frac{K_{II}}{\sqrt{2\pi r}}sin\left(\frac{\theta}{2}\right)cos\left(\frac{\theta}{2}\right)cos\left(\frac{3\theta}{2}\right) \quad (3.2)$$

$$\tau_{xy} = \frac{K_I}{\sqrt{2\pi r}}\cos\left(\frac{\theta}{2}\right)sin\left(\frac{\theta}{2}\right)cos\left(\frac{3\theta}{2}\right)+\frac{K_{II}}{\sqrt{2\pi r}}cos\left(\frac{\theta}{2}\right)\left[1-sin\left(\frac{\theta}{2}\right)sin\left(\frac{3\theta}{2}\right)\right]$$

$\sigma_z = 0$ for plane stress and $\sigma_z = v(\sigma_x + \sigma_y)$ for plane conditions.

From Equations 3.2, the stresses are singular at the crack tip ($r = 0$) and the stresses have a square-root singularity. The constants K_I and K_{II} are termed as the Mode-I and Mode-II stress-intensity factors, respectively. The stress-intensity factor describes the intensity of the stress field and is a measure of the severity of the crack.

Irwin (IRWIN 1957) calculated the work required to close a crack of length $a + \Delta a$ to length a. It is assumed that in case of brittle materials the energy that is supplied externally is used to create new crack surfaces as these materials undergo little or no plastic deformations. Thus, the work required to extend the crack from a to $a + \Delta a$ will be same required to close the crack from $a + \Delta a$ to a. as the crack increments are small, the crack opening displacement behind a new crack tip at $a + \Delta a$ will be same as those behind the original crack tip at a. thus the work required to extend the crack form a to $a + \Delta a$ is (see Figure ***3-3***);

$$W = \frac{1}{2}\int_0^{\Delta a} \sigma_y(\Delta a - r).v(r)dr \tag{3.3}$$

Irwin obtained the strain energy release, G, as;

$$G = \lim_{\Delta a \to 0} \frac{W}{\Delta a} = \lim_{\Delta a \to 0} \frac{1}{2\Delta a}\int_0^{\Delta a} \sigma_y(\Delta a - r).v(r)dr \tag{3.4}$$

the relationship between strain energy release rate and stress intensity factors for three Modes, can be written as;

$$G = G_I + G_{II} + G_{III} = \frac{K_I^2}{E'} + \frac{K_{II}^2}{E'} + (1 + v)\frac{K_{III}^2}{E} \tag{3.5}$$

Where G_I, G_{II}, and G_{III} are Mode I, Mode II, and Mode III strain energy release rates, respectively, G is the total strain energy release rate, E'=E the plane stress, $E' = E/(1 - v^2)$, in plane strain, and E is the Young's modulus of the materials.

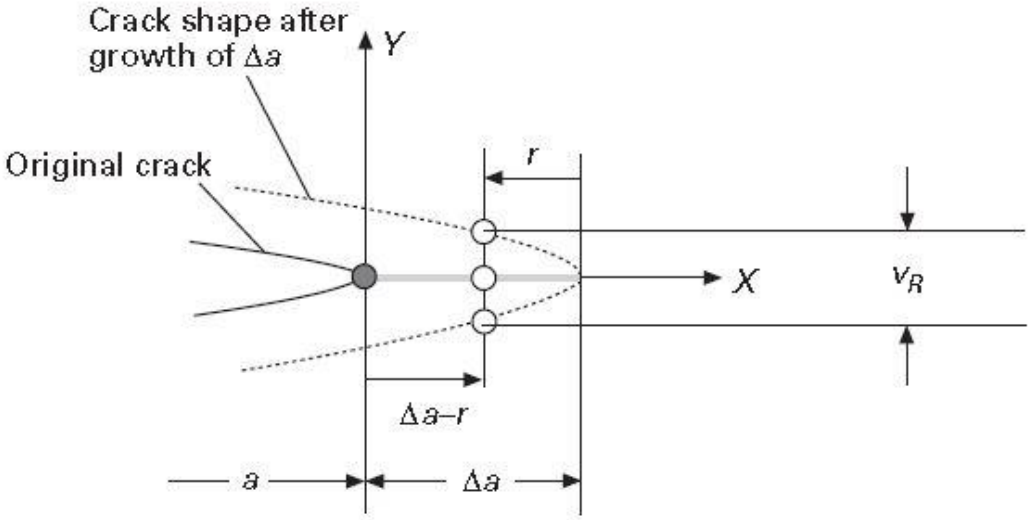

Figure 3-3 Irwin's crack closure concept.

3.2.2: Interface (delamination) crack problem

Consider the problem of an interface crack between two isotropic (orthotropic or anisotropic) materials as shown in Figure ***3-4***. Williams (1959) analysed the problem of a crack along the interface between two dissimilar isotropic materials. There are two common approaches for analysis of the microcracks and delamination in composite structures. Stress Intensity Factors approach (SIF) and Strain Energy Release Rate approach (SERR). SIF approach is used for detecting delamination in composite materials but due to the difficulty in extracting the stress field ahead of delamination crack tip, an alternative way is strain energy release rate (SERR) as the driving force parameter for the delamination growth (Xiang et al. 2014). Theoretical modelling of the mechanical response of multilayered structures is more complex than modelling homogeneous systems. For cracks in orthotropic or anisotropic materials, a similar square root singularity exists at the crack tip. The stress distributions are complex and involve material properties (Kashtalyan & Soutis 2000) defined in a manner similar to the isotropic case. The relationship between the *K* and *G* are more complex and are shown in Table ***3-1***. The strain energy release rate, *G*, associated with onset and growth is a measure of the delamination driving force. This *G*-value must be determined and compared to the measured fracture toughness, *Gc*, to predict delamination growth. Typically, a plot of the *G* components due to the three unique fracture Modes (G_I, G_{II}, G_{III}) and the total $G = G_I + G_{II} + G_{III}$ are calculated as a function of delamination length, *a*.

Energy balance approach can be used with Linear Elastic Fracture Mechanics (LEFM) besides the Elastic stress field (stress intensity factor). The energy balance approach is based on the concept that the crack is an extension when the energy release available for crack growth is adequate to overcome the resistance of material. This approach was proposed by Griffith (Griffith 1921) and then was followed by a more detailed treatment of the energy release rate, *G*, introduced by Irwin (IRWIN 1957). The energy release rate can be defined as the rate of change of potential energy with the crack area.

$$G = \pi\sigma^2 a/E \tag{3.6}$$

Where σ is remote stress, *a* is half of crack and E is Young's modulus.
There is an important relation between *G* and the change in compliance (inverse of stiffness) of a cracked material. This relationship is the main reason for using Strain energy release rate (*G*) to simulate/predict onset and propagation of cracks and delamination in laminated composite materials/structures.

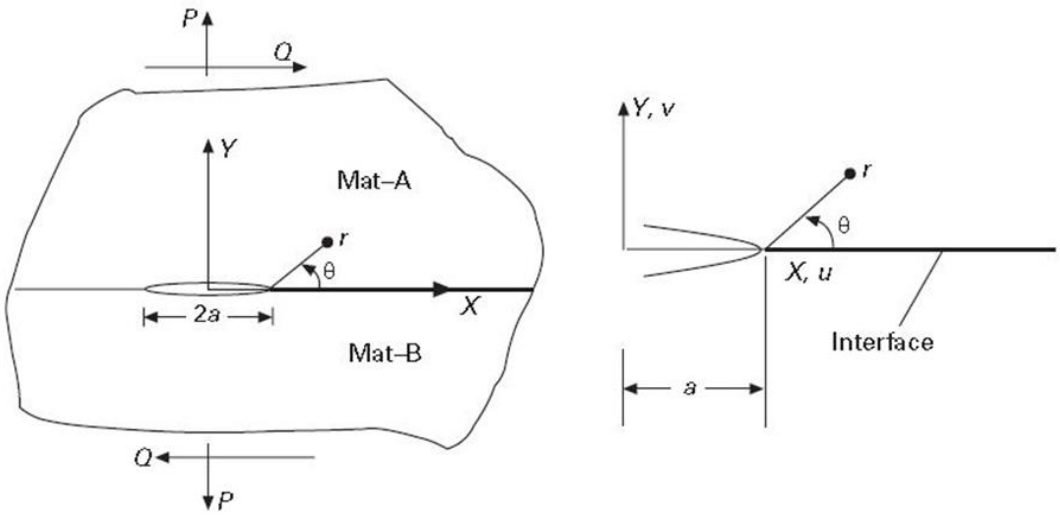

Figure 3-4 Interface crack at a bi-material interface

Table 3-1G to K conversion for orthotropic and anisotropic materials (Sridharan 2008)

$G_i = cK_i^2$

Value of c are given below for plane strain conditions		
Mode	**Orthotropic case**	**Anisotropic case**
I	$\sqrt{\frac{A_{11}A_{22}}{2}}\left[\sqrt{\frac{A_{22}}{A_{11}}}+\frac{2A_{12}+A_{66}}{2A_{11}}\right]^{1/2}$	$-\frac{A_{11}}{2}Im\left(\frac{\xi_1+\xi_2}{\xi_1\xi_2}\right)$
II	$\frac{A_{11}}{\sqrt{2}}\left[\sqrt{\frac{A_{22}}{A_{11}}}+\frac{2A_{12}+A_{66}}{2A_{11}}\right]^{1/2}$	$+\frac{A_{11}}{2}Im(\xi_1+\xi_2)$
III	$\frac{1}{2}(A_{44}A_{55})^{1/2}$	$\frac{1}{2}\frac{(A_{44}A_{55}-A_{45}^2)^{3/2}}{A_{44}A_{55}}$

Note: In this table the ξ_1 and ξ_2 are the roots of

$A11\xi^4 - 2A_{16}\xi^3 + (2A_{12} + A_{66})\,\xi^2 - 2A^{26}\xi + A^{22} = 0$,

where A_{ij} are coefficients of the A-matrix that relates strains, {ε}, to stresses, {σ}, through {ε} = [A] {σ}, and Im (·) denotes the imaginary part of the complex number in the parentheses.

3.2.3: Evaluation stress field around delamination crack in orthotropic material

In orthotropic materials as shown in Table ***3-1***, there is relationship between *G* and *K*. the relationship is $K_i = \sqrt{\frac{G_i}{c}}$, at delamination crack, the crack propagates in the interface of the laminated composite, and equation 3.2 can be rewritten as;

$$\sigma_x = \sqrt{\frac{G_I}{2\pi cr}}\cos\left(\frac{\theta}{2}\right)\left[1-\sin\left(\frac{\theta}{2}\right)\sin\left(\frac{3\theta}{2}\right)\right] - \sqrt{\frac{G_{II}}{2\pi cr}}sin\left(\frac{\theta}{2}\right)\left[2+cos\left(\frac{\theta}{2}\right)cos\left(\frac{3\theta}{2}\right)\right]$$

$$\sigma_y = \sqrt{\frac{G_I}{2\pi cr}}\cos\left(\frac{\theta}{2}\right)\left[1+\sin\left(\frac{\theta}{2}\right)\sin\left(\frac{3\theta}{2}\right)\right] + \sqrt{\frac{G_{II}}{2\pi cr}}sin\left(\frac{\theta}{2}\right)cos\left(\frac{\theta}{2}\right)cos\left(\frac{3\theta}{2}\right) \quad (3.7)$$

$$\tau_{xy} = \sqrt{\frac{G_I}{2\pi cr}}\cos\left(\frac{\theta}{2}\right)sin\left(\frac{\theta}{2}\right)cos\left(\frac{3\theta}{2}\right) + \sqrt{\frac{G_{II}}{2\pi cr}}cos\left(\frac{\theta}{2}\right)\left[1-sin\left(\frac{\theta}{2}\right)sin\left(\frac{3\theta}{2}\right)\right]$$

For the stress at θ=0 because FBG sensor has been embedded at the same delamination damage plane, equation 3.7 can be rewritten as;

$$\sigma_x = \sqrt{\frac{G_I}{2\pi cr}}, \sigma_y = \sqrt{\frac{G_I}{2\pi cr}}, \text{ and } \tau_{xy} = \sqrt{\frac{G_{II}}{2\pi cr}} \quad (3.8)$$

$\sigma_z = 0$ for plane stress and $\sigma_z = v(\sigma_x + \sigma_y)$ for plane conditions.

3.3: Elasto-plastic model of delamination damage

After the delamination crack initiation between composite layers, the laminate divides into two regions. It is reasonable to assume that elastic behaviour in the orthotropic laminate and the plastic behaviour of the epoxy in laminate causes the crack at the tip of delamination as shown in Figure ***3-5***.

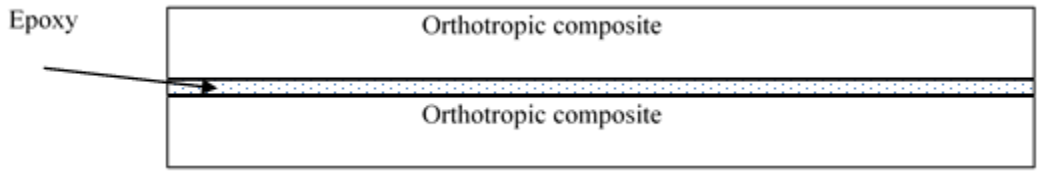

Figure 3-5 Schematic representation of composite beam as two different materials, one elastic orthotropic composite, and the other elastic purely Epoxy due to delamination crack (No Scale)

3.3.1: Mode I delamination damage (DCB test)

Due to local bending at the crack front (KakeiEpaarachchiIslam, et al. 2016) , plastic deformation is assumed to be significant at the thin inter-laminar region (epoxy) near the crack tip, at a distance equal to X. The threshold delamination crack length happens in the inter-laminar region, for $a = X_Y$ as shown in Figure ***3-6***. The beam material is assumed as perfectly elasto-plastic with yield strength σ_Y as shown in Figure ***3-7***. Y-axis is the direction of neutral axis of the beam section, measured perpendicularly to the plane of the undeformed beam as shown in Figure ***3-8***. The classical Euler-Bernoulli beam relations are assumed, and deformation in the thickness direction is related to the local of curvature by the expression;

$$\varepsilon(y) = \frac{y}{R} = y\frac{d^2y}{dx^2} \quad (3.9)$$

Where $\varepsilon(y)$ is the strain and $1/R$, is the curvature.

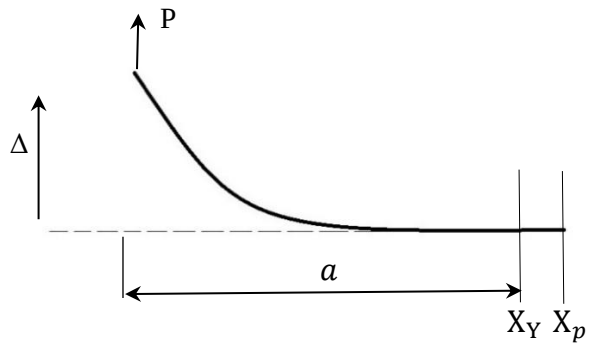

Figure 3-6 Schematic representation of beam, the section near the crack front is in the elastoplastic

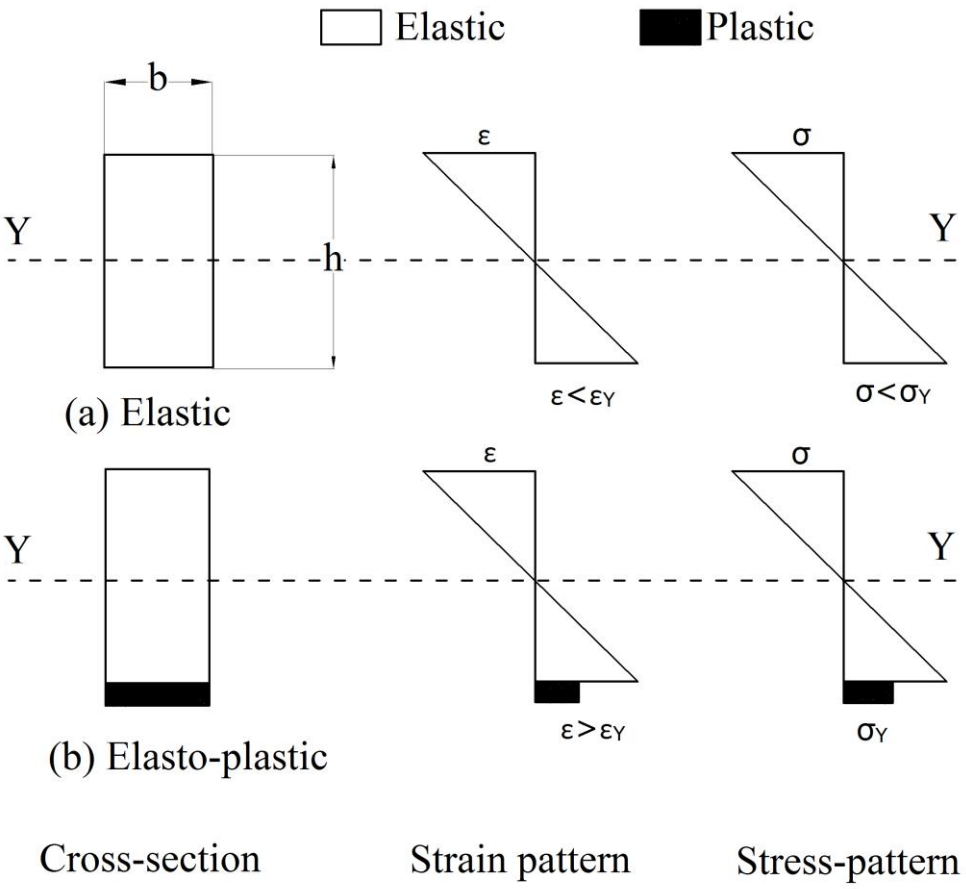

Figure 3-7 The transition from elastic to plastic state of a cross-section in bending in an inter-laminar epoxy layer due to delamination crack (Upper-half section)

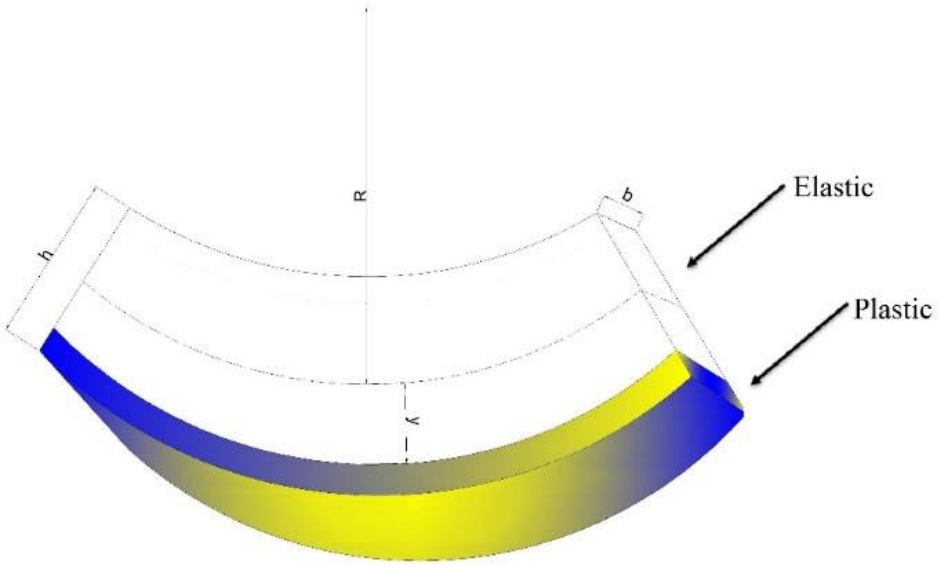

Figure 3-8 Schematic representation of the composite beam under crack delamination deformation. R corresponds to the radius of curvature (no scale)

The constitutive law for this composite beam (Figure ***3-8***) is described by the following equations for stresses (Chauffaille, Jumel & Shanahan 2011):

$\sigma(y) = E\varepsilon(y)$,For orthotropic composite (3.10)

$\sigma(y) = \sigma_Y$, For the matrix-epoxy material, $\varepsilon \geq \varepsilon_{Yepoxy}$ (3.11)

The bending moment of upper section is given by

$$M_u = b\int_0^{h/2} \sigma(y) y dy = \frac{bE\varepsilon_{max}^3 R^2}{3} \quad (3.12)$$

The bending moment of bottom section is given by

$$M_b = b\left[\int_0^{y_Y} \sigma(y) y dy + \int_{y_Y}^{h/2} \sigma_Y y dy\right] = b\left(\frac{E\varepsilon_Y^3 R^2}{3} + \frac{E_{ep}\varepsilon_Y h^2}{4} - \frac{E_{ep}\varepsilon_Y^3 R^2}{2}\right) \quad (3.13)$$

where E is the young modulus of composite specimen, and E_{ep} is Young modulus of epoxy (matrix) Total moment on the all beam section is given by

$$M = M_u + M_b \quad (3.14)$$

$$M = \frac{bE_{ep}\varepsilon_Y h^2}{4} + \frac{2bE\varepsilon_{max}^3 R^2}{3} - \frac{bE_{ep}\varepsilon_Y^3 R^2}{3} \quad (3.15)$$

Let$M(x) = Px$, and $R^{-1} = v^{"} = \frac{\partial^2 y}{\partial x^2}$ (3.16)

Then

$x = A + BR^2$, or $v^{"} = \frac{\sqrt{B}}{\sqrt{x-A}}$ (3.17)

Where, $A = \frac{bE_{ep}\varepsilon_Y h^2}{4F}$, and $B = \frac{1}{F}\left(\frac{2bE\varepsilon_{max}^3}{3} - \frac{bE_{ep}\varepsilon_Y^3}{3}\right)$ (3.18)

Slope: $v'(x) = -2\sqrt{B}\sqrt{A-x} + g_1$ (3.19)

Deflection: $v(x) = \frac{4}{3}\sqrt{B}(A-x)^{3/2} + g_1(A-x) + g_2$ (3.20)

3.3.1.1: Input energy in Mode I delamination damage

Assume that the energy input into the flexible composite beam leads to crack length a. Boundary conditions at the end of delamination cracked part of DCB are not the same as the clamped end of cantilever beam due to the "end of crack behaviour". The main concern is regarding the range $a < X \leq X_P$ (see Figure ***3-6***), where the combined elastic and plastic deformation exists due to delamination crack at the interface at *X* equal to X_P. Elastic energy per unit length of composite beam, e_S (along direction x with a perfect elastic condition);

For Upper-part

$e_{Su} = b\int_0^{\frac{h}{2}} \frac{\sigma^2(y)}{2E}\,dy = \frac{bER\varepsilon_{max}^3}{6};\ 0 < |y| \leq \frac{h}{2}$ (3.21)

where ε_{max} is the maximum strain measured in the surface of composite specimen.

For Bottom-part

$e_{Sb} = b\int_0^{y_Y} \frac{\sigma^2(y)}{2E}\,dy = \frac{bER\varepsilon_Y^3}{6};\ 0 < |y| \leq y_Y$ (3.22)

where ε_Y is the yield strain of epoxy measured in the matrix of composite.

The elastic energy, e_e(due to structural changes/ or dissipated from delamination crack) is given by;

$e_e = b\int_{y_Y}^{h/2} \left[\frac{1}{2}\sigma_Y\varepsilon_Y + (\varepsilon - \varepsilon_Y)\sigma_Y\right]dy = \frac{bE_{ep}\varepsilon_Y}{4}\left(\frac{h^2}{2R} - h\varepsilon_Y\right);\ y_Y < |y| \leq {}^{h}/_{2}$ (3.23)

The total energy expended per unit length of composite beam with a delamination, e_{total} is;

$$e_{total} = e_S + e_e = b\left(\frac{E_{ep}\varepsilon_Y h^2}{8R} - \frac{hE_{ep}\varepsilon_Y^2}{4} + \frac{ER\varepsilon_Y^3}{3}\right) \quad (3.24)$$

Integrating over the length range of x, the total energy input, E_{total} in the composite beam;

$$E_{total} = E_0 + \int_a^{x_p} e_{total}\, dx \quad (3.25)$$

3.3.1.2: Fracture energy in Mode I delamination damage

The energy input have estimated e_{total}, and is considered the energy balance for increment of the crack growth, Δa, associated with a simultaneous increase in Δv, the normal distance of the extremity of the composite beam from the initial plane(Chauffaille, Jumel & Shanahan 2011);

$$P\Delta v = \frac{\partial E_{total}}{\partial a}\Delta a + G_c b\Delta a \quad (3.26)$$

Leading to

$$G_{IC} = \frac{P}{b}\frac{\partial v}{\partial a} - \frac{1}{b}\frac{\partial E_{total}}{\partial a} \quad (3.27)$$

where, $G_C$is critical fracture energy for delamination crack. Taking boundary condition of the cantilever beam at $x = a$, $v(a) = v'(a) = 0$, the two constants, g_1 and g_2 can be found, and displacement is;

$$v(x) = \frac{4}{3}\sqrt{B}(x-A)^{3/2} - 2\sqrt{B}\sqrt{a-A}(x-A) + \frac{2}{3}\sqrt{B}(a-A)^{3/2} \quad (3.28)$$

The term $\partial v/\partial a$ can be obtained from derivative of equation *v* (a);

$$\frac{\partial v}{\partial a} = a\sqrt{B}/\sqrt{a-A} \quad (3.29)$$

And derivative equation (3.17) to obtain $\partial E_{total}/\partial a$value;

$$\frac{\partial E_{total}}{\partial a} = b\left(\frac{E\varepsilon_{max}^3\sqrt{a-A}}{3\sqrt{B}} + \frac{E_{ep}h^2\sqrt{B}}{8\sqrt{a-A}} - \frac{E_{ep}h\varepsilon_Y^2}{4}\right) \quad (3.30)$$

now, substituting values from (3.29), and (3.30) in Equation (3.27). Finally provides an expression for fracture energy (G_I) ;

$$G_I = \frac{P}{b}\frac{a\sqrt{B}}{\sqrt{a-A}} - \frac{E_{ep}\varepsilon_Y h^2\sqrt{B}}{8\sqrt{a-A}} - \frac{E\varepsilon_{max}^3\sqrt{a-A}}{3\sqrt{B}} + \frac{E_{ep}\varepsilon_Y^2 h}{4} \quad (3.31)$$

3.3.2: Mode II delamination damage (ENF test)

The Elasto-plastic model is extended to study the Mode II delamination damage. The End-notched Flexure (ENF) test is selected to study propagation Mode II delamination damage in laminated composite specimen. Plastic deformation is assumed at thin inter-laminar region (epoxy) near the crack tip at a distance *X*. The threshold delamination crack length happens in the inter-laminar region, for $a = X_Y$ as shown in Figure ***3-9***. Assume that the beam is perfectly Elasto-plastic material with yield strength σ_Y as shown in Figure ***3-8***. Let *y* axis is the neutral axis of the beam section, measured perpendicular to the plane of the un-formed beam as shown in Figure 3.9. According to Euler-Bernoulli beam relationship, thickness deformation is related to the local of curvature R^{-1} by the expression equation 3.9.

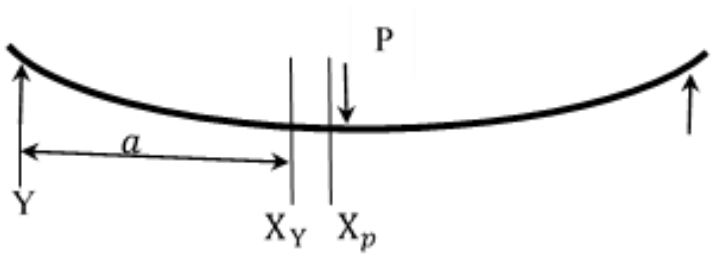

Figure 3-9 Schematic representation of beam, the section near the crack front is in the elasto-plastic

let $M(x) = Yx$, and $R^{-1} = v^{"} = \frac{\partial^2 y}{\partial x^2}$ (3.32)

where *M(x)* is the bending moment along beam section and *Y* is the internal force and is equal to $P/4$ (Arrese et al. 2010), substitute M(x) and *R* values in equation 3.32 to equation 3.15. Therefore, equation 3.17 can be written as the expression $x = A^{II} + B^{II}R^2$, or the curvature can be expressed as;

$$v^{"} = \frac{\sqrt{B^{II}}}{\sqrt{x - A^{II}}} \quad (3.33)$$

where, $A^{II} = \frac{bE_{ep}\varepsilon_Y h^2}{4Y}$, and $B^{II} = \frac{1}{Y}\left(\frac{2bE\varepsilon_{max}^3}{3} - \frac{bE_{ep}\varepsilon_Y^3}{3}\right)$ (3.34)

integration equation 3.34 gets slope $v'(x)$ in the beam as shown in equation 3.35;

Slope: $v'(x) = -2\sqrt{B^{II}}\sqrt{x - A^{II}} + g_1$ (3.35)

integration equation 3.35 for calculating deflection in the beam;

Deflection: $v(x) = \frac{4}{3}\sqrt{B^{II}}(x - A^{II})^{3/2} + g_1(x - A^{II}) + g_2$ (3.36)

where g_1 and g_2 are integration constants.

3.3.2.1: Input energy in Mode II delamination damage

Assume that the energy input into the flexible composite beam leading to crack length (a). The main concern is about the range $a < x \leq x_P$(see Figure ***3-9***), where the combined elastic and plastic deformation exists due to delamination crack at the interface. Elastic energy per unit length of composite beam, e_S (along direction x in a perfect elastic condition);

For upper part

$$e_{Su} = b\int_0^{\frac{h}{2}} \frac{\sigma^2(y)}{2E}\,dy = \frac{bER\varepsilon_{max}^3}{6};\ \ 0 < |y| \leq \frac{h}{2} \quad (3.37)$$

where ε_{max} is the maximum strain measured in the surface of composite specimen.

For Bottom-part

$$e_{Sb} = b\int_0^{y_Y} \frac{\sigma^2(y)}{2\bar{E}}\,dy = \frac{bER\varepsilon_Y^3}{6};\ \ 0 < |y| \leq y_Y \quad (3.38)$$

where ε_Y is the yield strain of epoxy measured in the matrix of composite specimen.

The elastic energy, e_e(due to structural changes or dissipated from delamination crack) is given by;

$$e_e = b\int_{y_Y}^{h/2} \left[\frac{1}{2}\sigma_Y\varepsilon_Y + (\varepsilon - \varepsilon_Y)\sigma_Y\right]dy = \frac{bE\varepsilon_Y}{4}\left(\frac{h^2}{2R} - h\varepsilon_Y\right);\ y_Y < |y| \leq {}^{h}/_{2}$$
(3.39)

the total energy expended per unit length of composite beam with crack delamination,e_{total} is;

$$e_{total} = e_S + e_e = b\left(\frac{E_{ep}\varepsilon_Y h^2}{8R} - \frac{hE_{ep}\varepsilon_Y^2}{4} + \frac{ER\varepsilon_Y^3}{3}\right) \quad (3.40)$$

Integrating over the length range of x, the total energy input,E_{total} in the composite beam is;

$$E_{total} = E_0 + \int_a^{x_p} e_{total}\,dx \quad (3.41)$$

3.3.2.2: Fracture energy in Mode II delamination damage

The energy input E_{total}, is considered the energy balance for increment of the crack growth, Δa, associated with a simultaneous increase in the normal distance of the extremity Δv of the composite beam from the initial plane (Chauffaille, Jumel & Shanahan 2011);

$$P\Delta v = \frac{\partial E_{total}}{\partial a}\Delta a + G_c b \Delta a \tag{3.42}$$

leading to;

$$G_{IIC} = \frac{Y}{b}\frac{\partial v}{\partial a} - \frac{1}{b}\frac{\partial E_{total}}{\partial a} \tag{3.43}$$

where $G_C$is fracture energy for delamination crack;

Taking boundary condition of the beam at $x = 0, v(0),\ at\ x = L, v'(L) = 0$, then it can be found the two constants, g_1 and g_2 in equation 3.27, and equation 3.28 can be written as ;

$$v(x) = \frac{4}{3}\sqrt{B^{II}}(x - A^{II})^{3/2} + 2\sqrt{B^{II}}\sqrt{L - A^{II}}(x - A^{II}) - \frac{4}{3}\sqrt{B^{II}}(A^{II})^{3/2} \tag{3.44}$$

displacement at a can be obtain as;

$$v(a) = \frac{4}{3}\sqrt{B^{II}}(a - A^{II})^{3/2} + 2\sqrt{B^{II}}\sqrt{L - A^{II}}(a - A^{II}) - \frac{4}{3}\sqrt{B^{II}}(A^{II})^{3/2} \tag{3.45}$$

the term $\partial v/\partial a$ is interpolated from equation $v\ (a)$ and evaluated;

$$\frac{\partial v}{\partial a} = 2\sqrt{B^{II}}(\sqrt{a - A^{II}} + \sqrt{L - A^{II}}) \tag{3.46}$$

and derivative equation (3.45) to obtain $\partial E_{total}/\partial a$value;

$$\frac{\partial E_{total}}{\partial a} = b\left(\frac{E\varepsilon_{max}^3\sqrt{a - A^{II}}}{3\sqrt{B^{II}}} + \frac{E_{ep}\varepsilon_Y h^2\sqrt{B^{II}}}{8\sqrt{a - A^{II}}} - \frac{E_{ep}h\varepsilon_Y^2}{4}\right) \tag{3.47}$$

now, substitute Equations (3.46), and (3.47) values in Equation (3.43) to arrive at expression for the fracture energy(G_{II});

$$G_{II} = \frac{2Y}{b}\sqrt{B^{II}}\left(\sqrt{a - A^{II}} + \sqrt{L - A^{II}}\right) + \left(\frac{E_{ep}h\varepsilon_Y^2}{4} - \frac{E\varepsilon_{max}^3\sqrt{a - A^{II}}}{3\sqrt{B^{II}}} - \frac{E_{ep}\varepsilon_Y h^2\sqrt{B^{II}}}{8\sqrt{a - A^{II}}}\right)$$

(3.48)

3.3.3: Mixed Mode I/II delamination damage (Axial load damage)

The Elasto-plastic model is extended to study the mixed Mode delamination damage. The Crack Lap Shear (CLS) test is selected to study propagation mixed Mode delamination damage in laminated composite specimen. An axial load is applied at the ends of CLS specimen as shown in Figure ***3-10***. The energy input has estimated E_{total}, and is considered the energy balance for increment of the crack growth, Δa, associated with a simultaneous increase in Δv, the normal distance of the extremity of the composite beam from the initial plane (Chauffaille, Jumel & Shanahan 2011);

$$G_C = \frac{P}{b}\frac{\partial v}{\partial a} - \frac{1}{b}\frac{\partial E_{total}}{\partial a} \tag{3.49}$$

Assuming the region at tip of delamination crack is plastic and the effect of delamination crack region is elasto-plastic as shown in Figure ***3-11***. The region near tip of delamination crack can be assumed perfectly plastic and the material status at the transforms as elasto-plastic. The total energy expended per unit length of composite beam with crack delamination, e_{total} is(Kakei, A. A. et al. 2018);

$$e_{total} = e_S + e_e = b\left(\frac{E_{ep}\varepsilon_Y h^2}{8R} - \frac{hE_{ep}\varepsilon_Y^2}{4} + \frac{ER\varepsilon_Y^3}{3}\right) \tag{3.50}$$

Integrating over the length range of *x*, the total energy input,E_{total} in the composite beam;

$$E_{total} = E_0 + \int_a^{x_p} e_{total}\, dx \tag{3.51}$$

Total moment on the beam section is given by(Kakei, A. A. et al. 2018);

$$M = \frac{bE_{ep}\varepsilon_Y h^2}{4} + \frac{2bE\varepsilon_{max}^3 R^2}{3} - \frac{bE_{ep}\varepsilon_Y^3 R^2}{3} \tag{3.52}$$

Total internal bending moment at the tip of the delamination crack is given by;

$$M(x) = Py(x) \tag{3.53}$$

The bending moment is related to the second derivative or curvature of the beam deflection. According to beam theory, a pair of second order differential equations for the deflection of the beam, y(x), is expressed in equations (3.54) and (3.55);

$$y''(x) - \lambda_2^2 y(x) = 0, \qquad x>0 \tag{3.54}$$

$$y^{"}(x) - \lambda_o^2 y(x) = 0, \qquad x<0 \tag{3.55}$$

The solution of equation Where $\bar{y}_2$ is the centroid location of the strap section, and $\bar{y}_o$is the centroid location of the combined section. The expressions λ_2 and λ_o are;

$$\lambda_2 = \sqrt{P/(EI)_2} \tag{3.56}$$

$$\lambda_o = \sqrt{P/(EI)_o} \tag{3.57}$$

The solution of equations (3.55) and (3.56) must satisfy the following conditions;

$$\lim_{|x|\to\infty}[y(x)] = \lim_{|x|\to\infty}[y'(x)] = 0 \tag{3.58}$$

$$\lim_{|x|\to 0}[y(|x|) - y(-|x|)] = \bar{y}_2 - \bar{y}_o \tag{3.59}$$

$$\lim_{|x|\to 0}[y'(|x|) - y'(-|x|)] = 0 \tag{3.60}$$

The deflection of the beam can be calculated using equations (3.58), (3.59) and (3.60);

$$y(x) = \frac{(\bar{y}_2-\bar{y}_o)\lambda_o}{\lambda_2+\lambda_o} e^{-\lambda_2 x}, x > 0 \tag{3.61}$$

$$y(x) = \frac{-(\bar{y}_2-\bar{y}_o)\lambda_2}{\lambda_2+\lambda_o} e^{\lambda_o x}, x < 0 \tag{3.62}$$

Where *(El)₂* and *(EI)ₒ* are the bending rigidities of the strap section and the combined (lap+ strap) section, respectively, and *P* is the applied loading.

Then

$$v^{"} = \sqrt{\frac{B^M}{Ce^{\lambda_o x}+A^M}} \tag{3.63}$$

Where

$$A^M = \frac{bE_{ep}\varepsilon_Y h^2}{4F}, B^M = \frac{1}{F}\left(\frac{2bE\varepsilon_{max}^3}{3} - \frac{bE_{ep}\varepsilon_Y^3}{3}\right) and\ C = \frac{(\bar{y}_2-\bar{y}_o)\lambda_2}{\lambda_2+\lambda_o}. \tag{3.64}$$

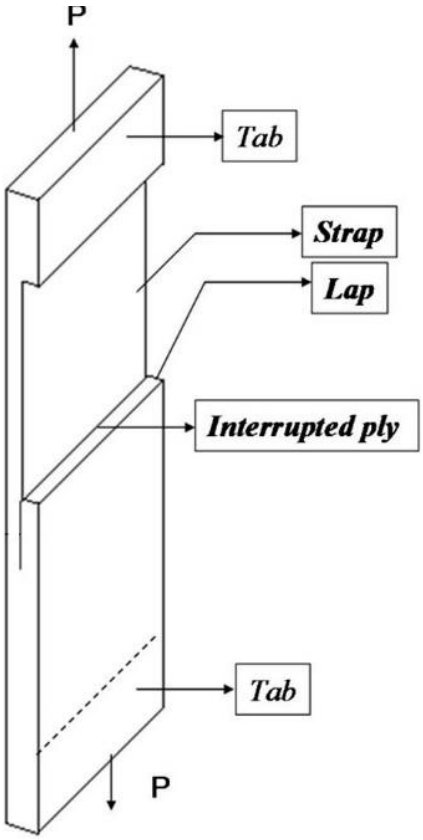

Figure 3-10 Cracked lap shear (CLS) specimen

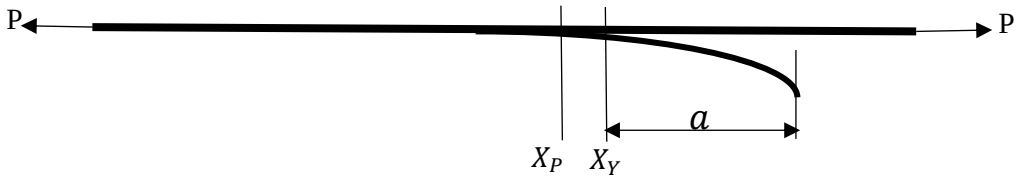

Figure 3-11 Schematic representation of the beam, the section near the crack front in the elasto-plastic for CLS test

3.3.3.1: Fracture energy in Mixed Mode delamination damage

The energy input has estimated, E_{total}, is considered the energy balance for increment of the crack growth, Δa, associated with a simultaneous increase in the normal distance of the extremity Δv of the composite beam from the initial plane (Chauffaille, Jumel & Shanahan 2011);

$$P\Delta v = \frac{\partial E_{total}}{\partial a}\Delta a + G_c b \Delta a \tag{3.65}$$

leading to;

$$G_{TC} = \frac{P}{b}\frac{\partial v}{\partial a} - \frac{1}{b}\frac{\partial E_{total}}{\partial a} \tag{3.66}$$

where $G_C$is fracture energy for delamination crack, $\frac{\partial v}{\partial a}$ can be calculated from integration equation 3.67 and take fixed boundary condition at the tip of delamination crack and then $\frac{\partial v}{\partial a}$ can be expressed as;

$$\frac{\partial v}{\partial a} = \frac{\sqrt{A^M B^M}\left(ln\left(\left|2\sqrt{B^M}\sqrt{A^M B^M}\sqrt{C^M e^{\lambda a}+A^M}-B^M(Ce^{\lambda a}+2A^M\right|\right)-\lambda a\right)}{A^M \lambda} \quad (3.67)$$

3.3.4: Delamination damage onset and propagation due to tensile axial loading

Delamination in the plate is shown in Figure ***3-12***. The thin plate geometry has thickness *2h,* width *b* and delamination distance h_1 from one surface. A uniform tensile loading P is applied in the width direction. Internal forces, considered are shown in Figure ***3-13***, where, ϕ_1 and ϕ_2 are the angle of rotations at the mid plane of upper and lower sections respectively. The relative crack tip displacement is evaluated by assuming that the two delaminating sub laminates deforms as a cantilever beam of length Δa (Valvo 2016). As such the rate of angle rotation for two sections is different.

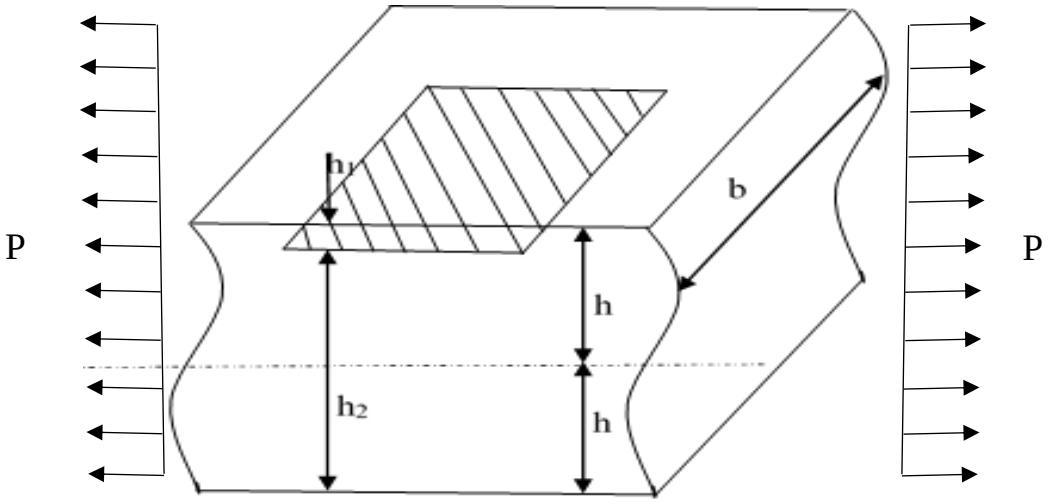

Figure 3-12 Delamination geometry and applied tensile loading P

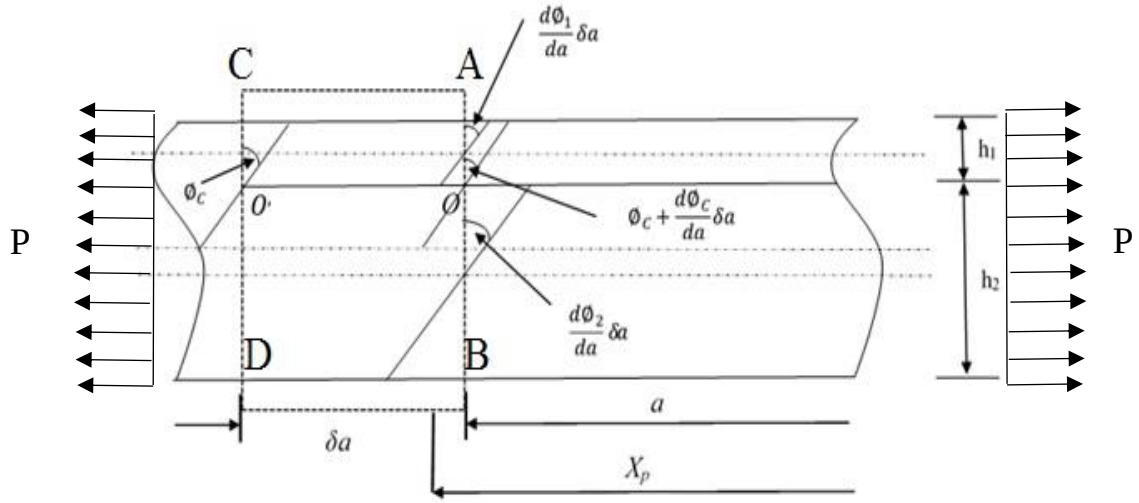

Figure 3-13 Crack tip contour with rotations

If the crack position is taken to be originally at *O* on *AB* and later it moves to *O'* on *CD* then it can be considered that the original angle crack rotation is ϕ_C at *CD* and $\phi_C+(d\phi_C/da)\delta a$ at *AB*. When the cracks moves from *O* to *O'* then the change in the angle of the crack plane is ;

$$\frac{d\emptyset_C}{da}\partial a = (\frac{d\emptyset_1}{da} - \frac{d\emptyset_2}{da})\partial a \tag{3.68}$$

The energy input has estimated E_{total}, and is considered the energy balance for increment of the crack growth, Δa, associated with a simultaneous increase in Δv, the normal distance of the extremity of the composite beam from the initial plane (Chauffaille, Jumel & Shanahan 2011);

$$G_C = \frac{P}{b}\frac{\partial v}{\partial a} - \frac{1}{b}\frac{\partial E_{total}}{\partial a} \tag{3.69}$$

As the applied load is normal to the shear plane, shear force *Q* is equal to zero. In this case the fracture energy is equal to the energy absorbed by the displacement (*v*) at the extremity of the composite beam, the equation 3.69 can be written as;

$$G_C = -\frac{1}{b}\frac{\partial E_{total}}{\partial a} \tag{3.70}$$

The region at tip of the delamination crack is plastic and the effect of delamination crack region is elasto-plastic as shown in Figure ***3-13***. The region near the tip of delamination crack can be assumed perfectly plastic and the material status at the transforms as elasto-plastic. The total energy expended per unit length of composite beam with crack delamination, e_{total} is;

$$e_{total} = e_S + e_e = b\left(\frac{E_{ep}\varepsilon_Y h^2}{8R} - \frac{hE_{ep}\varepsilon_Y^2}{4} + \frac{ER\varepsilon_Y^3}{3}\right) \quad (3.71)$$

where E is the young modulus of composite specimen, E_{ep} is Young modulus of epoxy (matrix), ε_{max} is the maximum strain measured in the surface of composite specimen, ε_Y is the yield strain of epoxy measured in the matrix of composite specimen, e_e is elastic energy due to structural changes/ or dissipated from delamination crack and e_S is elastic energy per unit length of composite beam (along direction x with a perfect elastic condition). The main concern is regarding the range $a < x \leq x_P$ as shown in Figure ***3-14***, where the combined elastic and plastic deformation exists due to delamination crack at the interface. Integrating over the length range of *x*, the total energy input,E_{total} in the composite beam;

$$E_{total} = E_0 + \int_a^{x_p} e_{total}\, dx \quad (3.72)$$

Once a moment develops in the section due to delamination crack, it works as a hard point in the section, and total moment on the section is given by;

$$M = \frac{bE_{ep}\varepsilon_Y h^2}{4} + \frac{2bE\varepsilon_{max}^3 R^2}{3} - \frac{bE_{ep}\varepsilon_Y^3 R^2}{3} \quad (3.73)$$

The delamination crack front failure mechanism is caused by local bending in the thin matrix (cohesive element) (KakeiEpaarachchiIslam, et al. 2016), let $M = \frac{EI_{total}}{R}$, where $I_{total} = I_{elastic} + I_{plastic}$, since $I_{plastic}$ value is too small and can be neglected, substitution of M values in the equation 3 provides:

$$B^A R^3 + A^A R - 1 = 0 \quad (3.74)$$

R is the curvature and can be calculated numerically, and $A^A = \frac{bE_{ep}\varepsilon_Y h^2}{4EI}$, and $B^A = \frac{1}{EI}\left(\frac{2bE\varepsilon_{max}^3}{3} - \frac{bE_{ep}\varepsilon_Y^3}{3}\right)$.

The relative displacement between crack surfaces causes shear strain at the matrix (epoxy) in the composite. The axial force produces a crack-tip sliding displacement or causes Mode II delamination damage. The crack-tip sliding displacement depends on the thickness of the upper (h_1) and lower (h_2) arms. From equation 3.68, it can be assumed that the total input energy at the crack plane system is equal to the difference between input energy at upper and lower arms of the plate, and equation 3.69 can be written as(Kakei & Epaarachchi 2018)

;

$$G_C = -\frac{1}{b}\left[\left(\frac{\partial E_{total}}{\partial a}\right)_{upper} - \left(\frac{\partial E_{total}}{\partial a}\right)_{lower}\right] \quad (3.75)$$

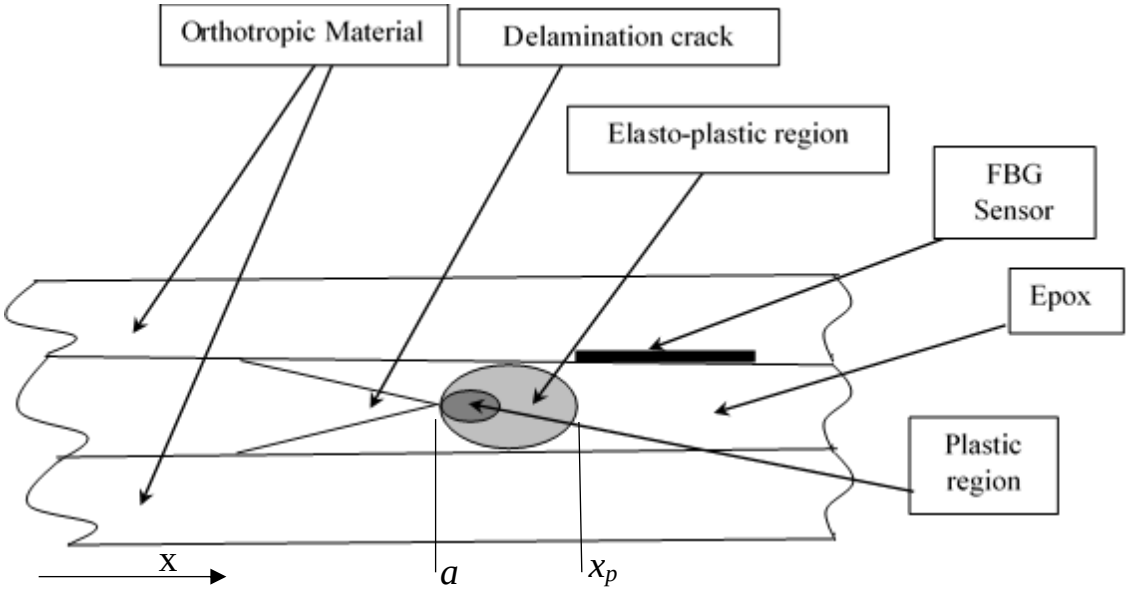

Figure 3-14 Scheme of the plastic and elasto-plastic deformation at the delamination tip (stress plane)

3.4: Finite Element Analysis of Composite Laminates

3.4.1: Mechanics of composite laminates (orthotropic lamina)

The in-plane stress-strain relationship in the materials coordinates $(\bar{x}_1, \bar{x}_2, \bar{x}_3)$ of a single orthotropic lamina is:

$$\begin{Bmatrix} \bar{\sigma}_1 \\ \bar{\sigma}_2 \\ \bar{\sigma}_6 \end{Bmatrix} = \begin{bmatrix} \bar{Q}_{11} & \bar{Q}_{12} & 0 \\ \bar{Q}_{12} & \bar{Q}_{22} & 0 \\ 0 & 0 & \bar{Q}_{66} \end{bmatrix} \begin{Bmatrix} \bar{\varepsilon}_1 \\ \bar{\varepsilon}_2 \\ \bar{\varepsilon}_6 \end{Bmatrix} \quad (3.76)$$

The bar over the $\bar{\sigma}s$, $\bar{Q}s$ *and* $\bar{\varepsilon}s$ has been depicted to distinguish from the corresponding variables in the coordinate system *(x_1, x_2, x_3)*, which describe the composite structure. Thus, $(\bar{x}_1, \bar{x}_2, \bar{x}_3)$ denotes the materials coordinate system and *(x_1, x_2, x_3) = (x, y, z)* denotes the coordinate system to formulate the governing equations of the structural problem as shown in Figure ***3-15***. The $\bar{Q}_{ij}$'s in equation 3.77 defines plane stress-reduced stiffness's. They are related to the engineering constants in the following manner.

$$\bar{Q}_{11} = \frac{E_1}{1-v_{12}v_{21}}, \bar{Q}_{22} = \frac{E_2}{1-v_{12}v_{21}} \tag{3.77}$$

$$\bar{Q}_{12} = \frac{v_{12}E_1}{1-v_{12}v_{21}}, \quad \bar{Q}_{66} = G_{12}$$

The material direction is always aligned with the fibre direction. When the material direction is not aligned with the coordinate system *(x,y,z)* used to describe the boundary value problem associated with a structure, coordinate transformation equations are employed to obtain the stresses in material coordinates,$(\bar{\sigma}_1, \bar{\sigma}_2, \bar{\sigma}_3)$, in terms of stresses in the global coordinates, $(\sigma_1, \sigma_2, \sigma_3) = (\sigma_x, \sigma_y, \sigma_{xy})$:

$$\begin{Bmatrix} \bar{\sigma}_1 \\ \bar{\sigma}_2 \\ \bar{\sigma}_6 \end{Bmatrix} = \begin{bmatrix} cos^2\theta & sin^2\theta & 2cos\theta sin\theta \\ sin^2\theta & cos^2\theta & -2cos\theta sin\theta \\ -cos\theta sin\theta & cos\theta sin\theta & cos^2\theta - sin^2\theta \end{bmatrix} \begin{Bmatrix} \sigma_1 \\ \sigma_2 \\ \sigma_6 \end{Bmatrix} \tag{3.78}$$

where θ denote the angle between the positive x-axis and positive $\bar{x}_1$-axis, measured counter-clockwise direction. Hereafter, the angle θ will be referred to as the lamination angle.

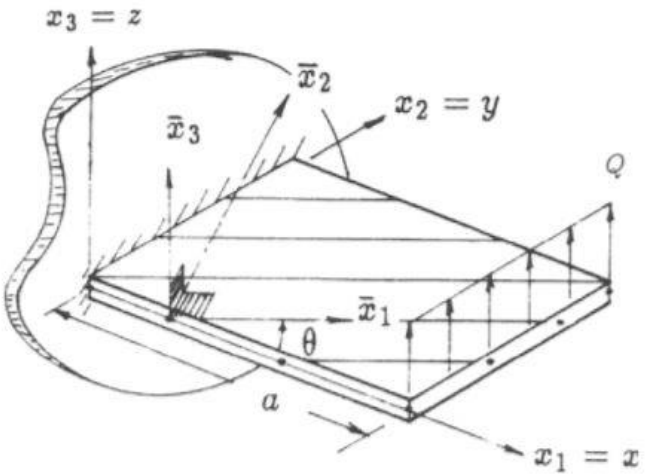

Figure 3-15 Coordinate system used for the description of the structure and the fibre direction

3.4.2: The classical laminated plate theory

The classical laminated plate theory (CLPT) is an extension of the classical plate theory to laminated plates. This theory is established to analyse fibre reinforcement composite. Fibre reinforcement composites are manufactured in the form of thin

sheet called laminae or layers. Laminated composite plate is manufactured by bonding the composite laminae together with desired thickness and stiffness.

The laminated constitutive equation related with force and moment resultants (N_i, M_i), strain $(\varepsilon_i^{(0)}, \varepsilon_i^{(1)})$, and indicated integration with respect to x, can be expressed as;

$$\begin{Bmatrix} N_1 \\ N_2 \\ N_6 \end{Bmatrix} = \begin{bmatrix} A_{11} & A_{12} & A_{16} \\ A_{12} & A_{22} & A_{26} \\ A_{16} & A_{26} & A_{66} \end{bmatrix} \begin{Bmatrix} \varepsilon_1^{(0)} \\ \varepsilon_2^{(0)} \\ \varepsilon_6^{(0)} \end{Bmatrix} + \begin{bmatrix} B_{11} & B_{12} & B_{16} \\ B_{12} & B_{22} & B_{26} \\ B_{16} & B_{26} & B_{66} \end{bmatrix} \begin{Bmatrix} \varepsilon_1^{(1)} \\ \varepsilon_2^{(1)} \\ \varepsilon_6^{(1)} \end{Bmatrix} \tag{3.79}$$

$$\begin{Bmatrix} M_1 \\ M_2 \\ M_6 \end{Bmatrix} = \begin{bmatrix} B_{11} & B_{12} & B_{16} \\ B_{12} & B_{22} & B_{26} \\ B_{16} & B_{26} & B_{66} \end{bmatrix} \begin{Bmatrix} \varepsilon_1^{(0)} \\ \varepsilon_2^{(0)} \\ \varepsilon_6^{(0)} \end{Bmatrix} + \begin{bmatrix} D_{11} & D_{12} & D_{16} \\ D_{12} & D_{22} & D_{26} \\ D_{16} & D_{26} & D_{66} \end{bmatrix} \begin{Bmatrix} \varepsilon_1^{(1)} \\ \varepsilon_2^{(1)} \\ \varepsilon_6^{(1)} \end{Bmatrix}$$

Where A_{ij} is the extensional stiffnesses (A matrix) of the k (the lamina), D_{ij} the bending stiffnesses (D matrix), and B_{ij} is the bending-extensional coupling stiffnesses (B matrix) of lamina.

$$\left(A_{ij}, B_{ij}, D_{ij}\right) = \sum_{k=1}^{N} \int_{z_k}^{z_{k+1}} Q_{ij}^{(k)} \, (1, z, z^2) dz \tag{3.80}$$

where $Q_{ij}^{(k)}$the material stiffness's of the k-the lamina, referred as the laminate coordinates. Since $Q_{ij}^{(k)}$ is constant with each layer, the integration over the thickness can be carried out easily. It is expressed as;

$$A_{ij} = \sum_{k=1}^{N} Q_{ij}^{(k)} (z_{k+1} - z_k)$$

$$B_{ij} = \frac{1}{2} \sum_{k=1}^{N} Q_{ij}^{(k)} ({z^2}_{k+1} - {z^2}_k) \tag{3.81}$$

$$D_{ij} = \frac{1}{3} \sum_{k=1}^{N} Q_{ij}^{(k)} ({z^3}_{k+1} - {z^3}_k)$$

Where N is the number of layers in the laminate, and (z_k, z_{k+1}) are the thickness coordinates of the bottom and top of the *k-th* layer. The transformation equations and summery of classical lamination theory can be seen in Appendix B.

3.4.2.1: Modelling of multilayer composite structures

The theory of composite structures classifies two fundamental approaches: Equivalent Single Layer (ESL) and Layer Wise (LW) Models. Composite stack has been represented as a single layer in the ESL approach description. The equivalent stiffness properties has assumed for multilayered composite structures. ESL approach takes advantage of built up models created for homogeneous structures, such as Bernoulli and Timoshenko bars, Kirchhoff and Reissner-Mindlin plates. The number of DOF in an ESL model is independent of the number of layers creating the laminate. The ESL description is effectively implanted into standard element formulations by simply stating a composite cross-section. Each single layer of the laminate in a Layer Wise (LW) modelling is obviously represented with its own DOF. A number of DOF in Layer Wise description have been presented that depend on the number of layers creating the laminate. In this manner the LW approach can become very difficult to analyse. FEM Modelling of an LW approach depends on utilizing of solid brick elements that are stacked to create the whole laminate (Barbero & Reddy 1991). ABAQUS also permits stacking of continuum-based (solid) shells in order to minimise the conditioning complications related to different element edge lengths (the laminate thickness generally being much smaller than the in-plane dimensions). It is apparent that the ESL design is less complex and requires less computing time. However, the LW approach may involve a separate design and calculation time, which can be significant, if it is chosen to utilise a number of finite elements over the composite cross-section.

It is essential to check, in case there is requirement for an advanced (LW) Model. With an advanced model, the results could be more accurate and detailed. However, sometimes the differences may be insignificant compared to the amount of work required to make a complex model. This thesis has made use of LW method modelling. The embedded FBG sensors report the strain between layers and hence, FEA data is available layer wise for comparison purposes. In an ESL Model, the number of DOF is independent of the number of layers constituting the laminate (Reddy 1993). In FEA, the ESL description is easily embedded into standard element formulations by simply stating a composite cross-section. If the layer wise variation of parameters is required, layer wise modelling should be utilising.

The conventional shell and continuum shell element types are normally utilised within the ABAQUS modelling environment for composites. Even if deformable in the 3D space, the conventional shell is the planar 2D representation of a solid element. A thickness is given to the planar element by assigning a section. In this case it is a composite one. However, since the geometry is characterised in the two-dimensional space, it is not conceivable to assign an element to each layer of the composite. This would always lead to an ESL Model. Solid elements should be used for LW modelling. The promising solid element used in composite modelling is the continuum shell element. Continuum shell elements are three-dimensional stress/displacement elements for use in Modelling structures. They are generally slender, with a shell-like response but continuum element topology. As explained in most cases, composite solid should model as a shell or continuum shell composite layup. However, when the normal stress cannot be ignored and it is required accurate interlaminar stresses, then it should be used a solid composite layup.

3.4.2.2: Modelling composite structures using FEA

Due to the anisotropic nature of composites, the material properties are commonly different in the three principal directions. The reinforcement of a composite is typically assigned the 1-direction, whereas the 2 and 3-directions are known as the transverse directions. Unlike 2-D conventional shell elements, the orientation of material properties must be explicitly assigned when using 3-D continuum elements.

Figure ***3-16*** shows a composite plate that has been built with continuum shell elements. The global coordinate system is used to define the material orientation. Since the global system does not rotate with the curvatures of the Model, it incorrectly defines material properties for the curved plate, in the x-y plane. Discrete or local coordinate systems can be used for which a normal and reference direction can be assigned depending on the reinforcement and transverse direction of the material. It is very important to have correct material orientation for accurate modelling of composite structures.

Composite are normally structures with significantly smaller thicknesses compared to other dimensions. Shell elements are used to model such structures. Normally

conventional shell elements, with thickness significantly smaller than the other dimensions, are used to model structures. It is possible to define the thickness in the property module while creating the section. In contrast, in assigning continuum shell elements to solid parts, ABAQUS determines the thickness from the geometry of the part. From a modelling point-of-view continuum shell elements look like three-dimensional continuum solids, but their kinematic and constitutive behaviour is similar to conventional shell elements. For example, conventional shell elements have displacement and rotational degrees of freedom, while continuum solid elements and continuum shell elements have only displacement degrees of freedom (Figure ***3-17***).

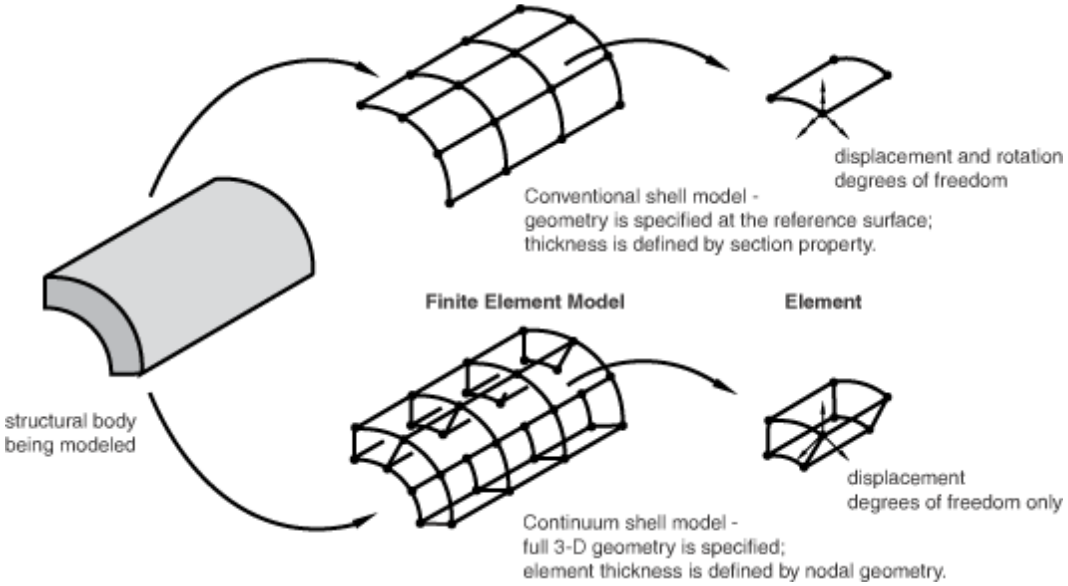

Figure 3-16 Conventional shell elements and continuum shell elements in ABAQUS (ABAQUS Analysis User manual)

Throughout the study, continuum solid elements (C3D8) have been used, because the normal stress cannot be ignored and it is required the accurate interlaminar stress at the near localised delamination damage crack. C3D8 stands for continuum stress/displacement solid with 8 nodes and reduced integration (Figure ***3-18***). It is required to have strain variations at particular locations when it comes to comparison of strain readings obtained from embedded sensors. The shape functions can be found in (Lapidus 1999). The node numbering follows the convention of Figure ***3-19***. The incompatible mode eight-node brick (C3D8I) element is a developed version of the C3D8-element. In particular, shear locking

is removed and volumetric locking is much reduced. The C3D8I element should be utilised in all occasion, in which linear elements are subject to bending.

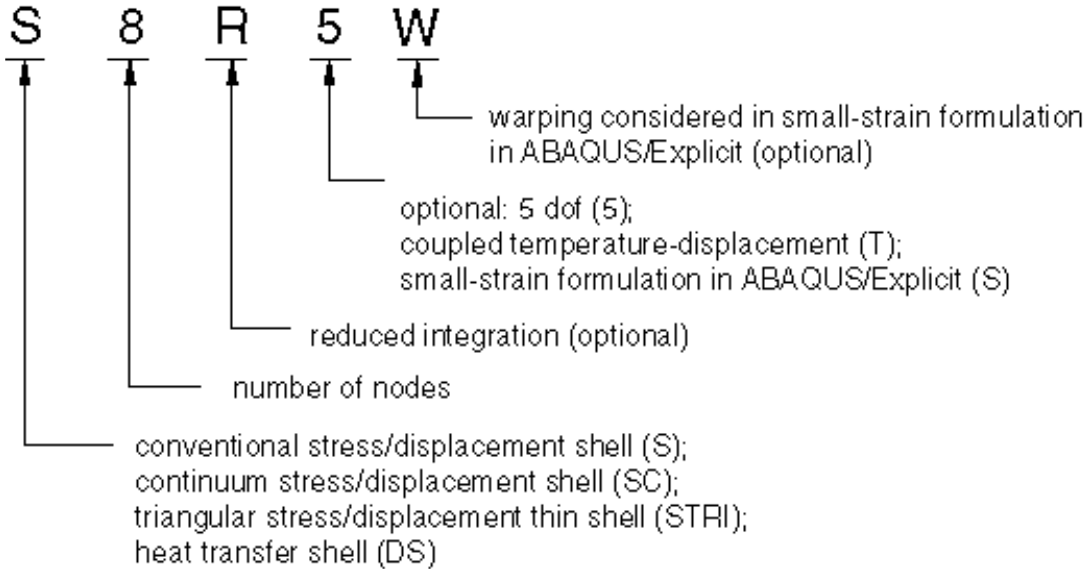

Figure 3-17 SC8R elements in ABAQUS (ABAQUS Analysis User manual)

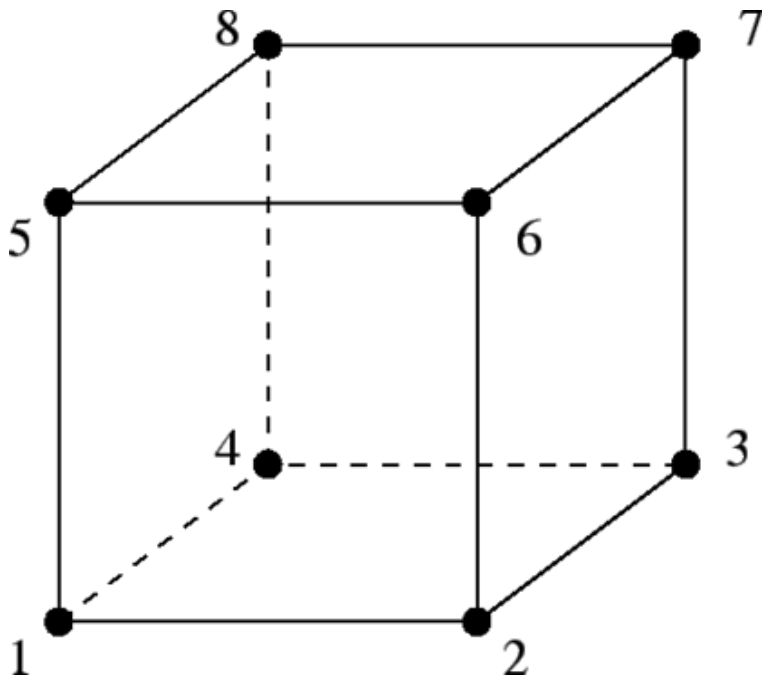

Figure 3-18 8-node brick element in ABAQUS (ABAQUS Analysis User manual)

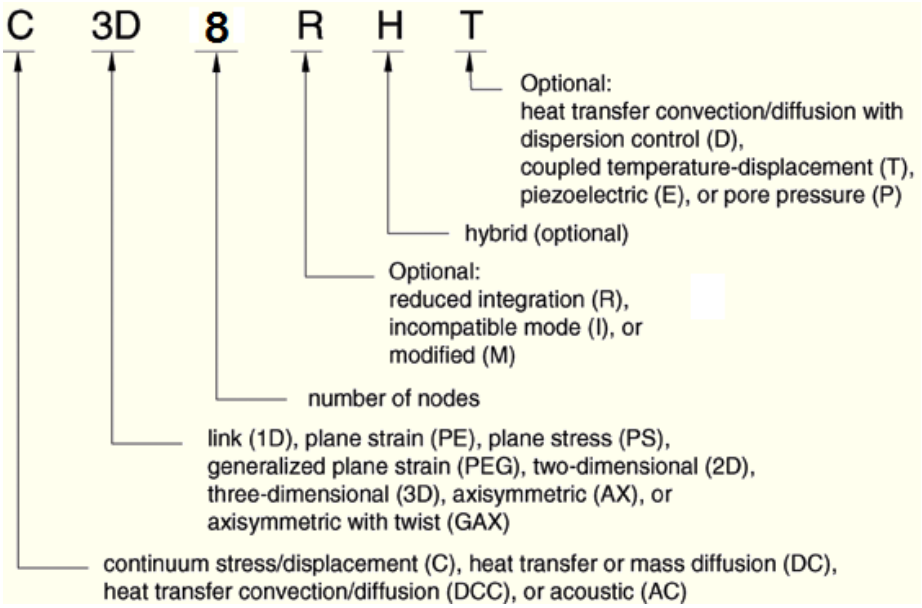

Figure 3-19 C3D8R elements in ABAQUS (ABAQUS Analysis User manual)

3.5: Finite Element Simulation of Crack Surface

Plated structures are widely used in many engineering constructions from aircraft to ships, off-shore structures, bridges and buildings. Given their diverse use in severe loading environments, it is vital that their behaviour is analysed and understood. When it comes to FRP composite plated structures, the layer wise behaviour needs to be analysed to model the complete structure. To model the deformation of laminated plates, approaches based on the classical laminate beam or plate theory have been developed (Crawley & Lazarus, 1989). Due to assumptions like linear strain distribution through the thickness and zero transverse shear stress, it should be restricted to thin plate applications. The transverse shear stresses are usually important in composite laminates. As a result, it is necessary to use shear deformation theory to address moderate to thick laminate constructions. The first-order shear deformation theory has been used for modelling the laminates using FEA. Additionally, the Layer Wise theory and Three-dimensional (3D) coupled-analysis model have also been used.

In FRP composite structures, damage can initiate from the inside of the structure as a crack or delamination. That is why use of embedded FBG sensors for damage detection in FRP composite structures offers a big advantage. FEA with LW modelling is essential for comparison and verification of experimental results.

Following case study was carried out to verify the FEA modelling for a composite laminate with embedded FBG sensors. Principle of FBG has been explained in Chapter 4. The Finite element method (FEM) provides reasonable tools to simulate delamination of composite structures. The Virtual Crack Closure Technique (VCCT) has been utilised in the investigation of delamination in many published work (Jokinen, Wallin & Saarela 2015; Shokrieh et al. 2012). VCCT analysis relies upon two basic hypotheses; i.e. that the energy released during crack growth is identical to the energy required to close the crack and the stress state does not change significantly when the crack is extended (Bonhomme et al. 2009). These hypotheses significantly influence the accuracy of the VCCT analysis as they explicitly ignore plasticity in the analysis (Jokinen, Wallin & Saarela 2015). However, a major drawback of the VCCT method is the requirement of prior knowledge of the initial crack size (Shor & Vaziri 2015). An alternative to VCCT is the Cohesive Zone Method (CZM) which is becoming more popular for the analysis of delamination of composite materials, largely because of its simplicity and usability (Wang & Xu 2015). CZM has been used in many studies for the simulation of delamination crack propagation in composite materials. A probabilistic CZM was developed by Shanmugam et al. (Shanmugam et al. 2013) to capture steady-state energy release rate variations in Double Cantilever Beam (DCB) delamination specimens. Wang and Xu (Wang & Xu 2015) proposed an approach using cohesive elements to simulate propagation of a delamination, including descriptions of both propagation direction and effective propagation length under high-cycle fatigue loading.

3.5.1: Cohesive element description

Cohesive zone model (CZM) has been extensively used in finite element analysis for delamination analysis of laminated composites besides analysis of fracture processes. This has been achieved by introducing a couple of virtual surfaces with the interfacial traction-separation relations defined by a constitutive law. The cohesive approach is based on the concept of cohesive crack model. This concept was developed by Barenblatt (Barenblatt, G. 1962) who introduced cohesive forces in order to solve the equilibrium problem in elastic bodies with cracks. The cohesive damage zone models relate tractions to displacement jumps at crack

interface. As shown in Figure ***3-20***, the area under the traction-displacement curve is equal to the fracture toughness G_C.

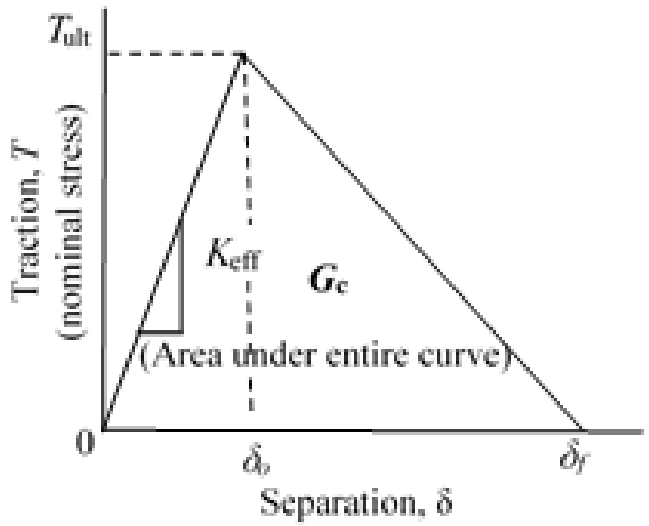

Figure 3-20 Cohesive parameters of typical bilinear traction-separation model (Chen, D & El-Hacha, R 2014)

3.5.2: User-defined subroutine (UMAT)

With a cohesive element library provided by the software package ABAQUS, specific constitutive laws of the CZM can be implemented into user subroutines. UMAT is the user material subroutine for implicit analysis and VUMAT for explicit analysis. The cohesive zone model is implemented through the cohesive elements incorporated with a user-defined subroutine (UMAT) in ABAQUS. The UMAT is a user subroutine that can be used to define the mechanical behaviour of a material in the program ABAQUS. It is referenced at all material calculation points of elements for which the material definition includes a user-defined material behaviour. It updates the solution-dependent state variables and provides the stress and material Jacobian matrix according to the constitutive model. The UMAT subroutine runs each time, after the state variables are initialized. It reads state variables, and the current deformation gradient, and then calculates the stress and tangent according to the given material model before returning the necessary variables.

In this research, the user cohesive elements technique was implemented by means of inputting a user material subroutine UMAT. Auto Desk_ Simulation composite analysis 2015 Plug-ins_ for ABAQUS 6.13 was used to create the UMAT subroutine to calculate the nine state variables for the cohesive materials (Wang & Xu 2015). These state variables are stored by ABAQUS at each individual integration point within the finite element model. They are represented in the ABAQUS/viewer application by the solution dependent state variables ‘‘SDVN” where N is the unique integer which identifies the state variable (SDV1, SDV2, . ., SDV9). The nine state variables are defined as follows: SDV1 represents the current damage state, SDV2 is a continuous real variable between zero and one, and indicates that the damage initiation criteria is satisfied, SDV3 is the effective traction at damage initiation, SDV4 is the effective displacement at damage initiation, SDV5 is the maximum effective displacement attained in the loading history, SDV6 is the damage variable D, a continuous real variable which varies between zero and one, SDV7 is the work done in the normal loading Mode (local 3-direction), SDV8 is the work done in the first shear loading Mode (local 1-direction), and SDV9 is the work done in the second shear loading Mode (local 2-direction). The cohesive elements in the model act as a ‘‘traction-separation” element type. Cohesive elements (COH3D8) with properties defined by UMAT were inserted between the specimen parts within the connected area. The influence of the COH3D8 elements on the model as a whole can be ignored as softening of the element was not taken into consideration. All mechanical and cohesive properties were determined experimentally according to ASTM standards in the Centre of Excellence in Engineering Fibre Composite Laboratories at the University of Southern Queensland. Mode I cohesive properties were obtained according to ASTM D5528-13 and Mode II cohesive properties were obtained according to ASTM D7905-14.

3.6: Effect of cracks and cavities on elasticity behaviours of composite materials

The micro cracks in the composites can cause significant damage in materials system. The results for micro cracks under external loads in tension and compression are anisotropic effective modulus because the micro cracks respond differently under loads and damage growth (Su, Santare & Gazonas 2007). The

result in anisotropic effective moduli of micro cracked media will differ depending upon the magnitude and location and direction of the boundary loads, so the prediction of these changes helps in the understanding the anisotropic damage in laminate composite structures. Much researcher has been attempted to analyse and understand the effect of cracks and cavities on effective modulus of general materials.

Several 2-D methodologies have been used to evaluate effective moduli due to distribution of cracks in the media. Shen et al Shen et al (Shen & Yi 2000) presented new equations to evaluate the effective bulk and shear moduli of solids with randomly dispersed cracks by assuming that potential energy released by embedding a circular or spherical representative volume element (RVE) with infinite matrix is equal to that induced by introducing. An eigen function expansion variational method (EEVM) of evaluating the relevant strains, the young's modulus and Poisson's ratio for 2D cracked square plated under tension load was presented by Chen by Chen (Chen, Donna & El-Hacha, Raafat 2014). Kushch et al (Kushch, Sevostianov & Mishnaevsky 2009), studied a solid containing multiple cracks with prescribed orientation statistics using the advantage of 2-D unit cell approach to reduce the boundary value problem. Xi-Qiao, et, al (Xie & Biggers 2006) presented the quasi-micromechanical model to calculate the complex damage associated with micro crack growth in brittle and quasi-brittle materials containing many distributed micro cracks and examined the effective moduli of random heterogeneous elastic solid by assemble-volume averaging process within a representative volume element (RVE). Santare et al (Santare, Crocombe & Anlas 1995) presented the generalized self-consistent method (GSCM) to calculate the anisotropic effective moduli of a medium containing damage consisting of micro cracks with an arbitrary degree of alignment. Ma et al (Ma et al. 2005) investigated the effect of non-uniform concentration distributions of micro cracks in the brittle or quasi-brittle material and present a novel numerical method to evaluate the effect of micro crack growth and coalescence on effective moduli and the tensile strength in brittle or quasi-brittle material. All this research leads to conclusion that the mechanical properties of cracked materials depend on the statistical distributions and interaction of micro cracks in the material. The statistical distributions and interaction of micro cracks impacts on transport properties such as the effective

moduli and tensile strength. Such transport properties basically depend on the statistical distribution of orientations, sizes and positions of micro cracks. Thus it can be concluded that the mechanical properties of cracked material is sensitive to the sizes, location and orientations of individual micro cracks, namely, the extreme values of micro crack distributions. Several methodologies have been used to evaluate the effect of cracks in reducing mechanical properties in isotropic materials but the effects of multiple cracks in anisotropic media is still lacking attention.

3.7: Stress concentration in laminated composite structures

The hole in composite structures can cause dangerous problems of stress concentration because of geometric discontinuity. Because of the anisotropic and brittle behaviour, the laminated composites are more sensitive to geometric discontinuity than metallic materials. One of the serious geometric discontinuities in laminated composite structures is delamination. Delamination occurs at the interface layer between two neighbours lamina. The problem of delamination cannot be detected and delamination stays hidden and propagates in the composites until damage occurs. Stress concentration in laminated composite or in orthotropic media has been analysed by many researchers. The solution for stress concentration around circular hole in infinite orthotropic plate was obtained by (Lekhnitskii 1968), (Savin 1961) and (Muskhelishvili 1953) using complex potential method. A solution for stress distribution around triangle hole in composite plate was presented by (Ukadgaonker & Rao 1999), whereas (Ukadgaonker & Rao 2000) and (Nageswara Rao et al. 2010) found stress states around square and rectangular holes. In general above mentioned research shows that the increase of hole size causes more severe stress concentration and the position of hole has much greater effect on the stress distribution in the anisotropic plate. Further, the stress concentration strongly depends on the layout of the laminates. Therefore, it is quite complex to analyse the stress concentration around holes in the laminated composites because of multiply boundary value problem.

The boundary values such as, hole geometry, materials properties, fibre orientation, stacking sequence, loading factor and loading angle has a significant effect on the stress distribution around hole. The discontinuity such as hole, works as stress raisers and may lead to catastrophic failure.

Stress concentration factor is seriously affected by fibre orientation and loading angle. Sharma (Sharma 2012) studied the stress concentration around circular, elliptical and triangular holes in infinite composite plate to obtain generalized stress functions. The result shows that the fibre orientation has significant effect on the tangential stress in the anisotropic plate.

This research will extend Kachanov (Tsukrov & Kachanov 2000) work for prediction of delamination propagation in laminated composite, the compliance in the layer (lamina) with hole (see Figure ***3-21***), can be expressed as;

$$S = S^o + H \tag{3.82}$$

Where S is the compliance of the matrix with elliptical hole, S^o is the compliance of the matrix with no imperfections, and H is the compliance of the cavity in the matrix. Above equation will be used in the classical laminated plate theory. Cavity in the matrix of the lamina causes the reduction of the mechanical properties of laminated composite plate. In addition, the stress at the interface of layers increases due to stress concentrations at cavities. Here in this research, FBG sensor strain will be used to evaluate the stress at the interface region of GFR composite materials. This increasing of the stress may causes propagation of delamination at interface of laminated composite plate.

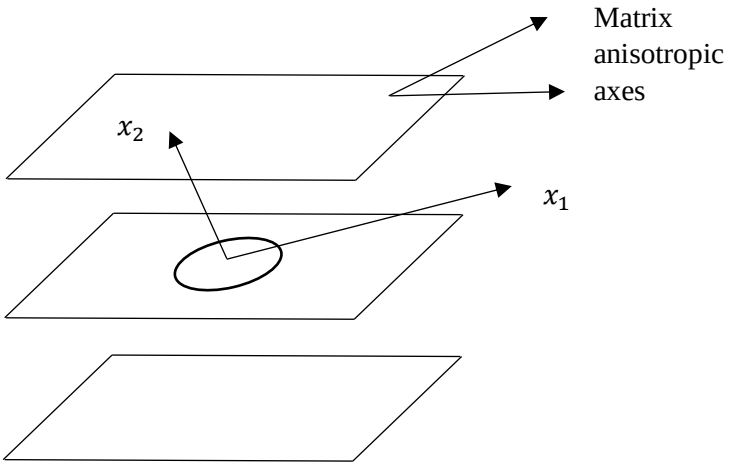

Figure 3-21 Laminated composite plate has sub-damage in one on lamina

3.8: Summary

In this chapter, the fracture mechanic concepts and crack tip stress field have been provided in details. The analysis of delamination damage shows that it can be calculated and stress around the delamination crack tip can be predicted exactly if

there is an accurate damage model and high advance technique for evaluating strain at the tip of delamination crack. It is a significant achievement.

The objective has been to develop Elasto-plastic model to understand delamination damage. The accurate damage (Elasto-plastic) model depends on the measurement of strain at the specimen surface and strain at the tip of delamination crack. The proposed model has been integrated with embedded FBG sensor strain. This model can be utilised for damage prediction depending on the composite damage mechanism. The proposed model will be experimented along with some delamination damage Modes. The strain at the delamination tip can be calculated by embedding FBG senor. Therefore, the stress at the delamination crack tip can be calculated. Furthermore, the delamination crack onset and propagation can be evaluated depending on critical energy release rat (G_c).

Another researched case is delamination propagation due to imperfection in sub-laminate. The model has been developed from Tsukrov and Kachanov (Tsukrov & Kachanov 2000). Matlab codes will be established for the case. The model will be applied to calculate the change of mechanical properties such as Young's Modulus (E_x, E_y) and shear (G_{xy}) due to embedded delamination damage, this depends on that the remote stress is equal to the stress around the void.

Damage accumulation in composite materials is a complex process. Further, prediction of life time of a composite component needs the loading history and other operational parameters such as load sequencing etc(Reifsnider 1980). The proposed model is principally depending on the delamination damage onset and its propagation using the strain at the crack tip. The extent of the damage can be predicted. However, the fatigue life or the remaining life-time is a totally different context which includes operation loading histories etc. and not a part of damage prediction model. The current model quantifies the extent of damage which may be an indication of the operational limits but not provide an indication of a remaining lifetime. The results of all theories provided in this chapter will be discussed in chapter 5 and applied on some case studies.

Chapter 4: EXPERIMENTAL AND SIMULATION INVESTIGATIONS OF MODE I, MODE II, AND MIXED-MODE I/II DELAMINATION MODES

4.1: Introduction

This chapter will describe the methodology of the experiment and FEA simulation that will be conducted to characteristics of delamination Modes (Mode I, Mode II, and Mixed Mode I/II). The general objectives and the scope of the experiment discuss the basic methods to establish accurate experimental test methodology for characterising and monitoring delamination damage development in GFRC specimens. In addition establishing empirical relations of apply loading (P) and displacement (Δ) which will be used for calculating and evaluating delamination onset and propagation in the next chapter. Beside empirical relationship the experimental program was also designed to assess the effect of specimen curing in the room temperature and to evaluate the effect of delamination crack on the shifting and distortion of embedded FBG sensor spectrum and describe the methodology test of Thermoelastic Stress Analysis (TSA). Those calculating data will be valuable input data for establishing Elasto-plastic model examinations. Furthermore FEA simulation has been described in detail in this chapter. An appropriate FEA meshing size has been selected to simulate delamination damage development in cohesive element. The experimental data required to accomplish these objectives were those will be used to evaluate and study delamination damage onset and propagation in GFRC specimens as well as characteristics of delamination damage modes.

4.2: FBG Sensor

A uniform FBG includes a segment of the optical fibre in which a periodic modulation of core refractive index is implemented. The principle of the FBG sensor is based on the shift of the centre wavelength of the Bragg Grating. The spectral response of a uniform FBG in its free state as shown in Figure ***4-1*** is a signal peak centred at the Bragg wavelength λ_B as defined by the Bragg condition (Sorensen et al. 2007).

$$\lambda_B = 2n_{eff}\Lambda \tag{4.1}$$

Where, n_{eff} is the effective refractive index for the guided Mode of interest and Λ is the constant nominal modulation period of the refractive index. When a mechanical deformation (strain) is subjected onto grating it will change the effective index of refraction as well as the periodic spacing index. The Bragg wavelength shift caused by the change of strain can be expressed in the form:

$$\frac{\Delta\lambda_B}{\lambda_B} = \varepsilon P_e \tag{4.2}$$

Where P_e is the strain optic coefficient and it's calculated as 0.789.

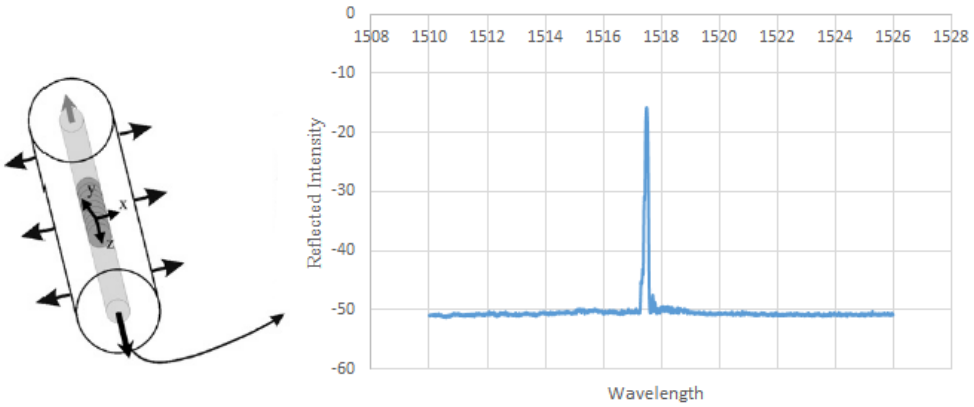

Figure 4-1 Spectral response of an FBG sensor at a uniform strain field

To identify the delamination cracks in the specimens, Distortion Index (DI) value is used. Distortion Index (DI) can be expressed as (Kahandawa, G. C. et al. 2013);

$$DI = \frac{D_{si}}{D_{so}} \tag{4.3}$$

where D_{si} is the current distortion and D_{so} is the distortion at the original condition (no loading). Distortion (D_s) can be expressed as;

$$D_s = \frac{FWHM}{F} \tag{4.4}$$

F is the peak value of the FBG sensor reflection spectra, and FWHM is the Full-Width Half-Maximum value of FBG spectra as shown in Figure ***4-2***. Peak Wavelength Ratio (PWR) of FBG sensor is used to evaluate delamination damage and it can be expressed as;

$$PWR = \frac{F_i}{F_{io}} \tag{4.5}$$

F_i is the current peak wavelength and F_{io} is the peak wavelength at the original condition (no loading). This phenomenon (DI and PWR) can be used to identify the presence of delamination damage in the composite specimens.

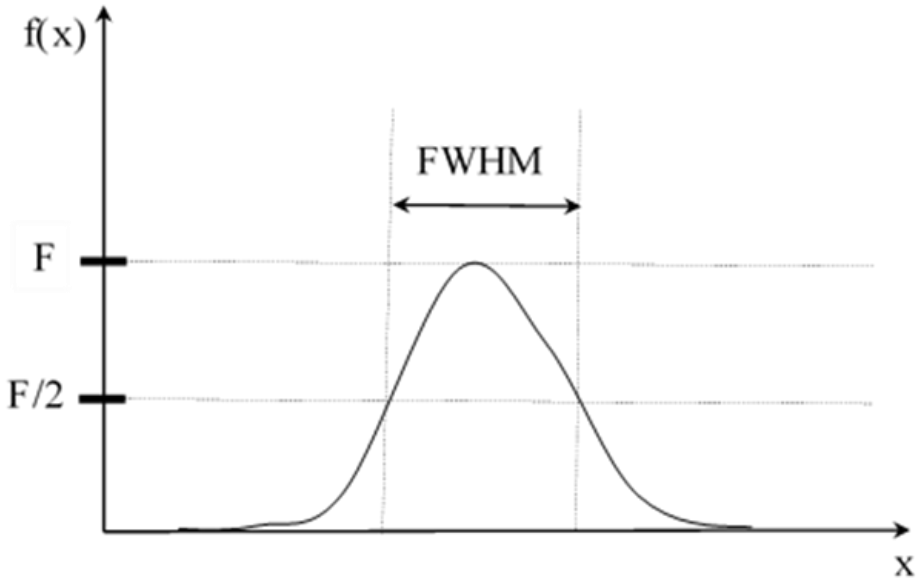

Figure 4-2 Full width at half maximum

4.3: Thermo-elastic stress analysis (TSA)

TSA is a branch of thermography-which analyse stress field measurement based on the thermo-elastic effect (Greene, Patterson & Rowlands 2008). Thermo-elasticity is majorly based on the thermos-elastic effect, similar to solid, liquid and gas change in temperature, if volume changes due to external loading. The Thermo-elastic effect was given a theoretical foundation by William Thomson (Lord Kelvin) in 1853. Thomson (Thomson 1853) presented a linear relationship between the temperature change of a solid and the change in the sum of principle stress for isotropic materials as:

$$\frac{\Delta T}{T_0} = -K_0 \Delta\sigma \tag{4.6}$$

Where, T_0 is the average temperature of the solid, $K_0 (=\lambda/\rho\ Cp)$ is the thermos-elastic constant, λ is the linear thermal expansion coefficient, ρ the mass density, Cp the specific heat at constant pressure, and $\Delta\sigma = \Delta(\sigma_1+\sigma_2+\sigma_3)$ is the variation of the first stress invariant.

This equation was formulated for a homogeneous isotropic materials, however has also been extended to orthotropic materials, by considering thermos-elastic constants in each material direction, due to the anisotropy (Colombo, Vergani & Burman 2012):

$$C_p \frac{\Delta T}{T_0} = -(\alpha_{11}\Delta\sigma_{11} + \alpha_{22}\Delta\sigma_{22} + \alpha_{12}\Delta\sigma_{12}) \quad (4.7)$$

Since the diagonal terms of the thermal expansion tensor of isotropic and orthotropic materials, are non-zero, $\alpha_{12}=0$ and the shear stress component has no effect. The expression of Equation 4.7 can be reduced as:

$$\rho C_p \frac{\Delta T}{T_0} = -(\alpha_{11}\Delta\sigma_{11} + \alpha_{22}\Delta\sigma_{22}) \quad (4.8)$$

The thermal expansion coefficients α_{11} and α_{22} are equal, if the ply orientation is chosen to be orthogonal (Harwood & Cummings 1991). Then the Equation 4.9 combines the variational sum of the stresses as:

$$\rho C_p \frac{\Delta T}{T_0} = -\Delta(\alpha_{11}\sigma_{11} + \alpha_{22}\sigma_{22}) \quad (4.9)$$

In order to apply Equation 4.9 in stress field mapping it is necessary to measure a spatial distribution of temperature changes on the sample surface. The recent advancements in IR imaging technology can be readily applied for measuring temperature changes with an acceptable level of accuracy.

4.4: Fabrication of specimens and Experimentation setups

4.4.1: Mode I (Double Cantilever Beam, DCB)

4.4.1.1: Material and process

The material examined in the present work is twelve layers of (0/90) AR 145 E-glass Woven Roving (Colan, 398 g/m^2 weight and 0.5 mm thick) and Kinetix R246TX epoxy resin matrix composite (WC/epoxy). Mechanical properties of the materials can be seen in Table ***4-1***. The overall specimen dimensions are chosen according to ASTM D-5528 standard for inter-laminar fracture toughness testing. The fibre weight fraction was 60%. The specimen dimension was 400×400×5.6 mm^3 and it includes a 50 mm long piece of 0.001 mm thick Teflon inserted between the centre plies at one end of the specimen to create a pre-crack a_o.

One of the advantages of FBG sensors is its ability to embed in between fibre layers because of its' small size. However, especial care is required to protect the sensor, during the fabrication process. A fibre Bragg grating (FBG) sensor with grating length 5 mm (SMF-280 Fibre type with centre wavelength (λ_b) equal to 1548±0.3nm) was embedded between the first and second layers above the centreline of the laminate. The FBG sensors are coated with acrylate. The coating around the grating location was stripped off before embedding it inside the composite. The FBG sensor was located approximately 5-6 mm from the delamination plane as shown in Figure ***4-3***.

The influence of the curing process of the laminate on the FBG sensor was observed. The description of the FBG spectra before and after embedment is shown in Figure ***4-4***. After embedment, the spectra splits into two peaks and shifted to the left. This distortion of spectra was caused by the effect of the transverse strain during the curing. The transverse strain is induced residual strain that promotes certain birefringence in the core of the fibre and the geometry of the fibre. Because of the axial strain, the wavelength of the sensor shifted. It was observed to be about 0.061 nm wavelength shift as shown in Figure ***4-5***.

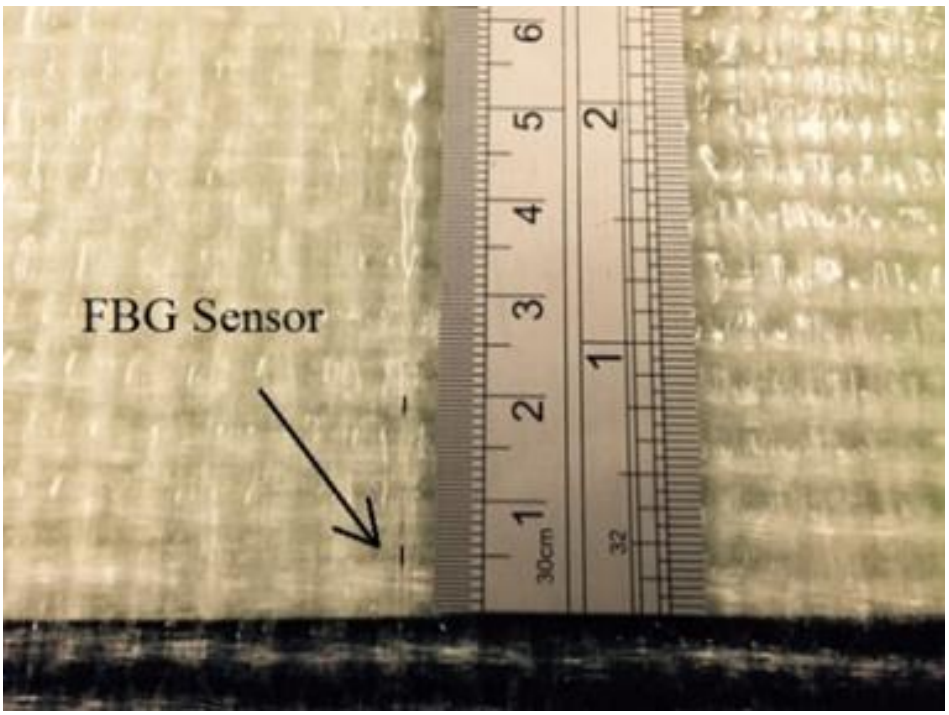

Figure 4-3 Location of Embedding FBG sensor in the specimen

Table 4-1 Mechanical properties for WC/epoxy specimen

Materials	E11 (GPa)	E22 (GPa)	E33 (GPa)	v12	v13	v23	G12 (GPa)	G13 (GPa)	G23 (GPa)	σ fracture (MPa)
Epoxy	2.435			0.29						77.8
WC/Epoxy composite	15	15	9.5	0.126	0.126	0.263	6.527	6.527	7	245

A Double Cantilever Beam (DCB) specimen was cut from the plate with a CNC water jet cutter. The dimension of the DCB sample was 210 mm x 30 mm, and composite tabs 30mm × 10mm × 10mm were attached as shown in Figure ***4-6***. Eight samples were prepared for testing. DCB test was performed on two groups of specimens. The first group contained five specimens numbered SD1, SD2, SD3, SD4, and SD5. These specimens have no embedded FBG sensors. This group of specimens was tested at loading rates ranging from 1 to 1.5 mm/min. The second group of specimens contained three specimens SDF1, SDF2, and SDF3 and each sample had an embedded FBG sensor. The second group of the specimen was tested at the same loading rates as the first group of specimens and stopped intermittently for the FBG signal measurements. The FBG signal was used to accurately find the yield strain(ε_Y).

Electrical resistance foil strain gauges were attached to the sample surface at 5mm distance from the end of initial delamination to measure the surface strains. The purpose of these strain gauges was to confirm the maximum strain (ε_{max}).

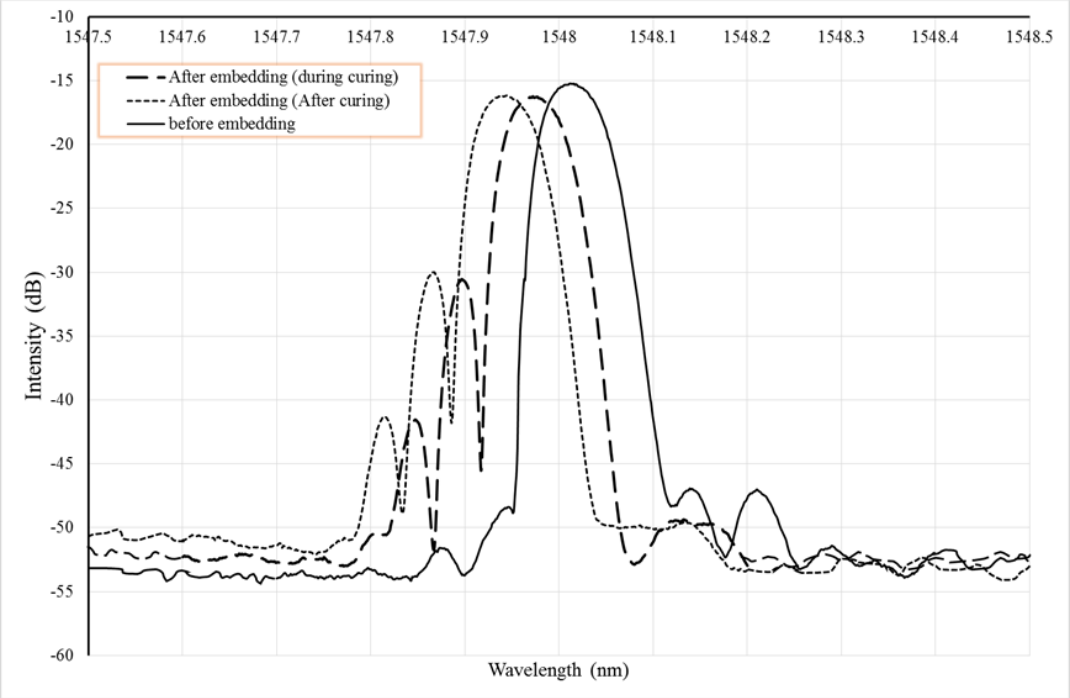

Figure 4-4 Comparison of FBG spectra before and after embedding

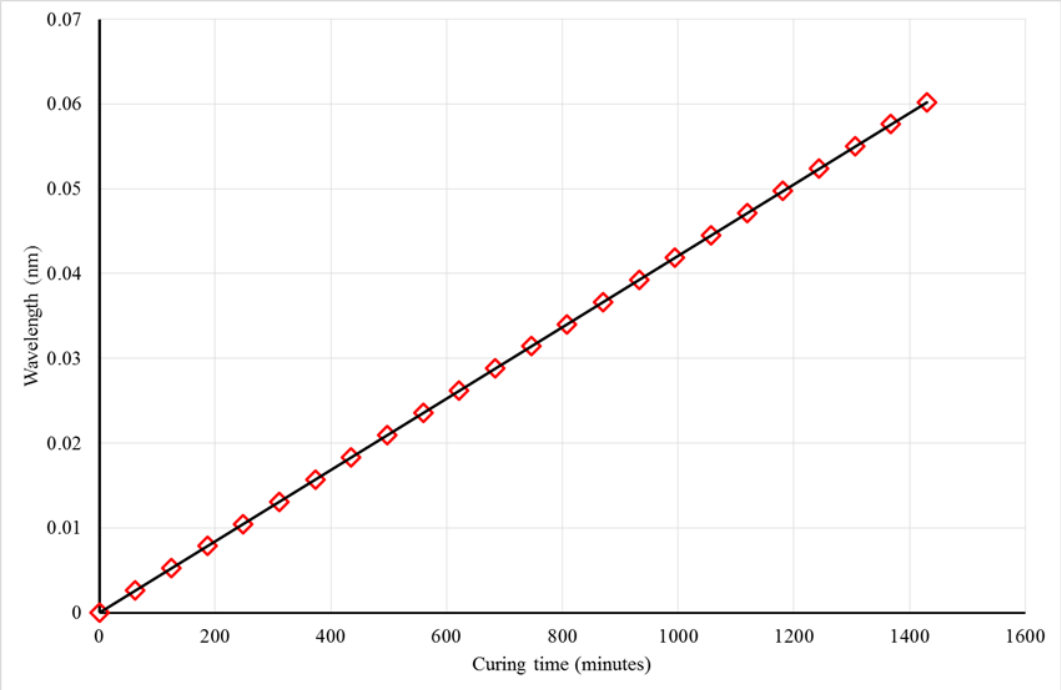

Figure 4-5 FBG wavelength shift during curing process

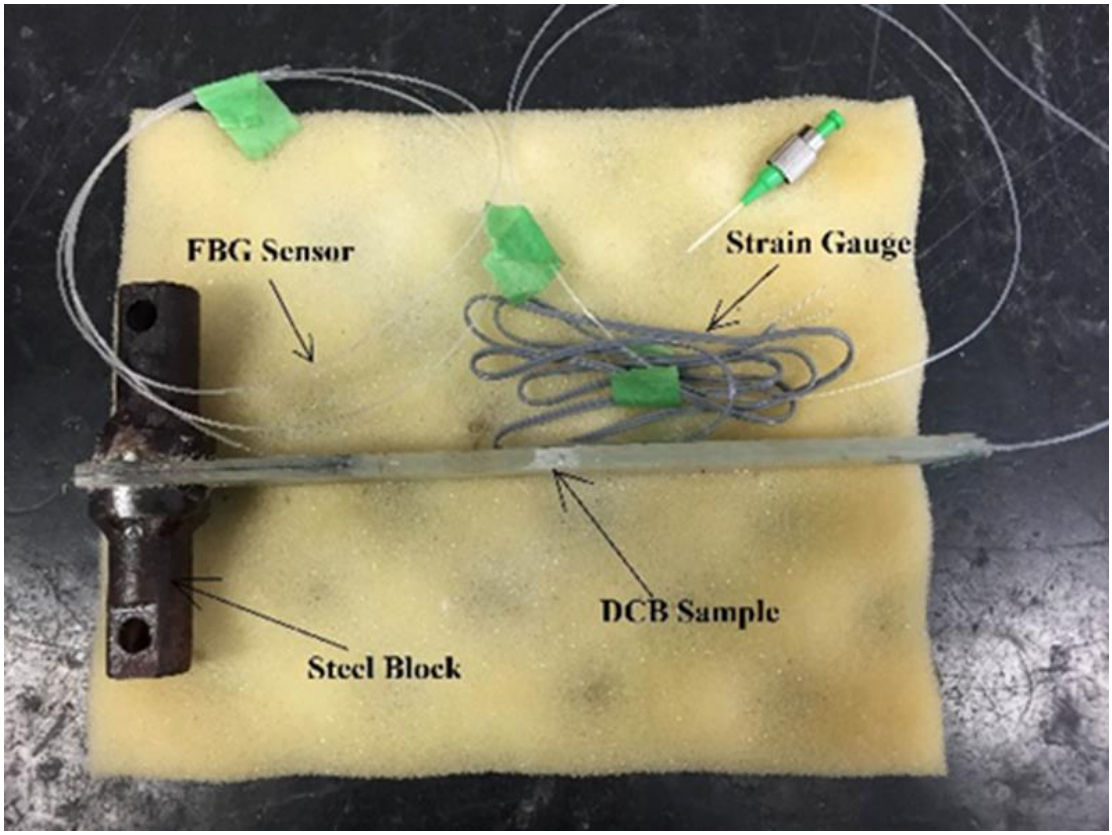

Figure 4-6 Specimen of WC/epoxy with embedding FBG sensor and bonding strain gauge

4.4.1.2: Energy release rate in double cantilever beam (DCB) specimens

A schematic of a DCB test is shown in Figure ***4-7***, the specimen thickness is given by 2h (mm), the crack length is represented by a (mm), and the applied load is represented by *P (N).* The energy release rate in a DCB specimen is defined in usual way;

$$G = \left(\frac{P^2}{2b}\right)\left(\frac{dc}{da}\right) \tag{4.10}$$

Where G is the fracture energy, b (mm) is the width of the specimens, c is the compliance ($^{\Delta}/_{P}$) and a is length in mm of the delamination crack. Ignoring the bridging effect, the deflection of an ideal cantilever beam (Lekhnitskii 1968), with length a (mm), under a load P is equal to;

$$v = \frac{P}{I}\left[\frac{(2\bar{S}_{12}\bar{S}_{16} - 3\bar{S}_{12}\bar{S}_{26})b^2}{24\bar{S}_{11}}y - \frac{\bar{S}_{12}}{2}xy^2 + \frac{(-2\bar{S}_{12}\bar{S}_{16} + \bar{S}_{11}\bar{S}_{26})}{6\bar{S}_{11}}y^3 + \frac{\bar{S}_{11}}{6}(x^3 - 3a^2x + 2a^3)\right] \tag{4.11}$$

Where, *I* is the second moment of inertia equals to $4bh^3/3$, and S_{nn} is compliance coefficients of the beam (Reddy 2004).

In order to determine deflection equation in symmetry, the axis of the beam y=0 is substituted into Equation (4.11) and on simplifying it;

$$v = \frac{P}{I}\frac{\bar{S}_{11}}{6}(x^3 - 3a^2x + 2a^3) \tag{4.12}$$

or

$$v = \frac{\Delta}{2}\left[\left(\frac{x}{a}\right)^3 - 3\left(\frac{x}{a}\right) + 2\right] \tag{4.13}$$

Where $\Delta = {Pa^3\bar{S}_{11}}/{3I}$ is the normal displacement of the flexible member from the initial plane, i. e, $v(0)$. The full opening (Δ) of the DCB equals the doubled deflection (2Δ), and the popular formula for the DCB is obtained:

$$G_I = \frac{3P^2\bar{S}_{11}a^2}{4b^2h^3} \tag{4.14}$$

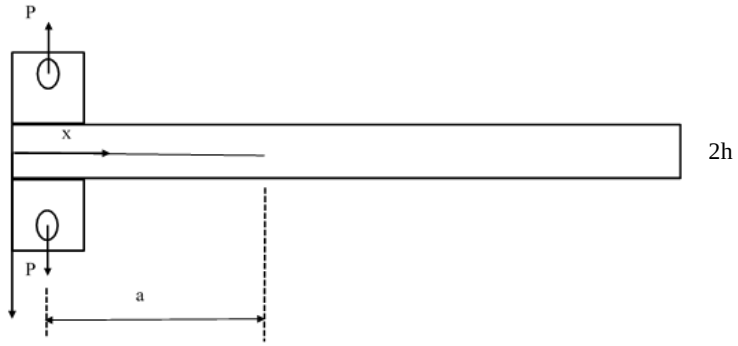

Figure 4-7 The schematic diagram of a DCB specimen

4.4.1.3: Inter-laminar fracture toughness test

DCB tests were performed according to ASTM D-5528 standard to determine inter-laminar fracture toughness. A 10 KN uniaxial MTS testing machine was used for loading the specimen. Modified Compliance Calibration method (ASTM-5528) was used for reduction of test data for Mode I delamination. The displacement Δ mm was increased at a rate of 1.5 mm/min. The crack tip was continuously monitored with Casio Exilim EX-FH20 high-speed camera that records up to 1000 frames per second and the time was recorded with the crack tip position (Figure ***4-8***). The specimens with embedded FBG sensors were loaded at a rate of 1.5 mm/min and stopped intermittently in order to record measurements of the FBG sensor response. After that, the specimen was reloaded to next load level.

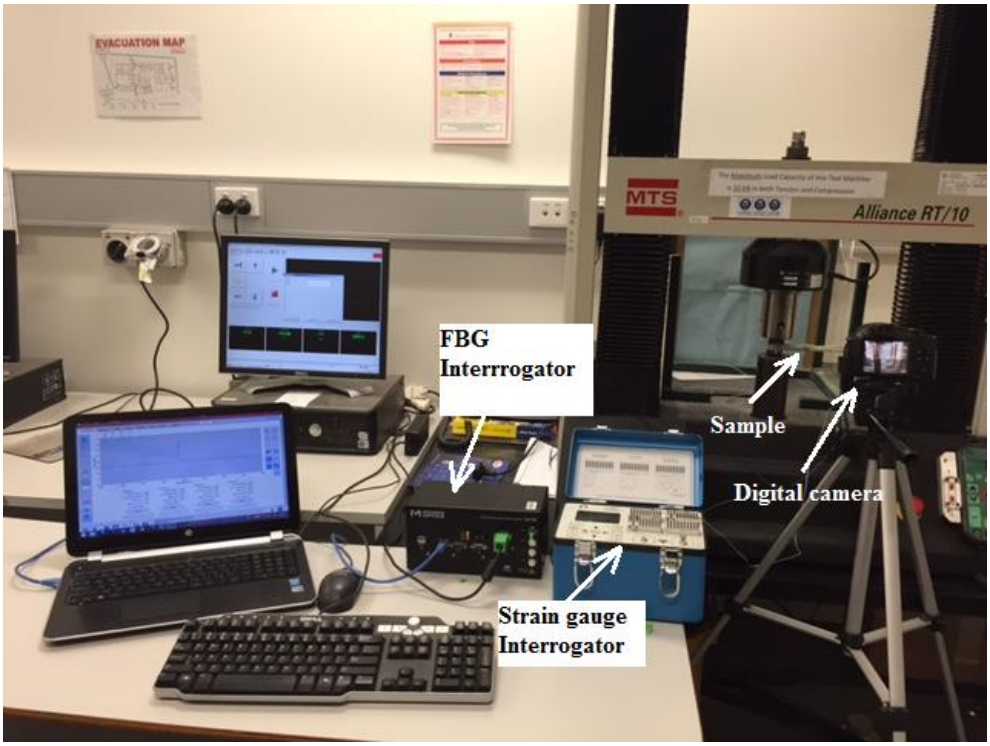

Figure 4-8 The configuration of the test rig

The thickness side of specimens was polished and marks were drawn in one millimetre intervals for first five millimetres and at five millimetres intervals for next twenty millimetres as shown in Figure ***4-9***. The crack propagation was measured using the high-speed camera. The values of P and Δ were measured and stored for each crack increment Δa =1mm. The specimen with extended open cracks is shown in Figure ***4-9***.

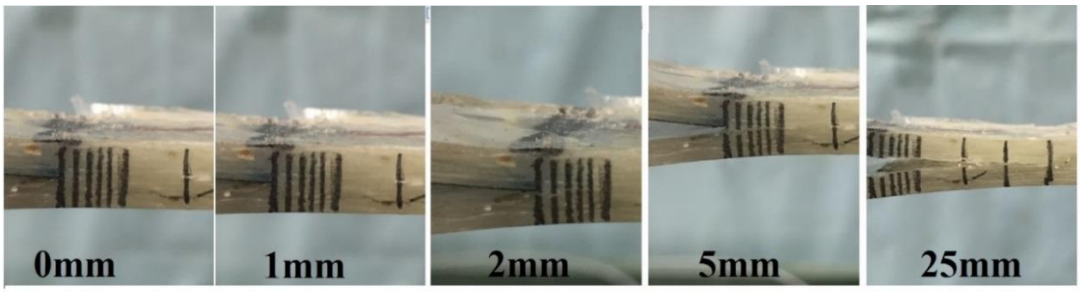

Figure 4-9 Propagating delamination cracks during DCB test in various displacement for WC/epoxy

4.4.1.4: Cohesive zone Model

A finite element model of the tested specimen was created in ABAQUS 6.13 to analyse and simulate Mode I delamination growth. Double node "Cohesive" elements were used to represent the bonded interfaces. The specimen geometry is

depicted in Figure ***4-10***. A purposely created 50mm long delamination was also created in the model as the test specimen configuration.

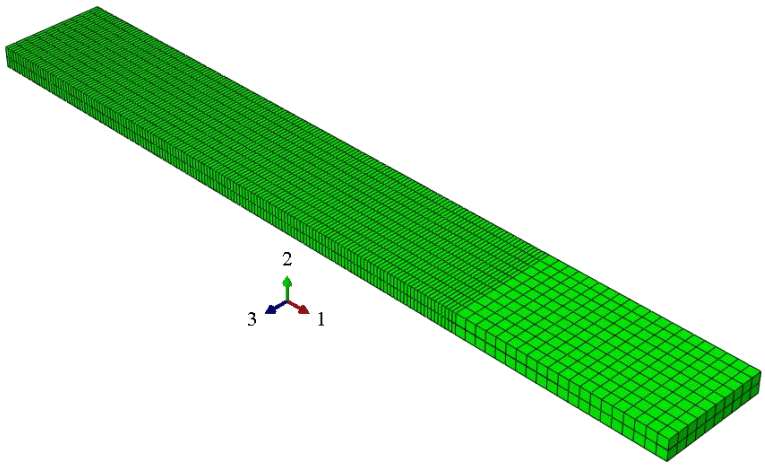

Figure 4-10 DCB specimen finite element model

The specimen was meshed using 3D solid elements C3D8I with the top and bottom parts of the specimen. Each part was separately meshed using different mesh sizing. Disbanded interfaces defined in the middle of the specimen, represent the delamination surface of the test specimen, (Figure ***4-11***).

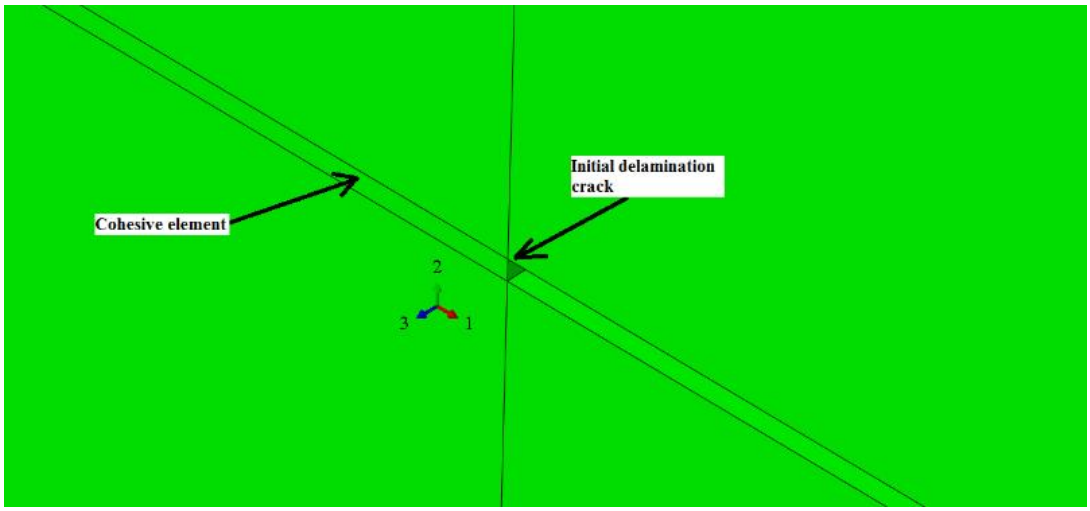

Figure 4-11 A cohesive element in finite element model

Delamination growth was simulated using 0.001 mm thick cohesive elements COH3D8 created at the interface. The user cohesive element technique was implemented by means of UMAT subroutine. Auto Desk© Simulation composite analysis 2015 Plug-ins© for ABAQUS 6.13 was used to create the UMAT

subroutine to calculate the nine state damage variables (SDVn) for the cohesive materials. These state damage variables are stored by ABAQUS at each individual integration point within the finite element model. Two state variables are used in this study to indicate the damage. SDV2 which is a continuous real variable between zero and one indicates the damage initiation and SDV6 which is the damage variable, indicates continuous real variable that varies between zero and one.

4.4.2: Mode II (End Notch Flexure, ENF)

4.4.2.1: Material and process

The material used in this research was twelve-layer (0/90) orthogonally AR 145 E-glass Woven Roving Manufactured by Colan (398 g/m^2 weight and 0.5 mm thickness) and Kinetix R246TX epoxy resin matrix (WC/epoxy) composite with a nominal density of 1698.514 kg/m^3. Woven Roving Fabrics are most suited for hand lay-up applications where thickness and strength is required. The plain weave structure of the laminate consists of two mutually orthogonal directions (warp and weft) with an approximate volume fraction of 60% reinforcing glass fibres. The overall specimen dimensions were chosen according to ASTM D-7905-14 standard for inter-laminar fracture toughness. Mechanical properties of materials can be seen in table 4.1. The $[0/90]s_6$ plates measure $400 \times 400 \times 6.5$ mm^3 and include a 50 mm long of piece of Teflon about 0.001mm thickness inserted between the centre plies at one end of specimen to create a pre-crack a_o as shown in Figure ***4-12***.

In this research, optical fibres with length 5 mm and centre Bragg wave length λ_B= 1548±0.3nm were embedded between the first and second layers above the centreline during fabrication of the laminated composite specimen. The FBG sensor was coated with acrylate. However, the coating around the grating location was stripped off for each FBG sensor before embedding it inside the composite specimen. The FBG was located approximately 5-6 mm from the delamination plane as shown in Figure ***4-13***. The sensor location was carefully selected to avoid damage while maintaining the allowable sensitivity of the sensor. The description of the FBG spectra before and after embedment is shown in Figure ***4-14***. After embedment, the spectrum was divided into two peaks and it shifted to the left. This distortion of spectra is caused due to the effect of the transverse strain during the curing. The transverse strain is induced residual strain that promotes certain

birefringence in the core of the fibre and the geometry of the fibre. Because of the axial strain, the wavelength of the sensor is shifted. The wavelength shift is observed to be around 0.061 nm as shown in Figure ***4-15***.

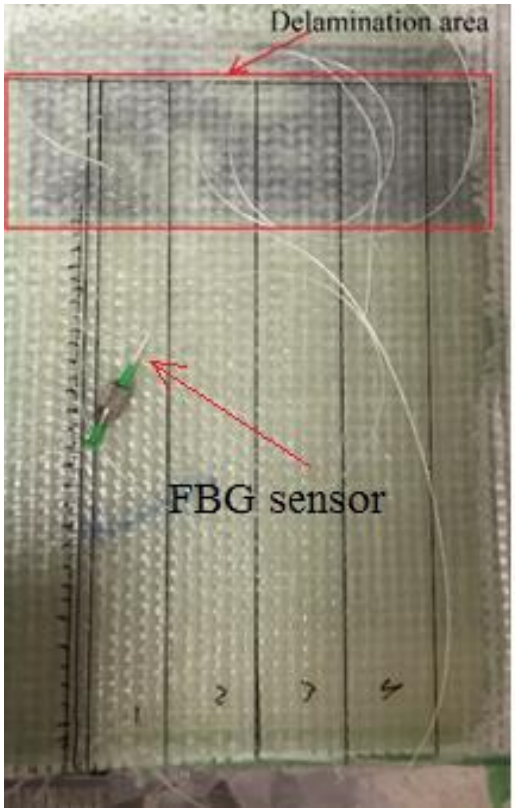

Figure 4-12 WC/epoxy composite plate with embedding FBG sensor before cutting

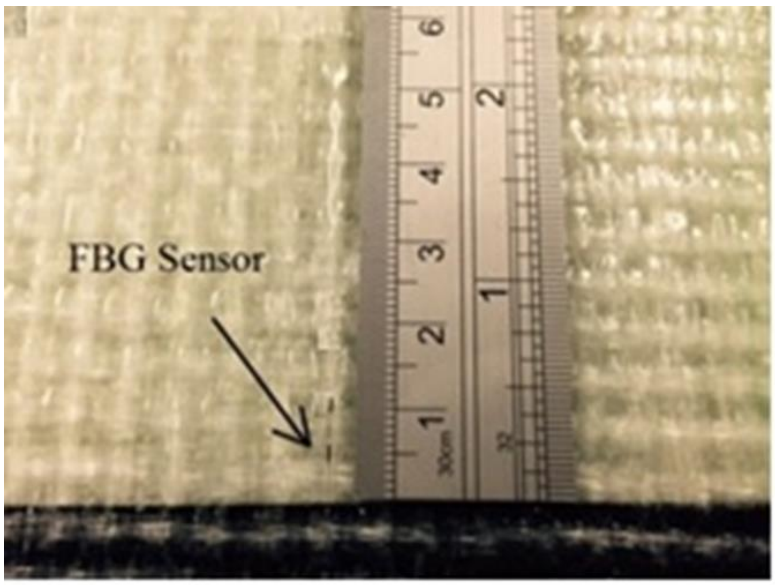

Figure 4-13 Location of embedding FBG sensor in the WC/epoxy composite specimen

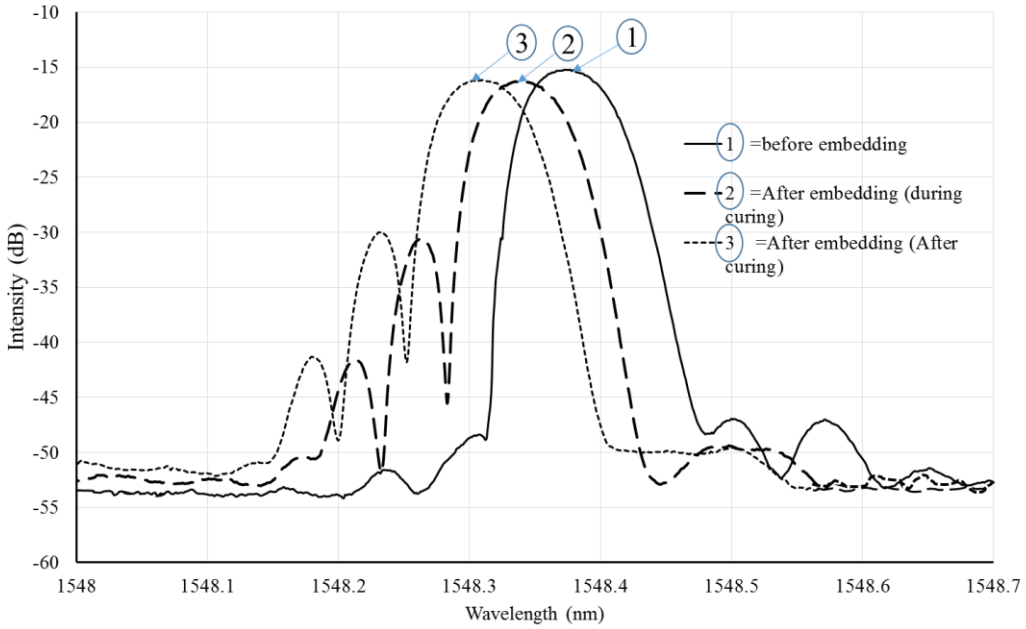

Figure 4-14 Comparison of FBG spectra peak shifting before and after embedment

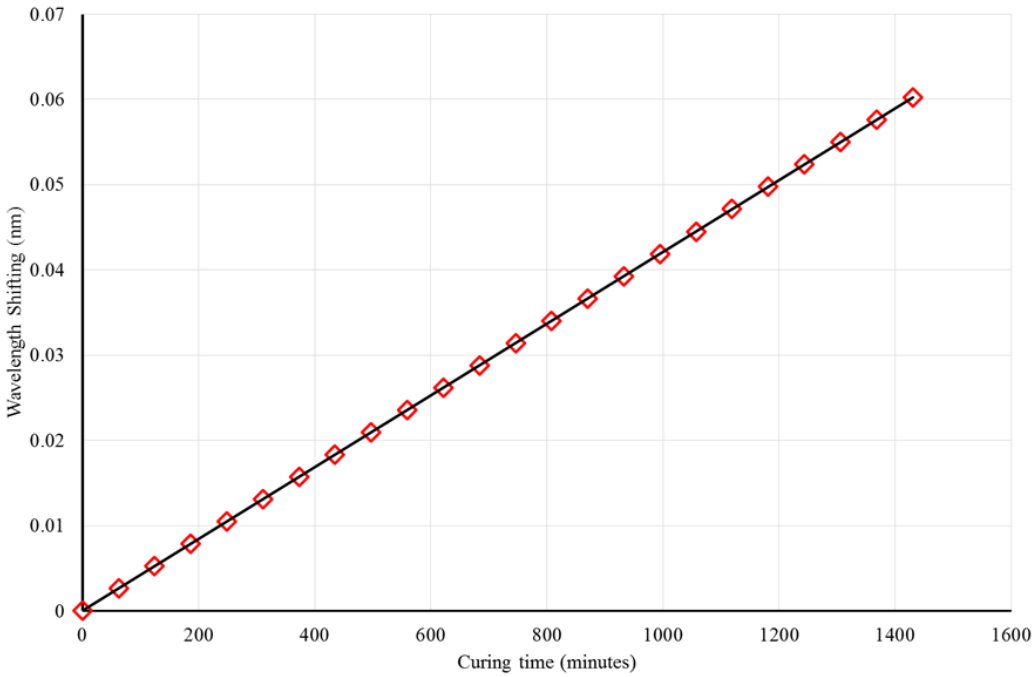

Figure 4-15 FBG wavelength shift during curing process at constant room temperature

An End Notch Flexure (ENF) beam specimen is cut from the fabricated plate as shown in Figure ***4.13*** using a water jut cutter. The dimension of the ENF sample was 280mm x 30mm. A strain gauge (FLA-5-11-1LL) was attached to the surface of the specimen as shown in Figure ***4-16***. Eight specimens were prepared for testing. ENF test was performed on two groups of specimens. First group contains

five specimens which were numbered as SN1, SN2, SN3, SN4, and SN5 with no embedded FBG sensors. This group was tested at loading rates from 1 to 1.5 mm/min. The second group contained three specimens as SNF1, SNF2, and SNF3 with embedded FBG sensors (FBG sensor was located about 5mm from the end of artificial delamination crack and one layer above delamination). Second group was tested at the same loading rates and stopped periodically for recording FBG measurements. The variation of loading regime did not affect force-displacement behaviour (Sorensen et al. 2007) within elastic limits. The FBG signal was used to find the yield strain(ε_Y) accurately. A foil strain gauge was attached to the sample surface at 5mm distance from the end of initial delamination to measure the surface strains. The purpose of these strain gauges was to verify the maximum strain (ε_{max}).

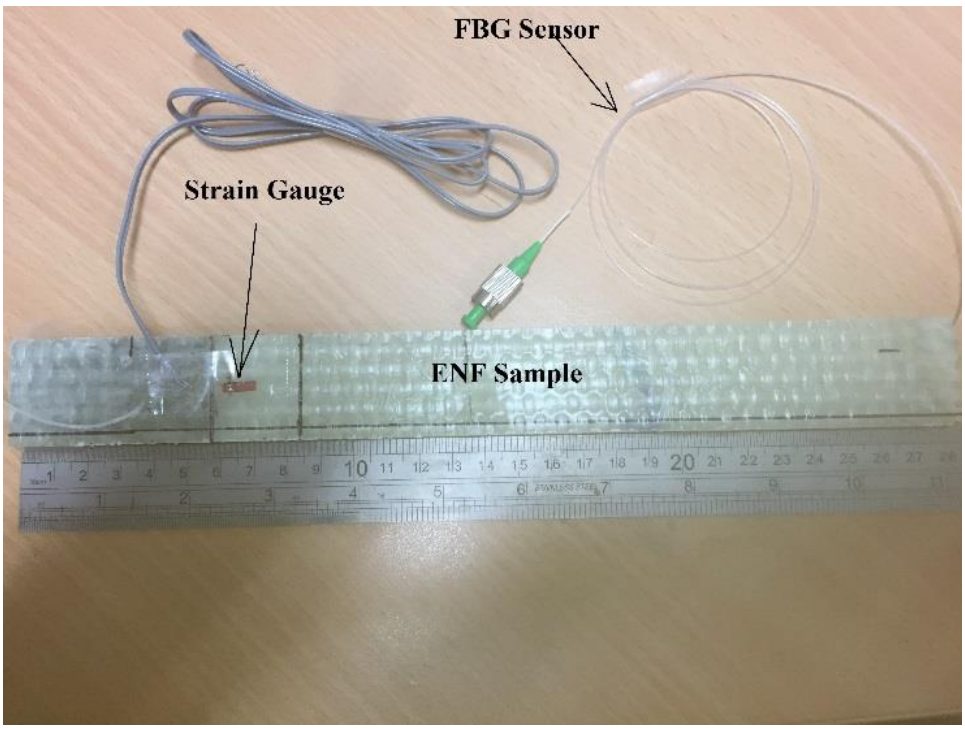

Figure 4-16 ENF specimen of WC/epoxy with embedding FBG sensor and bonding strain gauge

4.4.2.2: Energy release rate in End Notch Flexure (ENF) specimens

The classical data reduction schemes which are based on beam theory and compliance calibration has been developed to obtain the critical fracture energy in pure Mode II (G_{IIc}). The End Notch Flexure (ENF) test has been used to determine

the fracture energy in Mode II delamination damage in a laminated composites (Carlsson, Gillespie & Pipes 1986). Davidson and Sun (Davidson & Sun 10/2006) has proposed this standard test for Mode II unidirectional laminates and calculated G_{II}. A schematic of ENF test set up is shown in Figure ***4-17***. The specimen thickness is 2h (mm), the crack length is a (mm), width of the specimen is b (mm) and the applied load is P (N). The Mode II fracture energy (G_{II}), is define in a usual way as;

$$G_{II} = \frac{P^2}{2b}\frac{dC}{da} \tag{4.15}$$

where G is the fracture energy, b *(mm)* is the width of the specimen, a is the length of crack from the support roller and C is the compliance and equal to;

$$C = \frac{\Delta}{P} \tag{4.16}$$

where Δ is the centre loading roller displacement. From Direct Beam Theory (DBT), the Mode II fracture energy (G_{II}) is given by;

$$G_{II} = \frac{9a^2P\Delta}{2b(2L^3+3a^3)} \tag{4.17}$$

where L is half of span and equal to 50 mm, and initial crack (a_o) is equal to 30 mm. in the case of ENF test, the Correction Beam Theory (CBT) presented by Wang and Williams (Wang & Williams 1992).

$$G_{IIc} = \frac{9(a+0.42\Delta_I)P^2}{16b^2h^3E_1} \tag{4.18}$$

where E_1 is the axial modulus, h is the half thickness of the ENF specimen and Δ_I a crack length correction to account for shear deformation

$$\Delta_I = h\sqrt{\frac{E_1}{11G_{13}}\left[3-2\left(\frac{\Gamma}{1+\Gamma}\right)^2\right]} \tag{4.19}$$

$$\Gamma = 1.18\sqrt{\frac{E_1E_2}{G_{13}}} \tag{4.20}$$

where E_2 and G_{13} are the transverse and shear modulus respectively.

The Compliance Calibration Method (CCM) is based on the Irwin-Kies equation (Kanninen & Popelar 1985). Cubic polynomials ($C = C_1 a^3 + C_o$) were used to fit the *C= f(a)* curves, leading to

$$G_{IIc} = \frac{3P^2 C_1 a^2}{2b} \tag{4.21}$$

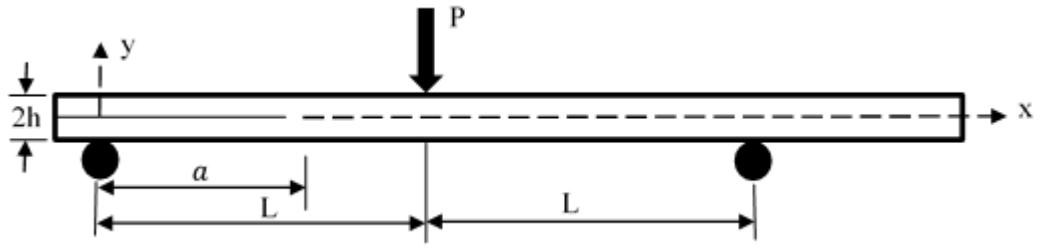

Figure 4-17 The schematic of ENF specimen

4.4.2.3: Inter-laminar fracture toughness tests

Static Mode II or End notched flexure (ENF) pre-crack tests were performed according to ASTM D-7905-14 the standard test method to determine inter-laminar fracture toughness. A 10 KN MTS testing machine was used at room temperature for loading the specimen. The displacement of Δ mm was increased at a rate of 1.5 mm/min. Different rates were used to determine the appropriate loading rate. The crack tip was continuously monitored with Casio Exilim EX-FH20 high speed camera that records up to 1000 frames per second and photographs were taken manually and the time intervals were recorded with the crack tip position (see Figure ***4-18***). The specimens with embedded FBG sensor were loaded at a rate of 1.5 mm/min and stopped intermittently in order to record measurements of the FBG sensor response. After that, the specimen was reloaded to next load level. Optical sensing interrogator Micron Optics sm 125 was used to acquire FBG readings. The thickness side of specimens, marks were drawn at one millimetre intervals for first five millimetres and five millimetres intervals for twenty millimetres as shown in Figure ***4-19***. The crack propagation was captured using a high-speed camera. The values of P and Δ are measured and stored for each crack increment Δa =1mm. The specimens with extended cracks are shown in Figure ***4-19***.

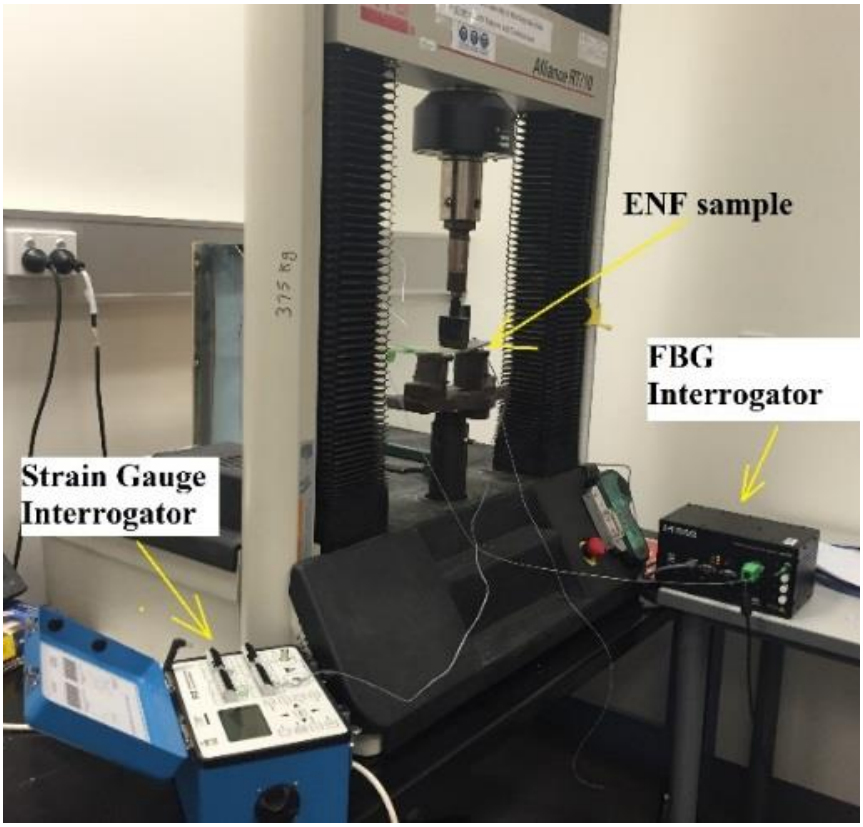

Figure 4-18 The configuration of the testing system

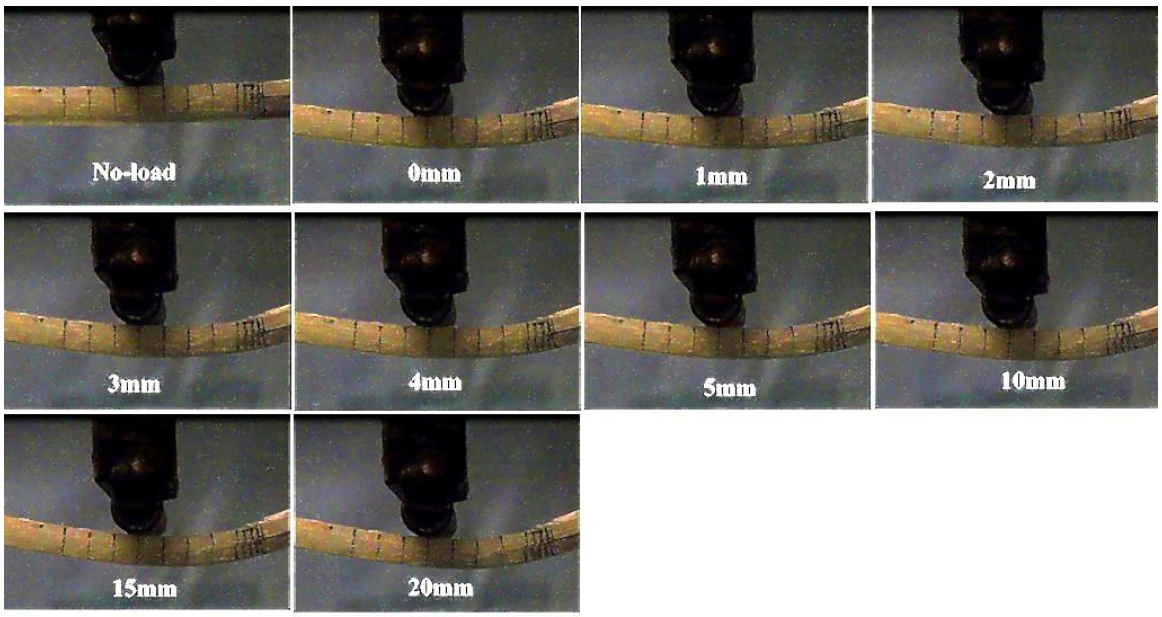

Figure 4-19 Propagating delamination crack during ENF test in various displacement

4.4.2.4: Cohesive zone model

A finite element model of the test specimen was created on commercial FEA software ABAQUS 6.13 to analyse and simulate Mode II delamination growth.

Simply supported boundary conditions were applied at the steel support rollers below the laminate as shown in Figure ***4-20***a. A displacement-controlled load was applied at the centre steel loading roller, which is in contact with the top ply of the composite specimen. Cohesive elements (double nodes) were used to represent the bonded interfaces. The specimen ($280\times30\times6.5mm^3$) with 50 mm initial delamination cracks, is depicted in Figure ***4-20***b. Inter-laminar cohesive layers were meshed with three-dimensional COH3D8 using sweep mesh control. The interface region was discretised with a single layer of small thickness (0.001mm) cohesive elements having shared nodes with ply elements. Composite laminate specimen was meshed with three-dimensional solid elements, incompatible Mode eight-node brick element C3D8I was used with sweep mesh control. Each part was separately meshed using different mesh sizing for reducing computational model time. The concern (delamination damage propagation region) area was meshed with 0.5 mm size and the rest of the composite specimen was meshed with 5mm elements. A debonded interface was defined in the middle of the specimen, consistent with the actual delamination in the test specimen (see Figure ***4-21***).

The user cohesive element technique is implemented by means of user material sub-routine UMAT. Auto Desk© Simulation composite analysis 2015 Plug-ins© for ABAQUS 6.13 was used to create the UMAT subroutine to calculate the nine state variables (SDVn) for the cohesive materials. These state variables are stored by ABAQUS at each individual integration point within the finite element model. Two state variables (SDV) are used in this study to indicate the damage. SDV2 is a continuous real variable between zero and one which indicates the damage initiation. SDV6 is the damage variable D and is a continuous real variable varying between zero and one.

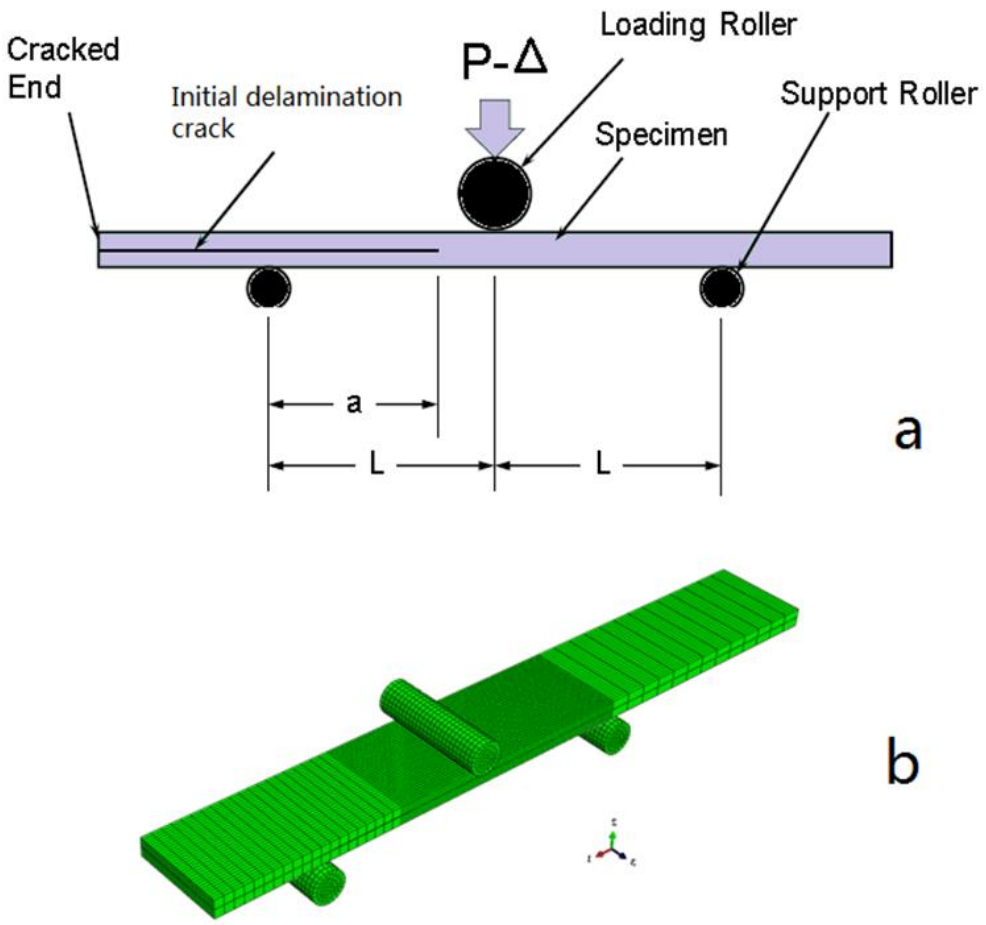

Figure 4-20 (a) End-notched Flexure (ENF) 3-point bend test, (b) Finite element model

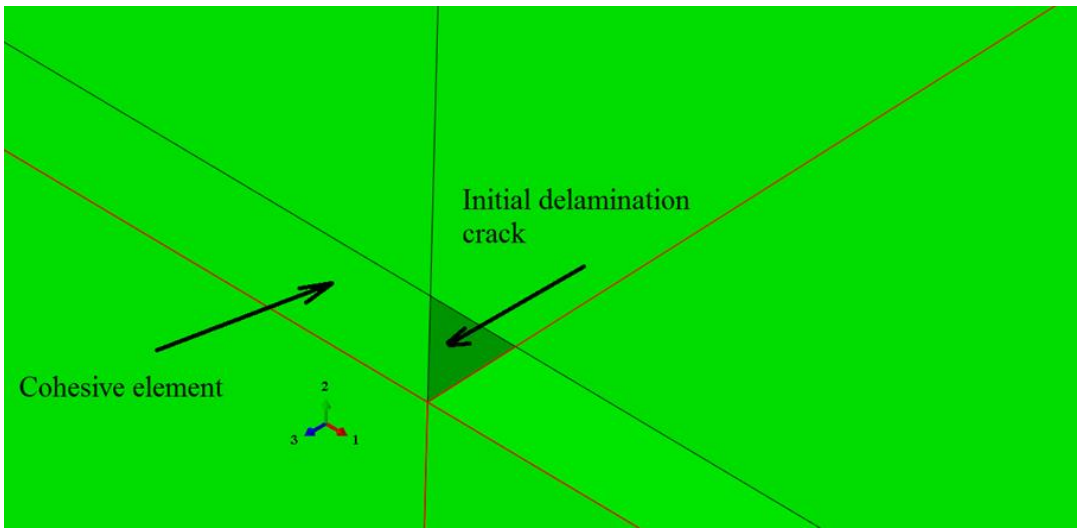

Figure 4-21 Cohesive element in finite element model (no scales)

4.4.3: Mode II delamination damage under axial tensile loading

4.4.3.1: Materials and specimen geometry

The material examined in the present work is a fifteen-layer (0/90) AR 145 E- glass Woven Roving (Colan398 g/m^2 weight and 0.5 mm thick) fibre-reinforced epoxy resin matrix composite that has a nominal density of 1698.514 kg/m^3. Woven Roving Fabrics (WC) is the best glass material for hand lay applications where uniform thickness and transverse strength is required. The WC fabric offers good coverage, drape-ability and fast wet-out. Kenetix R246TX epoxy resin was used as the matrix material. The plain weave structure of the WC laminate consists of two mutually orthogonal directions (warp and weft) with an approximate volume fraction of glass was 60%. Two artificial delamination with 50 ×40 mm^2 area were made between 4th-5th and 11th-12th layers respectively (counted from the bottom) by embedding Teflon papers (0.001mm thickness) during the manufacture of composite plates. An optical fibres with grating length 5 mm and Bragg wave length λ_B= 1548±0.3nm were established between the 4th–5th layers. The FBG is located approximately 10±1 mm from the delamination plane. The sensor location was carefully selected to avoid damage while maintaining the optimum sensitivity of the sensor to the anticipated damages. Rectangular 400 × 40 (mm^2) specimens were cut using water jet cutting as shown in Figure ***4-22***a and b. The specimens were coated with 2 passes of RS matt black paint to provide uniform surface conditions, and to increase emissivity and minimise reflection.

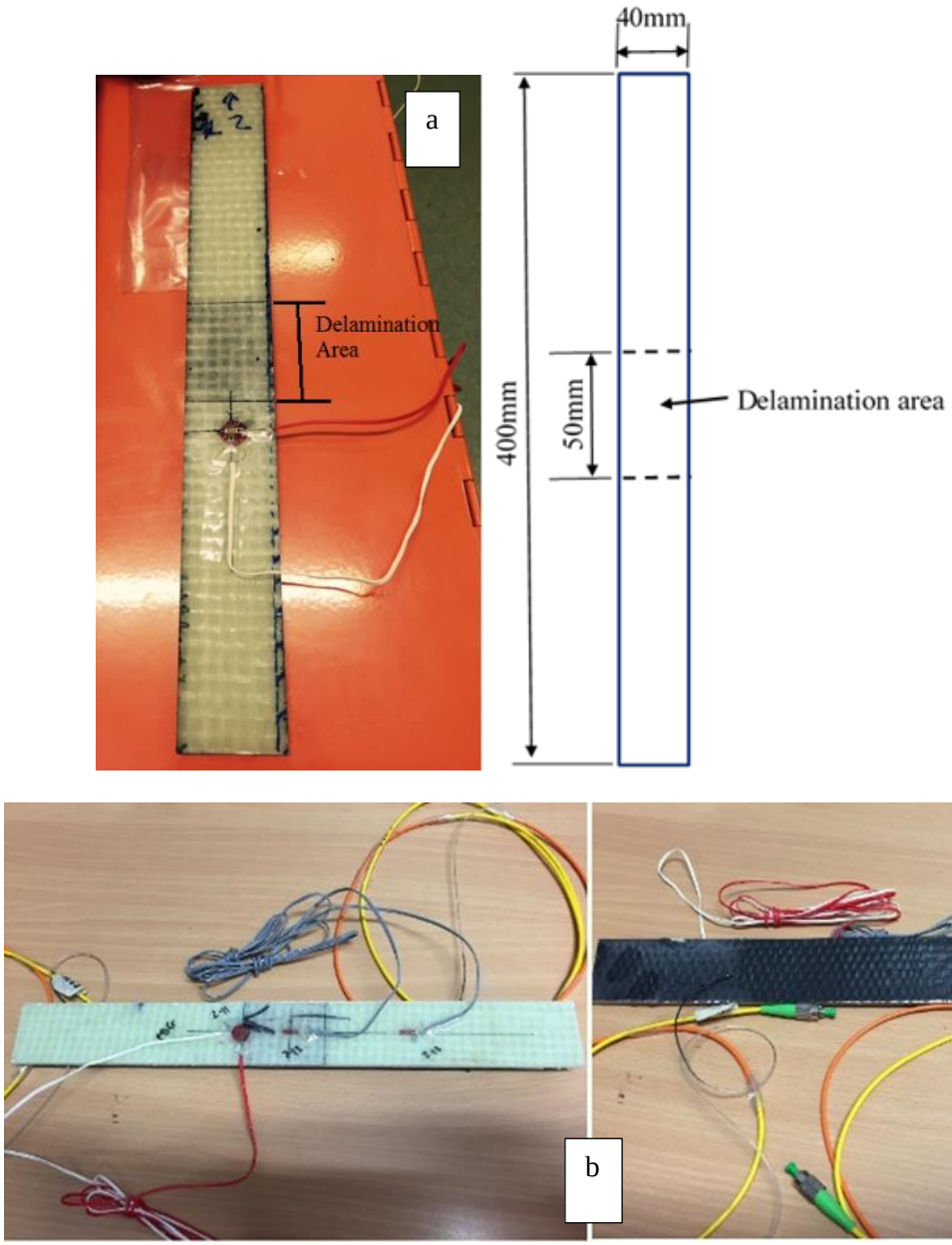

Figure 4-22 (a) Glass/Epoxy specimen (400 mm x 40 mm x 7.5 mm) without FBG sensor (b) Phototype delaminated specimen with embedded FBG sensor and bonded strain gauges (both sides)

4.4.3.2: Mechanical testing

Quasi-Static and subsequent cyclic loading were applied to the samples as shown in Figure ***4-23***. The quasi-static loading was applied at a rate of 1.5 mm/min at displacement control Mode and cyclic mean load level was varied from 5kN to 35kN in steps of 5kN, and stress ratio was R= 0.1, and cycles less than 10000 were followed. All the tests were conducted on MTS 810 100kN uniaxial testing machine which is fitted with hydraulic grips. Specimen was fastened to the machine with approximately 50 mm in length held by the hydraulic grips. Load and

displacement were acquired from the load cell and displacement sensors of the MTS machine. The foil type strain gauges were attached to the sample surface and used to measure the strains during the applied loading and, are used as a reference single for TSA. The mean load is ramped monotonically, and at selected stress levels a cyclic load was applied at frequency of 5 Hz. The load and displacement signals were fed to MITE© software through a NI USB-6008 card to synchronize the IR images and the thermal cycles. Both static and cyclic loadings are the basic requirements in this work for FBG sensor and TSA signals. The specimen was loaded and FBG spectrums were recorded. Micron Optics 3.1 sm125 optical spectrum analyser was used to measure FBG spectrum and cyclic loading was applied to capture TSA signal from TSA system.

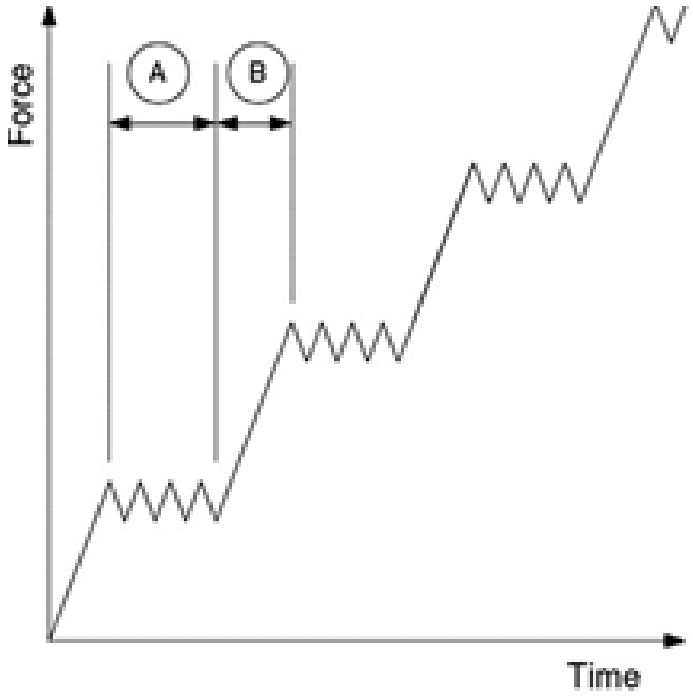

Figure 4-23 TSA test method, a static load step is applied, followed by a cyclic loading about this mean loading level (Johnson 2014)

The mean load levels were increased in 5 kN increments, followed by the 10000 Cycles at the stress ratio R = 0.1. The small cyclic loading imparts a very little strain energy to the delamination area even at high mean load. Therefore low cycle fatigue damage was neglected (Johnson 2014) and not considered in the analysis.

The schematic of the TSA setup is shown in Figure ***4-24***. The TSA system is developed using a FLIR A325 low-grade commercial microbolometer camera. This device contains a 320 (H) × 240 (V) Vanadium Oxide (VOx) array with a nominal

NEDT of 50 mK. The output is in 16-bit digital form and is supplied at a fixed frame rate of 60 Hz. The infrared (IR) camera captured images at a rate of 456 frames per second (fps).

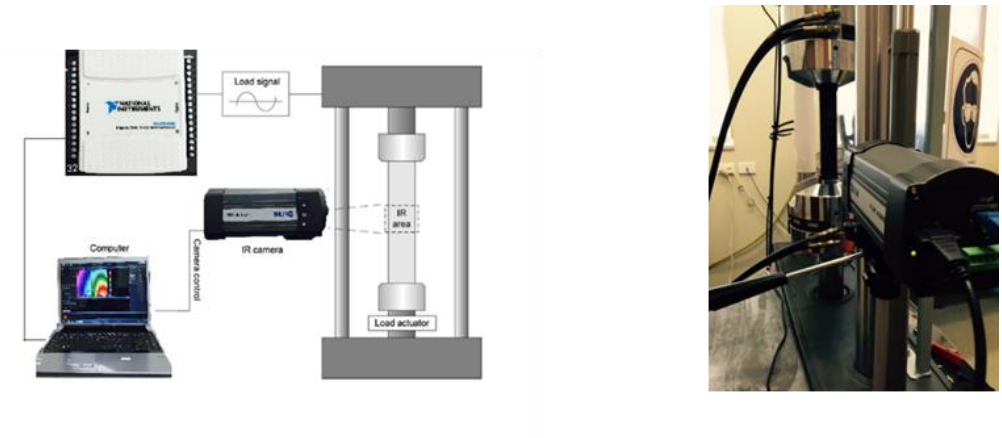

Figure 4-24 Thermo-elastic stress analysis (TSA) testing setup

4.4.3.3: Cohesive zone model

A finite element model of the aforementioned specimen was created in ABAQUS 6.13 and used to predict mixed-mode multi-delamination growth. Cohesive elements or double nodes were used to represent the bonded interfaces. The specimen geometry and loading regime are depicted in Figure ***4-25***. The layered specimen dimensions are 300 mm long, 7.5mm thick (15 layers) and 40 mm wide, loaded at one end in the longitudinal direction and fixed at the other end. The model includes two initial delamination cracks. Both initial cracks are 50 mm in length and are located 125 mm from the end of the specimen. The first crack is located 1.75 mm below the mid-plane of the specimen, whilst the second crack is located symmetrically 1.75 mm above the mid-plane. The distance between the two initial cracks is 3.5 mm.

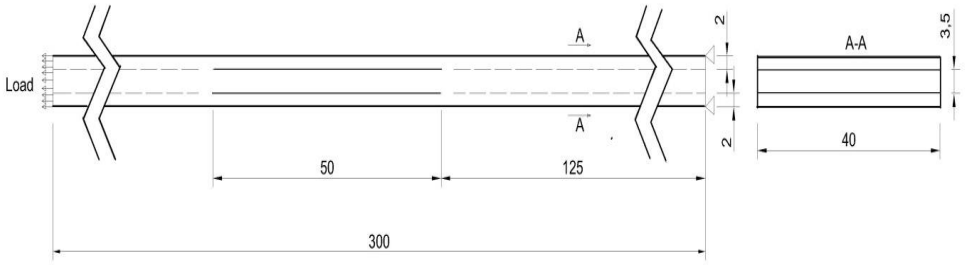

Figure 4-25 Model Geometry (dimensions are in millimetres)

The specimen was modelled using 3D solid elements (C3D8I) with the top and bottom parts of the specimen (i.e above and below the cracks) consist of 8 layers (a thickness of 4 mm), and the middle section 6 layers (a thickness of 3.5 mm). Each part was separately meshed using different mesh size. The finite element model is shown in Figure ***4-26***. Two de-bonded interfaces were defined, one between the 4^{th} and 5^{th} layers and the other between the 11^{th} and 12^{th} layers, consistent with the actual delamination (see Figure ***4-27***). Delamination growth was simulated using cohesive elements (COH3D8) 0.001 mm in thickness embedded at the interface. The user cohesive elements technique was implemented by means of feeding user material sub-routine UMAT. Auto Desk© Simulation composite analysis 2015 Plug-ins© for ABAQUS 6.13 were used to create the UMAT subroutine to calculate the nine state variables for the cohesive materials (Wang & Xu 2015). These state variables are stored by ABAQUS at each individual integration point within the finite element model. They are represented in the ABAQUS/viewer application by the solution-dependent state variables "SDVN" where N is the unique integer which identifies the state variable (SDV1, SDV2…, SDV9). The nine state variables are defined as follows: SDV1 represents the current damage state, SDV2 is a continuous real variable between zero and one which indicates that the damage initiation criteria is satisfied, SDV3 is the effective traction at damage initiation, SDV4 is the effective displacement at damage initiation, SDV5 is the maximum effective displacement attained in the loading history, SDV6 is the damage variable D, a continuous real variable which varies between zero and one, SDV7 is the work done in the normal loading Mode (local 3-direction), SDV8 is the work done in the first shear loading Mode (local 1-direction), and SDV9 is the work done in the second shear loading Mode (local 2-direction). The cohesive elements in the model act as a "traction-separation" element type. Cohesive elements (COH3D8) with properties defined by UMAT were inserted between the specimen parts within the connected area. The influence of the COH3D8 elements on the model as a whole can be ignored as softening of the element was not taken into consideration. All mechanical and cohesive properties were determined experimentally according to ASTM standards at the Centre of Excellence in Engineering Fibre Composite Laboratories at the University of Southern Queensland. Mode I cohesive properties were obtained

according to ASTM D5528-13 and Mode II cohesive properties were obtained according to ASTMD7905-14.

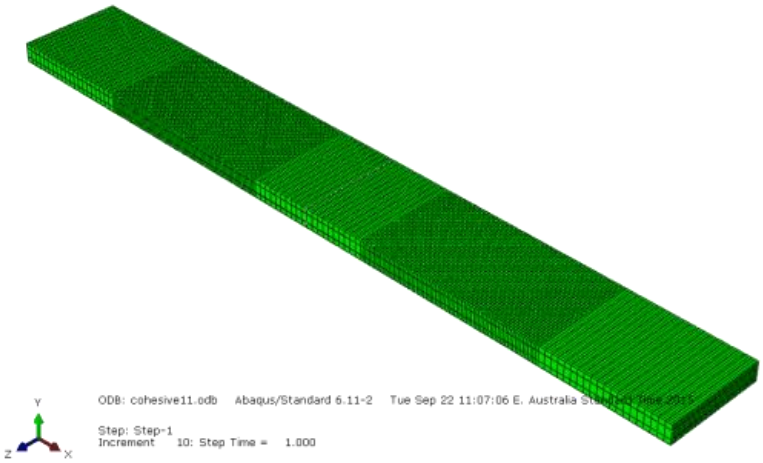

Figure 4-26 Three dimensional finite element model of the delaminated specimen

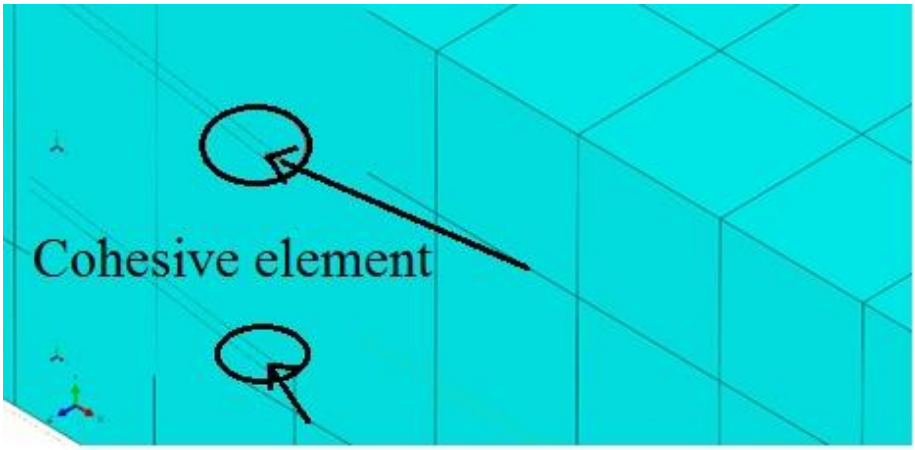

Figure 4-27 Cohesive elements

4.4.4: Mixed Mode I/II delamination damage (Crack Lap Shear, CLS)

4.4.4.1: Material and process

Crack lap shear (CLS) specimens were prepared by rectangular sections of 20-layer (0/90) AR 145 E-glass woven roving (398 g/m^2 weight and 0.5 mm thickness) fibre-reinforced epoxy resin matrix. Kenetix R246TX epoxy resin was used as the matrix material. Additionally, 32 mm long tabs of the same material were bonded at one side of the specimen (Figure ***4-28***). Optical fibres with grating length 5 mm and Bragg wavelength λB = 1548 ± 0.3nm were embedded between the layers above the purposely created delamination. The FBG was located approximately 10 ± 1 mm from the delamination crack tip. The sensor location was carefully selected

to maintain the maximum sensitivity of the sensor to receive changes at the damage front.

4.4.4.2: Inter-laminar fracture toughness tests

This test was conducted using specimens with a geometry that includes a discontinuity located at different location of the thickness as shown in Figure ***4-28***. A 100 kN MTS testing machine was used at room temperature for loading the specimen. Optical sensing interrogator Micron Optics sm 125 was used to acquire FBG readings. The thickness side of specimens, marks were drawn at one millimetre intervals for first five millimetres and five millimetres intervals for twenty millimetres as shown in Figure ***4-29***. The crack propagation was captured using a high-speed camera. To correlate the crack length with the change in compliance, the specimens were instrumented with strain gauge. The complete setup is shown in Figure ***4-30***. Specimen was fastened onto the machine with approximately 50 mm in length held by the hydraulic grips. Load and displacement were acquired from the load cell and displacement sensors of the MTS machine. The foil type strain gauges were attached to the sample surface and were used to measure the strains during the applied loading and are used as a reference single for TSA. The mean load is ramped monotonically, and at selected stress levels a cyclic load was applied at frequency of 5 Hz. The load and displacement signals were fed to MITE© software through a NI USB-6008 card to synchronize the IR images and the thermal cycles as shown in Figure ***4-31***. The crack propagation was measured using the high-speed camera as shown in Figure ***4-32***.

4.4.4.3: Cohesive zone model

A finite element model of the aforementioned specimen was created in ABAQUS 6.13 and used to predict mixed-Mode multi-delamination growth. Cohesive elements or double nodes were used to represent the bonded interface. The specimen ($300\times30\times10mm^3$) with 16 mm initial delamination cracks, depicted in Figure ***4-31*** was loaded at one end in the longitudinal direction and fixed at the other end. The specimen geometry and loading regime are depicted in Figure ***4-33***. Inter-laminar cohesive layers are meshed with three-dimensional COH3D8 using sweep mesh control. The interface region was discretised with a single layer of small thickness (0.001mm) cohesive elements having shared nodes with ply elements as shown in Figure ***4-34***. Composite laminate specimen was meshed with

three-dimensional solid elements, while incompatible Mode eight-node brick element C3D8I used sweep mesh control. Each part was separately meshed using different mesh sizing for reducing computational model time. The concern (delamination damage propagation region) area was meshed with 0.5 mm size and the rest of the composite specimen was meshed with 5mm elements. A debonded interface was defined in the middle of the specimen, consistent with the actual delamination in the test specimen.

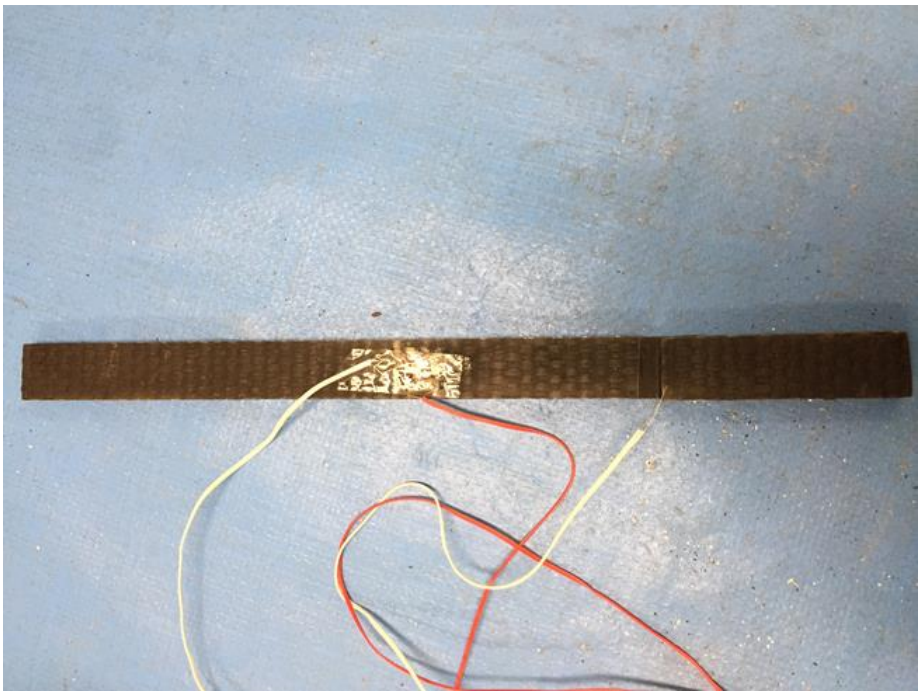

Figure 4-28 CLS specimen

Figure 4-29 CLS specimen read for testing

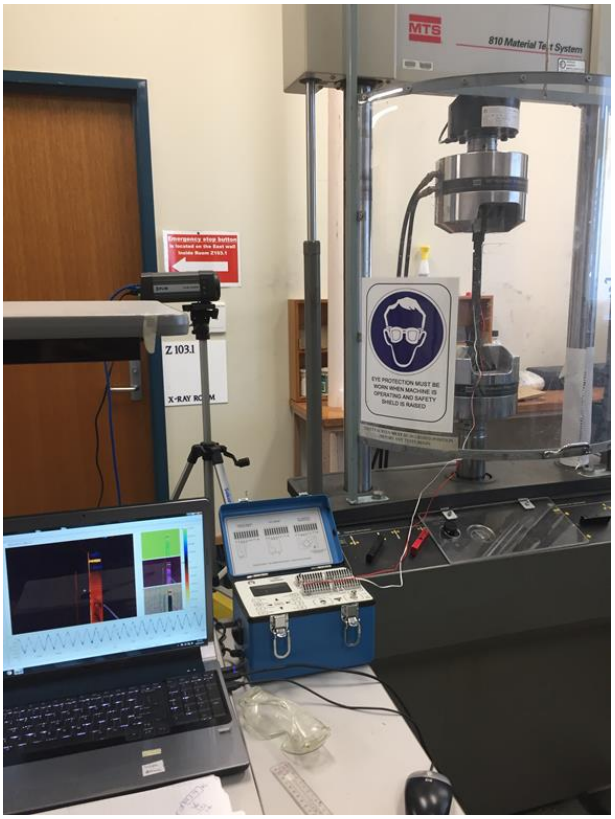

Figure 4-30 The configuration of the testing system

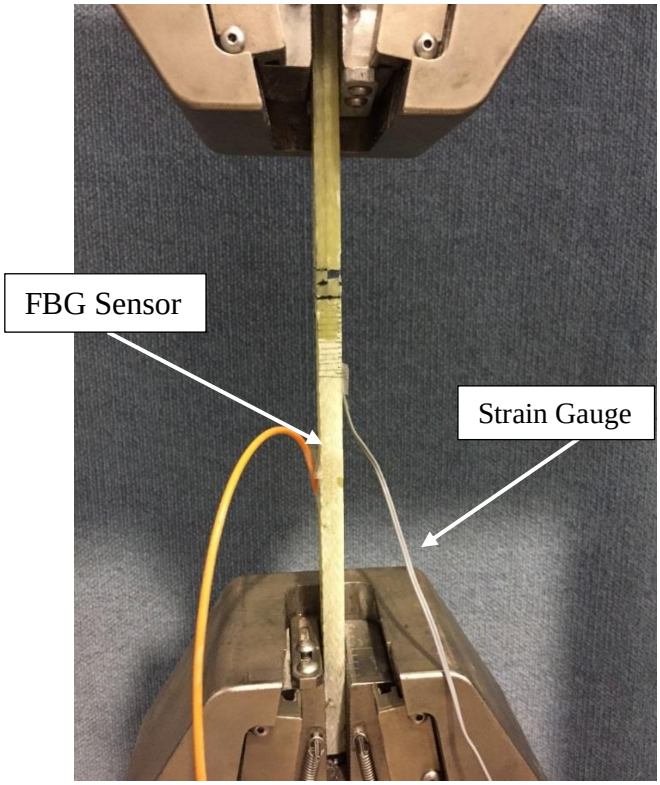

Figure 4-31 CLS specimen under tensile loading

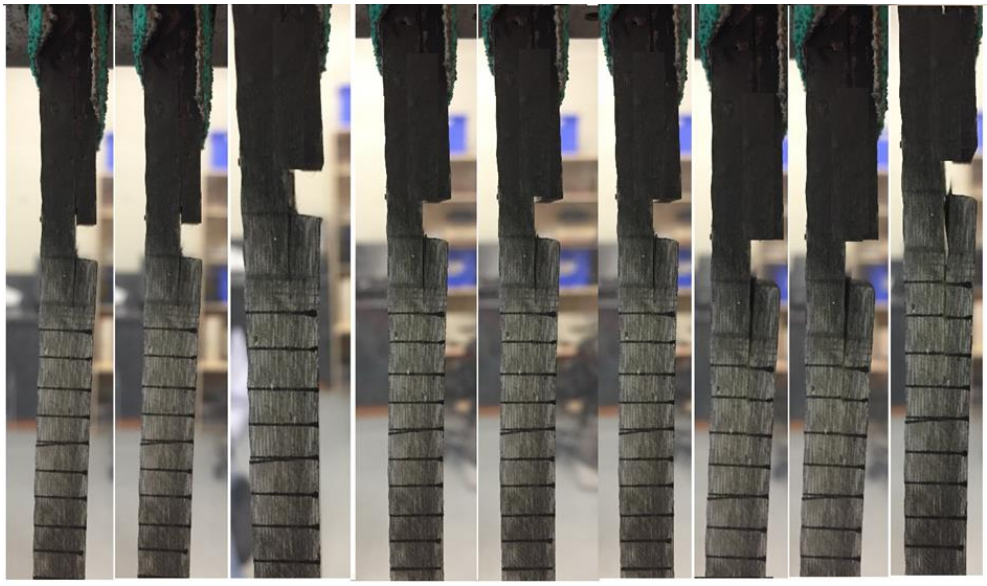

Figure 4-32 Propagating delamination cracks during CLS test in various displacement for WC/epoxy

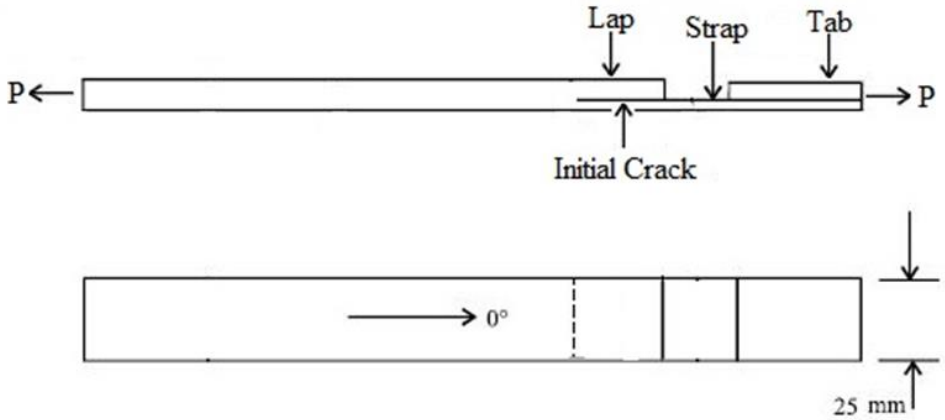

Figure 4-33 Schematic of CLS specimen

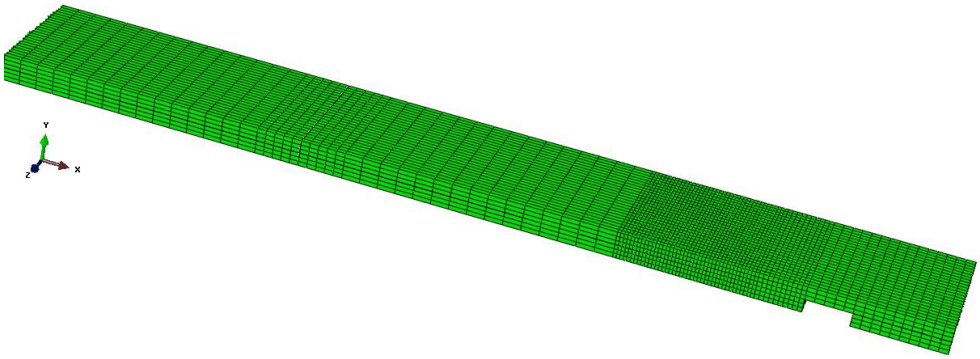

Figure 4-34 Three dimensional finite element model of the CLS specimen

4.5: Summary

In this chapter the experimental and simulation works of delamination from crack onset to propagation were described. The specimens of Mode I, Mode II and Mode I/II were prepared according to ASTM D-5528 and D-7905-14 standards. Simulation of a delamination crack was performed using ABAQUS 6.13 commercial FEA software. Auto Desk © Simulation analysis 2015 Plug-ins for ABAQUS 6.13 was used to create the UMAT subroutine to input status of the material to material module of ABAQUS FEA software. The damage status provided by state variable SDV2 and SDV6 will be compared with the experimental results (FBG sensor and TSA technique results) which will be detailed in next chapter.

Both FBG sensor and TSA technologies were described. FBG sensors were embedded successfully in GFRP during the manufacture. The shrinkage effect during the curing period of the sample at the room temperature was recorded as a

function of FBG sensor reading. There was some distortion of reflected FBG sensor was noted during the cure. The proposed Elasto-plastic model has provided accurate results using FBG sensor strain readings. TSA experimental was setup to evaluate and monitor delamination damage development. MITE© software was used to synchronize the IR images and strain field mapping.

Chapter 5: RESULTS AND DISCUSSIONS

Associated publication:

Kakei, A & Epaarachchi, JA 2018, 'Use of Fibre Bragg Grating Sensors for Monitoring Delamination Damage Propagation in Glass-Fibre Reinforced *Composite Structures', Frontiers of Optoelectronics*, vol. 11, no. 1, pp. 60-8.

Kakei, A, Epaarachchi, JA, Islam, M & Leng, J 2018, 'Evaluation of Delamination Crack Tip in Woven Fibre Glass Reinforced Polymer Composite Using FBG Sensor Spectra and Thermo-Elastic Response', *Measurement*, vol. 122, pp. 178-85.

Kakei, A, Epaarachchi, JA, Islam, M, Leng, J & Rajic, N 2016, 'Detection and Characterisation Of Delamination Damage Propagation in Woven Glass Fibre Reinforced Polymer Composite using Thermoelastic Response Mapping', *Composite Structures*, vol. 153, pp. 442-50.

Kakei, AA, Islam, M, Leng, J & Epaarachchi, JA 2018, 'Use of An Elasto-Plastic Model and Strain Measurements of Embedded Fibre Bragg Grating Sensors to Detect Mode I Delamination Crack Propagation in Woven Cloth (0/90) Composite Materials', *Structural Health Monitoring*, vol. 17, no. 2, pp. 363-78.

Kakei, A, Islam, M, Leng, J & Epaarachchi, JA 'Evaluation of Onset and Propagation of Mode II Delamination Crack In Glass Fibre Reinforced Composite Materials Using Elasto-Plastic Model'. It is ready to submit to *Structural Health Monitoring*.

Kakei, A, Islam, M, Leng, J & Epaarachchi, JA "Monitoring Delamination Crack Tip in Fibre Reinforced Polymer (FRP) Composite Components Using Fibre Bragg Grating (FBG) and Thermal Stress Mapping Techniques". It is ready to submit to *IEEE Sensors*.

Kakei, A, Islam, M, Leng, J & Epaarachchi, JA 'An Investigation of Mixed Mode Delamination Propagation Use Elasto-Plastic Model in Fibre Reinforced Polymer'. It is ready to submit to *Composite A.*

5.1: Mode I delamination damage case study

5.1.1: Load-displacement response

The measured load-displacement curves for specimens are shown in Figure ***5-1***. Each point on the curves corresponds to crack increment Δa = 1mm for the first five millimetre and Δa=5mm for the next 20mm length. These curves were used for calculating R-curve (G (a)). Although there is a deviation in the curves but it generally follow a similar pattern. The deviation found in the curves is due to the

different elastic responses of the specimens. As Figure ***5-1*** shows, *P*-Δ curves follow the same pattern for the delamination crack. The load (*P*) rises linearly until onset of delamination crack. Subsequently load (*P*) is increased incrementally until delamination crack starts propagating. At the final stage of the crack propagation, significant fluctuation is observed in the curve due to non-uniform propagation process of the crack. This behaviour can be attributed to the woven pattern of the composite layer (Suppakul & Bandyopadhyay 2002). The fluctuation in *P-Δ* curve affects the accuracy of calculated R-curves and fracture energy (G) of woven composite.

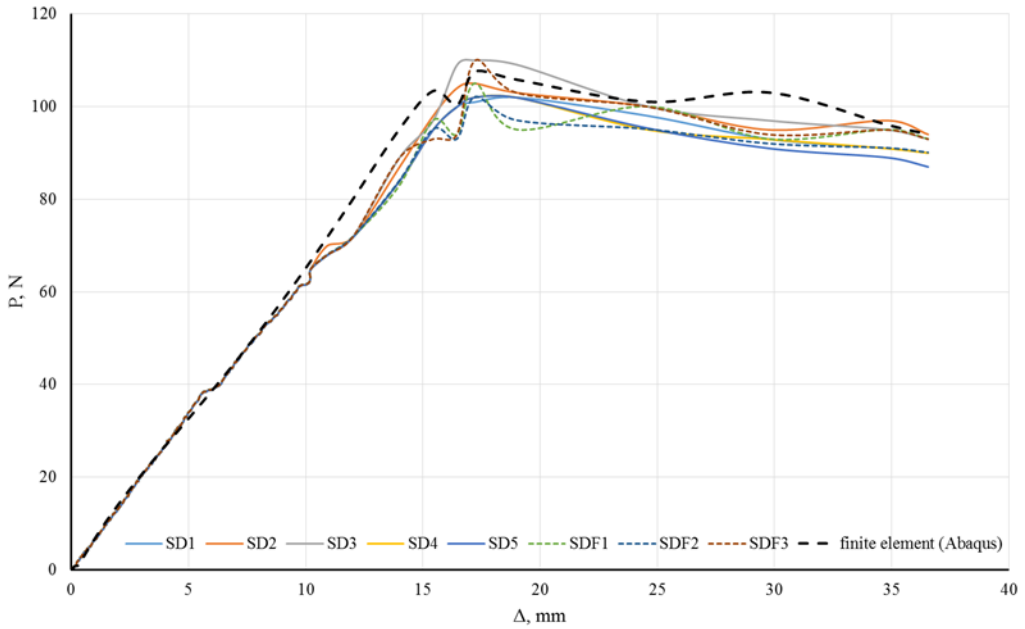

Figure 5-1 Force–displacement measurements for DCB specimens with (solid lines) and without (dash lines) embedded FBG sensors for WC/epoxy specimen

5.1.2: Onset and propagation of delamination crack

Mode I delamination crack was examined under a microscope to investigate the onset and propagation of delamination. Figure ***5-2*** shows the nature of delamination damage growth in the specimen during the test. The microscopic investigation shows two different regions according to the delamination crack spots. Region (I) is the initiation of delamination damage. In region (I) of Figure ***5-2***, the matrix cracking is identified as primary damage region. This region contains brighter regions than the surrounding area due to micro-crack growth within the matrix layer. These microcracks cause stress concentration in the interface region around

the crack tip. With the increase of loading, coalesce of microcracks occurs. Coalesce of these microcracks drives the delamination crack. The region (II) in Figure ***5-2*** shows delamination crack propagation along the interfaces of the matrix and the WC fibre layer. Figure ***5-3*** shows the delamination crack propagation which is specific to WC fibre layers. The microscopic investigation of a delamination crack (Figure ***5-3***) shows two different regions. The first region is a bright region due to a delamination crack. The second region is a resin fill region (dark region). A close microscopic examination shows a discontinuity in delamination crack propagation which causes "jumping" behaviour of the crack propagation in woven composite layers.

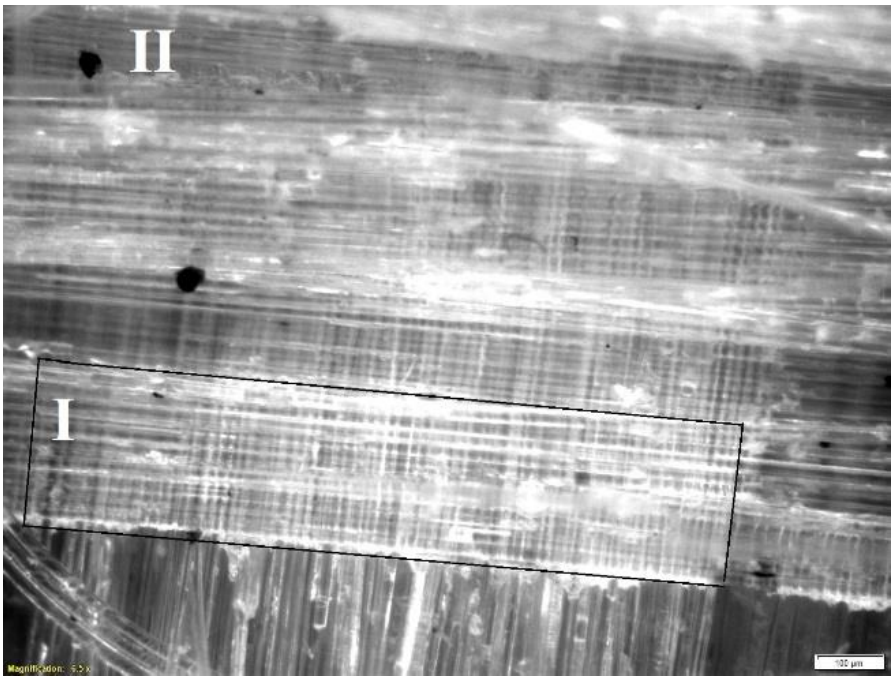

Figure 5-2 Microscopic view of a DCB test specimen; brighter microcrack spots (Region I) and propagation of delamination crack (Region II)

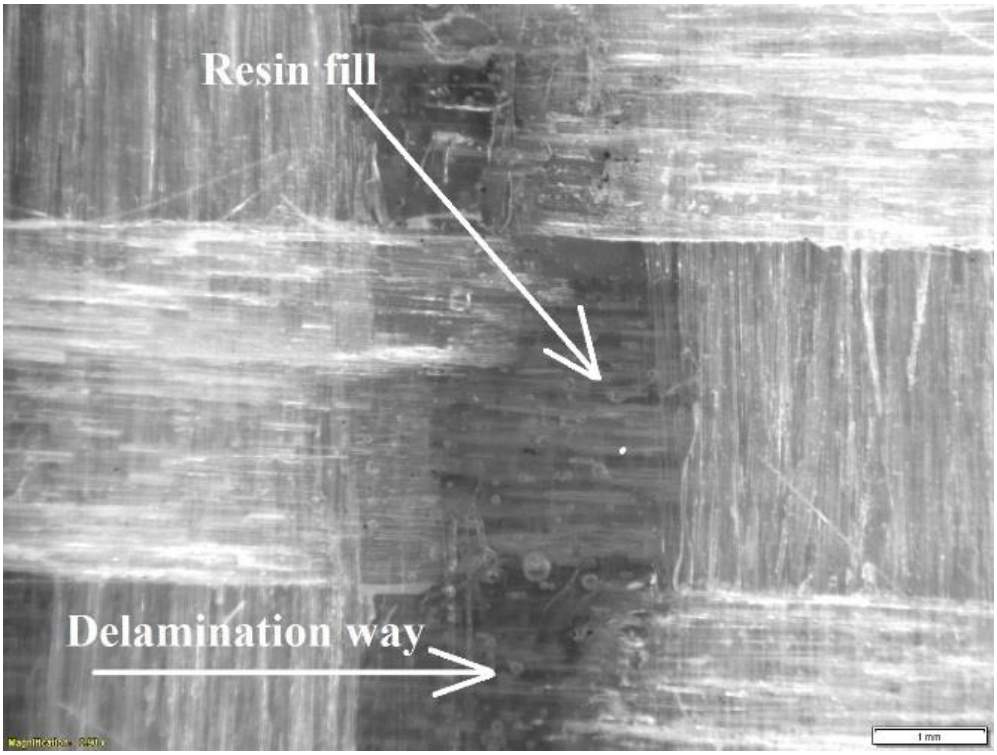

Figure 5-3 Microscopic view of a DCB test specimen shows the behaviour of delamination crack

As shown in Figure ***5-4*** slope of linear elastic part of the P-Δ curve is drawn to determine the starting point of non-linear deformation. The starting point also defines the initiation of delamination crack and the fracture energy G_{IOnset}. Figure ***5-4*** indicates the onset and propagation of delamination crack in the sample SDF2 and the FEA results. At Δ =10.23 mm and the load = 65N, the elastic property of the sample starts to change from linear to non-linear indicating the propagation of delamination crack. On reaching the maximum force around 110N, the load remains constant because the specimen resistance has been affected due to the delamination crack growth. This trend is visible with all the specimens. A summary of the G_{IOnset} , G_{IC} using ASTM equation (equation 4.14), the force onset of delamination crack (P_{Onset}) and displacement onset of delamination crack (Δ_{Onset}) is shown in the Table ***5-1***.

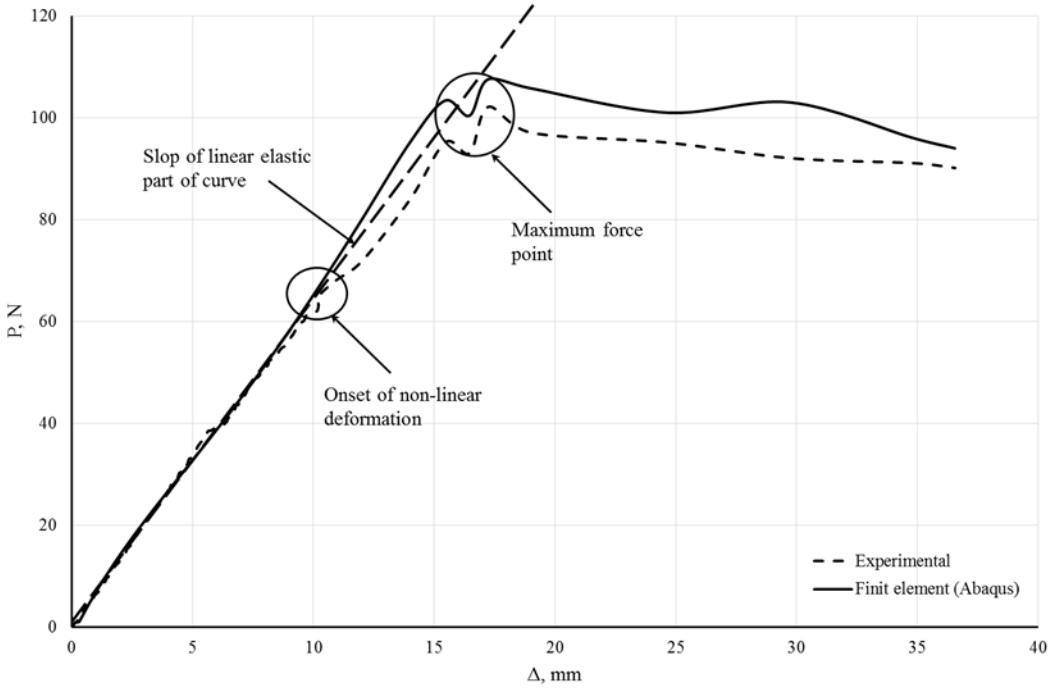

Figure 5-4 Load-displacement curve (hiding line is experimental results, the solid line is finite element result) for WC/epoxy specimen

Table 5-1 Load and *G* result for all WC/epoxy specimens

Sample	**P_{Onset} (N)**	**ΔOnset (mm)**	**G_{IOnset}**	**G_{IC}**
SD1	65.45	10.412	0.227	0.413
SD2	65.23	10.265	0.219	0.400
SD3	65.57	10.430	0.233	0.426
SD4	65.49	10.427	0.234	0.421
SD5	65.21	10.231	0.223	0.410
SDF1	65.454	10.416	0.230	0.414
SDF2	65.52	10.424	0.231	0.428
SDF3	65.32	10.341	0.224	0.435
Finite element	65.58	10.418	0.238	0.447

5.1.3: FBG sensors strain measurements

Responses of embedded FBG sensor were measured and stored in two forms, peak wavelength and the reflected spectrum. As shown in Figure ***5-5***, wavelength shifts increases with the applied displacement. There is a significant increase of spectral

response at 17.23mm imposed displacements. This change is an indication of the initiation of a number of damages in the specimen. The FBG sensor was embedded about 5-6mm from the tip of the initial delamination crack, thus the change of reflected spectra at 17.23 mm imposed displacement can be due to the initiation of delamination crack. The change of FBG wavelength was compared with the corresponding load-displacement curve (Figure ***5-4***). The comparison shows that the changes in the *P*-Δ curve and the wavelength of FBG sensor occurred at 17.23 mm imposed displacements. This observation has confirmed that significant change in the FBG spectral response is a definite indication of the initiation of a delamination crack.

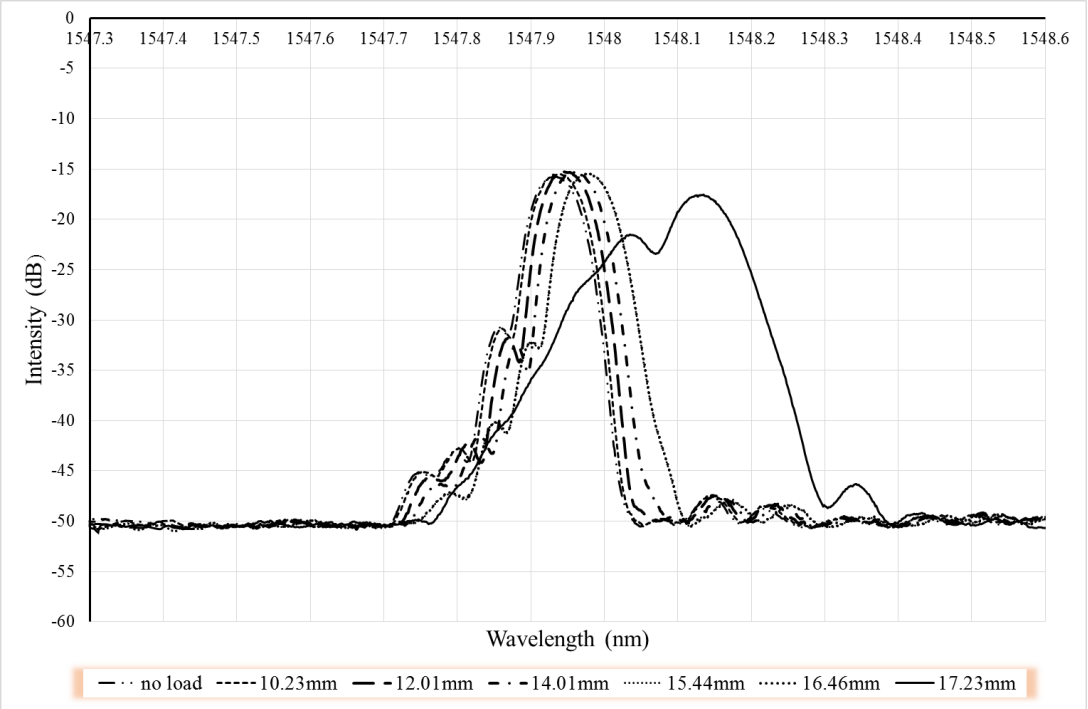

Figure 5-5 Spectra of embedded FBG in WC/epoxy specimen under Mode I delamination test with increasing displacement

While the delamination crack was growing, the centre wavelength of the FBG was shifting and the spectra were chirping (Figure ***5-5***). After 17.23 mm imposed displacements, the FBG signal shifts to left because the crack tip is reasonably away from the FBG sensor.

The second step in the elastoplastic method is to evaluate changes in local strain during crack initiation and propagation of the delamination crack. The equation 4.2 was used to calculate the strain in the plane of delamination crack. The local strain

results obtained from FBG sensor during the test are shown in Figure ***5-6***. These results show that the local strain in the plane of delamination crack has three regions. The first strain region state is the elastic strain. Before the crack onset, the strain increases with the increase of applied displacement. With the increase of displacement, the strain-displacement curve nature changes from linear to non-linear. The main reason for this change can be attributed to the elastoplastic behaviour of the epoxy resin. A close inspection of Figure ***5-7*** reveals elastic-plastic strain and plastic stress in the epoxy material. As a consequence, this region can be declared as elastic-plastic. Interestingly, the strain increases linearly until it reaches 10.23mm imposed displacements. The strain at the onset of delamination crack is 1350με, measured by the FBG sensor. The corresponding stress is 101MPa ($\sigma = E_{ep}\varepsilon$). FBG sensor response indicates that the local matrix strain at the plane of the delamination crack is the most appropriate place for measurement and calculation of stress at the crack tip. The interface failure stress is considerably smaller than the failure stress at the composite specimen which is equal to 245MP as shown in Table ***5-1***. However according to Figure ***5-4*** the delamination crack starts at 101MPa. Figure ***5-6*** can be divided into two regions, stable cracks and unstable cracks according to imposed critical displacement 10.23mm. At critical imposed displacement, the strain at FBG sensor location was measured as 0.00075 mm/mm. Thereafter the delamination crack starts at 0.00125 mm/mm strain value. The crack becomes unstable after 0.00175 mm/mm strain value and delamination crack propagates. The strains field at the embedded FBG sensor were simulated and evaluated using Finite Element Analysis (FEA). As shows in Figure ***5-8*** (a & b), FEA results have shown an excellent correlation with strain readings obtained from the FGB sensor experimentally.

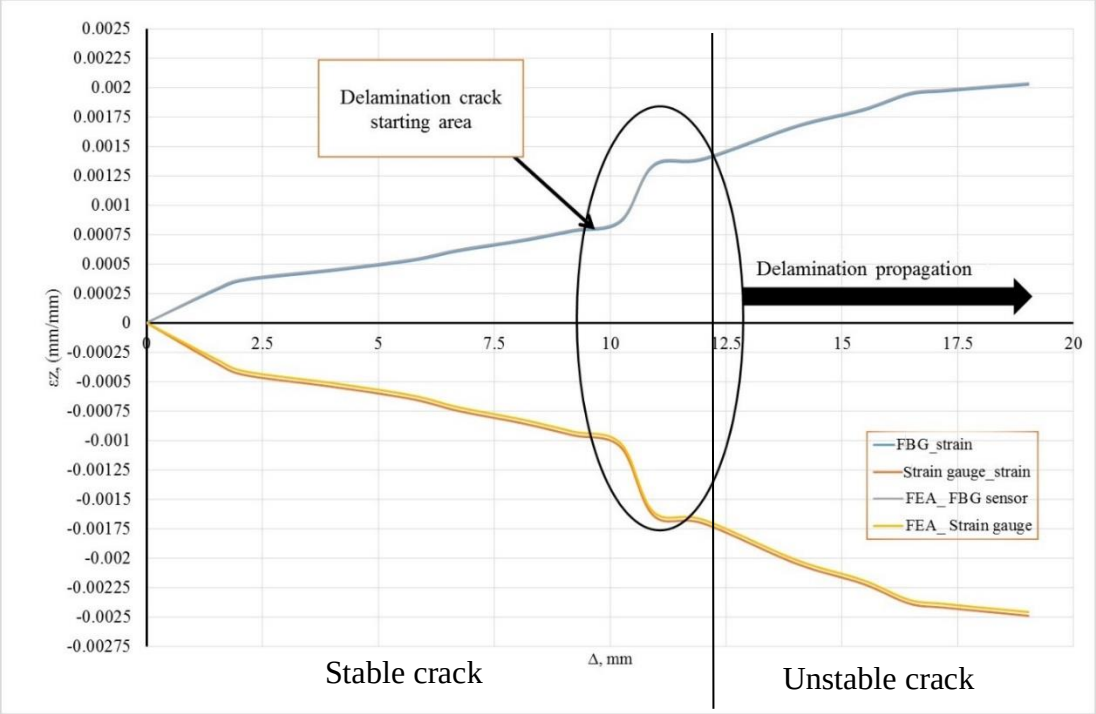

Figure 5-6 Strain-displacement relationship with increasing delamination cracks for WC/epoxy specimen

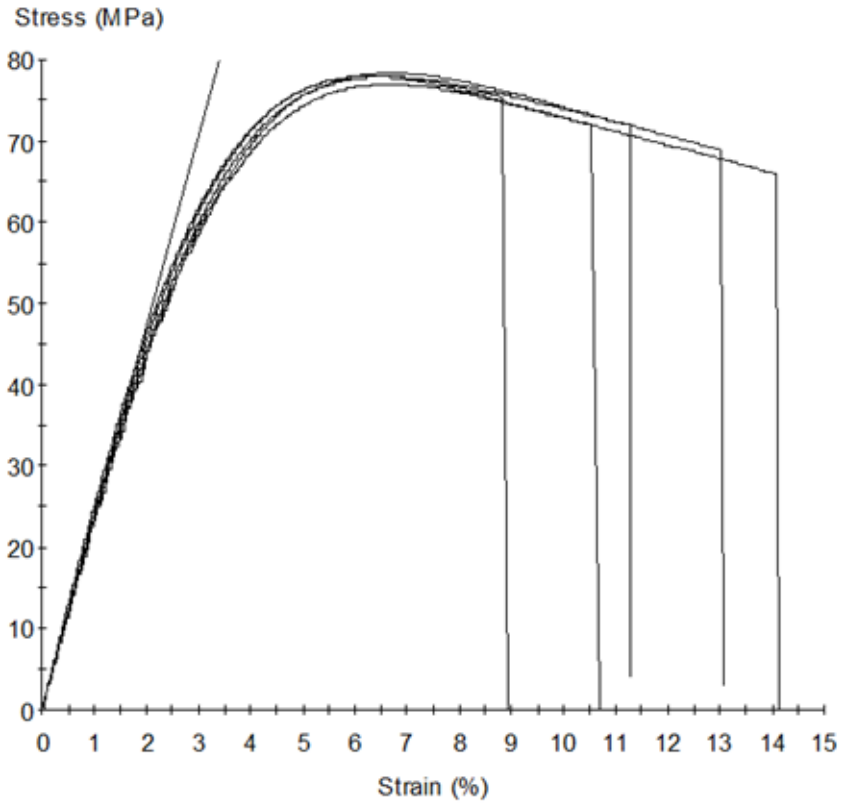

Figure 5-7 Stress- Strain diagram (tensile test) for neat epoxy

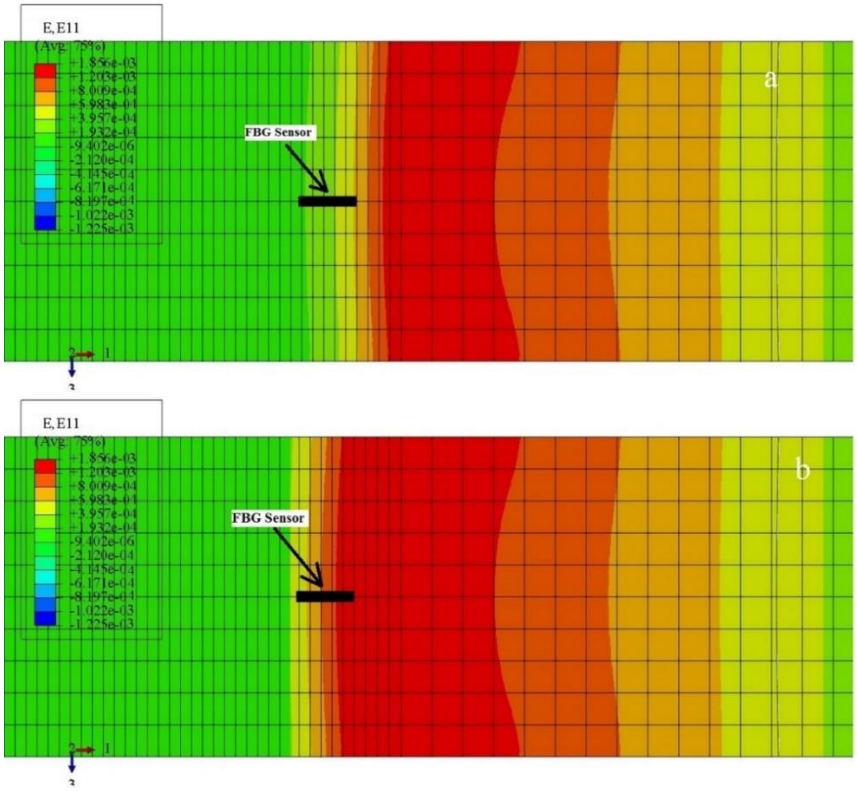

Figure 5-8 Strain field at FBG sensor in finite element model for WC/epoxy at imposed displacement, (a) at 10.23 mm and (b) at 17.23 mm

5.1.4: Calculation of R-curve

The fracture energy G_I as a function of delamination crack propagation can be evaluated using both equations 4.14 and 3.31 and FBG strain readings. As shown in Figure ***5-9***, R curve is calculated after delamination crack extends to 10 mm because the FBG sensor is embedded about 5-6 mm away from the artificially created delamination crack. The calculations of G_{IC} show that both equations provide similar results for this region. However, R-curves calculated from equations 4.15 and 3.31 have shown some differences when the crack is propagating. This difference is due to the equation 4.15 which is valid for isotropic materials and linear crack propagation cases. Hence the equation 4.15 may not be suitable for R curve calculations of WC/epoxy composite materials.

An estimate of delamination crack stability can be performed using G_I/G_{IC} ratio and FBG sensor strain. This estimate is presented in Figure ***5-10***. The delamination crack is stable when the ratio G_I/G_{IC} is less than 1. The delamination monotonically increases with the increase of imposed displacement (Δ), as

anticipated. The crack becomes unstable when the G_I/G_{IC} ratio is equal or greater than 1.

Elasto-plastic model (equation 3.31) and the equation 4.14 were used to calculate R-curves for different laminated composite materials for comparison. The mechanical properties of composite materials were used for calculation as shown in Table ***5-2*** and the P-Δ curve shown in Figure ***5-11***. Figure ***5-11*** shows that composite materials exhibit an onset of delamination point (initiation of non-linear deformation range). This point has different values and depends on mechanical properties (elasticity, cohesive and wave geometry) of composite materials. The initiation of delamination in Figure ***5-12*** is the second region after linear (elastic) strain region. Finite element analysis using ABAQUS has been used to simulate the local strain at the location of FBG sensor and strain at the surface of the specimen. Figure ***5-13*** shows R-curves for tested composite materials. The result shows that equation 4.14 and elastoplastic model (equation 3.31) have same R-curve value and behaviour for unidirectional composite materials. As anticipated for woven cloth composite materials, the R-curves from equation 4.14 and 3.31 are significantly different. However, R-curves calculated from equation 4.14 and equations 3.31 for unidirectional composites have shown similarities.

Table 5-2 Mechanical properties for different composite materials

Materials	**E11 (GPa)**	**E22 (GPa)**	**E33 (GPa)**	**v12**	**v13**	**v23**	**G12 (GPa)**	**G13 (GPa)**	**G23 (GPa)**	**GI(mJ)**	**type of materials**	**Ref.**
GF/PCBT	14.73	14.73	10.9	0.25	0.5	0.5	1.789	1.43	1.43	1.5	woven 0/90	(Yang et al. 2015)
CF/PCBT	25.7	25.7	15.9	0.2	0.35	0.35	3.5	1.43	1.43	1.5		
WC/epoxy	15	15	9.5	0.126	0.126	0.26	6.527	6.527	7	0.414		(Kakei et al 2016)
HS160RM	109	8.819	8.819	0.342	0.342	0.38	4.315	4.315	3.2	0.4	unidirectional 0	(Sambors ki 2016)
T300/977-2	150	11	11	0.25	0.25	0.45	6	6	3.7	0.352		(Soto et al. 2016)

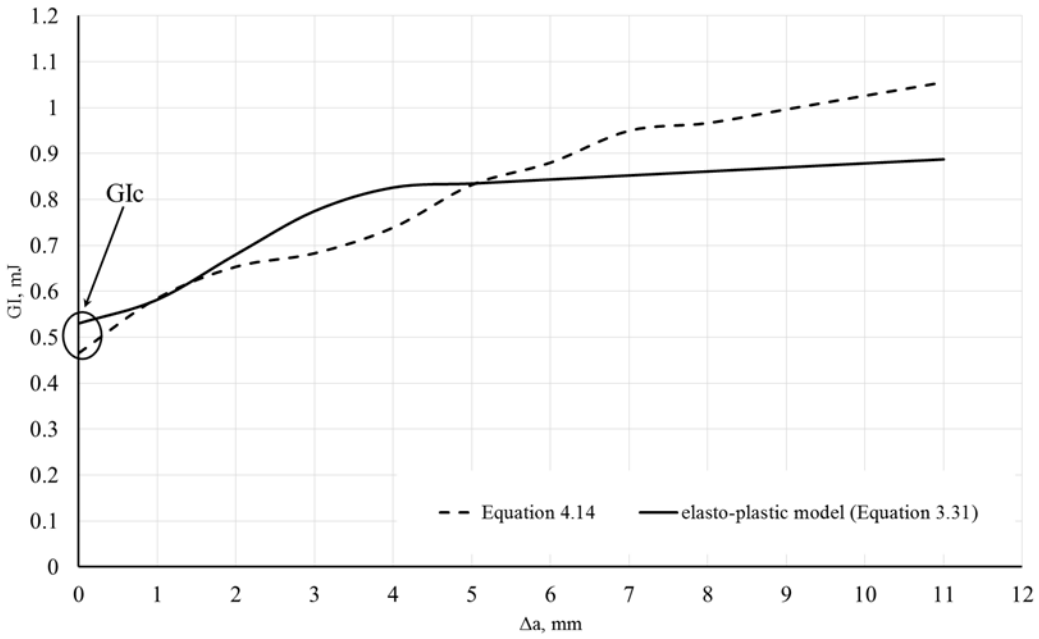

Figure 5-9 Experimental R-curve as a function of delamination cracks length and strain for WC/ epoxy specimen

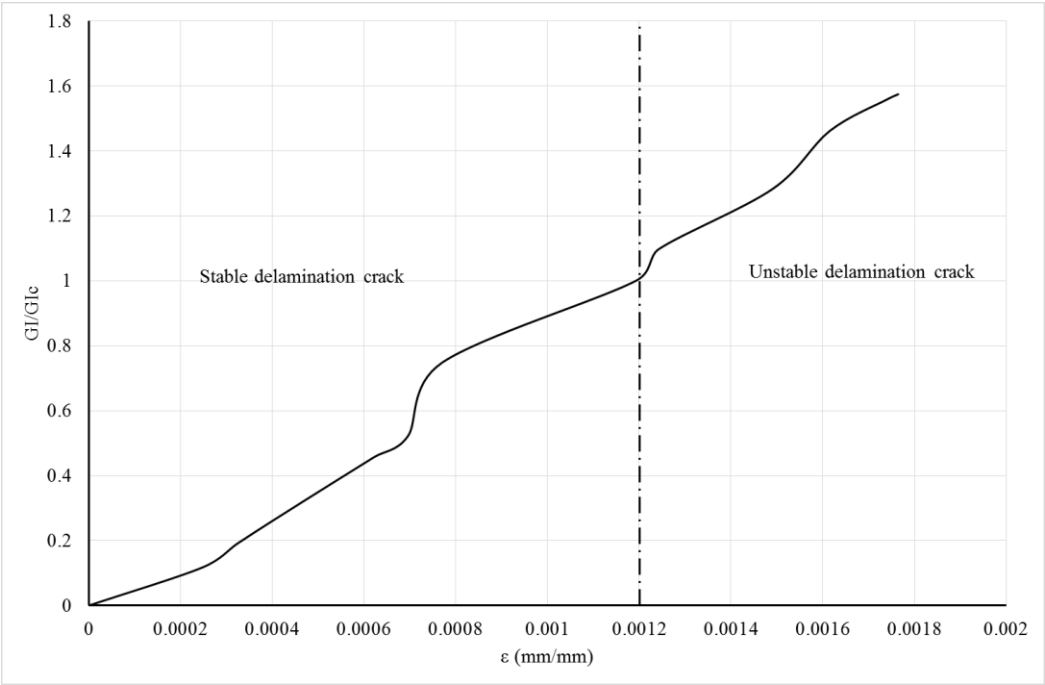

Figure 5-10 Examining stability of delamination crack Mode I depending on GI/G_{Ic} ratio and strain measuring from FBG sensor for WC/epoxy specimen

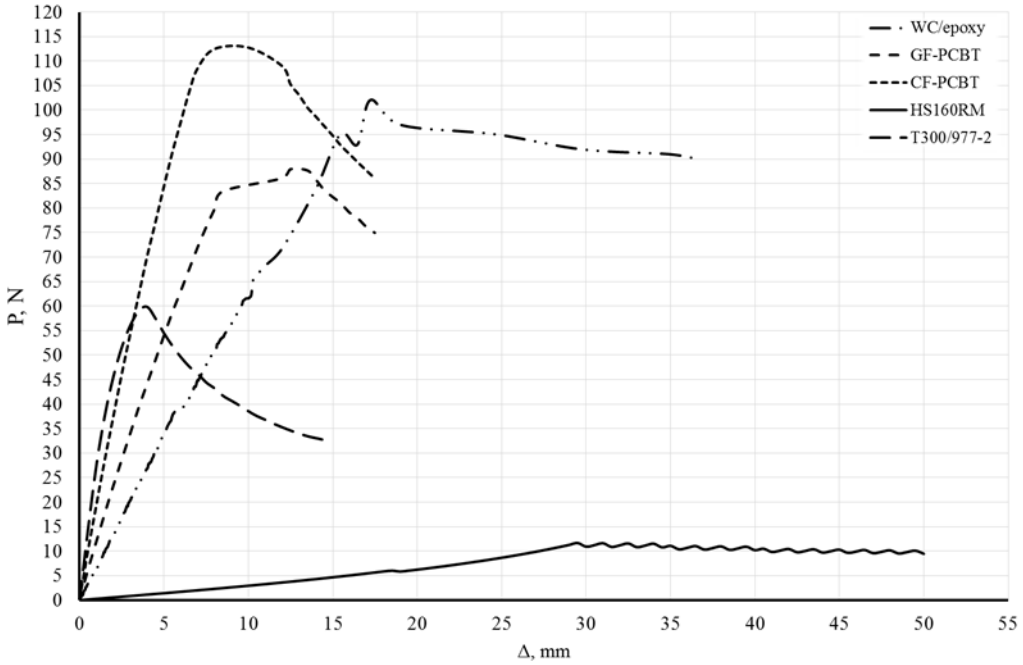

Figure 5-11 Force–displacement measurements for DCB specimens for different composite materials

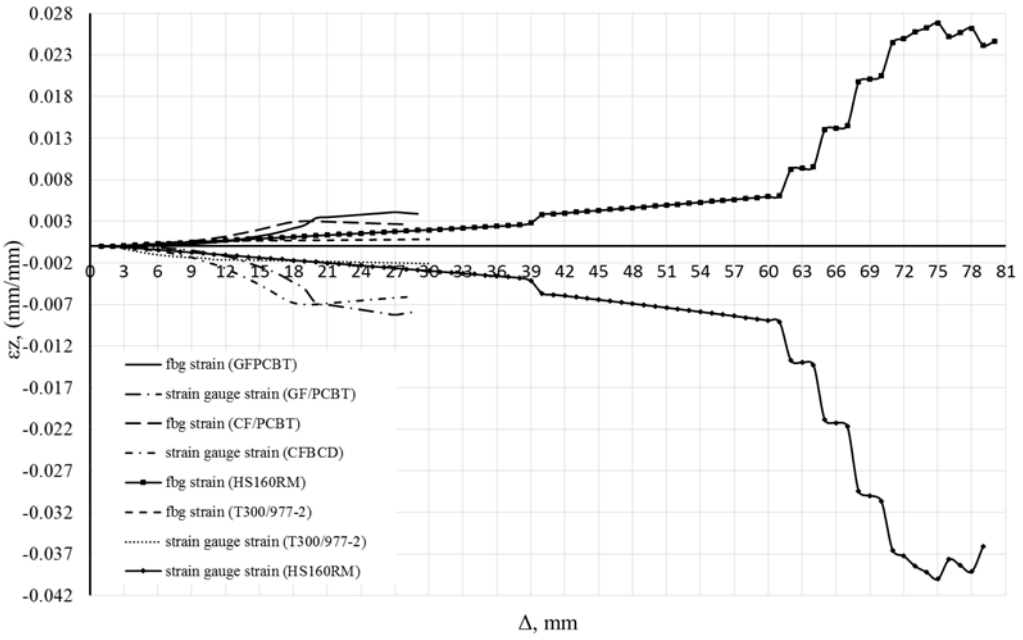

Figure 5-12 Strain-displacement relationship with increasing delamination cracks

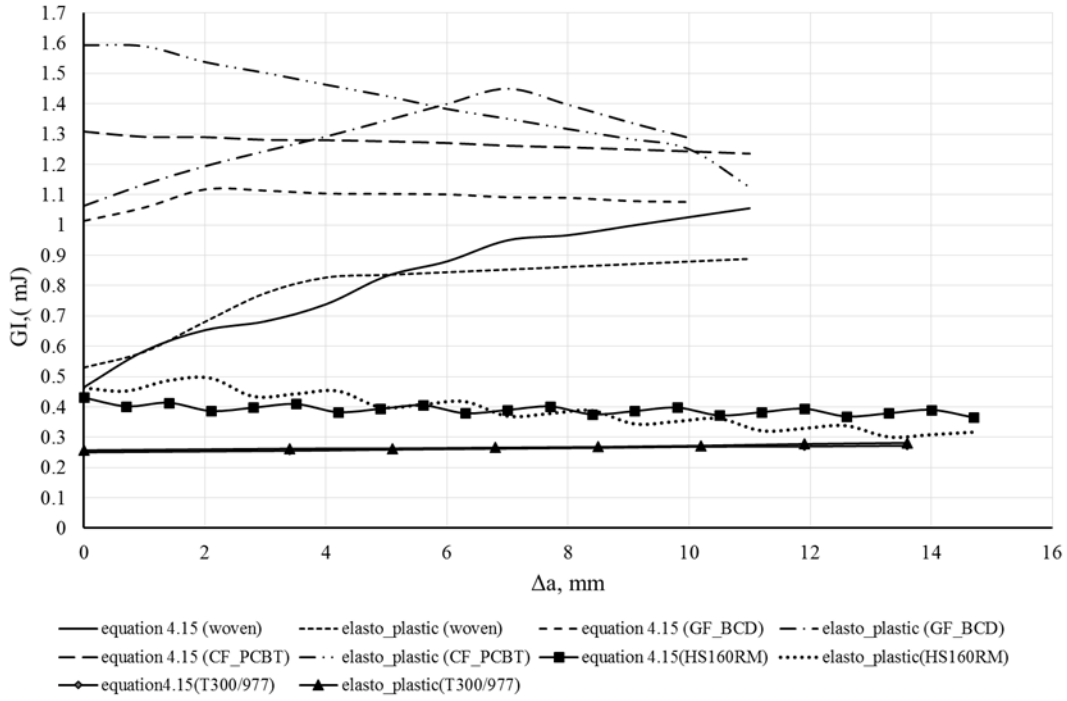

Figure 5-13 Experimental R-curve as a function of delamination cracks length and strain

The R-curve (G(a)) is calculated from state damage variables SDV2 and SDV6 and the strain at FBG sensor location at FEA strain plots which are shown in Figure ***5-14***, Figure ***5-15*** and Figure ***5-16*** respectively. SDV2 value is obtained for FBG sensor and surface mounted strain gauge positions. The interface cohesive elements were used to calculate the load-displacement curve $P(\Delta)$, and R-curve ($G(a)$) for the specimens. Mode I delamination was evaluated using FEA Simulation. The nine state damage variables (SDV1, SDV2…, SDV9) were used as a criteria to evaluate crack onset and the cohesive elements for crack surface (see Figure ***5-14***). Since, the state damage variables SDV2 and SDV6 before imposed displacements of 10.23 mm in Mode I is almost zero, as shown in Figure ***5-15*** and Figure ***5-16***. When the crack propagates beyond 10.23 mm imposed displacement, the set values of SDV2 and SDV6 are equal to 1. This means that the crack in the specimen is dynamic and the delamination is propagating. The finite element result was compared with the experimental observations, captured with the high speed camera. The comparison shows that the cohesive element model gives accurate results, close to the experimental observations especially at the crack onset point.

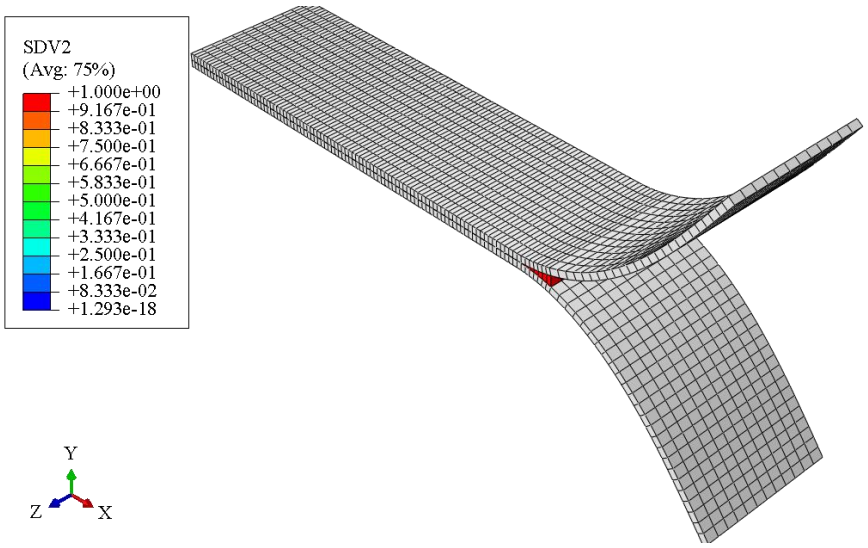

Figure 5-14 SDV2 values with developing crack delamination in cohesive element model

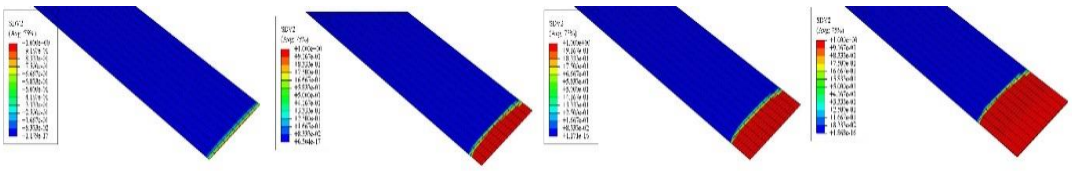

Figure 5-15 SDV2 developing in cohesive elements with increasing displacement

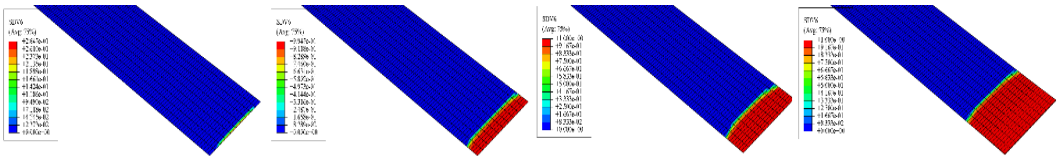

Figure 5-16 SDV6 developing in cohesive elements with increasing displacement

5.2: Mode II delamination damage case study

5.2.1: Load-displacement response

The measured load-displacement curves for all tested specimens are shown in Figure ***5-17***. Each point on the curves corresponds to crack increment Δa= 1mm for the first five millimetre and Δa=5mm for the 20mm length. These curves have been used for calculating R-curve. Although there are some differences in the curves but in general two groups of specimens shows similar behaviour. The difference in the curves can be attributed to the differences in elastic response of the specimens as anticipated.

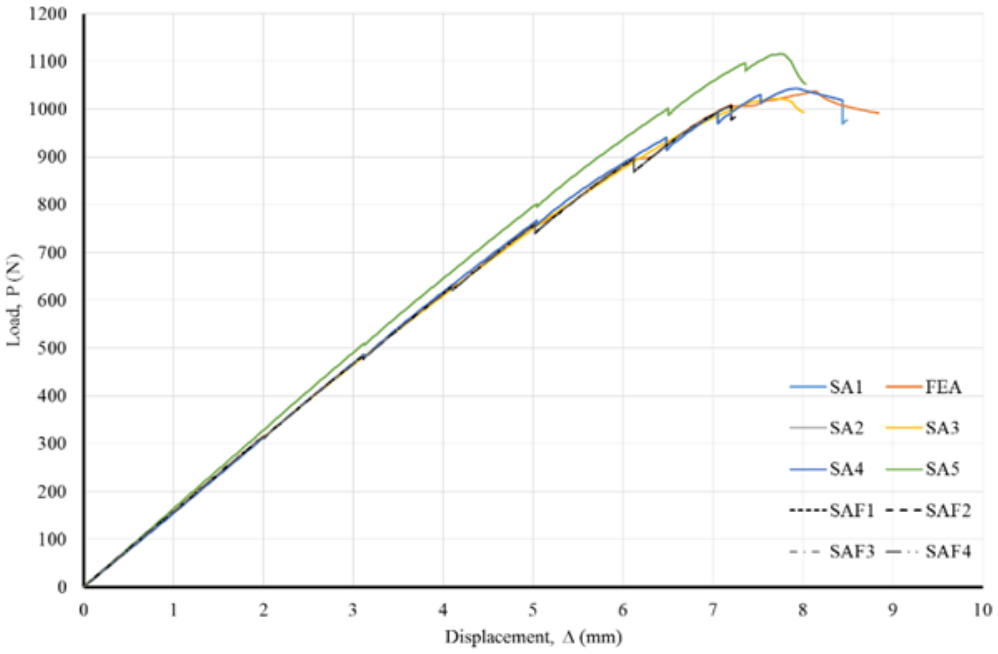

Figure 5-17 Force–displacement measurements for ENF specimens with (solid lines) and without (dash lines) embedded FBG sensors for WC/epoxy specimen

5.2.2: Identification of initiation and propagation of delamination crack

A microscopic evaluation was also used to investigate the initiation and propagation of delamination crack. Numerous pictures of surface of delaminated specimen were analysed to evaluate the nature of delamination crack. The microscopic investigations reveal the path of delamination crack in the interface layer of the composite specimens. As shown in Figure ***5-18***, uniform bright regions are the spot of Mode II delamination cracks, extended from the initial delamination region (Teflon region). Microscopic pictures provide micro-cracks as shown in Mode I delamination crack (Kakei, A. A. et al. 2018) , unfortunately micro-crack spots cannot be seen clearly. Micro-crack spots may disappear due to friction and abrasion between the layers during the test. However it is correct to assume that coalesce of the micro-cracks is driving the delamination crack. The microscopic investigation will assists in determination of the nature of delamination propagation of WC/epoxy layers. As shown in Figure ***5-19***, the microscopic investigation shows two different regions. The first region is uniform bright region due to Mode II delamination crack. The second region is a resin fill region (dark region). A discontinuity in delamination crack can be seen in the microscope examination which may be due to jumping behaviour of the crack in woven composite layers.

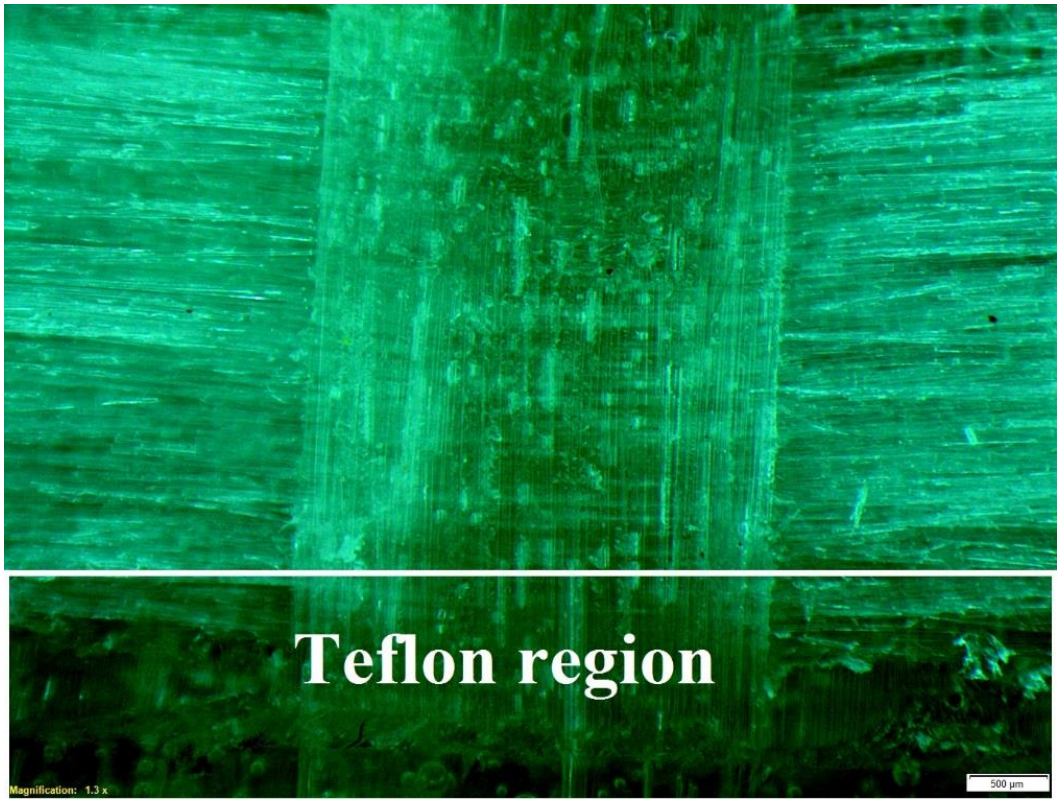

Figure 5-18 Microscopic view of ENF test specimen using Olympus XC10 microscope equipment; delamination cracks (uniform bright region) propagating from initial delamination crack (Teflon region)

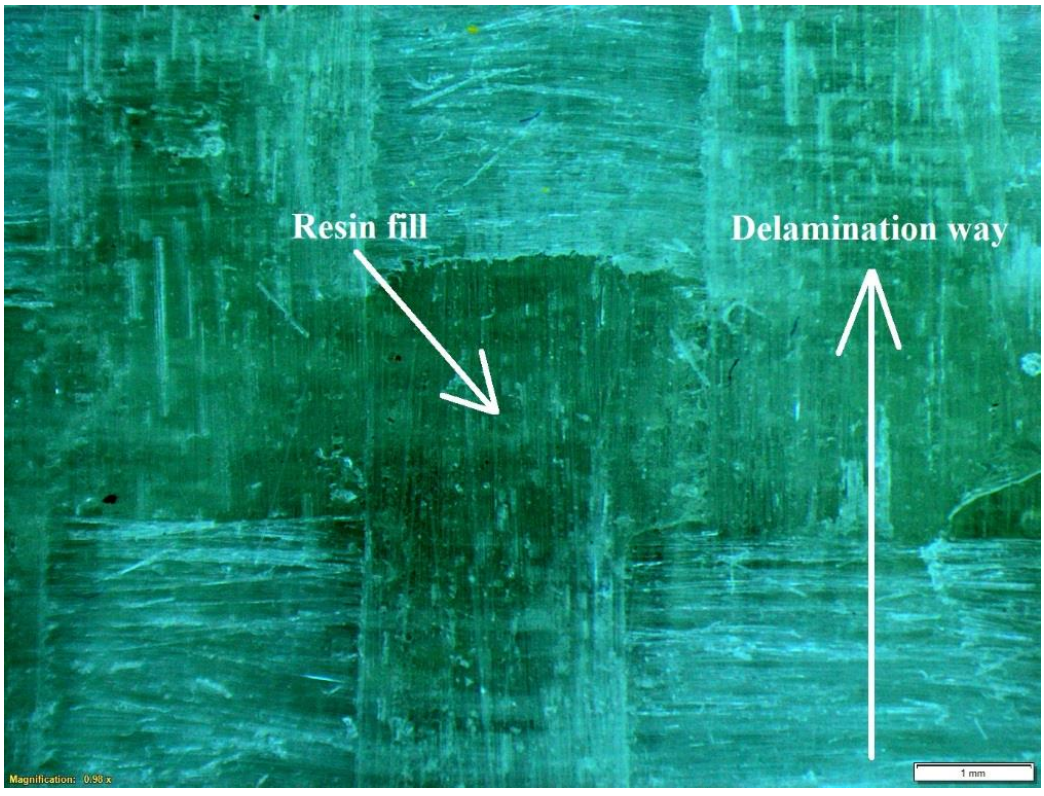

Figure 5-19 Microscopic view of ENF test specimen using Olympus XC10 microscope equipment shows the behaviour of delamination crack

Mode II delamination crack was also examined using load-displacement data obtained during the static test. Figure ***5-20*** indicates the onset of delamination crack and propagation of crack in the sample SA2. As shown in Figure ***5-20*** slope of linear elastic part of the P-Δ curve is drawn to detect the onset of non-linear deformation. The initiation of delamination crack was located, and critical as well as the maximum values of fracture energy ($G_{IIOnset}$, G_{IIC} , G_{II}) were calculated

At the initiation stage of delamination crack, the crack is onset at 3 mm displacement and 490N force on the sample. After onset of the crack the elastic region of the sample changes to non-linear due to progression of delamination crack. With increase in load the delamination crack propagates until it reached the maximum force of 1022 N at 8mm displacement. Beyond the maximum value the force remains constant due to the specimen resistance to the crack propagation which has been the cause of dramatic reduction of the maximum load. At this stage the epoxy (matrix) at the delamination crack tip has reached plastic region. The investigation shows that all samples follow the same non-linear deformation point at the same maximum force. A summary of the $G_{IIOnset}$ and G_{IIC} using equation (4.21), the force onset of delamination crack (P_{Onset}) and displacement onset of delamination crack (Δ_{Onset}) is listed in Table ***5-3***.

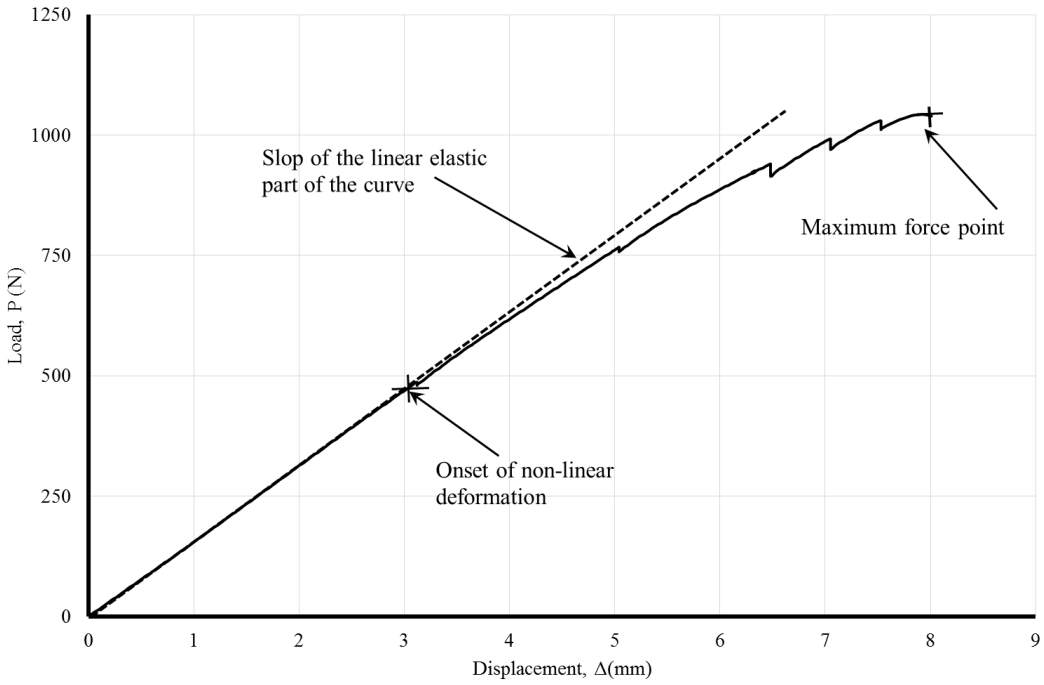

Figure 5-20 Load-displacement curve (solid line is experimental results, hiding line is finite element result)

Table 5-3 Load and *G* result for all specimens

Specimens	P_{Onset} **(N)**	Δ_{Onset} **(mm)**	$G_{IIOnset}$ **(mJ)**	G_{IIC} **(mJ)**
SA1	961.552	3.0727	0.417292	1.0525
SA2	961.524	3.0758	0.417118	1.051
SA3	961.538	3.0834	0.418746	1.0525
SA4	961.539	3.0753	0.417527	1.0522
SA5	961.511	3.0827	0.418611	1.0524
SAF1	961.538	3.0861	0.419391	1.0532
SAF2	961.546	3.0765	0.41765	1.0521
SAF3	961.533	3.0752	0.417632	1.0525
SAF4	961.547	3.0821	0.418967	1.0535
FEA Results	961.525	3.0724	0.41728	1.053

5.2.3: FBG sensors' strain measurements

Peak wavelength and the reflected spectrum of embedded FBG sensor was acquired and stored during the experimentation. As shown in Figure ***5-21***, centre wavelength of the FBG sensor increases with the increase of applied displacement (loading). There is a significant increase of spectral response after 3mm imposed displacements. This change indicates a change of damages state in the specimen. FBG sensor was embedded 5-6mm from the tip of initial delamination crack. Therefore the change of wavelength is an indication of delamination crack initiation. The shifting and distortion of FBG wavelength is compared with the change of elastic property of load-displacement curve (Figure ***5-20***). The comparison shows that the FBG response changes for both specimen types in the linear-elastic region of P-Δ curve. The respective wavelength of FBG sensors shows the distorted peaks after 3 mm imposed displacements, indicating the onset of delamination crack. Once the delamination crack arrives underneath the FBG sensor, the spectrum gets completely distorted. After 8.61 mm of imposed

displacements, the distortion of FBG signal stops and shifts to leftward because the crack tip is relatively away from the FBG sensor.

Distortion Index (DI) and Peak Wavelength Ratio (PWR=*Fi/Fio*) indexes were used to locate the onset and propagation delamination cracks under Mode II delamination test. As shown in Figure ***5-22***, D_{si} is equal to D_{so} for nil delamination crack propagation. The same result visible in the Distortion Index (DI) which is equal to unity. With the delamination crack onset, the spectrum of the FBG sensor expands (FWHM increases), while the intensity of peak wavelength of the spectrum decreases (PWR decreases). The results show a significant distortion to the FBG sensor spectra with onset of delamination damage (see Figure ***5-21***). The distortion Index (DI) increases dramatically after the initiation of crack propagation. The distortion Index (DI) remains constant with increase in delamination cracks until the crack arrives underneath the FBG sensor. The distortion Index (DI) increases again as shown at 8.61 mm imposed displacement. Simultaneously the Peak Wavelength Ratio (PWR) of FBG sensor shows a similar trend i.e. remains at unity before onset of delamination crack and with the propagation of delamination crack, Peak Wavelength Ratio (PWR) drops linearly. Both DI and PWR indexes have provided accurate results to capture the condition of delamination damage in composite specimens under Mode II delamination experiment.

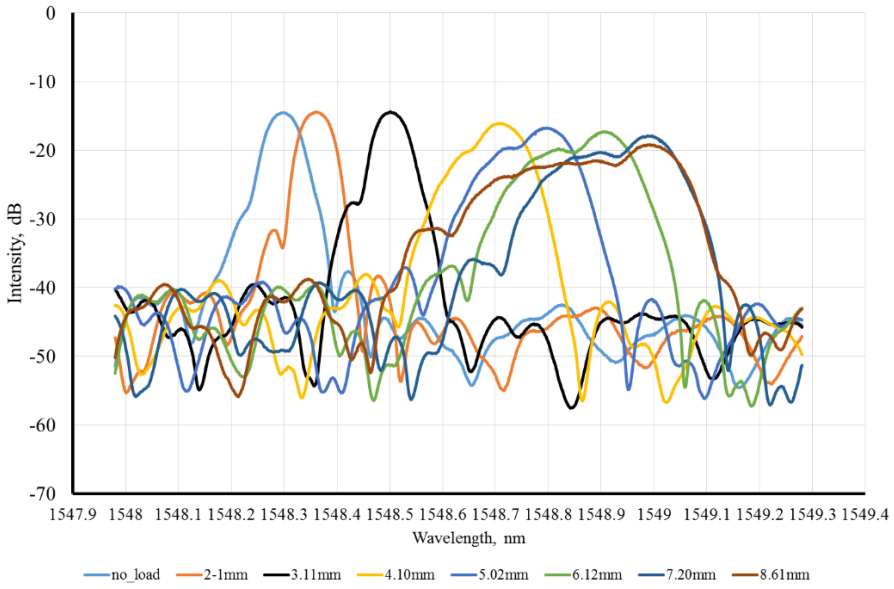

Figure 5-21 Spectra of embedded FBG in Glass fibre reinforced composite sample under Mode II delamination test

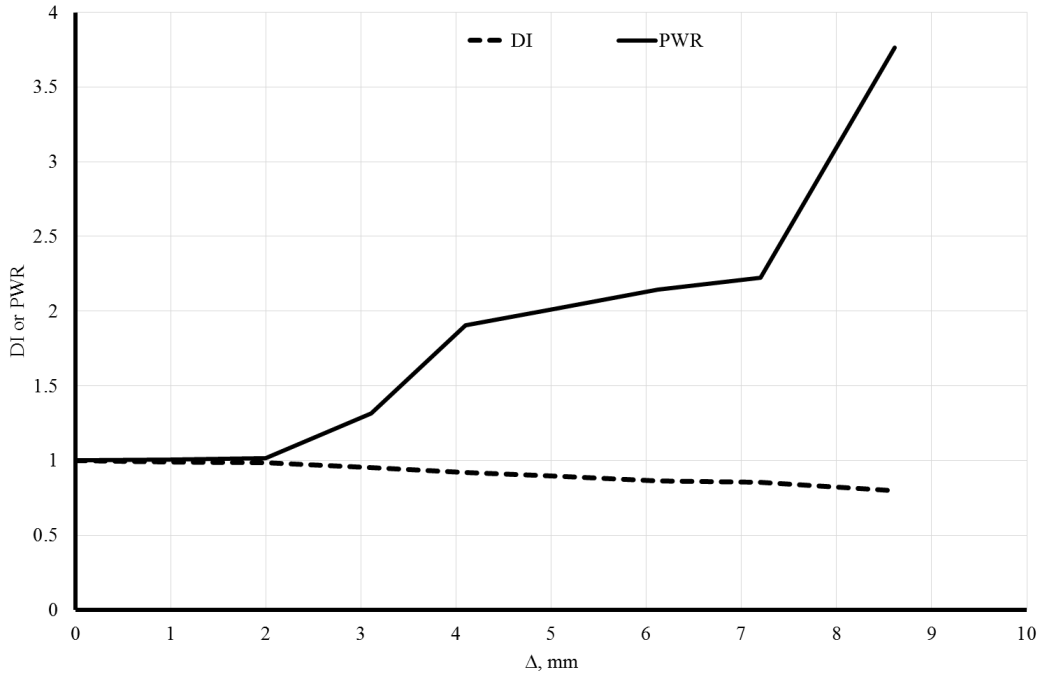

Figure 5-22 Detection of delamination crack onset and propagation for WC/epoxy in ENF Mode II delamination test use both DI and PWR parameters. Vertical axis is DI or PWR values

Equation 4.2 is used to calculate strain in the plane of delamination crack. The local strain was measured using FBG sensor. The measured strain is shown in Figure ***5-23***. The results show three regions of local strain in the plane of delamination crack. The first strain region shows an elastic behaviour. Before the crack initiation, the strain increases linearly with the increase of applied displacement as anticipated. With of increase of imposed displacement, the linear elastic behaviour of the curve changes to non-linear pattern showing an increase of strain. This change can be attributed to change of matrix material (epoxy resin) elastic range to elasto-plastic range. Figure ***5-24*** shows stress strain diagram at the crack tip under imposed displacement. It clearly shows linear elastic, elasto-plastic and elastic ranges of epoxy. In Figure ***5-23***, the region circled with the dotted lines indicates the strain levels similar to elasto-plastic strain of neat epoxy. This observation strongly justifies the assumption of the on-set of crack at the beginning of this stage. Interestingly the strain increases linearly until it arrives to 3 mm imposed displacements (Figure ***5-22***). As such, the onset of delamination crack happens when the local strain reaches 3350με. Figure ***5-23*** shows two regions of crack, stable crack and unstable crack at imposed critical displacement 3.11mm. At

3mm displacement, the strain at FBG sensor location is measured as 3000με and the crack onset at 3350με strain. The crack becomes unstable after 3954με strain. Delamination Figure ***5-25***, shows calculated DI and PWR indexes. Both indexes show a significant change in the region marked by dotted lines. The changes are noticeable when the imposed displacement has passed 2 mm mark. The strain field at the embedded FBG sensor have been simulated and studied using finite element analysis (FEA). As shown in Figure ***5-26*** a & b, FEA results have an excellent correlation with experimental results.

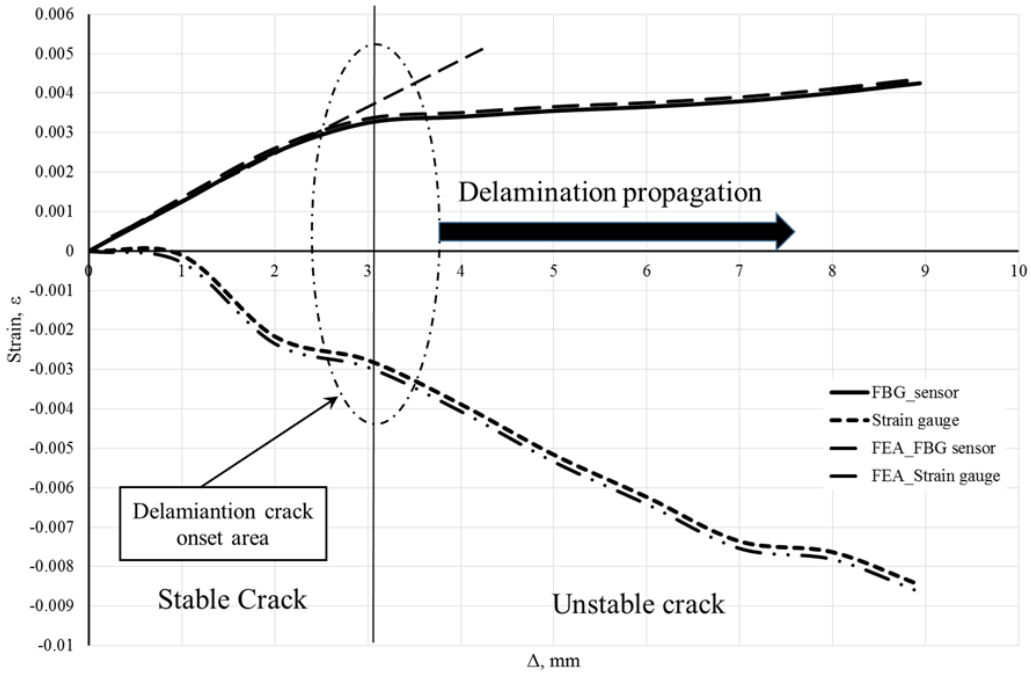

Figure 5-23 Strain-displacement relationship with increasing Mode II delamination cracks

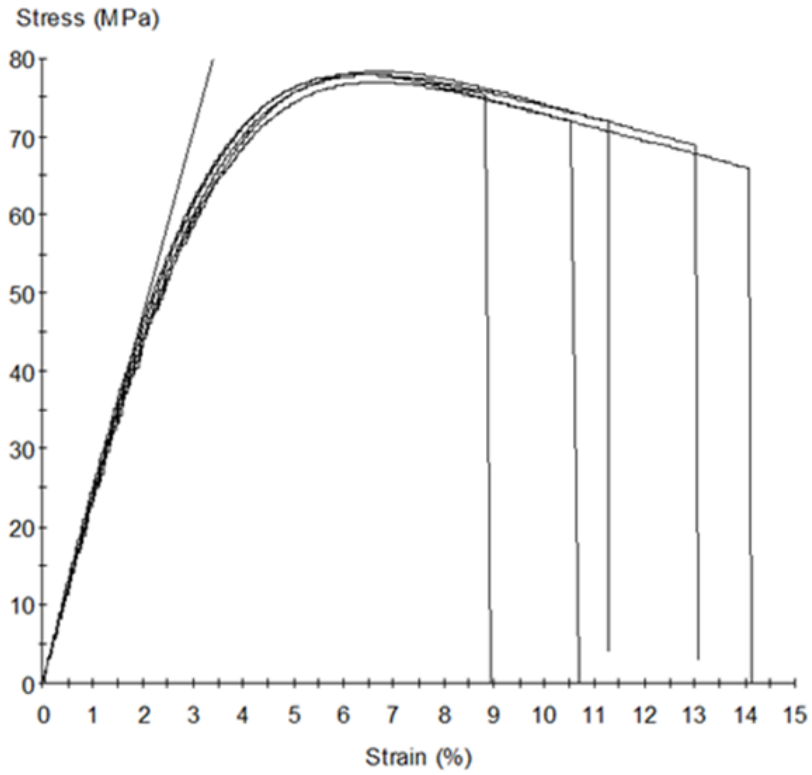

Figure 5-24 Stress- Strain diagram (tensile test) for neat epoxy

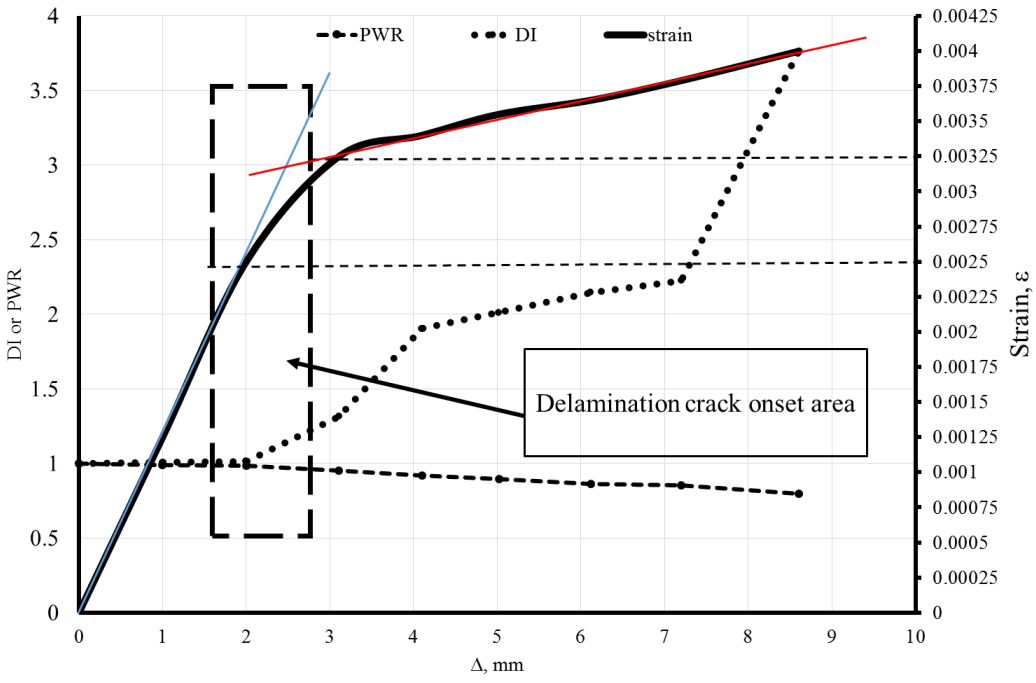

Figure 5-25 An examination for delamination crack onset use strain behaviour, DI and PWR parameters for WC/epoxy in ENF Mode II test. Vertical Right axis is DI or PWR

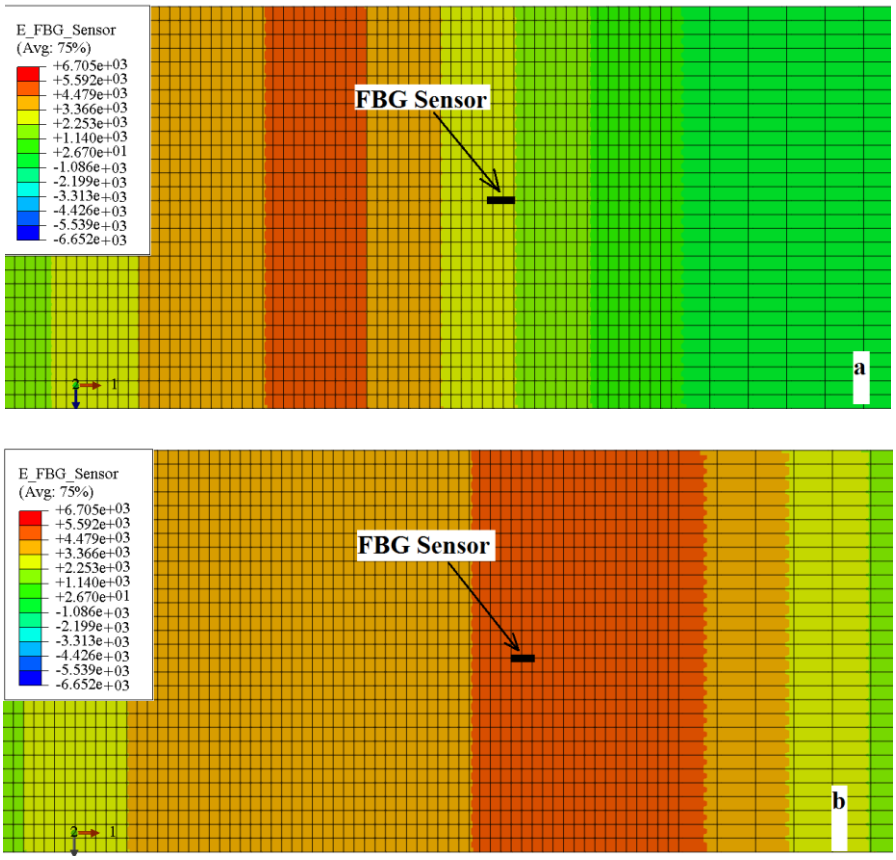

Figure 5-26 Strain measurement at FBG sensor in finite element model

5.2.4: Evaluation of Mode II delamination propagation

Three classical experimental methods namely DBT, CBT and CCM were used for evaluating of delamination propagation. The experimental parameters such as P, Δ, and a were used to calculate the critical fracture energy in pure Mode II delamination damage. The critical fracture energy was obtained as a function of the crack length in DBT, CBT and CCM. The correction crack length Δ_I was calculated for all specimens. An average Δ_I value of 2.14mm was calculated. The curve was determined using from the respective experimental P-Δ curves. The values of calculated critical fracture energy are presented in Table *5-4*. As expected the value of critical fracture energy was evaluated in CCM is greater than CBT. The value of critical fracture energy was evaluated from DBT is greater than other methods due to no crack length correction was used in the calculation.

The comparison between four methods is presented in Figure ***5-27***. Since the FBG sensor was embedded about 5 mm from initial crack and the length of the grating was 5mm, Elasto-plastic model R-curve was plotted for first 5 mms of the crack length. However, G_{IIC} that calculated for the Elasto-plastic model is slightly lower

for CCM and is higher than CBT. Figure ***5-27*** shows the R-curve which was calculated for 10 mm extension of delamination crack. There is a significant difference in DBT and Elasto-plastic model in G_{IIc} and when the crack is propagating because the effect of crack length was not consider. But the R-curve value in Elasto-plastic model is slightly higher than values in CBT and CCM. But Elasto-plastic model result is close to CCM.

Table 5-4 Fracture energies in pure Mode II obtained by the DBT, CBT, CCM and Elasto-plastic model

Methods	G_{IIc} **(mJ)**
CBT	0.8901629422
DBT	2.144909366
CCM	1.037140538
Elasto-plastic model	0.9834495278

An estimate of delamination crack stability can be established using G_{II}/G_{IIC} ratio and the strain measured by the embedded FBG sensor. This estimate is presented in Figure ***5-28***. The R-curve has increased linearly when the ratio is less than one where as the curve sharply increased when the ratio is greater than one. The delamination is monotonically increasing with the increase of imposed displacement (Δ), however the crack, growth is unstable (when the G_{II}/G_{IIC} ratio is equal or greater than one) due to fracture energy (G_{II}) is greater than critical fracture energy (G_{IIC}). Figure ***5-29*** shows normalized indexes G_{II}/G_{IIc} ratio, DI and PWR. These indexes DI and PRW parameters show onset of delamination region and stability of delamination crack however, G_{II}/G_{IIc} ratio is not able to indicate onset of delamination crack region. However a linear line is drawn to capture changes of the curve (Figure ***5-29***). As shown the curve changes linear to non-linear at delamination crack onset area.

The R-curve is calculated from state damage variables of ABAQUS SDV2 and SDV6 and the strain at FBG sensor location. FEA strain plots are shown in Figure ***5-30***, Figure ***5-31***, and Figure ***5-32***. The nine state damage variables (SDV1, SDV2,…, SDV9) were used as a criteria to simulate crack onset and the cohesive elements for crack surface (see Figure ***5-30***). As the state damage variables SDV2

and SDV6 before imposed displacements 3.11 mm in Mode II is almost zero, as shown in Figure ***5-31*** and Figure ***5-32***. When the crack propagates beyond 3.11 mm imposed displacement, the set values of SDV2 and SDV6 are equal to 1 which means the crack in the specimen is dynamic and the delamination being propagated. The extension of delamination crack (Δa) is calculated from SDV2 result is compared with the experimental results that captured from the high speed camera as shown in Figure ***5-33***. The comparison shows that the cohesive element has accurately simulated propagation of delamination.

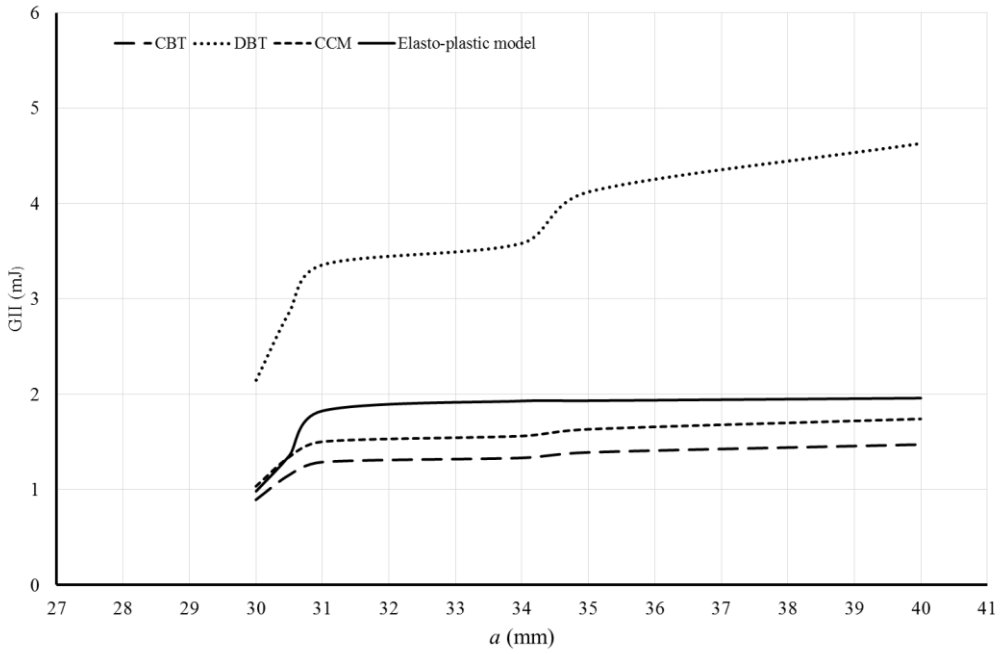

Figure 5-27 Experimental R-curve as a function of delamination crack length and strain

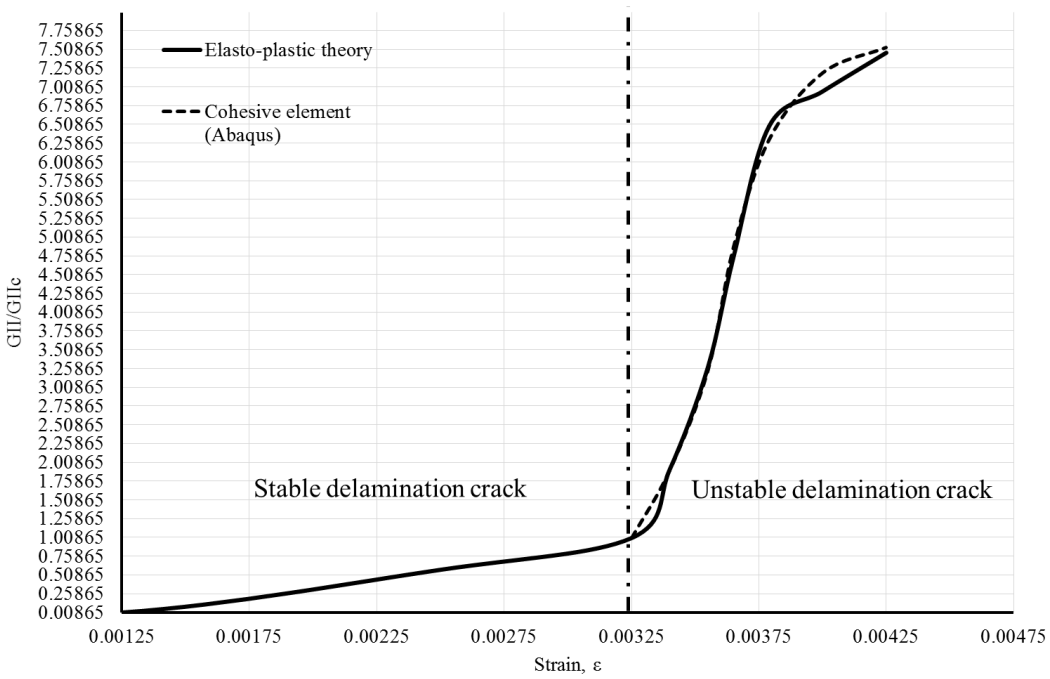

Figure 5-28 Examining stability of delamination crack Mode II depending on G_{II}/G_{IIc} ratio and strain measuring from FBG sensor for WC/epoxy specimen

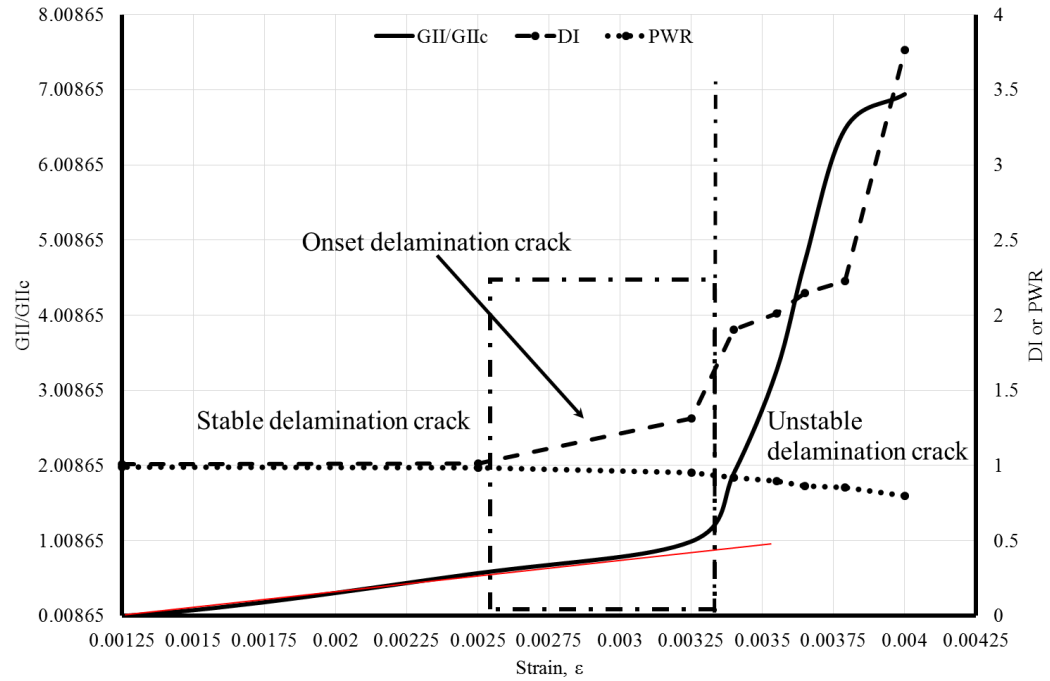

Figure 5-29 Examining stability and onset of delamination crack Mode II depending on G_{II}/G_{IIc}, DI and PWR parameters with strain measuring from FBG sensor for WC/epoxy specimen. Left vertical axis shows normalized DI or PRW values

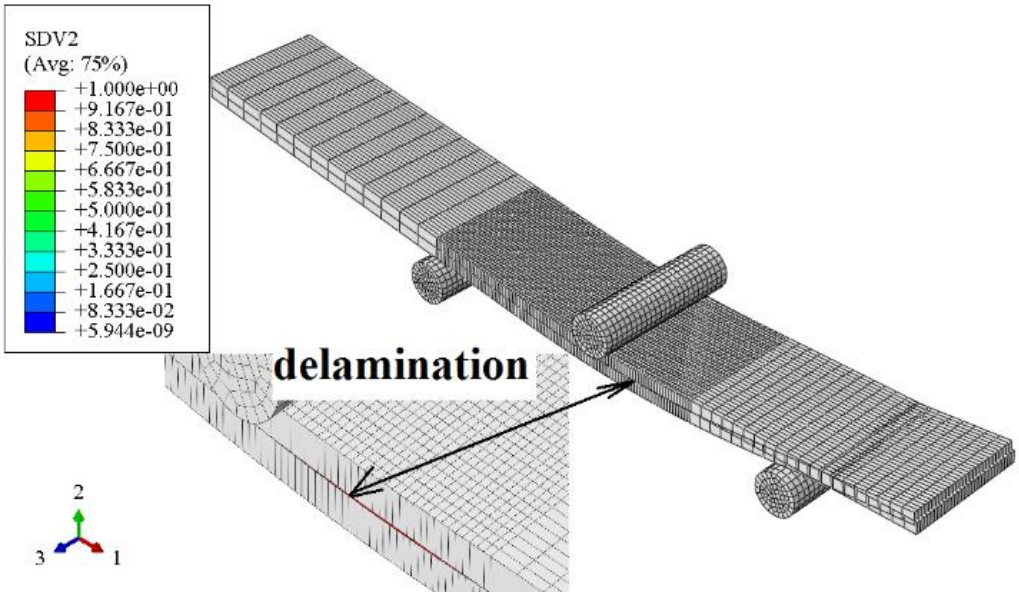

Figure 5-30 SDV2 values with developing delamination crack in cohesive element model

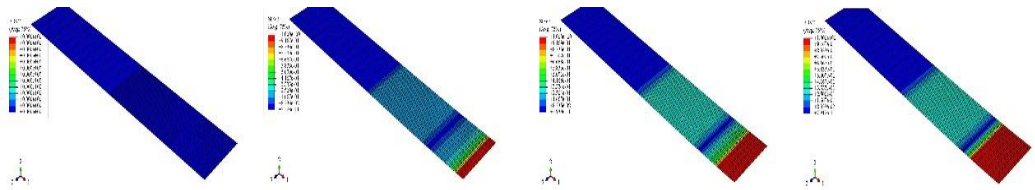

Figure 5-31 SDV2 developing with increasing displacement

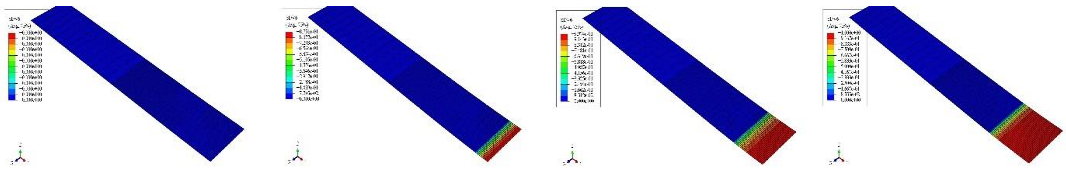

Figure 5-32 SDV6 developing with increasing displacement

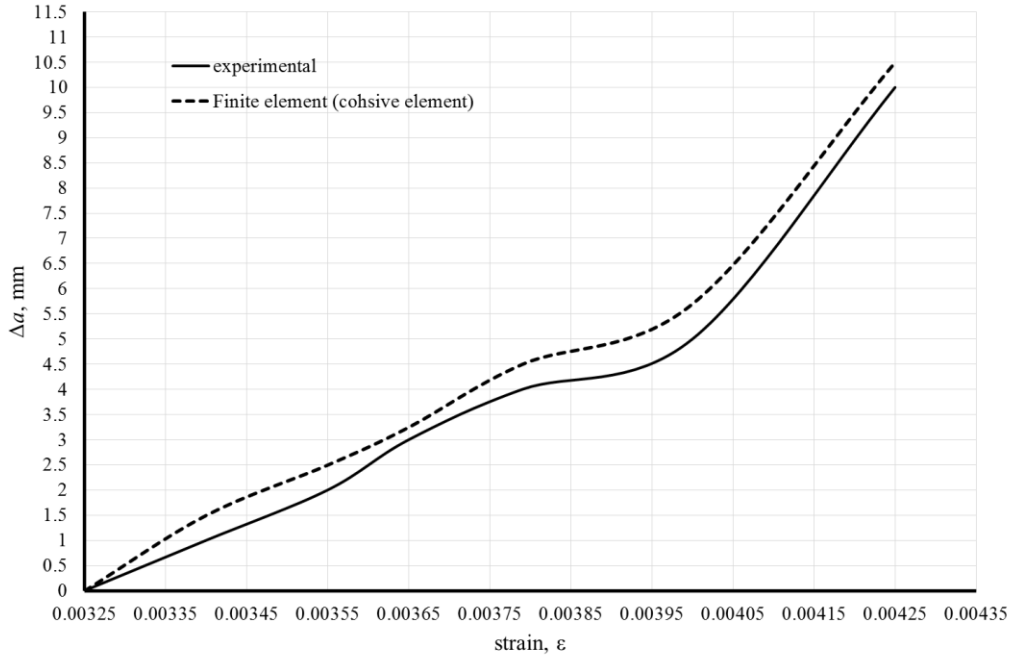

Figure 5-33 Comparison between experimental results (Elasto-plastic model) with finite element (cohesive element) depending on state damage variable SDV2 for calculating actual extension of delamination crack (Δ*a*) under Mode II delamination test

5.3: Mode II delamination damage under axial tensile loading case study

5.3.1: Evaluation of delamination crack tip in woven fibre glass reinforced polymer composite using FBG sensor spectra and thermoelastic response

Figure ***5-34*** shows the thermoelastic phase response of the sample measured during cyclic loading of the sample. The variations in colour correspond to variation in the phase of the thermoelastic response relative to the load, with the largest variations in phase occurring near the bottom edge of the delamination zone. The original size of the delamination is approximately shown by the red dotted line in frame (a) to (g). This is seen to correspond reasonably well with an area of perturbed phase response (defined by red hues) at the lowest mean load of 5 kN (0.11% strain). As the mean load is increased this area grows, and reaches a maximum at the final mean load of 35 kN (0.77 % strain).

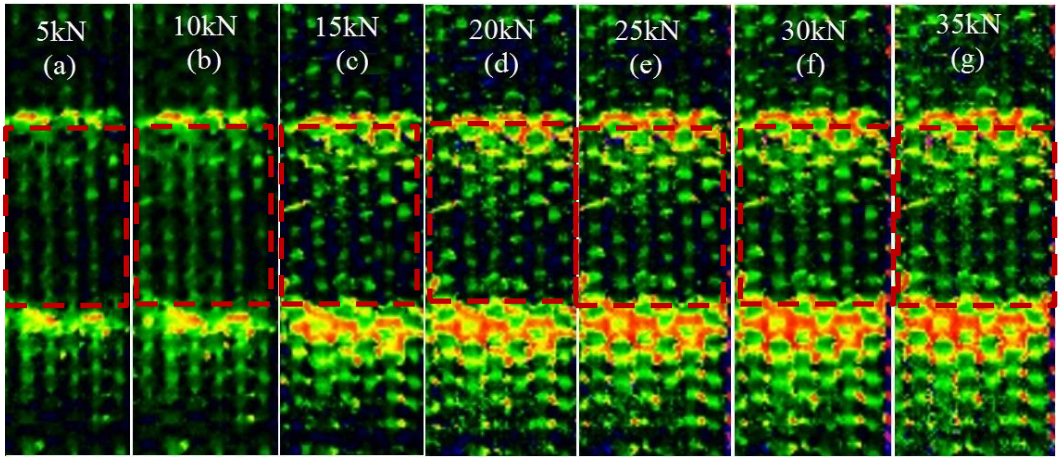

Figure 5-34 Delamination crack front propagation (θ-component). Red dotted line outlines the boundary of the initial delamination. Delamination zone is seen to increase as a function of mean load

The quadrature component of the thermoelastic response signal, which is driven by heat conduction and is therefore quite sensitive to stress gradients, was examined along the centre line of the specimen through the delamination as shown in Figure ***5-35***. Figure ***5-36*** shows the signal magnitude along this line for load cases (a), (d) and (g) in Figure ***5-34***. The tip of the delamination is seen to correspond to an increasingly positive quadrature signal. The magnitude of this signal and the area it envelops increases with increasing mean load.

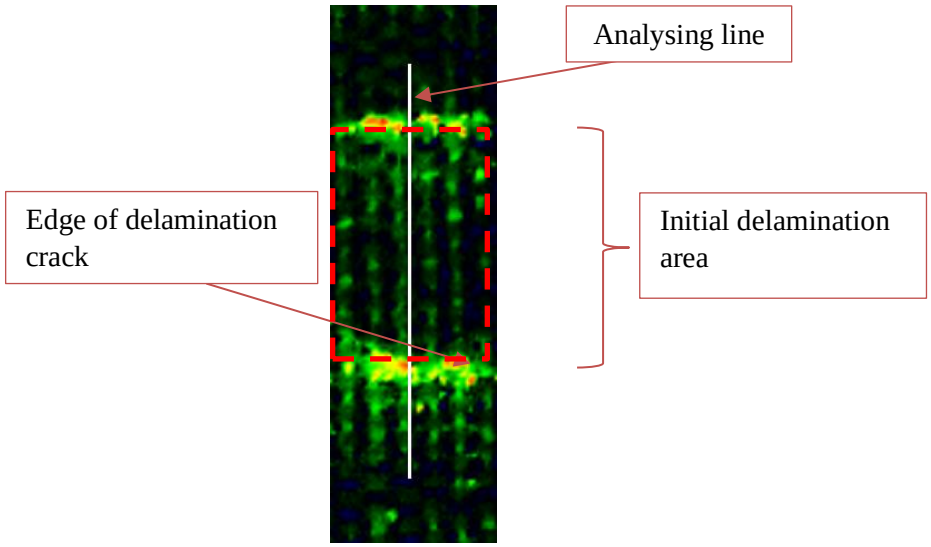

Figure 5-35 Analysis line used in estimating the delamination crack length.

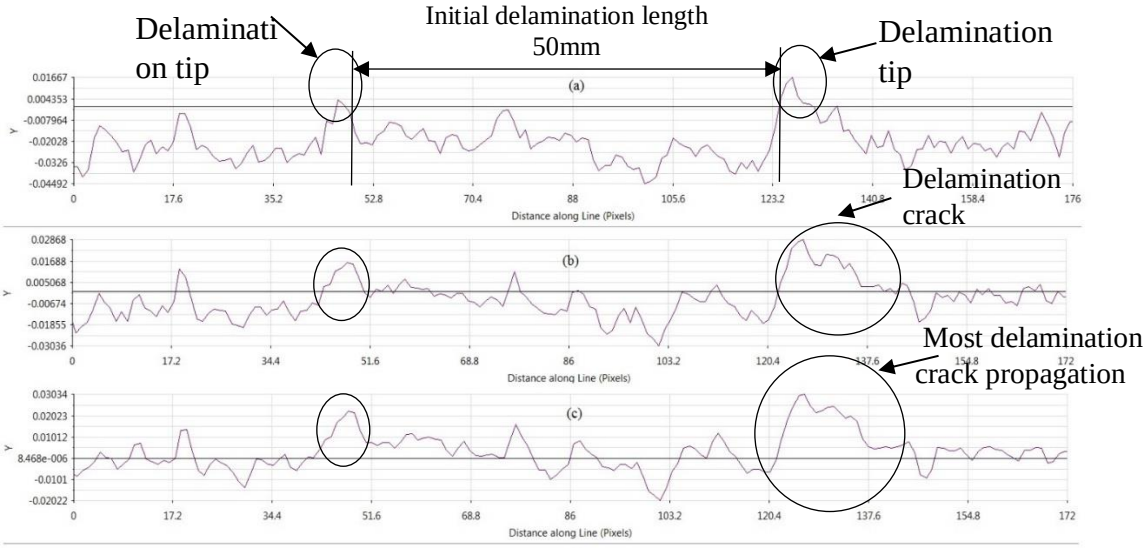

Figure 5-36 Quadrature signal (Y) in the delamination region at mean loads of: (a) 5 kN (0.11% max strain), (b) 20 kN (0.44 % max strain) and (c) 35 kN (0.78% max strain) with propagating delamination crack. The vertical axis is in Kelvin (nom.), and the horizontal axis corresponds to distance in pixels (50 mm = 76.7 pixels)

An estimate of the delamination crack length was extracted from the quadrature signal by measuring the distance between the extremities of the peaks circled in Figure ***5-36***. These estimates are presented in Figure ***5-37***. The delamination grows monotonically with increasing load, as expected, however the rate is seen to decline. This is possibly a result of an increasing number of local cracks in the composite sample. The agreement between the experimental and numerical results is generally good in terms of the overall trend, but the latter yields consistently higher estimates for the delamination length. The fact there is a difference is not surprising as the peak value in the measured quadrature response is not necessarily coincident with the position of the delamination crack front, though as Figure ***5-37*** confirms there is a reasonable correlation. Further modelling work is underway to develop a deeper understanding of the relationship between the two.

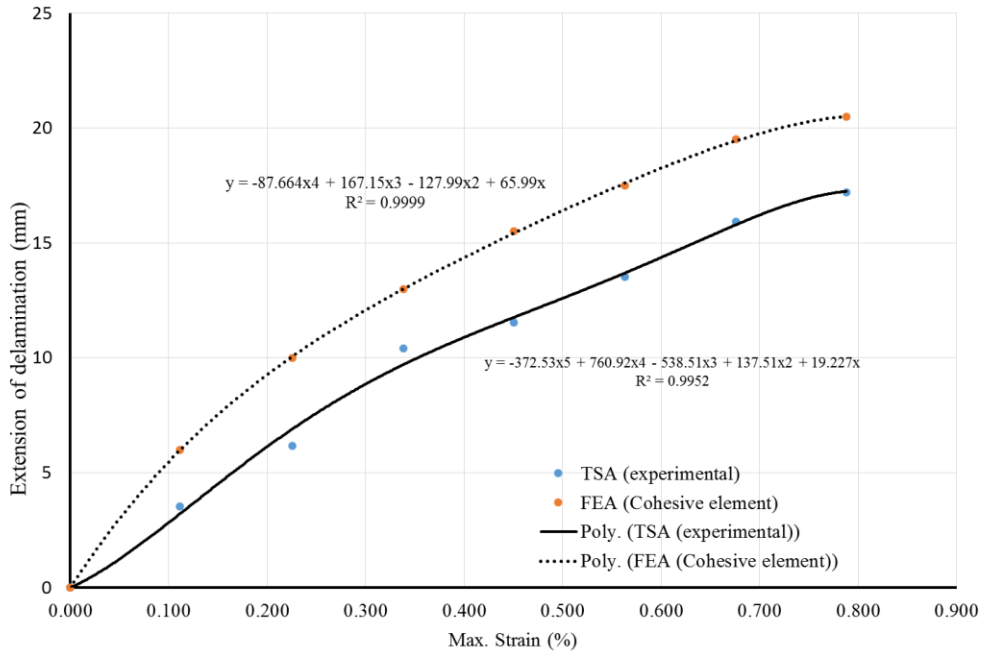

Figure 5-37 Average extension delamination length- Max. Strain % of woven glass fibre reinforced polymer [0/90] specimen under different loadings corresponding with delamination crack propagation in Figure 5-34

ABAQUS solution dependent state variables, SDV2 and SDV6, are displayed in Figure ***5-38*** and Figure ***5-39*** respectively. State variable SDV2 represents the failure index at each integration point. It is a continuous variable that can have a value between 0 and 1. A value of 0 indicates there are no stresses at the integration point. A value of 1 indicates that the failure initiation criterion has been satisfied and the process of damage evolution (stiffness reduction) has begun at the integration point. Another useful state variable is SDV6, which is referred to as the damage variable D. SDV6 is a continuous variable with a value between 0 and 1 where a value of 0 corresponds to an undamaged integration point that has its original (full) stiffness, and a value of 1 corresponds to a fully degraded (zero stiffness) integration point.

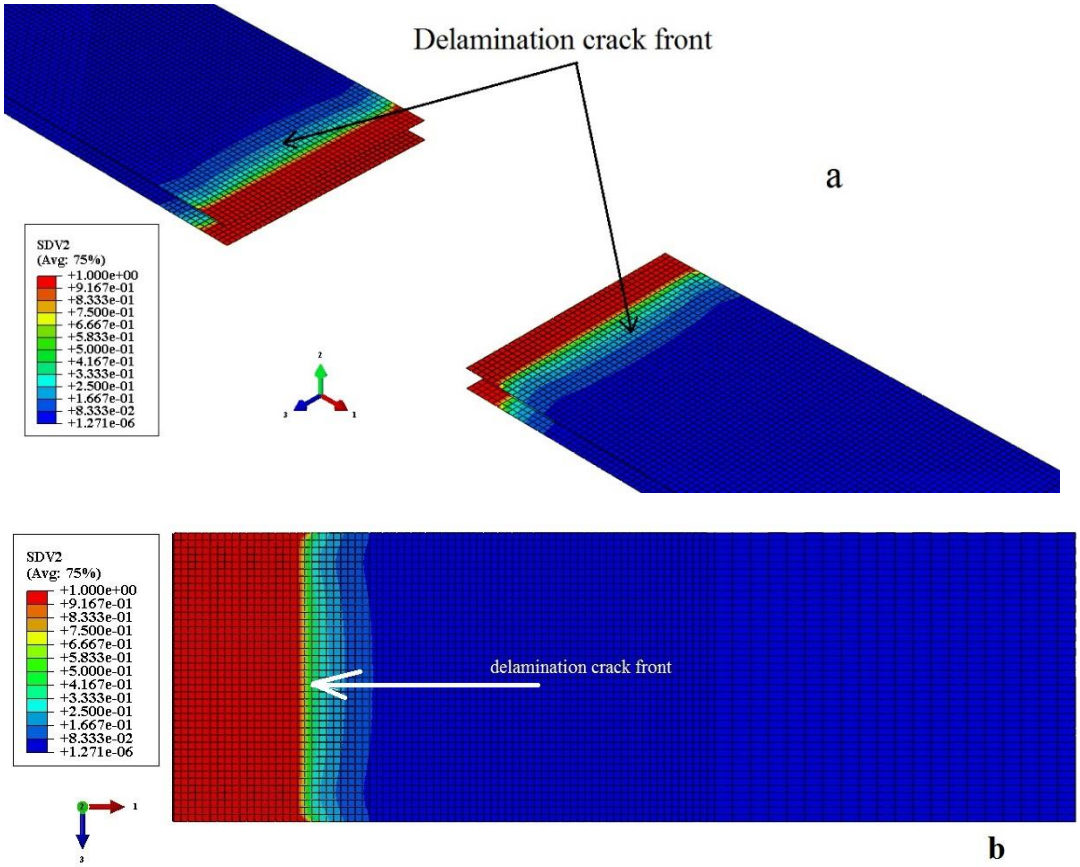

Figure 5-38 Plot of the damage variable SDV2, (a) damage in the cohesive elements (full model) at 5kN (0.111% strain), (b) damage in the cohesive element in one of the cohesive sections at 25 kN (0.563 % strain)

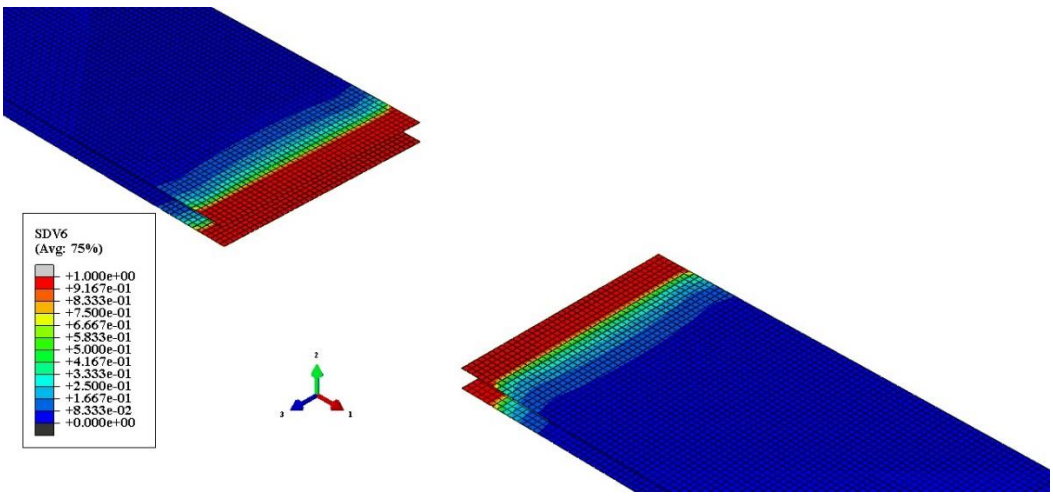

Figure 5-39 Plot of the damage variable SDV6

The primary failure mechanism was thought to be a combination of Mode I and Mode II damage at the delamination crack front caused by local bending. This was investigated using a cohesive element model in ABAQUS 6.13 software. Figure ***5-40*** shows the normal displacement in the cohesive elements in front of the delamination crack at an applied load of 35 kN. The displacement pattern is

consistent with local bending which supports the proposed failure mechanism. The delamination crack propagation has caused a reduction in the bending stiffness. Multicontinuum Theory (MCT) state variable 'SDV7' was deployed to investigate the local bending phenomenon. For woven composites SDV7 stores the work done for longitudinal cracking (direction 1) in the fill-matrix constituent used for hysteresis heating computations. Figure ***5-41*** shows the simulated delamination crack propagation and provide an accurate insight to the local bending phenomenon.

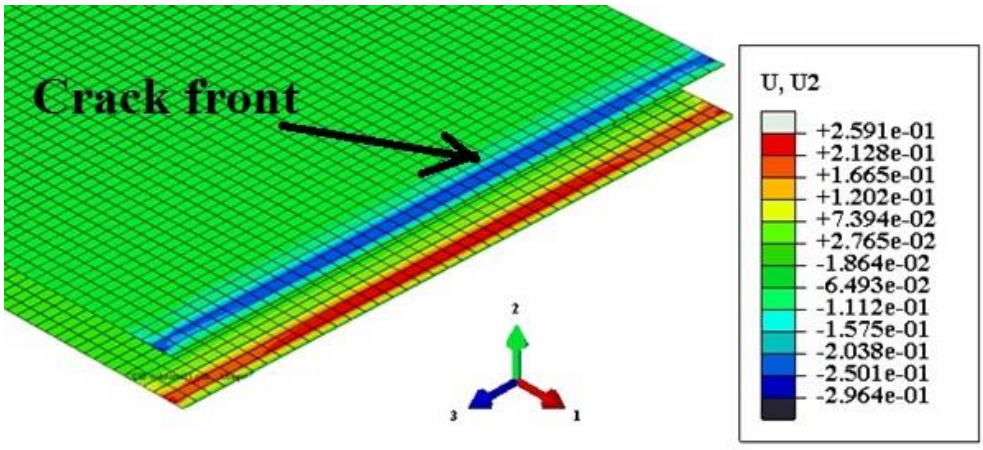

Figure 5-40 Deformation Mode in thickness direction (2) indicates significant local bending in front of delamination crack at 5NK

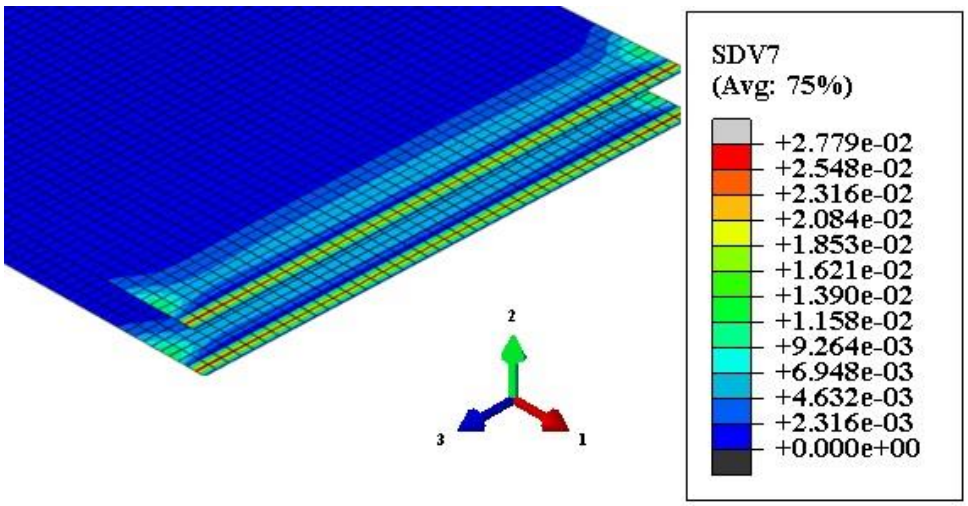

Figure 5-41 SDV7 state variable for cohesive elements (local bending) in front of delamination crack

To corroborate the information obtained from TSA the specimen was investigated under an optical microscope. Figure ***5-42*** shows a detailed micrograph of the delamination crack in the specimen following completion of the last step in the

loading sequence to a peak value of 35 kN. Based on a visual determination of the crack tip location the crack length was estimated at 16.34 mm. This is consistent with the value determined by TSA, which as shown in Figure ***5-37*** is approximately 17 mm. Although the two values are remarkably close one should recall that assigning the peak quadrature response as an estimate for the crack tip location was done on a somewhat arbitrary basis. Further study is required to understand the relationship between this particular metric and the physical location of the crack tip. On another cautionary note, the strongly heterogeneous response evident in Figure ***5-34***, which is due to the woven structure of the laminate, leads to a position dependency in the estimate derived for the crack tip, an effect that was not considered in the present work. This also requires further study.

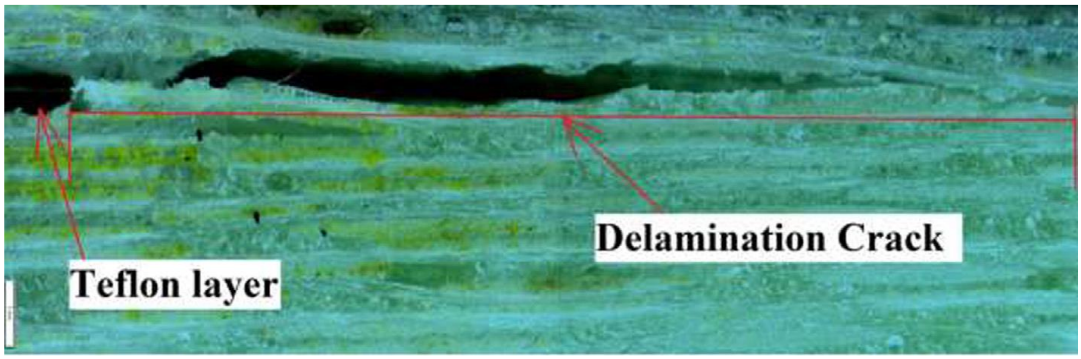

Figure 5-42 Photograph showing a 16.34 mm delamination crack extending from a Teflon insert, after loading to 35 kN

Figure ***5-43*** shows the FBG spectra changes with Progression of the crack (crack tip). Figure ***5-43*** is compared with signals that captured from thermoelastic response as showed Figure ***5-34*** and Figure ***5-37*** to evaluate the delamination crack tip. The results obtained have indicated of FBG sensor and thermoelastic response for capturing delamination crack tip and propagation of delamination damages (Kakei, A. et al. 2018).

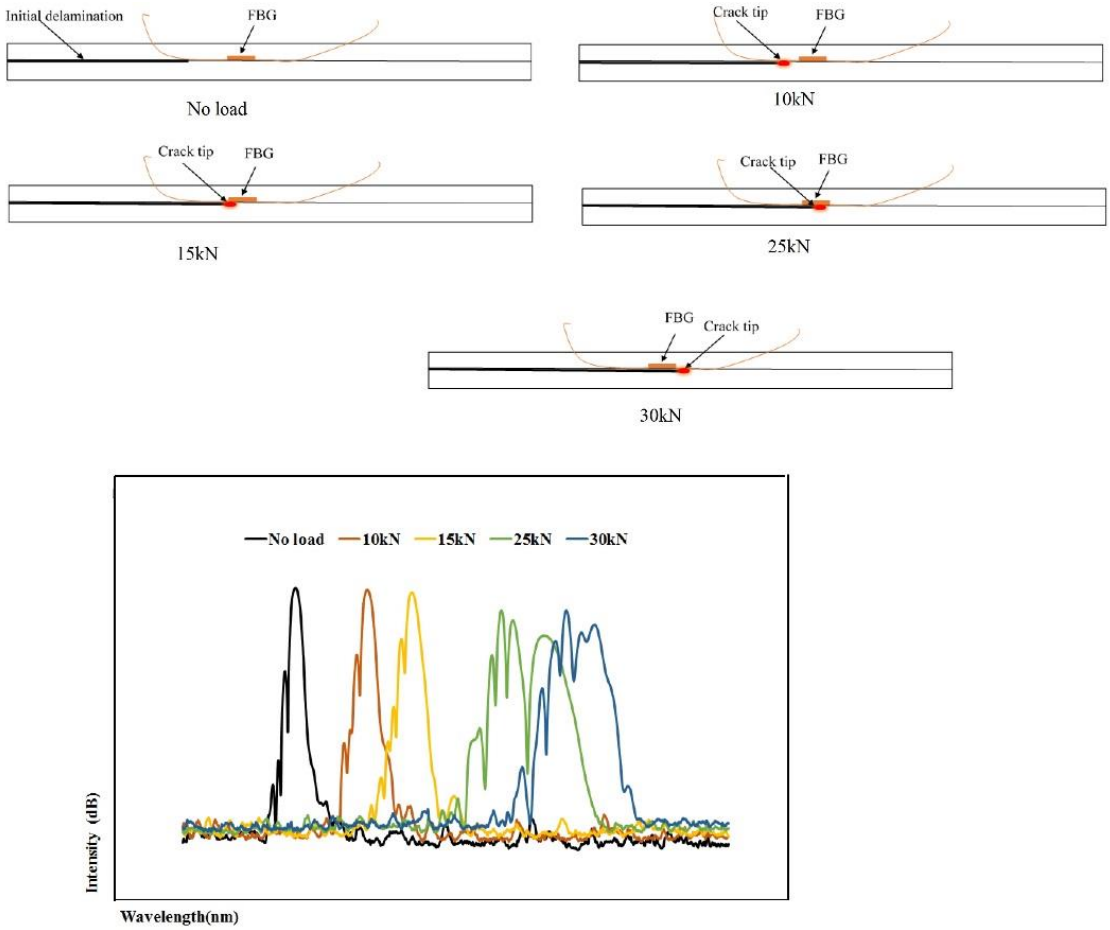

Figure 5-43 Different stages of the FBG response under a crack growth event corresponding with increasing tensile loadings in composite specimen

5.3.2: Prediction of developing delamination damage in WC/epoxy specimens

A few uniaxial strain gauges (FLA-5-11-1L) were bonded on the surface of specimens in different places to measure change of strain and indicate delamination damage. The strain gauges are numbered as shown in Figure ***5-44***, strain gauge '1' was bonded at 10 mm from the end of delamination (embedded FBG sensor is located directly underneath), strain gauge '2' was bonded on the delamination area, and strain gauge '3'was bonded 55mm from end of initial delamination. With the increase in tensile loadings the strain measured at gauges 1 and 3 have shown initial linear response and later transformed to non-linear response as shown in Figure ***5-45***. Both strain gauges show the same values at linear region as anticipated. After 25 kN applied load some failures happened in the composite specimen at the region between strain gauges 1 and 3 leadings to sharp increase in the strain measured by strain gauges 1 and 3. At the same time, increased loads caused the non-linear strain behaviour in strain gauge 2. This non-linearity may be attributed to delamination

underneath of strain gauge 2 which caused debonding between composite specimen layers. The extent of delamination significantly influenced the strain measurements. As shown in Figure ***5-45***, measured strain from gauge 2 was less than measured strains by Gauges 1 and 3. This difference may be an indication of local bending at the middle of the delamination area due to hard point of delamination crack tip. This strain behaviour became non-linear after 5kN applied load. Measured strain by gauge 2 is shown in Figure ***5-46*** for specimens with delamination at various depths (changing $\mu=h_1/h_2$). The strain increased with increase in delamination through thickness μ. The effect of delamination was diminished after the delamination thickness μ equal to 0.5. With the increase in delamination through thickness μ, the strain gauge could not sense strains due to delamination damage μ equal to unity. The attitude of strain values (strain gauge 2) confirms assumption that there is a change of angle rotation rate at delamination crack plane (as shown in Figure ***5-46***) as a result delamination propagates when the rotation rate of both arms (upper and lower layers) is not same. Here, although strain gauge has detected delamination damage in some cases but it could not predict delamination development in the specimens. Therefore, more robust techniques were used to monitor and measure the development of the delamination damage. A comprehensive approach with TSA techniques and embedded FBG sensor is suggested in this work to evaluate the size of delamination and predict exact development of the damage.

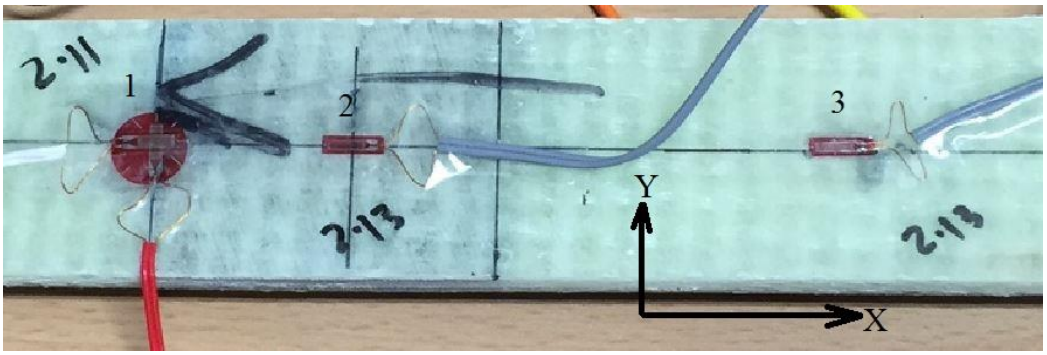

Figure 5-44 WC/epoxy Specimen with bonded strain gauges

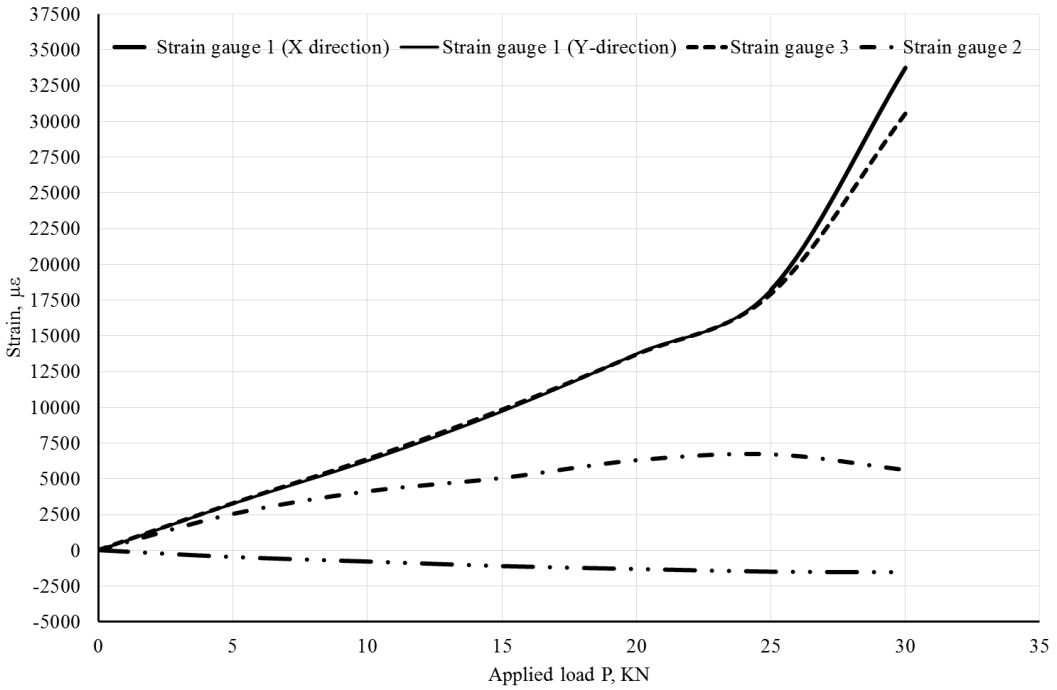

Figure 5-45 The effect of delamination location on the strain gauges reading, μ=0.3636

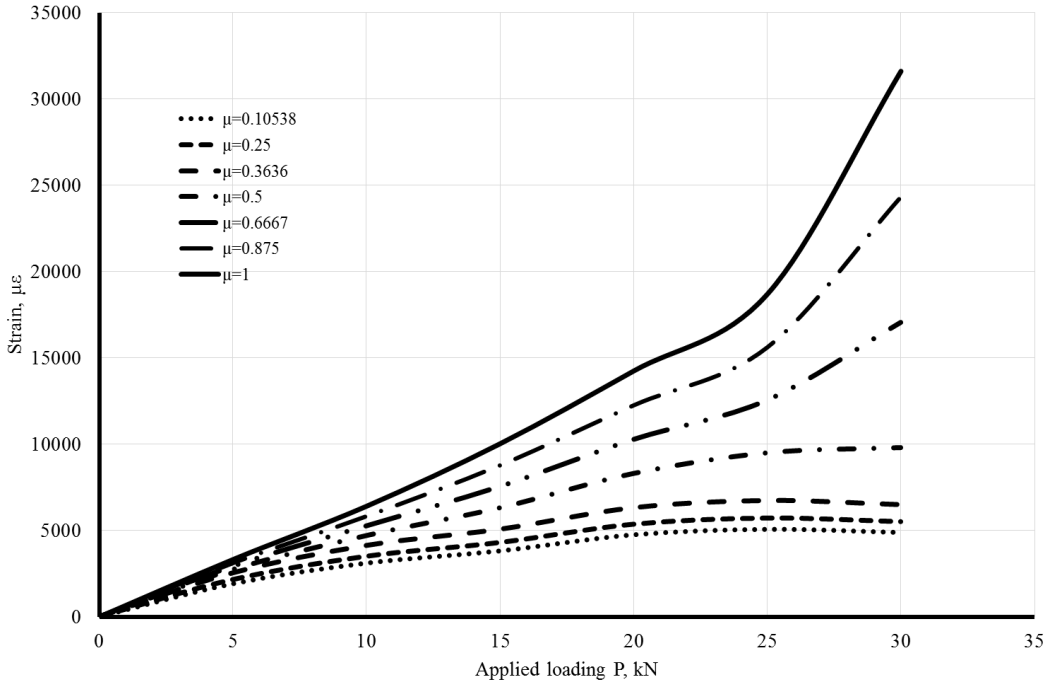

Figure 5-46 The effect of delamination location on strain in the middle of delamination. The strain value is calculated by strain gauge in the surface of specimen

The distortion of FBG spectrum occurs when the delamination crack tip reaches FBG sensor region due to the effect of non-uniform strain at the tip of delamination crack (Pereira, McGugan & Mikkelsen 2016). Figure ***5-47*** shows the change and shift in FBG spectrums with the advancement of delamination cracks for μ equal to 0.3636. A uniform spectrum of FBG sensor response indicates that the strain is uniform and perfectly elastic. Some change in FBG spectrum can be seen at 15 kN loading indicating the reach of crack tip close to FBG sensor. Finally the FBG spectrum has shown a significant distortion response after 20kN applied load. Progression of the crack has caused a non-uniform (plastic) strain field around the crack tip. Interestingly, for μ =0.18, the FBG sensor sensed the crack damage at 10kN and it reflected distorted spectra after 10kN applied load as shown in Figure ***5-48***. Furthermore the sensitivity of embedded FBG sensor is unaffected with the increase of μ (Figure ***5-47*** and Figure ***5-48***). The change reflectivity was simulated using free software FBG_SiMul V1.0 software (Pereira, McGugan & Mikkelsen 2016). FBG SiMul V1.0 was used as a tool to study the implementation of Fibre Bragg Grating (FBG) sensors solutions in any subjectively loaded structure. This software is designed as an interface programme to calculate longitudinal strain at FBG sensor region from ABAQUS software and then calculate distortion in the FBG sensor spectrum. As shown in Figure ***5-49*** and Figure ***5-50*** the distortion in the FBG sensor was captured successfully at two different location of delamination damage. Finite element results of cohesive elements indicated good agreement with experimental results.

The distortions of FBG sensor spectrum with the applied loads provide an index to detect delamination damage in the laminated composite structures. Both experimental and finite element simulation were used to evaluate the change in the FBG sensor spectrum. Two parameters DI (equation 4.3) and PWR equation (4.5) were used to evaluate delamination damage growth and elasto-plastic region in the matrix with applied loads. For μ equal to 0.3636, both parameters were equal to unit before 4 kN applied loading. Some change was realized in both parameters during the increase of loads from 4 kN to 15 kN. This behaviour was due to elasto-plastic region created at the delamination crack tip (Figure ***5-51***) during the propagation of the crack. The index DI and PWR remain at unity when the delamination crack tip is perfectly elastic. Once the tip of delamination crack

changes from elastic to elasto-plastic region, the stress concentration at the crack tip causes the distortion of FBG sensor as shown in Figure ***5-50***. As shown in Figure ***5-52***, DI calculated from FEA shows the same trend as the experimental observation. The distortion in FBG spectrum at the onset of crack confirms the elasto-plastic state in the epoxy (matrix) at the crack tip. With the advance of crack front until it reaches the FBG location, the spectra of FBG gradually distorts due to increase in strain concentration (Pereira, McGugan & Mikkelsen 2016) as shown in Figure ***5-53***. Figure ***5-54*** show, the strain (equation 4.2) increases sharply due to high non-uniform strain at the tip of delamination crack. This significantly high strain is possibly caused by the crack, propagating through the grated region of FBG sensor. The strain value becomes stable again when the crack leaves the FBG sensor. The change of FBG sensor spectrum provides excellent prediction and evaluation of initiation and propagation of delamination damage but it cannot calculate accurately the size of delamination damage in the WC/epoxy specimens.

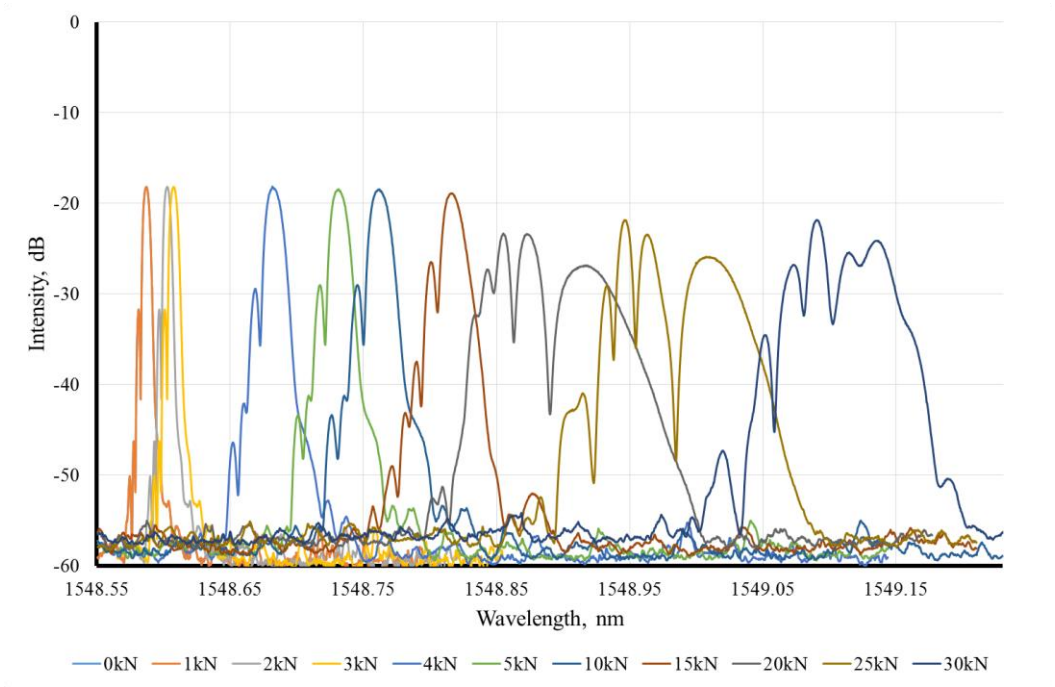

Figure 5-47 Spectra of embedded FBG in WC/epoxy specimen under tensile loading (delamination test) with increasing applied loadings (experimental result) at μ = 0.3636

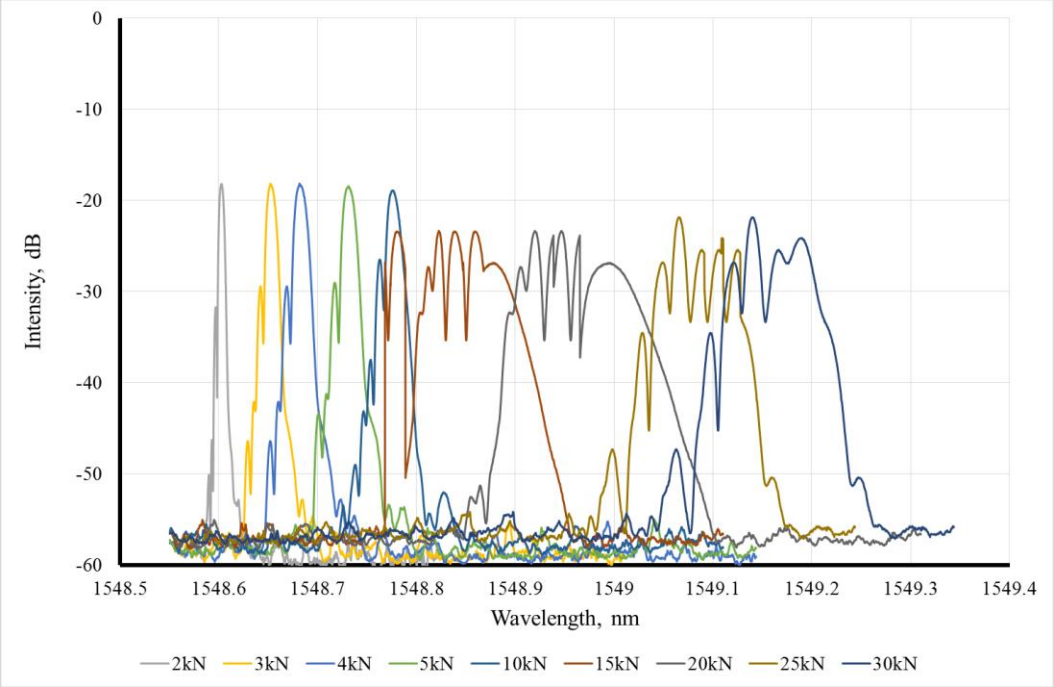

Figure 5-48 Spectra of embedded FBG in WC/epoxy specimen under tensile loading (delamination test) with increasing applied loadings (experimental result) at μ = 0.1538

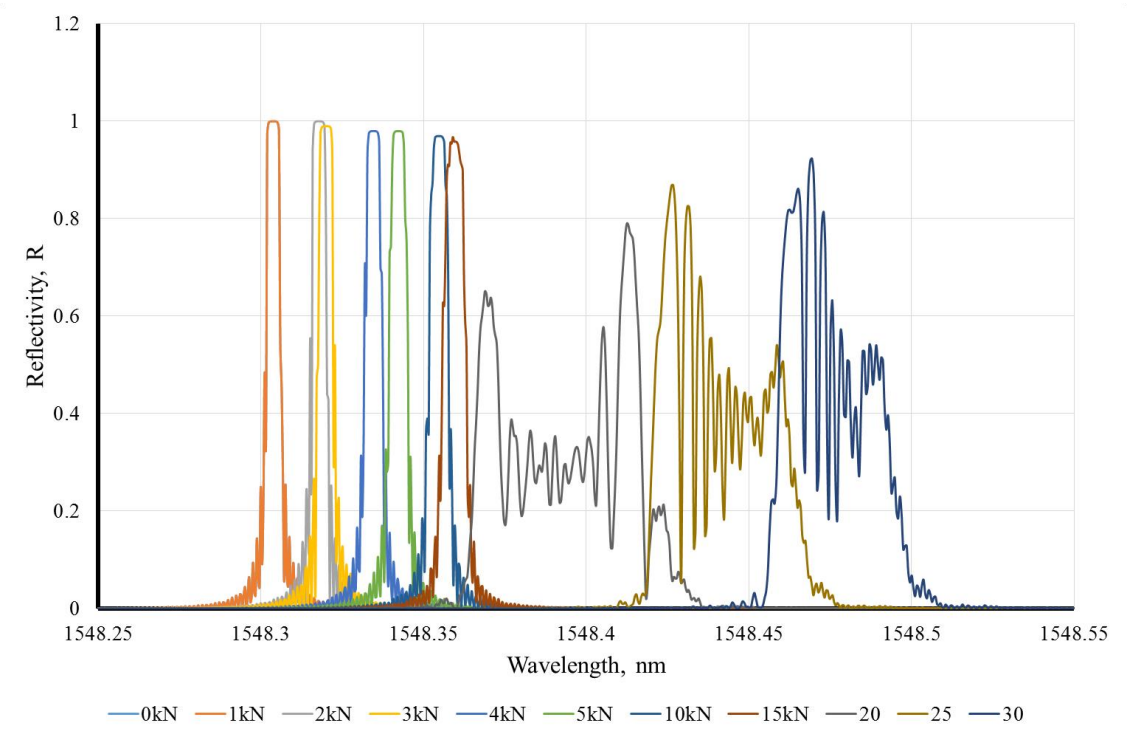

Figure 5-49 Spectra of embedded FBG in WC/epoxy specimen under tensile loading (delamination test) with increasing applied loadings at μ= 0.3636 using Cohesive element with FBG_SiMul V1.0 software

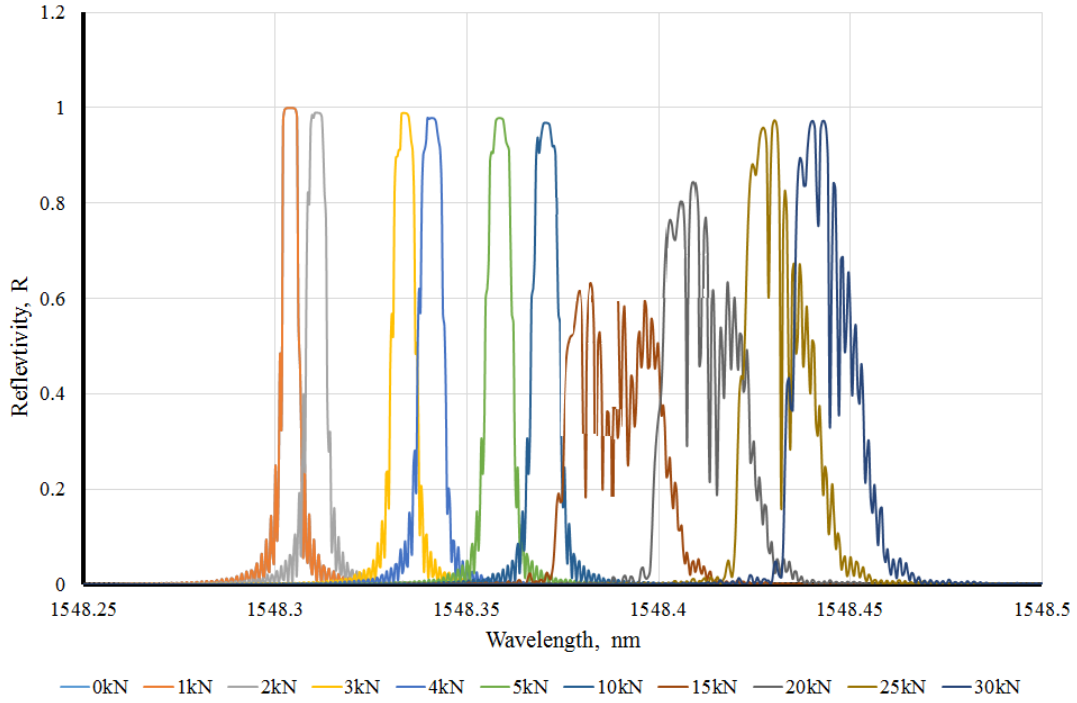

Figure 5-50 Spectra of embedded FBG in WC/epoxy specimen under tensile loading (delamination test) with increasing applied loadings at μ= 0.1538 using Cohesive element with FBG_SiMul V1.0 software

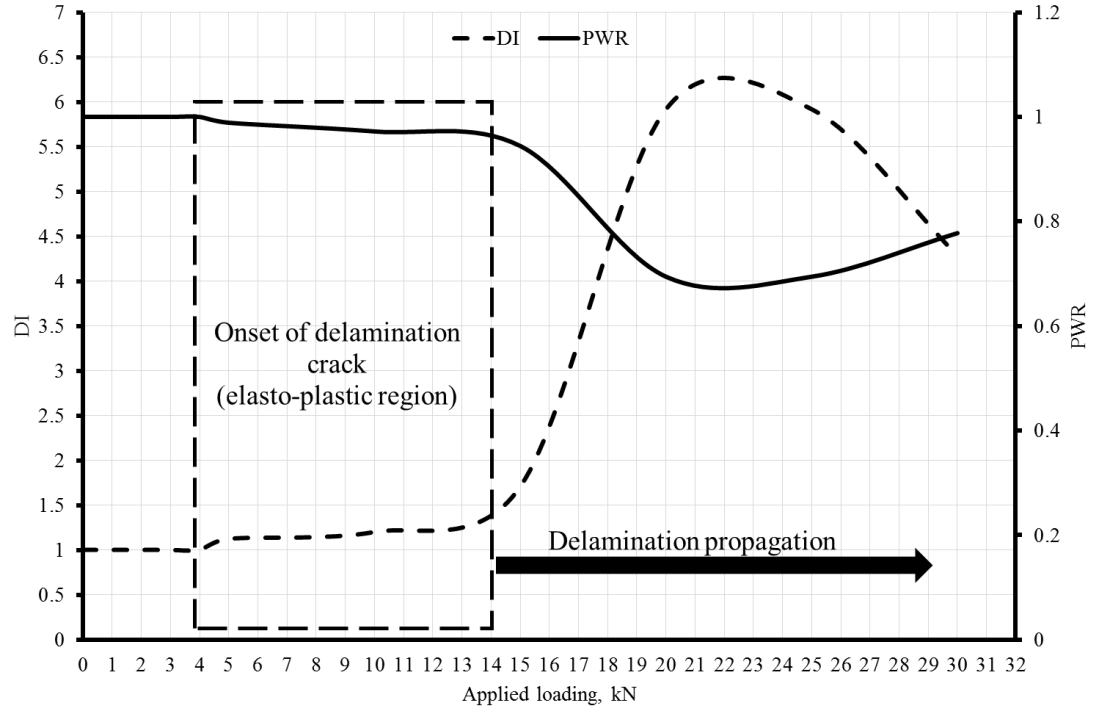

Figure 5-51 Detection of delamination crack onset and propagation for WC/epoxy under tensile loadings use both DI and PWR parameters (experimental results)

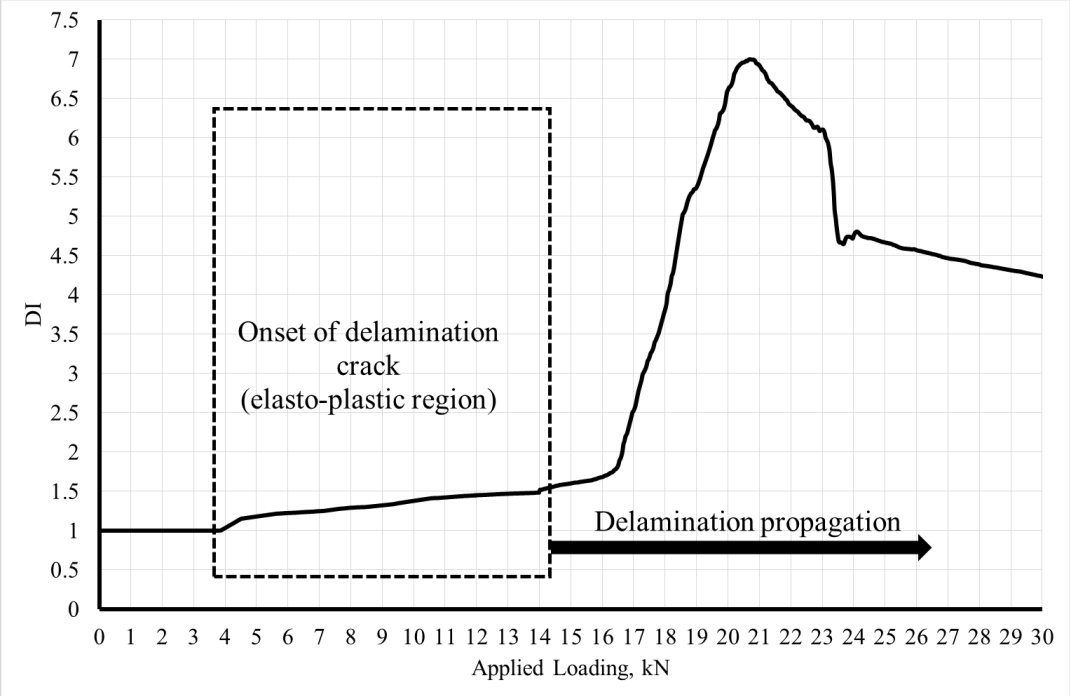

Figure 5-52 Detection of delamination crack onset and propagation for WC/epoxy under tensile loadings use DI parameter (cohesive element result)

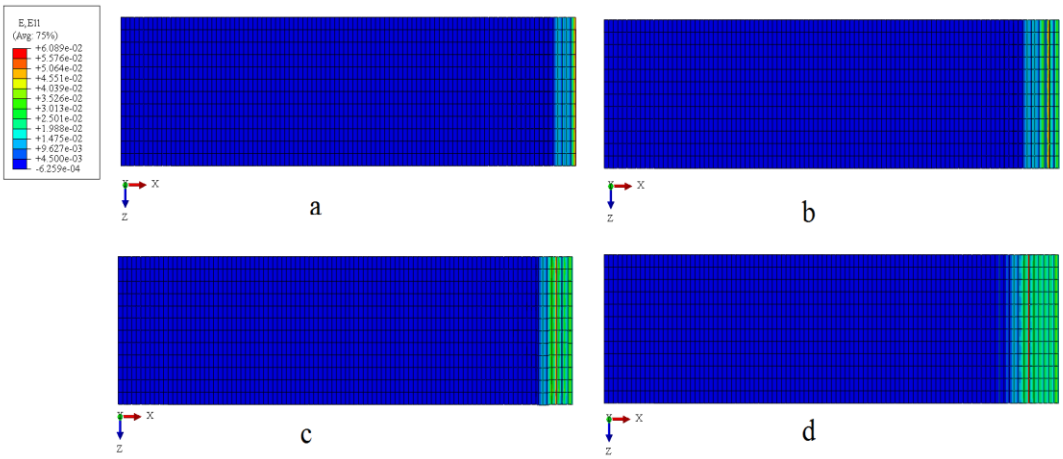

Figure 5-53 The concentration strain of delamination damage influence on the cohesive element at different applied tensile loadings

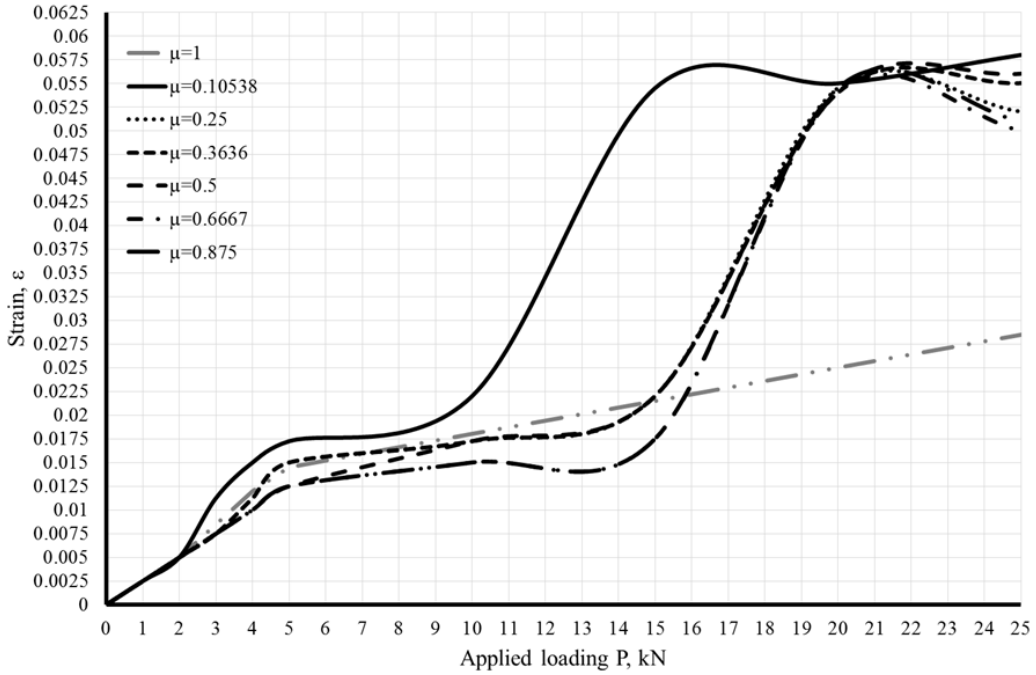

Figure 5-54 Strain-load relationship with change delamination crack location

Delamination damage extension is impossible to monitor by visual methods and delamination is treated as a hidden killer due to this reason. Recently Kakei et al. (KakeiEpaarachchiIslam, et al. 2016) have successfully shown that the use of Thermo-Elastic Stress Analysis (TSA) and cohesive element finite element techniques to determine the extension of delamination crack length (Δa). The thermoelastic phase response had been measured during cyclic loading. As shown in Figure ***5-55*** and Figure ***5-56***, the largest variations in the phase happened at the tip of delamination crack. Delamination length had reached underneath of FBG senor at 15 kN for all values of μ. As such maximum applied loading of 15 kN was selected for investigation of delamination length (Δa). The original delamination size is shown as the red dotted line frame (Figure ***5-56***). The area of perturbed phase response is shown in blue hues. The quadrature component of the thermoelastic response signal was examined along the centre line of the specimen through delamination. As shown in Figure ***5-57*** the delamination tip was following positive quadrature signal for different load cases. An estimate of the delamination crack length was determined from the quadrature signals by measuring the distance between the extremities of the circled peaks (see Figure ***5-58*** & Figure ***5-59***). TSA signals have provided solid evidence of extension of crack. The TSA results are strongly agree with the spectral responses obtained from FBG sensors under qusi-

static loading. A detailed Finite element analysis was performed to simulate the crack propagation under quasi static loading. Auto Desk_ Simulation composite analysis 2015 Plug-ins_ for ABAQUS 6.13 was used to create the UMAT subroutine to calculate the SDV2 state variables for the cohesive materials. SDV2 state variable is an excellent indicator for detection of delamination damage using cohesive elements. State variable SDV2 represents the failure index at each integration point. It is a continuous variable that can have values between 0 and 1. SDV2 equal to 0 indicates zero damage whereas 1 indicates damage. The delamination crack tip can be seen in the cohesive element in Figure ***5-60***a. As shown in Figure ***5-60***b, full delamination damage in the cohesive element was captured at the tip of delamination crack (SDV2 is equal to 1). Then the effect of the delamination damage tip extended to the region in front of the tip of the crack i.e. the value of the SDV2 between 0 and1. Finally SDV2 was equal to zero at the region far from the crack tip. However, the damage in the cohesive element that captures from SDV2 can be divided into three states, plastic region at the tip of the crack, elasto-plastic at the delamination crack tip and healthy region or no damage region (see Figure ***5-60***b). Another useful state variable is SDV6, which is referred as the damage variable D. SDV6 is a continuous variable with a value between 0 and 1. Where value nil corresponds to an undamaged integration point that has its original (full) stiffness. Value of 1 corresponds to a fully degraded (zero stiffness) integration point. SDV6 provides delamination damage extension in cohesive element equally as SDV2 (Figure ***5-61***). The engagement between TSA and FBG senor's techniques has provided accurate evaluation and calculation of delamination damage state and development.

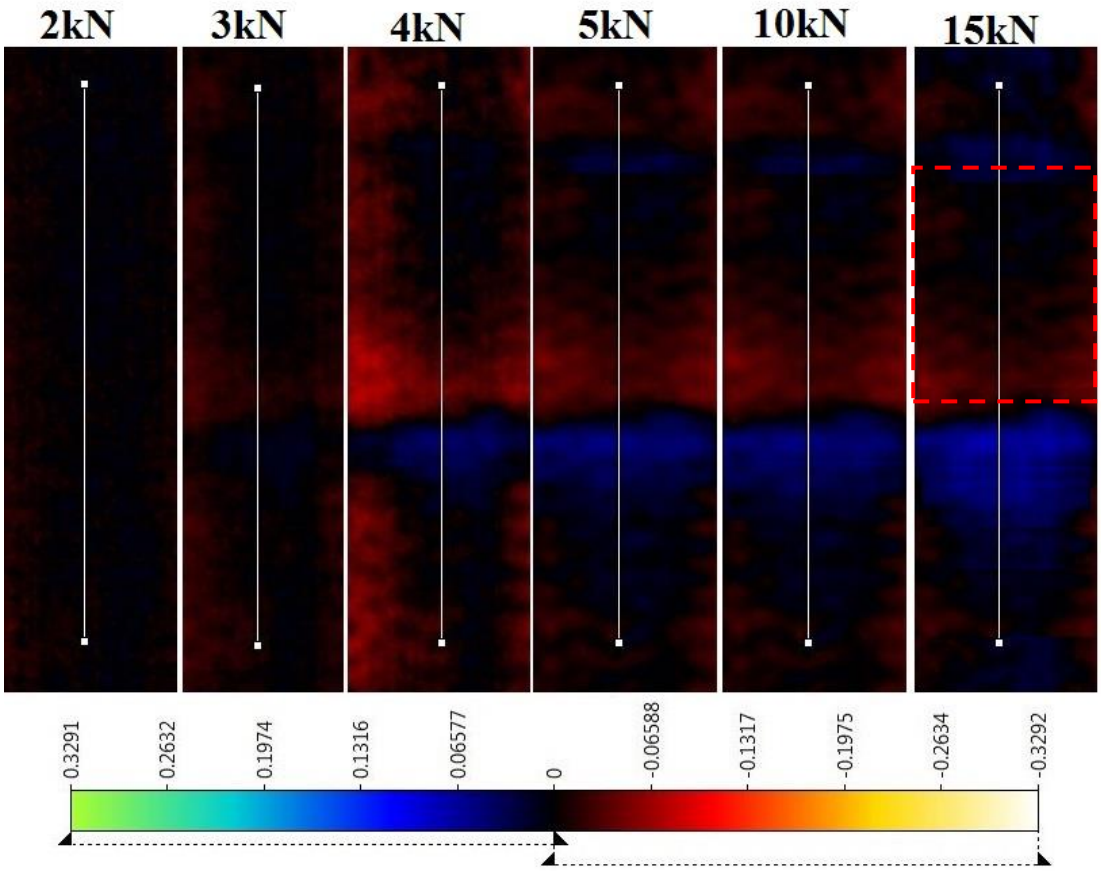

Figure 5-55 Delamination crack front propagation (θ-component). Red dotted line outlines the boundary of the initial delamination. Delamination zone is seen to increase as a function of mean load, μ=0.135

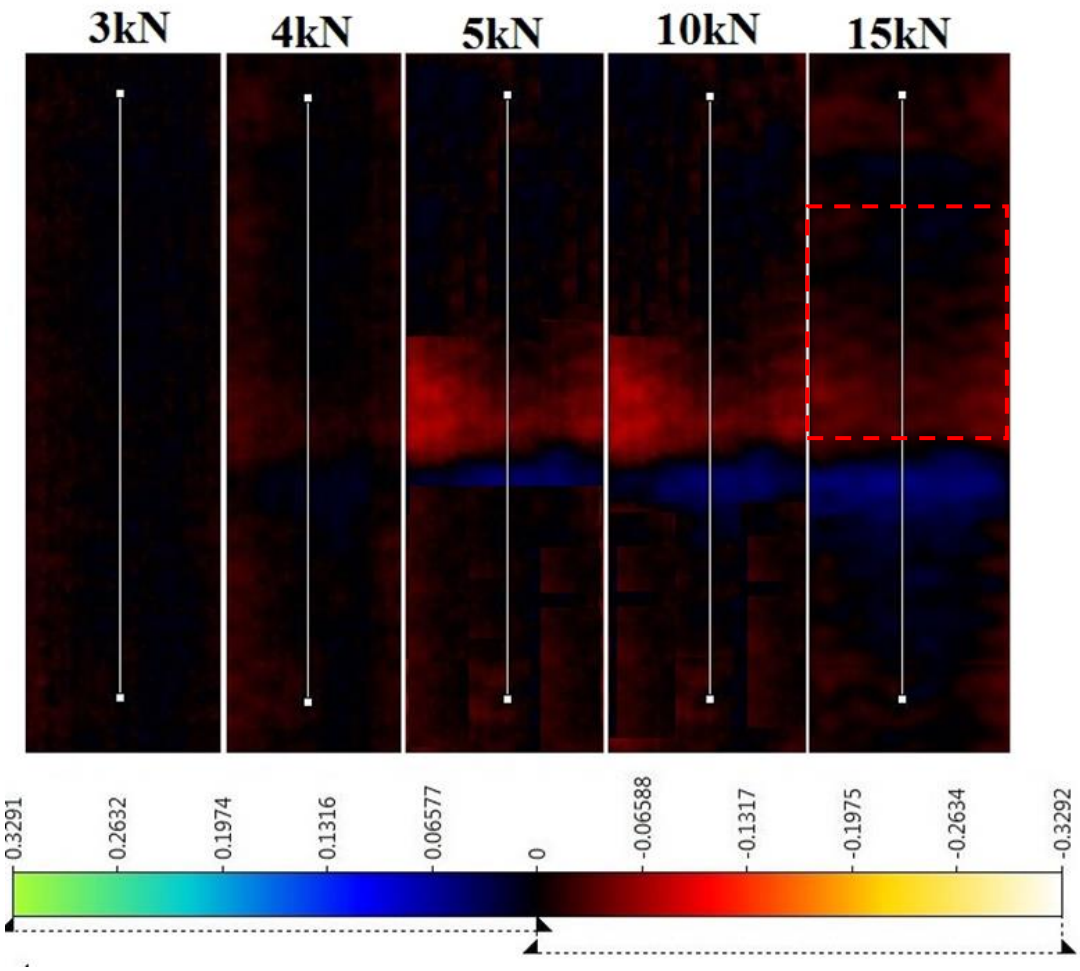

Figure 5-56 Delamination crack front propagation (θ-component). Red dotted line outlines the boundary of the initial delamination. Delamination zone is seen to increase as a function of mean load, μ=0.363

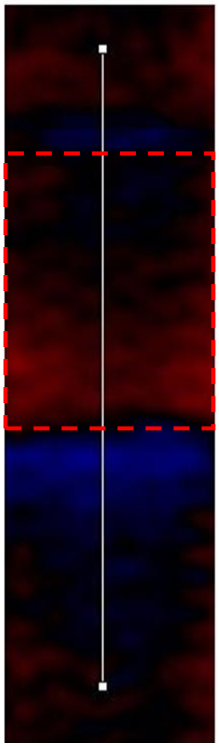

Figure 5-57 Delamination crack front propagation (θ-component). Red dotted line outlines the boundary of initial delamination. Delamination zone is seen to increase as a function of mean load. μ=0.130, 5kN loading

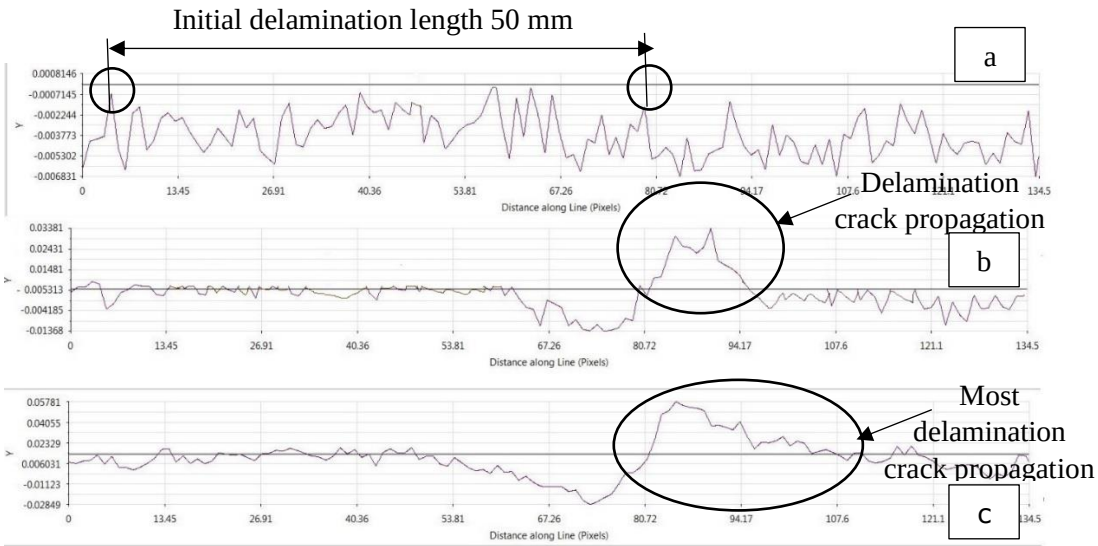

Figure 5-58 Quadrature signal (Y) in the delamination region at mean loads of. (a) 2 kN, (b) 10 kN and (c) 15 kN (with propagating delamination crack for μ=0.135. The vertical axis is in Kelvin (nom.), and the horizontal axis corresponds to distance in pixels (50 mm = 67.7 pixels)

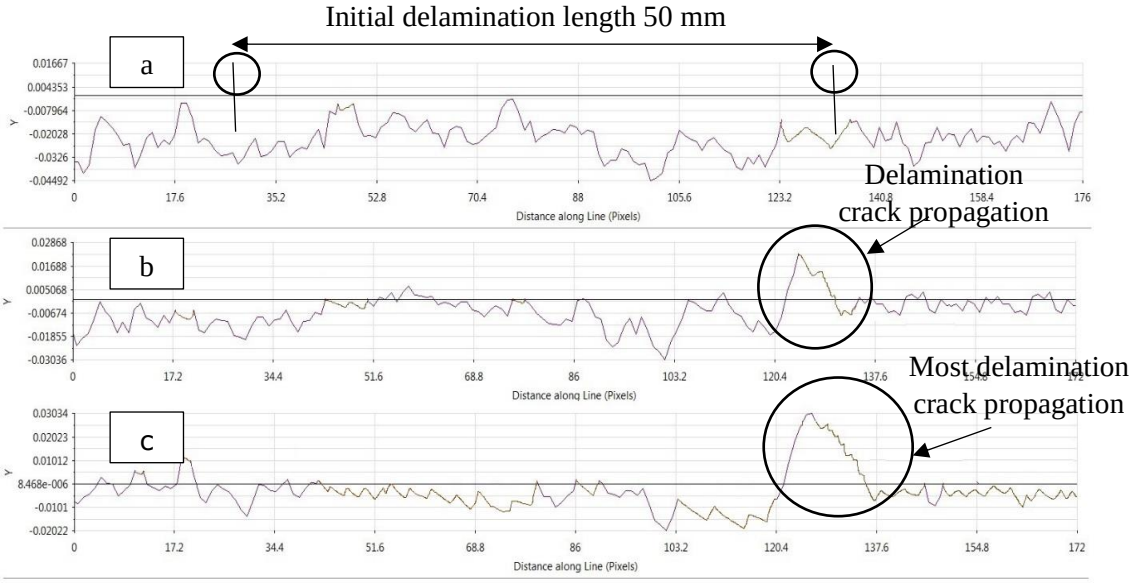

Figure 5-59 Quadrature signal (Y) in the delamination region at mean loads of. (a) 4kN, (b) 10 kN and (c) 15 kN (with propagating delamination crack for μ=0.353. The vertical axis is in Kelvin (nom.), and the horizontal axis corresponds to distance in pixels (50 mm = 67.7 pixels)

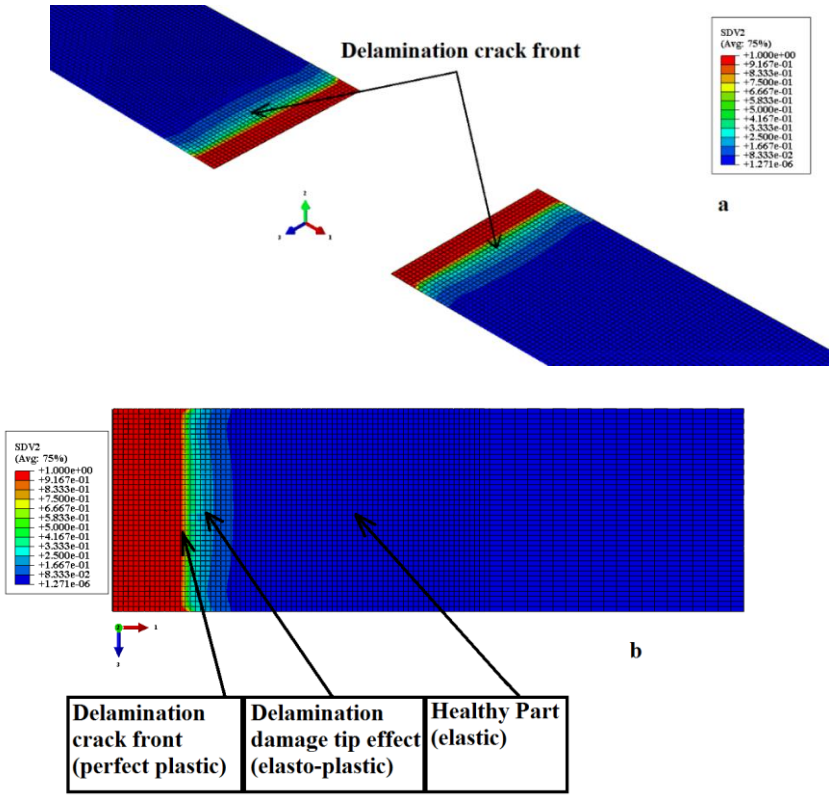

Figure 5-60 Plot of the damage variable SDV2, (a) damage in the cohesive elements (full model) at P=5 kN, (b) damage in the cohesive element in one of the cohesive sections at P=20 kN

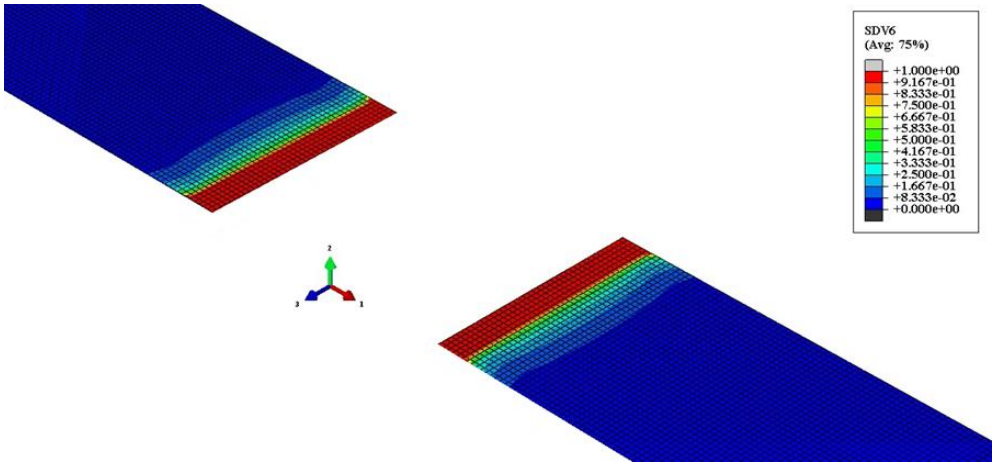

Figure 5-61 Plot of the damage variable SDV6

5.3.3: The effect of delamination through thickness μ ratio on stability of embedded delamination damage.

The location of the delamination crack in the thickness direction has influenced the fracture energy *G*, calculated from equation 3.75 and shown in Figure ***5-62***. In this case, the delamination damage Mode was perfectly Mode II delamination because no space for crack opening was possible. Critical delamination fracture energy G_C of WC/epoxy is equal to 1.05 mJ (KakeiEpaarachchiIslam, et al. 2016). When a delamination is closer to the surface of the composite specimen the highest fracture energy G/G_C ratio was recorded at the same applied tensile load level. Delamination damage propagates when the delamination fracture energy (G) is equal to Critical delamination fracture energy (G_c) or the delamination fracture energy (G/G_C) equal 1. Delamination propagation strain increases with increase in delamination location through thickness. As shown in the Figure ***5-63*** the strain at delamination crack tip is equal to 0.0065 (G/G_c=1) for μ equal to 0.1538 but the strain at delamination crack tip is equal to 0.044 (G/G_C=1) for μ equal to 0.875 as shown in Figure ***5-63***. But the fracture energy G/G_c ratio is equal to zero for μ equal to 1 because G is equal to zero for μ equal to 1 as provided in Elasto-plastic model. It can be inferred that the delamination tolerance depends on the delamination location through thickness μ ratio. The area under equal 1 could be considered as delamination crack tolerance region. G/G_C-strain curve shows in Figure ***5-63*** can suitably be used for design tolerance of composite structures.

The variation of delamination through thickness μ was examined under constant applied tensile loadings. Figure ***5-64***, Figure ***5-65***, Figure ***5-66***, and Figure ***5-67*** show the fracture energy *G/Gc* ratio produced by Mode II (shear force) as a function μ which was calculated using Elasto-plastic model. The Elasto-plastic model also predicts the decrease of fracture energy *G* with increasing μ. In addition the present method also confirms *G/Gc* equal to zero for μ equal to 1 for a symmetrical laminate configuration. This results agree with predictions by P.S. Valvo (Valvo 2016), while the other methods proposed in (Andrews & Massabò 2007; Liu et al. 2014; Zhigang & John 1990) predict $G>0$. In present method, it can be seen that high variations in G/G_C is recorded when the delamination crack was near the surface due to unsymmetrically delaminated laminate. Furthermore the delamination near surface does not necessarily follow internal delamination damage in the rest of the laminate composite. Near surface delamination represents a more difficult state than internal delamination (Bolotin 1996; Bolotin 2001). However, *G/Gc* ratio increases with increase in applied loading as a result of increase in strain in the specimens. With increasing μ the ratio decreased gradually due to increasing symmetrically delaminated laminate. As shown the highest G/G_C was recorded at highest applied loading (30kN) and this ratio equal to zero for μ, and was equal to 1 at all different applied tensile loadings. Depending on the observed results, it can be said that *G/Gc* applied loadings curve could suitably be used for designing the component of tensile loading for evaluating delamination point tolerance.

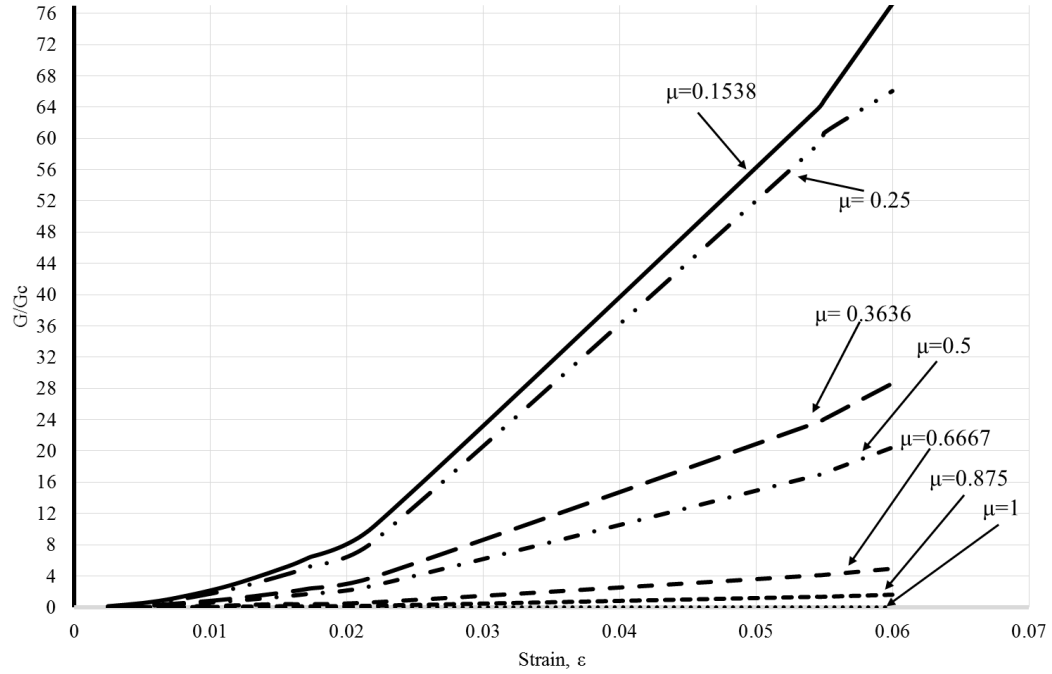

Figure 5-62 The effect of delamination depth on the *G/Gc* ratio with increasing tensile strains at different μ

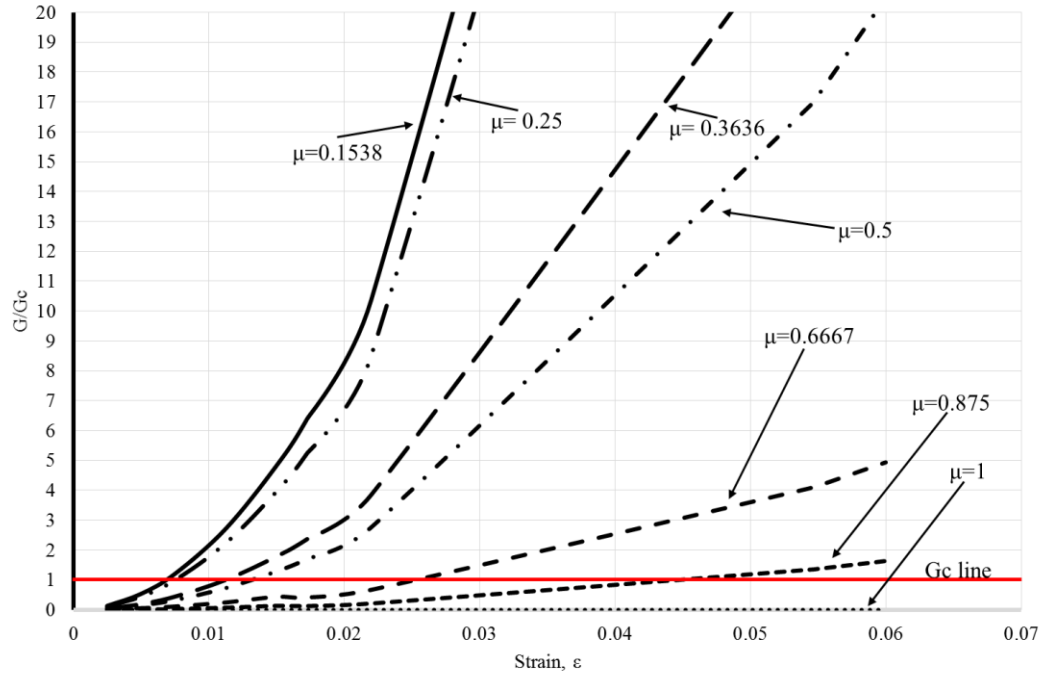

Figure 5-63 The examination of delamination stability with increasing depth of delamination location depending on the *G/Gc* ratio at different μ values

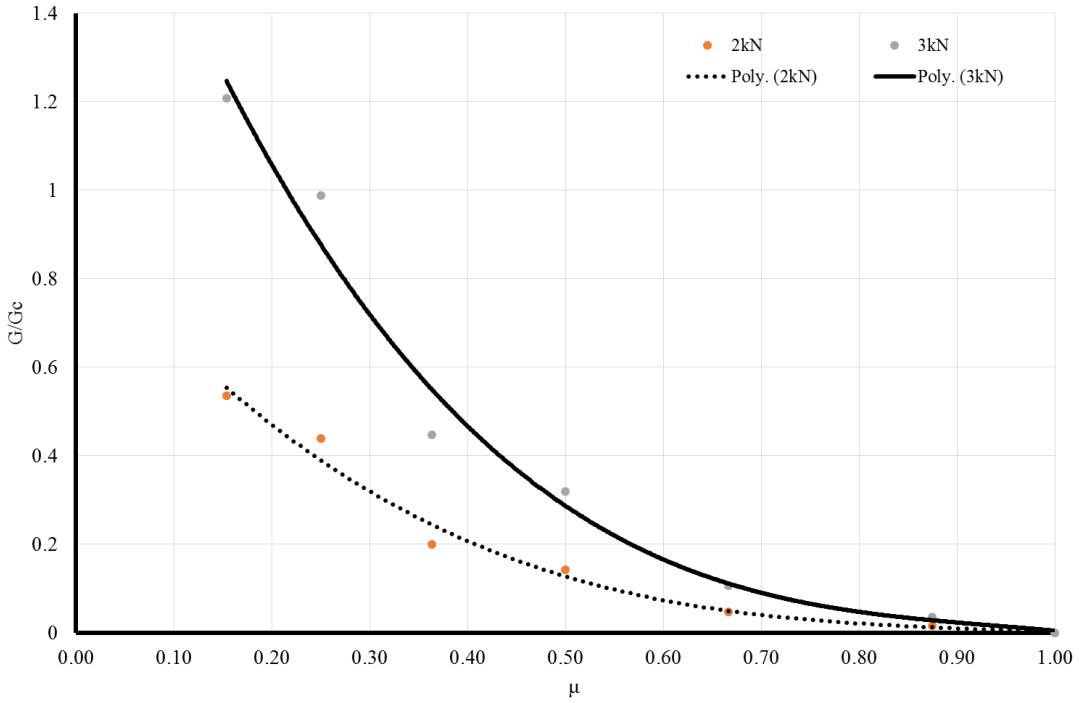

Figure 5-64 The variation of *G/Gc* ratio with increasing delamination through thickness μ for P=2kN and P=3kN

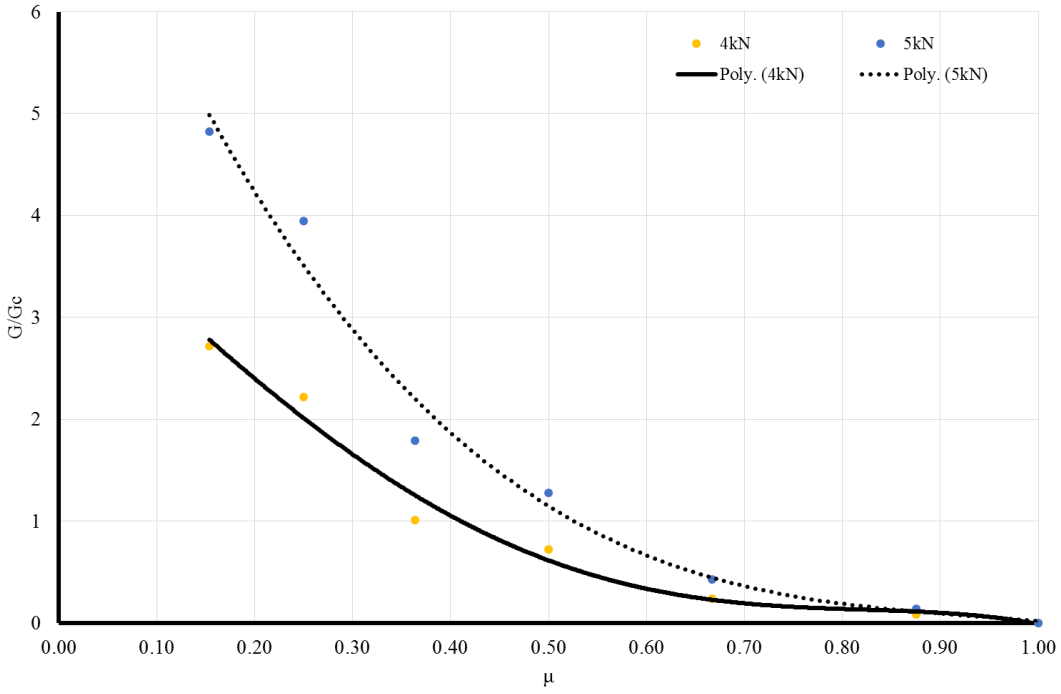

Figure 5-65 The variation of *G/Gc* ratio with increasing delamination through thickness μ for P=4kN and P=5kN

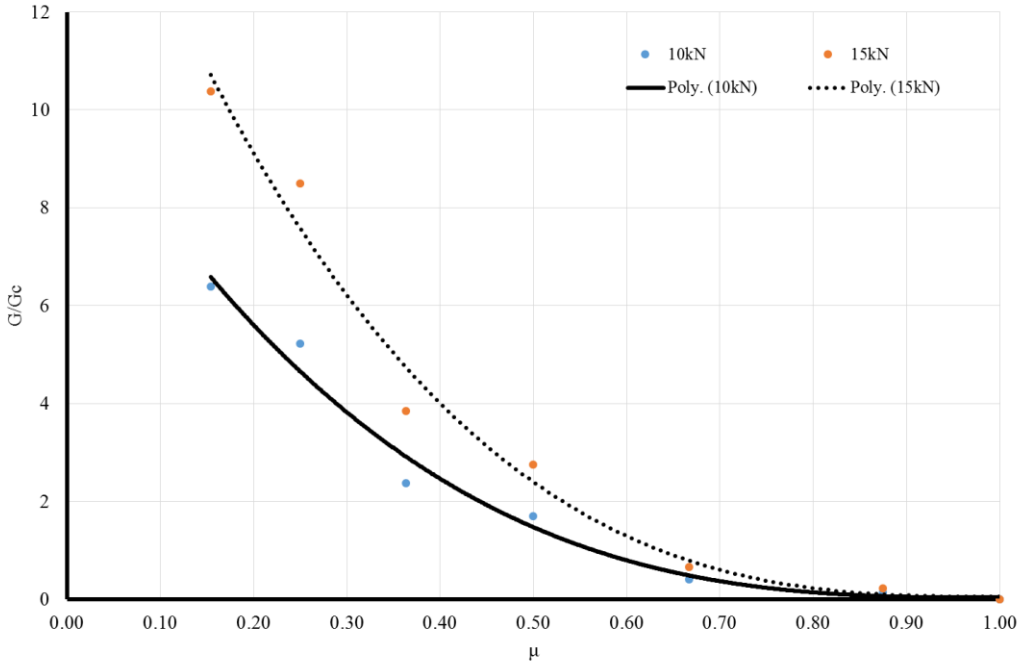

Figure 5-66 The variation of *G/Gc* ratio with increasing delamination through thickness μ for P=10kN and P=15kN

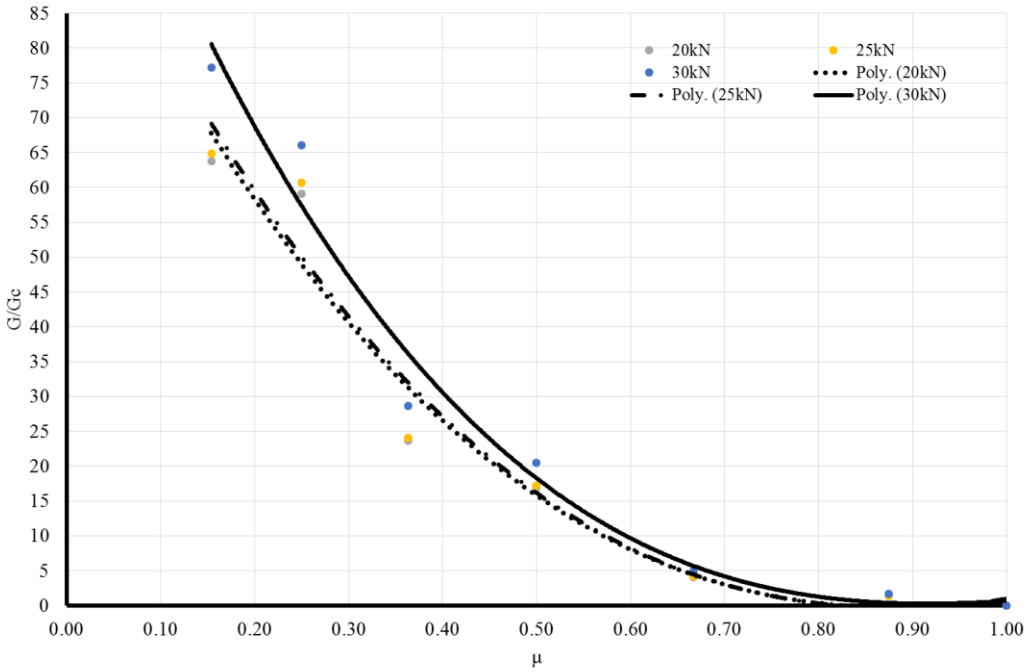

Figure 5-67 The variation of *G/Gc* ratio with increasing delamination through thickness μ for 20kN, P=25kN and P=30kN

As shown in Figure ***5-68*** the delamination through thickness μ has significant influence on the extension of delamination (Δ*a*). The extension of the delamination (Δ*a*) decreased with increasing μ. As a result delamination resistance damage for

WC/epoxy specimens was impacted. Here plot of *G* versus crack length shows a characteristic R-curve behaviour for delaminated specimens. The fracture energy *G* increases with crack length as shown in Figure ***5-69***. The reason for the increased resistance to delamination crack is the development of the damage zone around the crack tip (Briscoe, Court & Williams 1993; Briscoe & Williams 1993; Kessler & White 2001). As shown in Figure ***5-69***, the R-curve behaviour decreases with increasing delamination through thickness μ because the damage zone around the crack tip decrease. Delamination resistance depends on delamination through thickness μ. In Figure ***5-69*** the delamination resistance was examined for different μ ratios at 15 kN maximum applied loadings. The results show that the Elasto-plastic model provided accurate result for evaluating delamination damage resistance for different delamination through thicknesses μ under tensile loading.

According to FBG sensor spectrum responses some elasto-plastic occurred in the matrix of the specimens due to delamination damage. Then the behaviour of elasto-plastic should be considered. FBG elasto-plastic damage sensing response was examined using cohesive element and SDV2. Some change of SDV2 value can be seen at FBG sensor region even the delamination damage tip is far away from the FBG sensor region as shown in Figure ***5-70***. Detecting of elasto-plastic region in front of delamination crack gives excellent opportunity to evaluate damage stability.

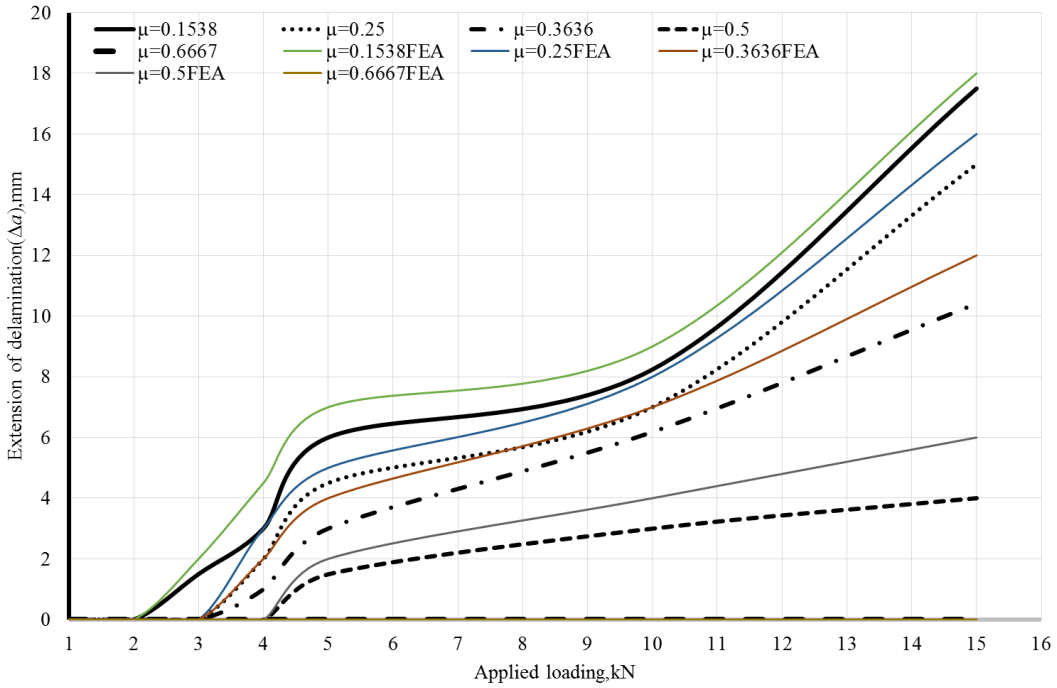

Figure 5-68 Extension of delamination (Δa)-Applied loading (black lines are experimental results (TSA results), and coloured lines are finite element results (SDV2) for WC/epoxy specimens. Maximum applied loading is equal to 15kN

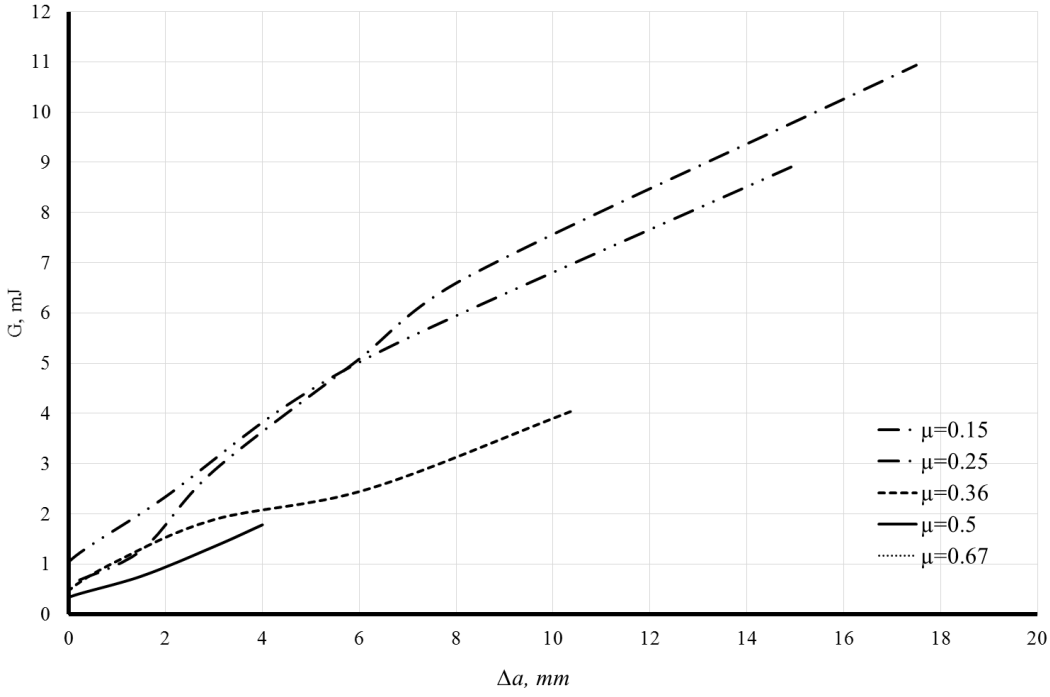

Figure 5-69 The effect of delamination depth on delamination resistance (R-curve) of WC/epoxy composite specimens under tensile loading. Maximum loading P=15kN

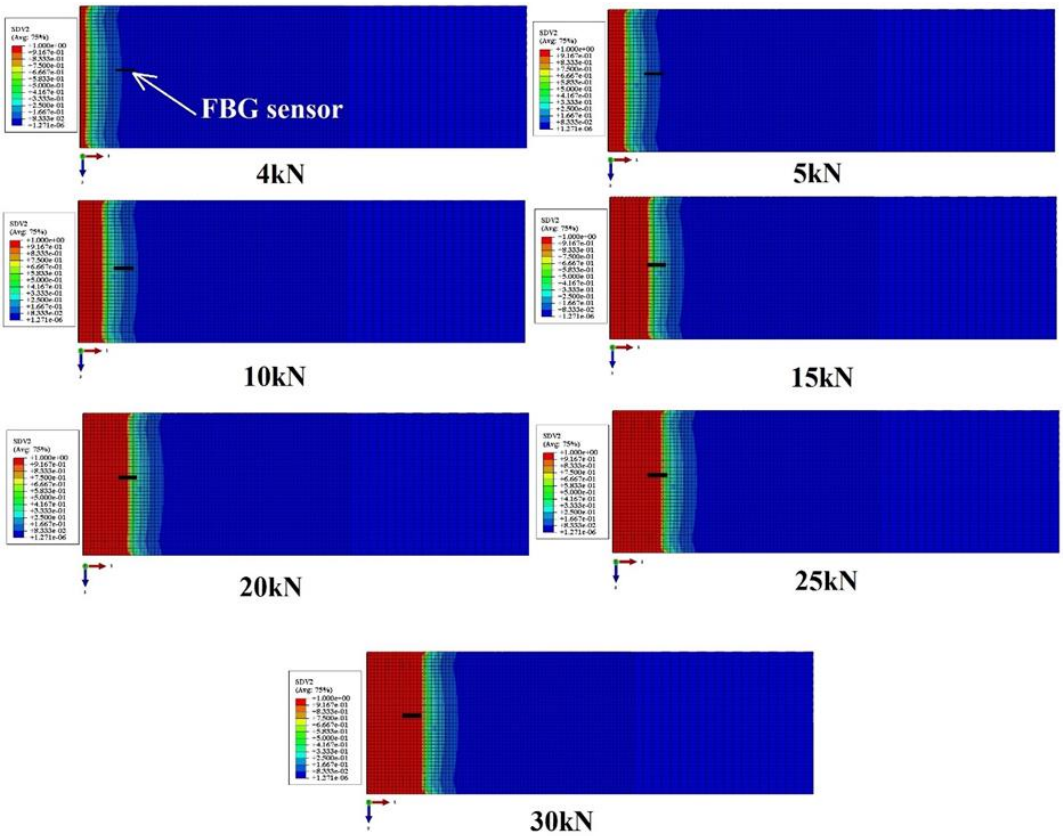

Figure 5-70 Delamination damage propagation (SDV2) in cohesive element and it is effect on the FBG sensor senses (corresponding with Figures 6.25 and 17), μ=0.363

5.4: Mixed Mode I/II delamination damage (Uni-Axial load damage) case study

5.4.1.1: Delamination damage monitoring using FBG sensor

As shown in section 4.4.4, 5 mm length FBG sensor was embedded. The tensile load was applied to the end of CLS delamination to exam the delamination propagation. Figure ***5-71*** shows the spectra on FBG moved to the right gradually due to applied tensile strain. This spectrum of FBG sensor was uniform. The measured strain by FBG sensor values were equal to the strain measured from strain gauges, fixed at the surface of CLS specimens as shown in Figure ***5-72***.

As shown in Figure ***5-72***, A and C specimens strain increases gradually with increase in applied loading. In these group tests, the delamination damage crack tip did not reach underneath of FBG sensor location. As result the embedded FBG sensor and strain gauge strain had the same values. On the other hand at group B, embedded FBG sensor increased dramatically at 15 KN applied loadings because

the delamination damage crack tip reached underneath of FBG sensor location. This caused non-uniform strain at the delamination crack tip. This effect also causes distortion of FBG sensor spectra.

Changes to spectra of embedded FBG sensor shape (length and width) occurs due to sensing by FBG senor at delamination crack tip. The sensing of delamination depends on delamination distance from the embedded FBG sensor location. As shown in Figure ***5-73***, the spectrum of embedded FBG senor was uniform before 15 kN applied loading. After that loading it gets distorted. Some increase in embedded FBG strain can be seen between 10 and 15 kN. This increase in strain values may be due to sensing of delamination crack tip. The delamination crack tip causes an elasto-plastic region in front. This phenomenon can be compared with TSA technique.

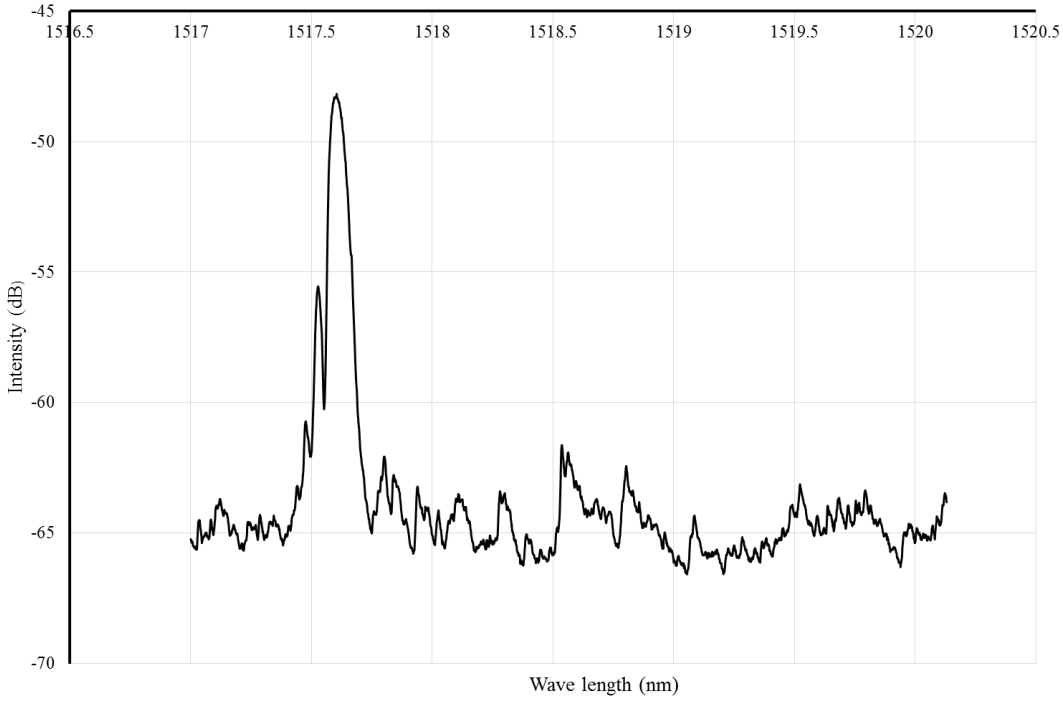

Figure 5-71 Spectra of embedded 5mm FBG sensor in glass fibre reinforced composite CLS specimen

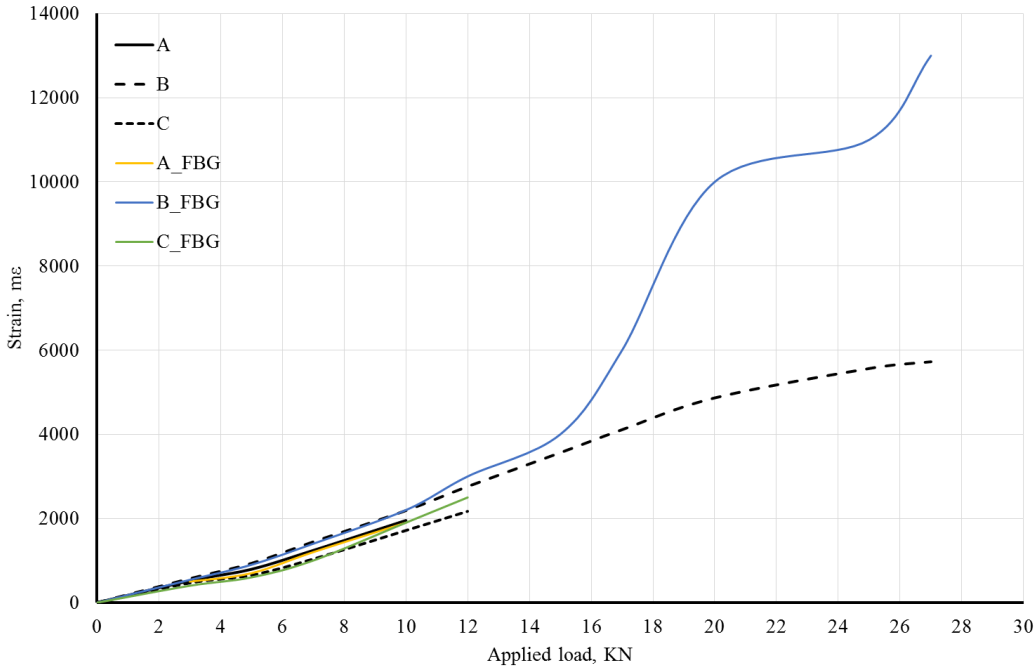

Figure 5-72 Strain values that measured from strain gauges and embedded FBG sensor in CLS specimen under mixed Mode delamination test

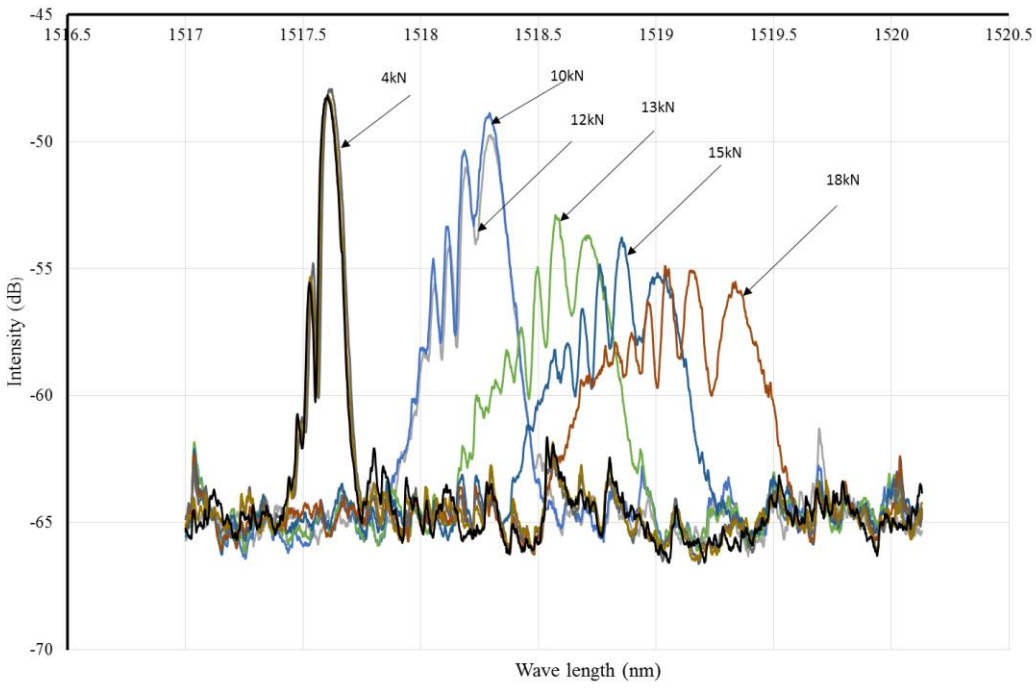

Figure 5-73 Spectra of embedded 5mm FBG sensor in glass fibre reinforced composite CLS specimen under different applied tensile loads

5.4.2: Delamination damage monitoring using TSA technique

TSA technique was used to evaluate the tip of delamination damage crack. This technique has been applied on three groups. Green colour is the tip of delamination

crack. Figure ***5-74*** shows the thermoelastic phase response of the CLS specimen measured during cyclic loading of the sample. The variations in colour correspond to variation in the phase of the thermoelastic response relative to the load, with the largest variations in phase occurring near the bottom end of the delamination zone. The delamination crack tip is shown by the green colour in frame (a) to (j). As the mean load is increased this green moves, and reaches a maximum at the final mean load (broken loading at g). On the other hand the tip of delamination crack in groups A and C is not clear due to the depth of delamination crack as shown in Figure ***5-75*** and Figure ***5-76***. The resin between layers works as an isolated layers and prevents TSA signal. The delamination damage can be seen in both groups but the delamination crack tip cannot be recognized as much as in group B.

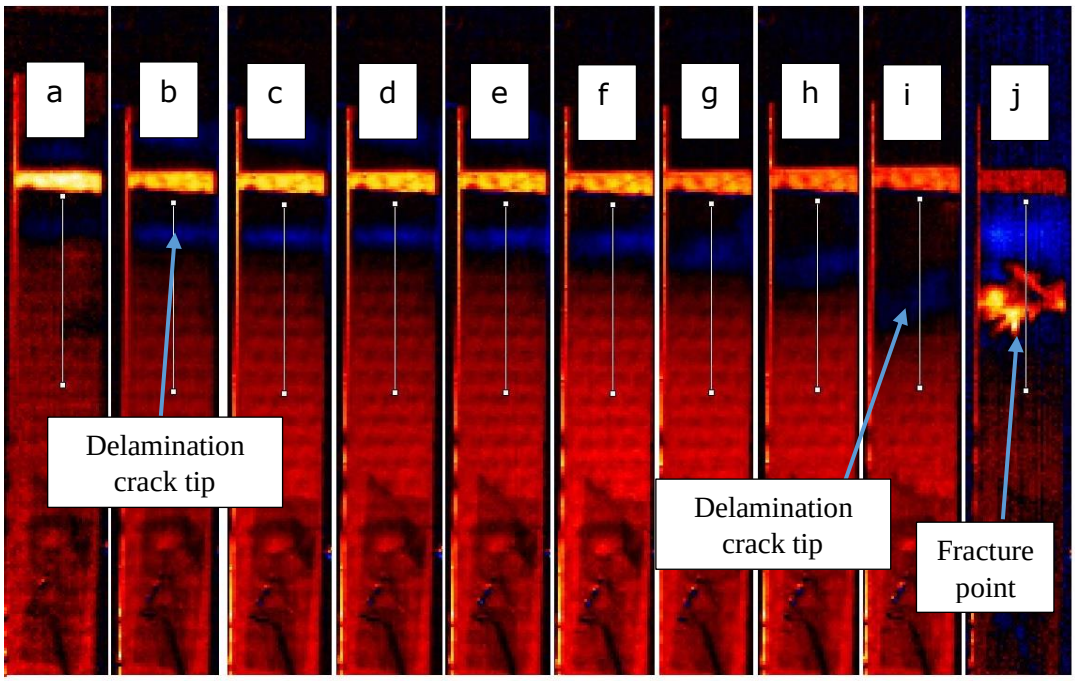

Figure 5-74 Delamination crack front propagation (θ-component). Red dotted line outlines the boundary of the initial delamination. Delamination zone is seen to increase as a function of mean load (Group B)

The quadrature component of the thermoelastic response signal, which is driven by heat conduction and it is therefore quite sensitive to stress gradients, was examined along the centre line of the specimen through the delamination as shown in Figure ***5-74***, Figure ***5-75*** and Figure ***5-76***. The tip of the delamination is seen to correspond to an increasingly positive quadrature signal. The magnitude of this signal and the area it envelops increases with increasing mean load for all group specimens. An

estimate of the delamination crack length was extracted from the quadrature signal by measuring the distance between the extremities of the peaks circled in Figure ***5-75***, Figure ***5-76*** and Figure ***5-77***. The results show that the delamination damage size was constant while it was moving or developing. As shown the quadrature component of thermoelastic response signal can detect movement of embedded delamination crack.

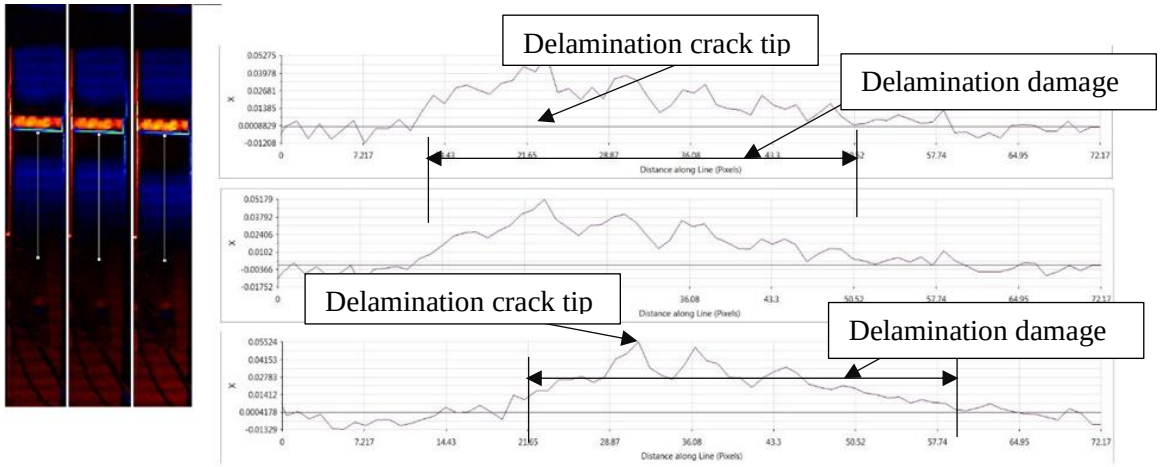

Figure 5-75 Delamination crack front propagation (θ-component). Red dotted line outlines the boundary of the initial delamination. Delamination zone is seen to increase as a function of mean load (Group A)

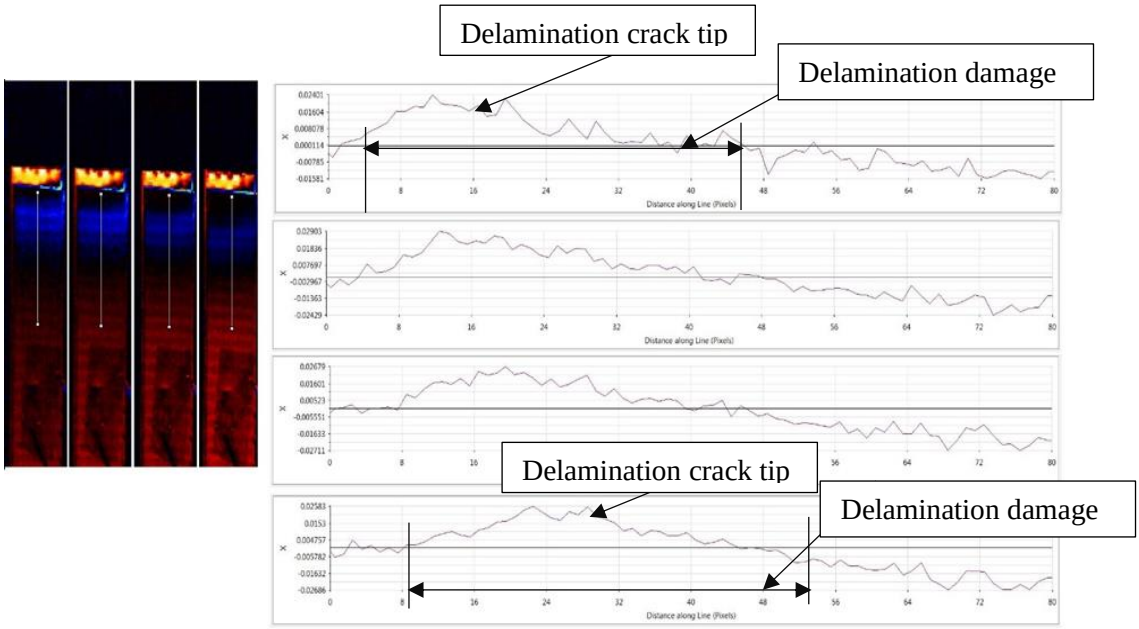

Figure 5-76 Delamination crack front propagation (θ-component). Red dotted line outlines the boundary of the initial delamination. Delamination zone is seen to increase as a function of mean load (Group C)

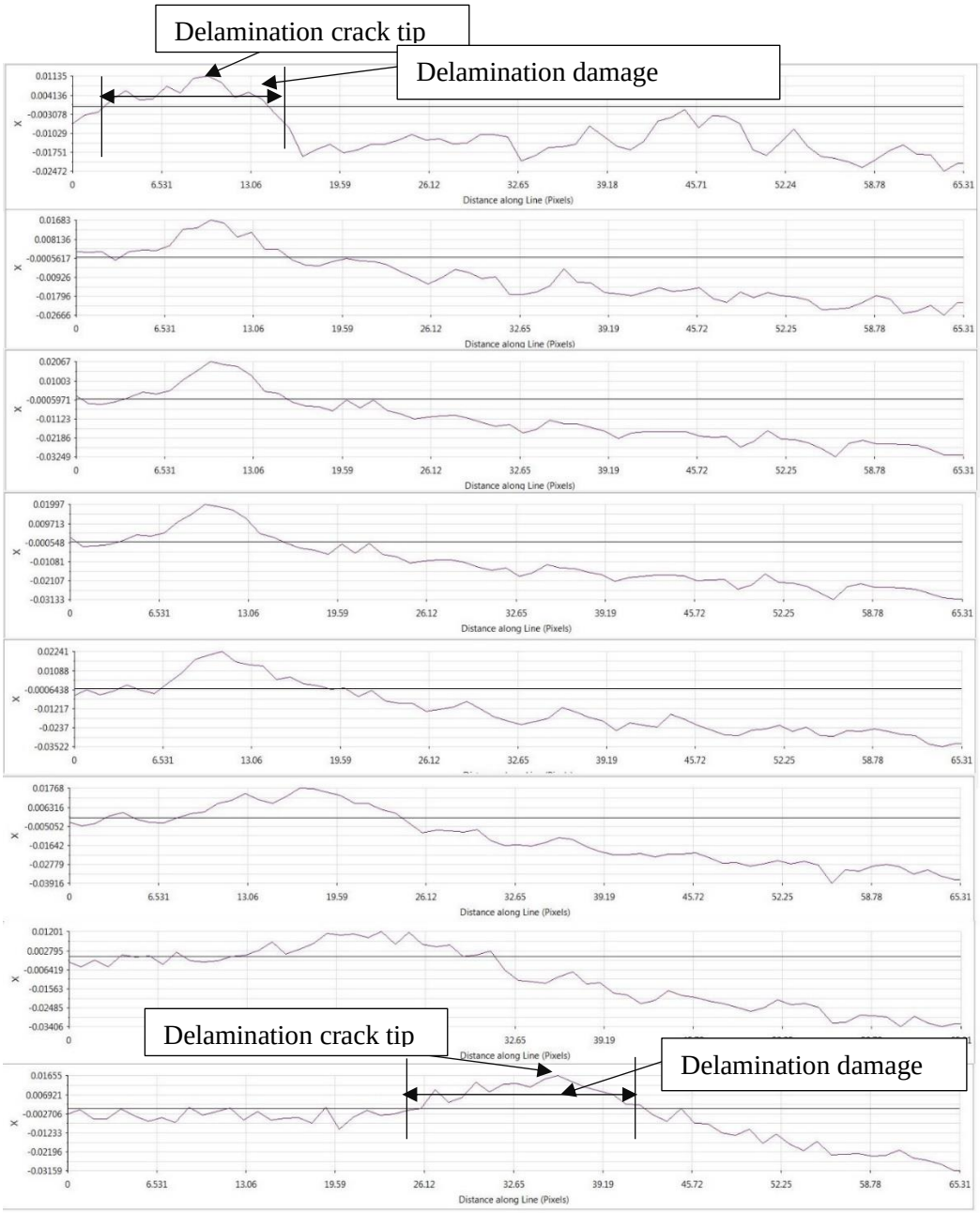

Figure 5-77 Delamination crack front propagation (θ-component). Red dotted line outlines the boundary of the initial delamination. Delamination zone is seen to increase as a function of mean load (Group B)

5.4.3: Evaluation of matrix thickness effect on the TSA signal in laminated composite specimen

The effect of matrix (resin) thickness on the TSA signal has been examined. CLS specimens were used with different location for the embedded delamination crack in the thickness as shown in Table ***5-5***. As shown in Figure ***5-75***, Figure ***5-76***, and Figure ***5-77***, the delamination through thickness has a significant influence on the reliability of TSA signal. The opening of delamination crack in three groups was almost same as shown in Figure ***5-78***, therefore the change of TSA signal in

different groups was due to the matrix thickness. It is assumed that the matrix or resin between the laminated composite works as an isolated layer. Figure ***5-79*** shows the average size of delamination crack. Group B shows the smallest delamination crack size because the lap thickness in Group B was smaller than other groups. On the same hand, an examination for the effect of lap thickness on the delamination crack size, captured by TSA techniques is shown in Figure ***5-80***. Figure ***5-81*** shows the error in TSA signal due to increase in lap thickness. As shown the error in TSA signal decreases with decreasing lap thickness. Therefore it can be assumed using TSA technique that the increase in delamination crack size with increase in lap thickness was due to increase in TSA signal dispersion in the matrix (epoxy) layers.

Table 5-5 Dimensions of CLS specimens

specimens	**Width (mm)**	**Strap (mm)**	**Lap (mm)**	**Thickness (mm)**	**Initial delamination a_0 (mm)**
A	25	2.5	6.5	9	8
C	25	4	5	9	7
B	25	6	4	10	8
All Samples have length equal to 300mm					

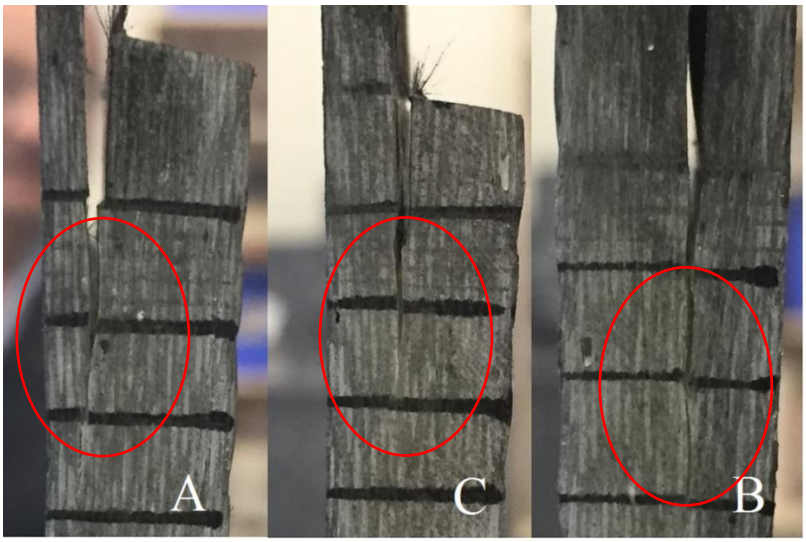

Figure 5-78 Delamination crack in three groups of CLS specimens

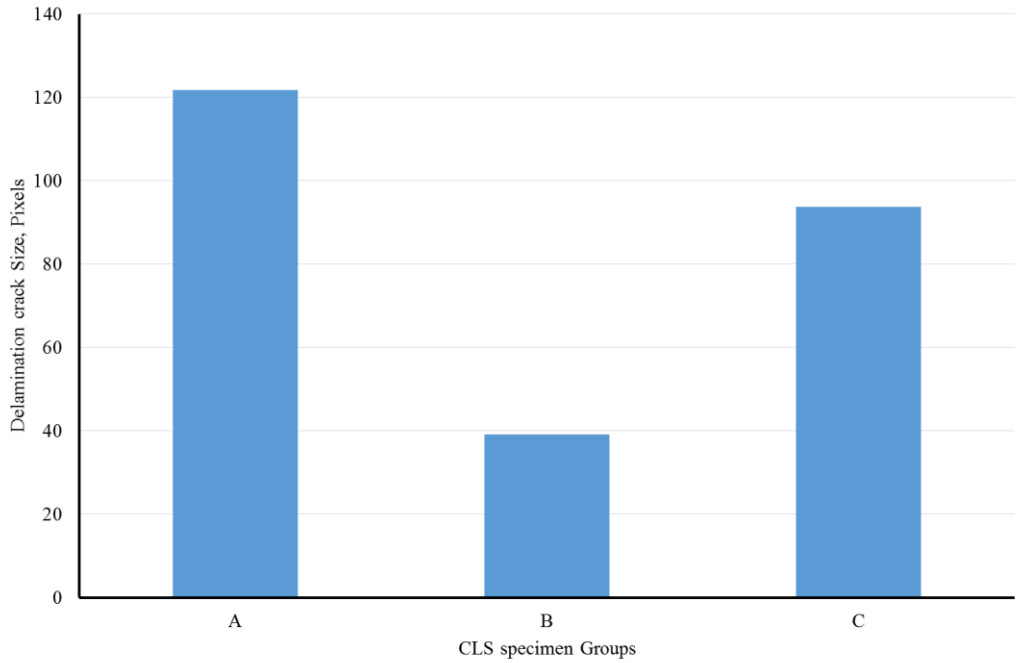

Figure 5-79 Delamination crack size (Pixels) for three CLS groups, corresponding with Figures 5-75 to 5-77

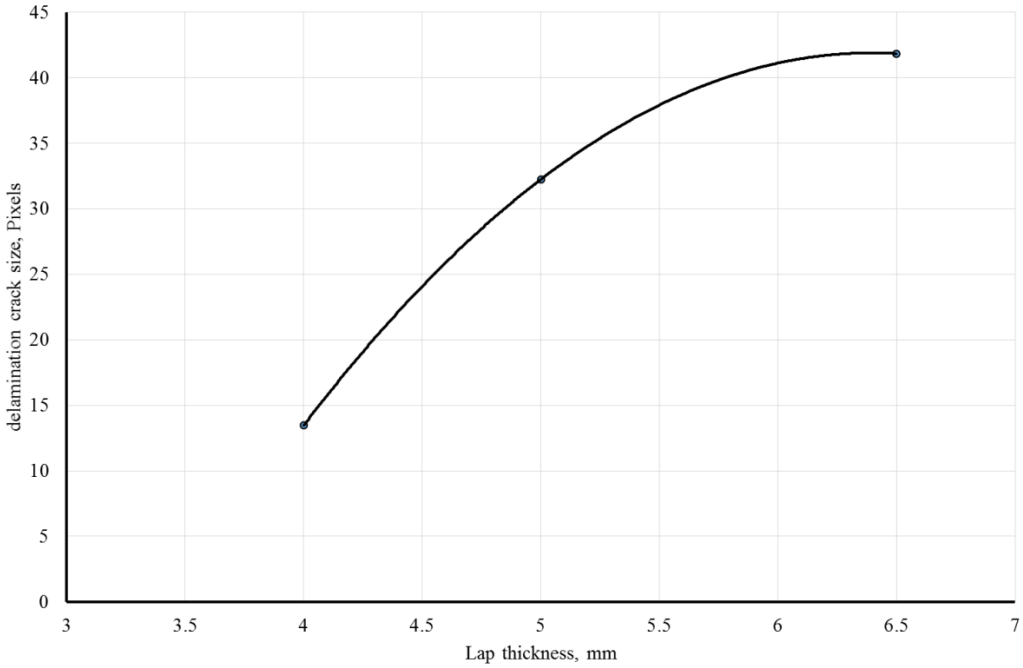

Figure 5-80 The effect of matrix thickness on the TSA signal

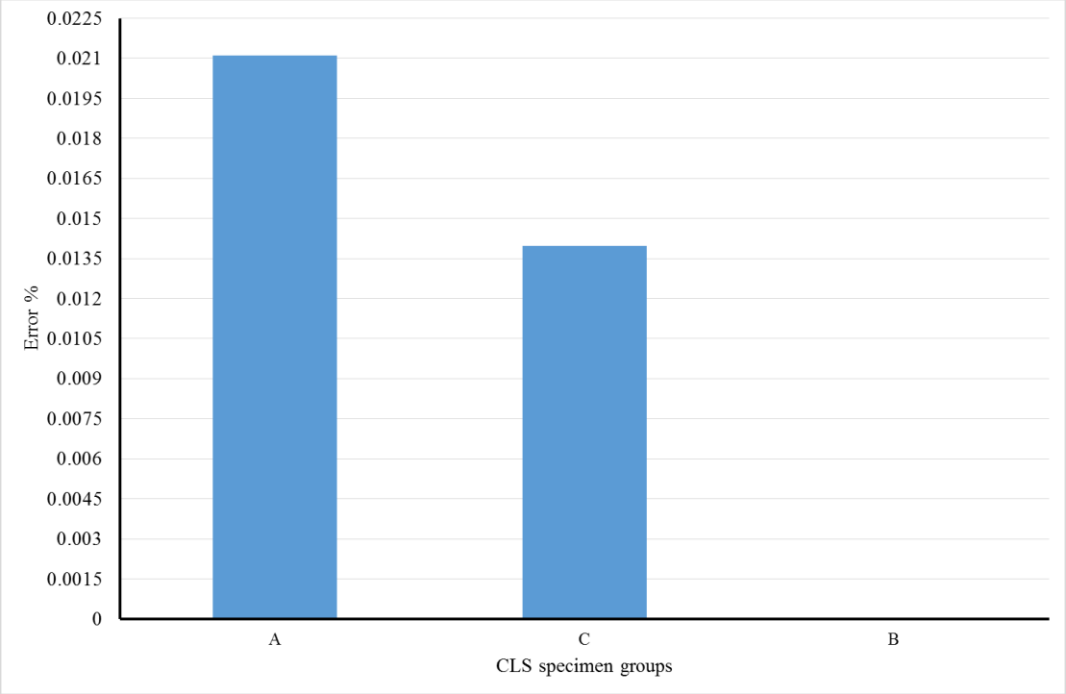

Figure 5-81 Error of TSA signal due to thickness of matrix based on group B lap thickness (4mm)

5.4.4: Evaluation of elasto-plastic region and crack propagation

The fracture energy $G_{I/II}$ as a function of delamination crack propagation has been evaluated using equation 3.66 and FBG strain readings. As shown in Figure ***5-82***, the delamination crack propagates smoothly till the crack reaches near FBG sensor location. Once the crack reaches underneath FBG sensor location the Fracture energy (G) increased dramatically due to non-uniform strain at delamination crack tip. The fracture energy (G) was calculated after delamination crack was extended to 10 mm because the FBG sensor was embedded about 10-12 mm away from the purposely created delamination crack. Figure ***5-83*** shows the effect of delamination crack tip on the embedded FBG sensor reading. Elasto-plastic model (equation 3.66) shows a limitation. The limitation has been shown in Figure ***5-83***. The acceptable result are shown as Region I after extension of delamination crack to 10mm. Region II is unacceptable due to effect of non-uniform strain of delamination crack tip, which influenced the FBG sensor reading.

Equation 3.66 (Elasto-plastic model) has been compared with two classic theories. Figure ***5-84*** shows R-curve was calculated for mixed Mode delamination damage. One of theory was presented by Johnson (Johnson 1987) (see Appendix D). The propagation of delamination crack was calculated from three equations provides

similar results. But the Elasto-plastic model provides more information for evaluating elasto-plastic region in front of delamination crack that cannot be evaluated by using classic models.

An estimate of delamination crack stability can be established using G_T/G_{TC} ratio and the strain measured with embedded FBG sensor. This estimate is presented in Figure ***5-85***. The G_T/G_{TC} ratio increases linearly when the ratio is less than one, however the curve increases sharply when the ratio is greater than one. The elasto-plastic can be seen clearly and equal to about 2mm.

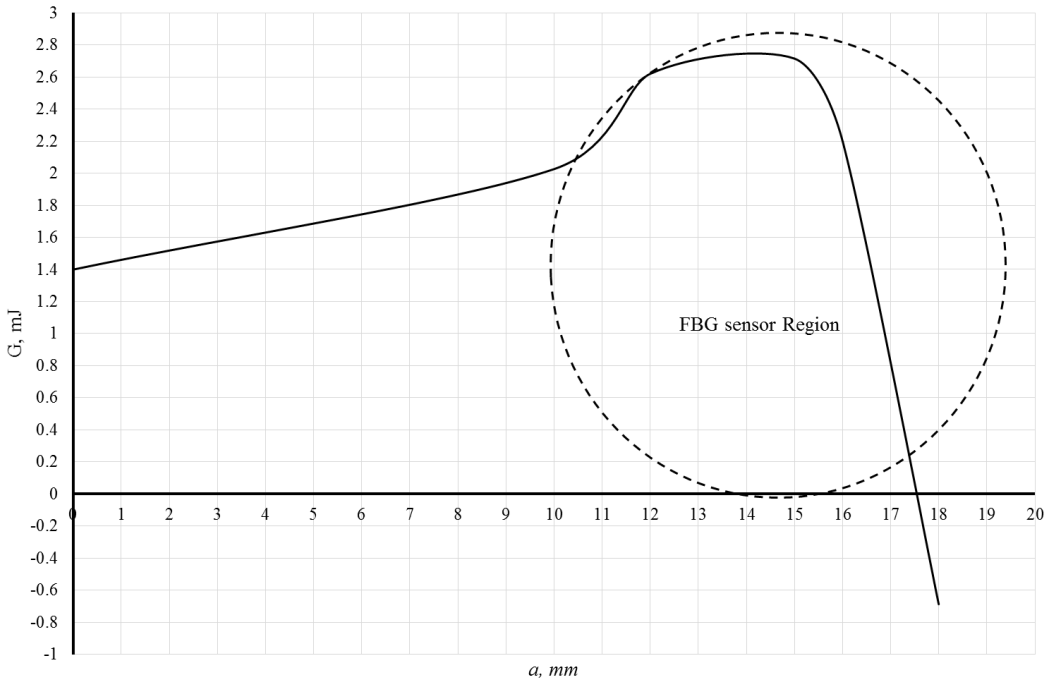

Figure 5-82 Relationship between propagation delamination crack and increasing of fracture energy use Elasto-plastic model

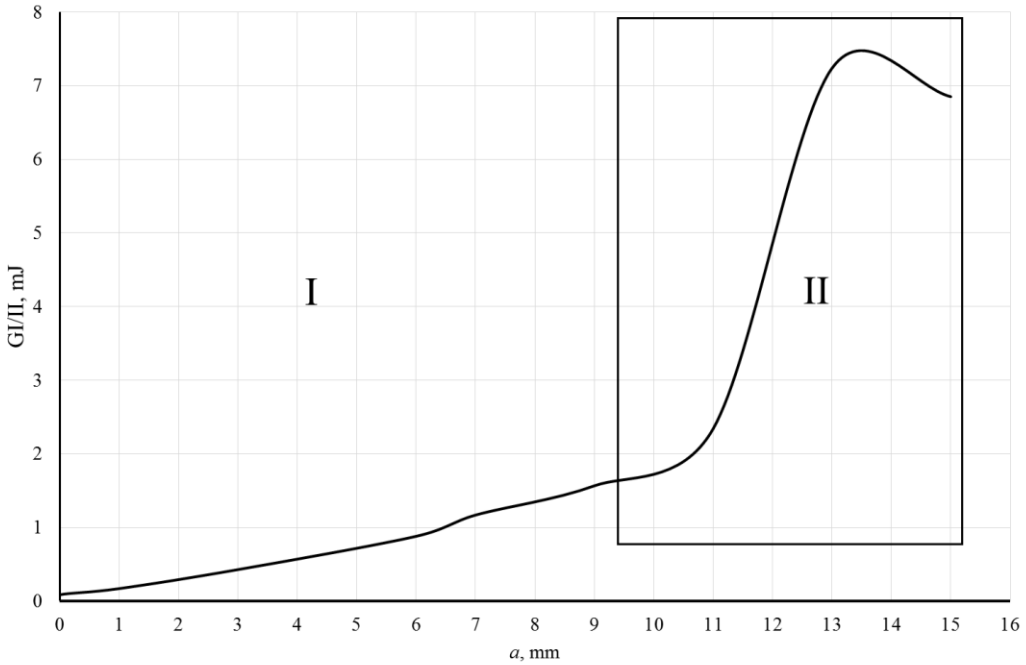

Figure 5-83 The effect of non-uniform strain at delamination crack tip on the FBG sensor reading use Elasto-plastic model

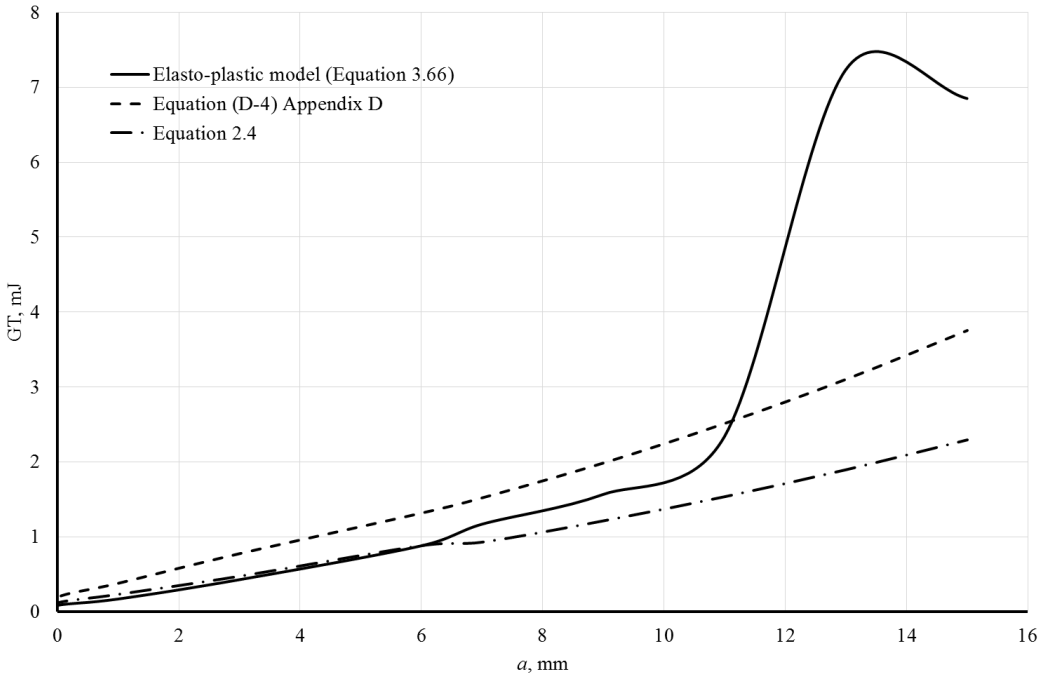

Figure 5-84 R-curve calculation use different theories

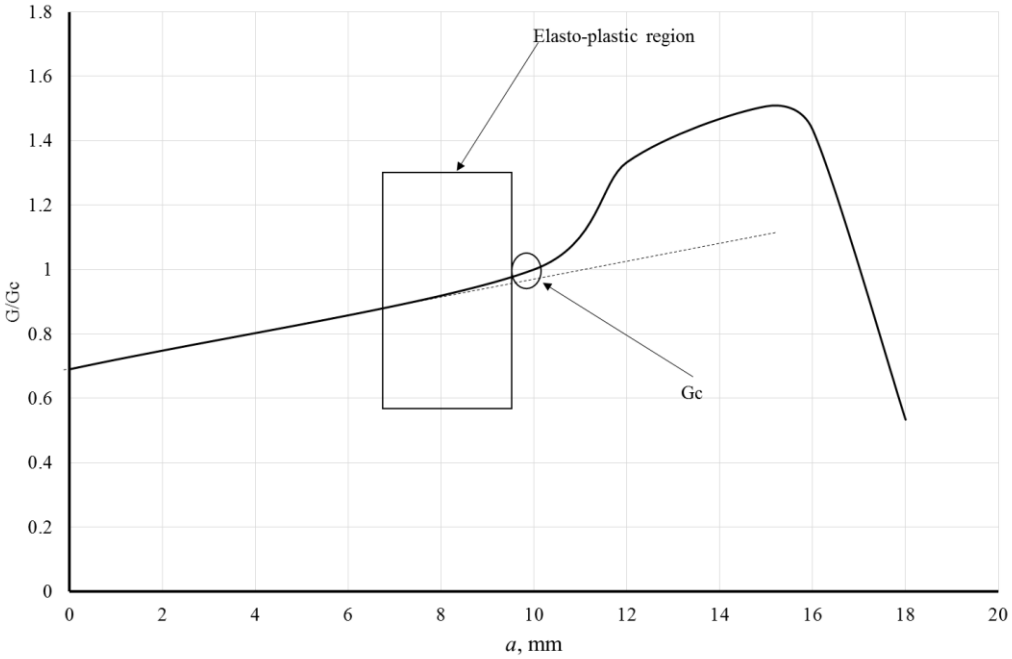

Figure 5-85 Crack stability and elasto-plastic examination (use Elasto-plastic model)

ABAQUS solution dependent state variables, SDV2 and SDV6, are displayed in Figure ***5-86*** and Figure ***5-87*** respectively. State variable SDV2 represents the failure index at each integration point. It is a continuous variable that can have a value between 0 and 1. A value of 0 indicates there are no stresses at the integration point. A value of 1 indicates that the failure initiation criterion has been satisfied and the process of damage evolution (stiffness reduction) has begun at the integration point. Another useful state variable is SDV6, which is referred to as the damage variable D. SDV6 is a continuous variable with a value between 0 and 1 where a value of 0 corresponds to an undamaged integration point that has its original (full) stiffness, and a value of 1 corresponds to a fully degraded (zero stiffness) integration point.

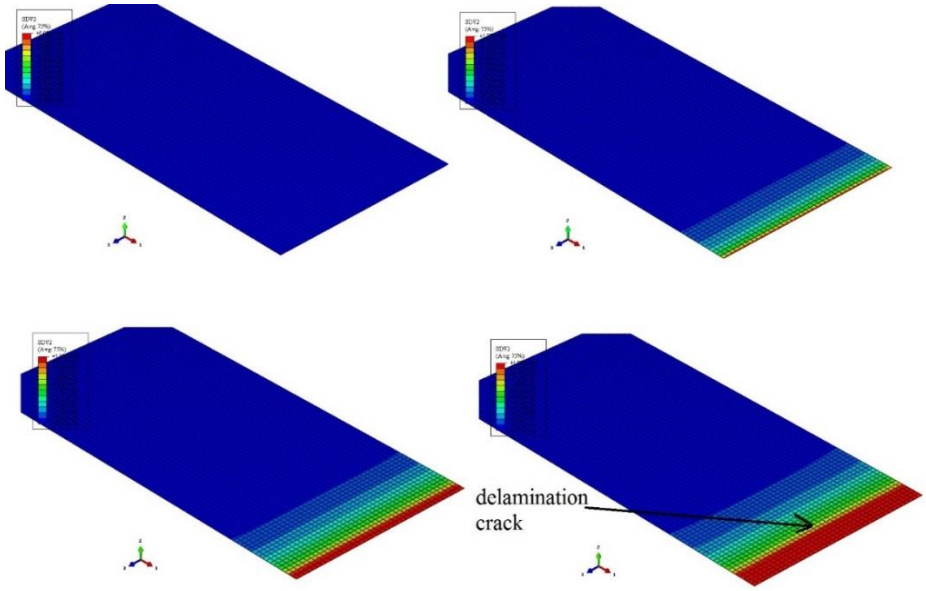

Figure 5-86 Plot of the damage variable SDV2 in cohesive element with increasing loading

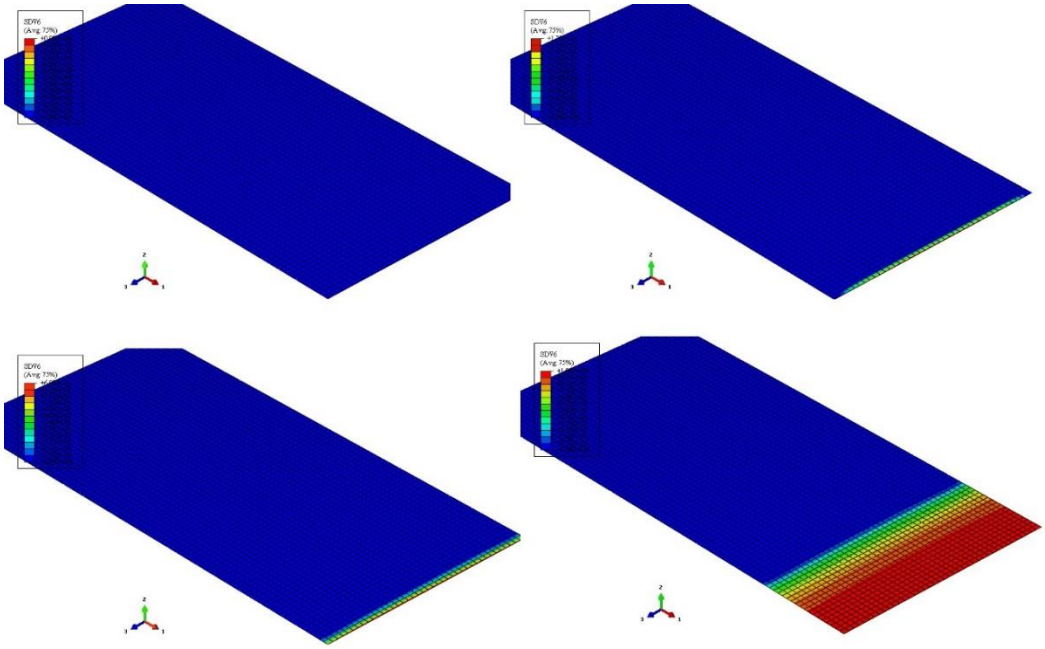

Figure 5-87 Plot of the damage variable SDV6 in cohesive element with increasing loading

5.5: Calculation of stress field around delamination crack

Due to non-uniform strain at the tip of delamination crack, embedded FGB sensor in the plane of delamination crack provides excellent opportunity to calculate stress

at delamination damage crack. The stress field around delamination crack in orthotropic material has been evaluated use Equation 3.8. The strain energy release rate (G) has been calculated use FBG sensor and elastoplastic theory. In this work just $\theta=0$ has been discussed due to laminated behaviour. The fibre behaves as isolated material for stress signal that comes from delamination crack tip. Equation 3.8 can provide stress field around delamination crack. But this equation cannot provide exact stress at the tip of delamination. Interpolation has been used to calculate the stress at delamination crack tip ($r=0$) to overcome the limitations of the theory. As shown in Figure ***5-88*** the stress at the delamination tip equal to 13.679Mpa in Mode I test, and equal to17.935 Mpa in Mode II test, shown in Figure ***5-89***. The development of delamination crack under axial tensile loading has been studied too. The stress field around delamination crack has been evaluated as shown in Figure ***5-90***. As shown the stress at the tip of delamination crack in Mode II is bigger than Mode I because in Mode I the crack opens up and it is easy to develop delamination crack. In Mode II delamination crack develops due to the sliding of two face of crack (shear stress). The study of axial force shows high value due to uniform tensile loading and it is not easy to develop delamination crack.

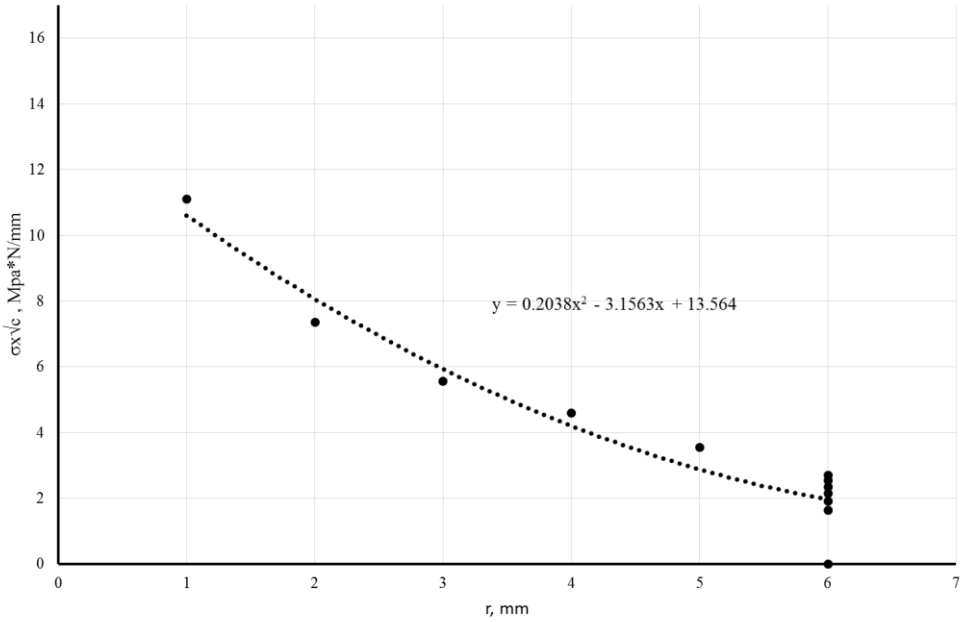

Figure 5-88 Stress field around delamination crack experimentally in Mode I (DCB) test

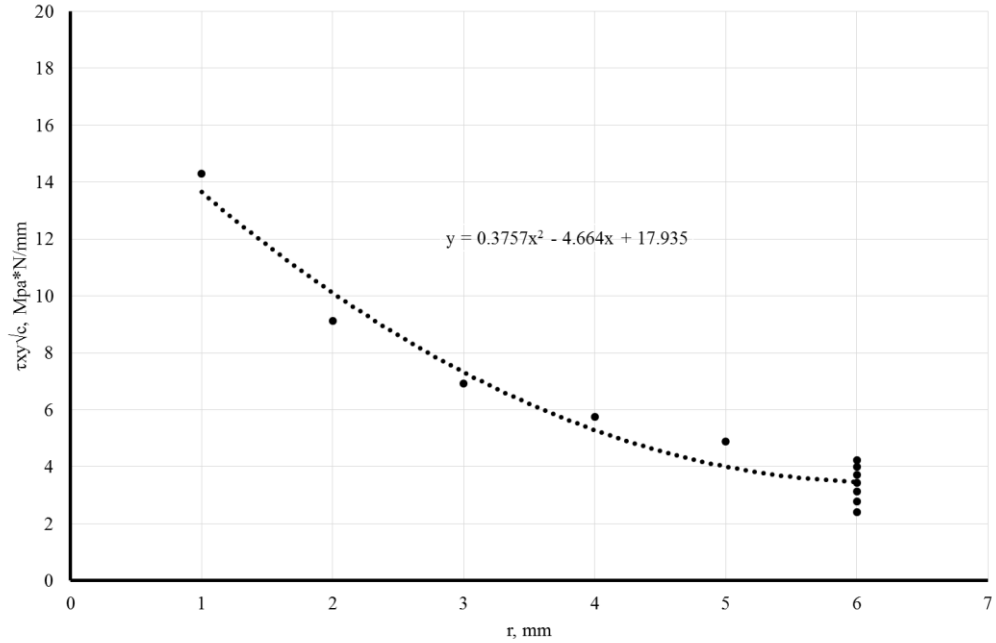

Figure 5-89 Stress field around delamination crack experimentally in Mode II (ENF) test

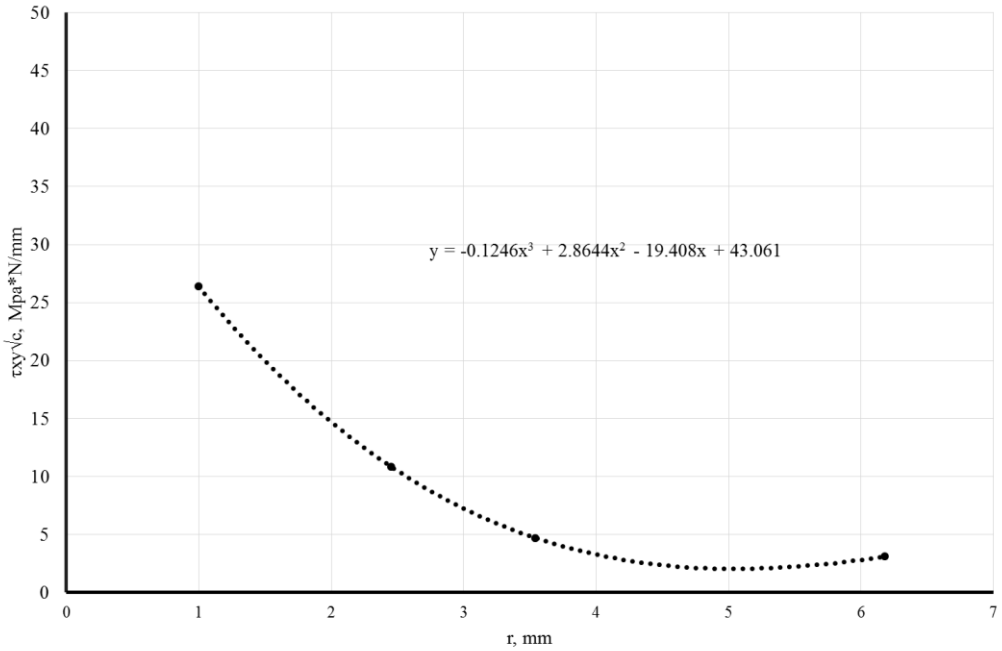

Figure 5-90 Stress field around delamination crack experimentally in Mode II axial tensile loading

5.6: Stress concentration in laminated composite structure due to crack and inclusion

In this section, the Tsukrov and Kachanov model (Tsukrov & Kachanov 2000) has been extended to evaluate the effects of embedded crack and inclusion on the

stiffness and stress in the laminated composite. This model discusses the effects of crack and inclusion in orthotropic media. Here in this work the crack and inclusion have been assumed as elliptical holes. Many basic Matlab codes were built for proving this assumption (see Appendix C). A Matlab code has been built to calculate H tensor (Equation E-13)

After applying Matlab code, the effect of crack in orthotropic media on the H tensor is shown in Figure ***5-91***. As shown the angle φ of embedded damage had a significant effect on the H tensor due to orthotropic behaviour of laminated composite materials

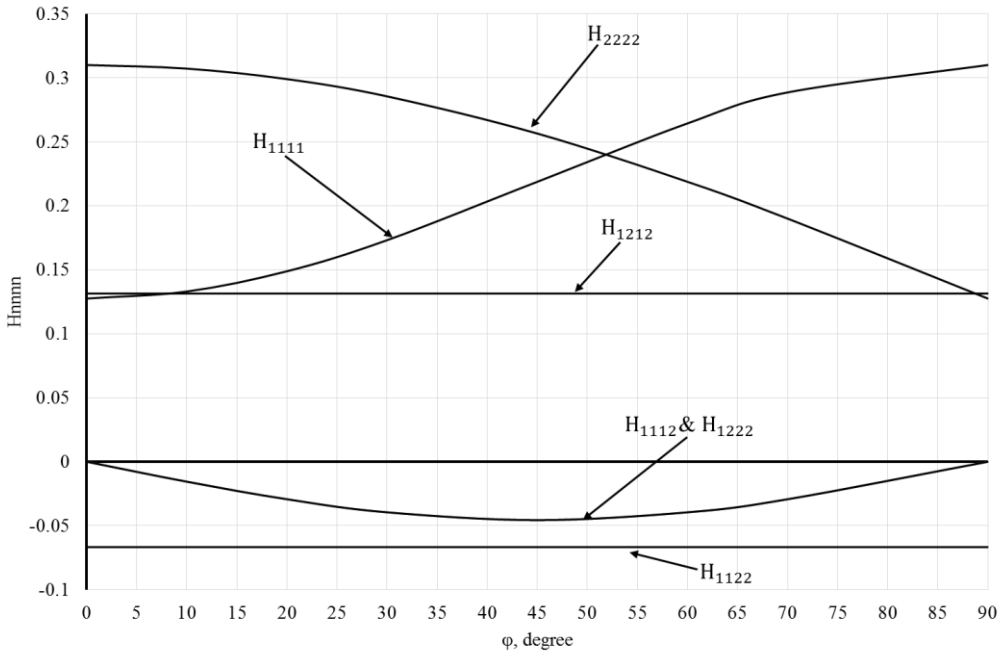

Figure 5-91 The effect of elliptical hole in the orthotropic matric in different angles

The effect of embedded elliptical hole in the laminated composite has been evaluated. A Matlab code has been established to calculate the mechanical properties of laminated composite with embedded crack as shown in Appendix E. Figure ***5-92***, Figure ***5-93*** and Figure ***5-94*** show the effect of embedded hole on the mechanical properties (E_x, E_y, G_{xy}, *and* v_{xy}). The embedded crack causes decrease in mechanical properties of laminated composite (Equation 3.82). The angle of embedded crack has significant effect on mechanical properties of laminated composite. These reductions in mechanical properties were examined for the GFR composite specimens under axial tensile loading case. The delamination

investigation requires high technique Structural Health Monitoring such as embedded FBG sensor and thermos-elastic stress analysis.

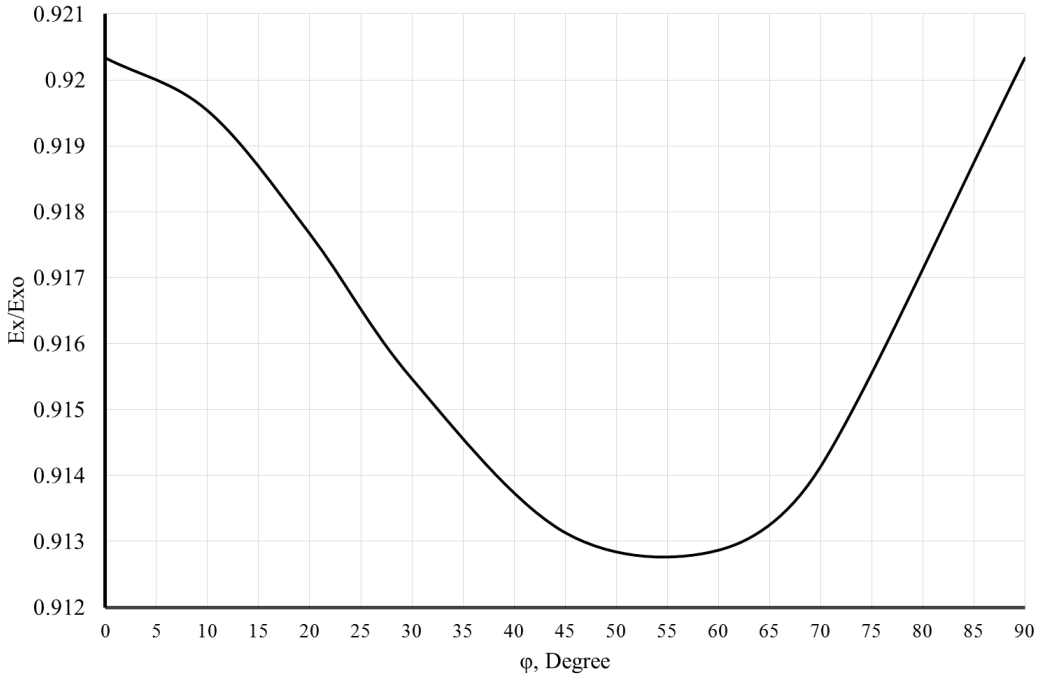

Figure 5-92 The effect of embedded crack on the axial Young modulus in laminated composite

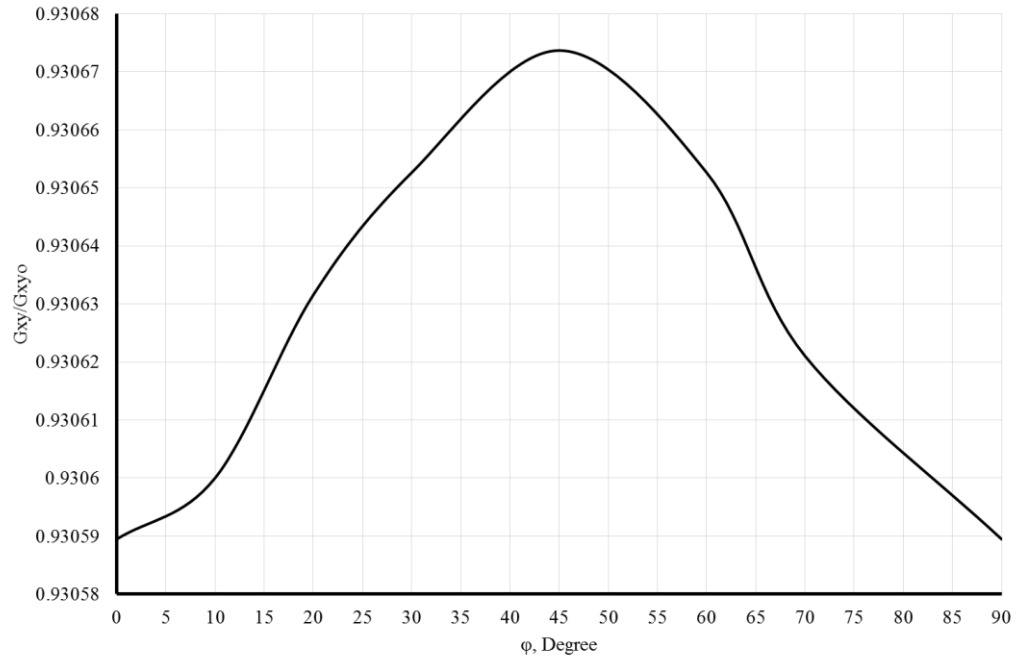

Figure 5-93 The effect of embedded crack on the shear modulus in laminated composite

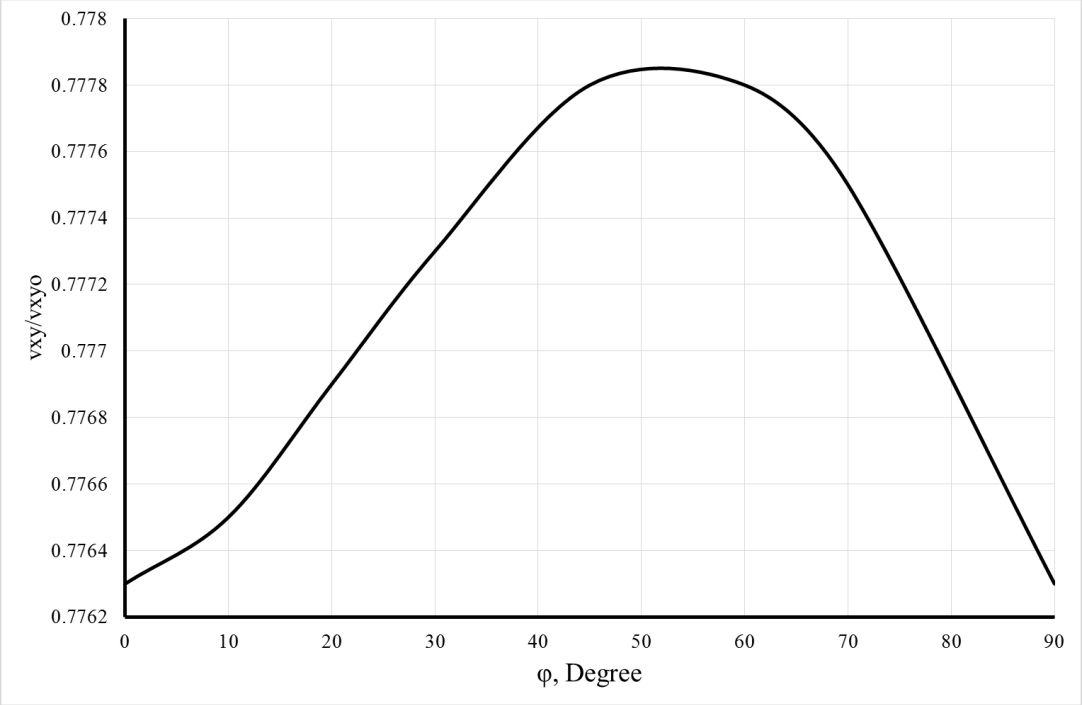

Figure 5-94 The effect of embedded crack on the Poisson's ration laminated composite

5.7: Calculation of stress variation due to elliptical delamination crack in laminated composite material using extended Tsukrov and Kachanov model

As shown the delamination crack has a significant effect on the elastic properties of laminated composite materials. To calculate the variation stress due to elliptical inclusion, a Matlab code has been built. The Matlab code can calculate $\sigma_{x,}\sigma_y$ and τ_{xy} as shown Appendix E. As shown in Figure ***5-95***, Figure ***5-97*** and Figure ***5-99***, the effect of the embedded damage can be clearly seen. Mode II delamination propagation under axial tensile loading case has been selected to compare the data from Figure ***5-45*** "tip of crack' and the data from this section. The strain has been calculated with embedded FBG sensor. The shear stress at the lamina has embedment damage higher as compared to other laminas as shown in Figure ***5-95***. The damage at 90^o lamina causes increase in shear stress. On the other hand the shear stress at the 0^o increases but it is smaller than from 90^o lamina. This phenomenon is due to orientation of fibre. Figure ***5-96*** shows the shear stress variation at the healthy laminated composite structure. As shown the embedment damage causes a dramatic increase of shear stress at the composite specimen. In addition, the embedded damage causes change in axial stress (σ_x) and transverse

stress (σ_y). As shown in Figure ***5-98*** and Figure ***5-100*** the stresses are uniform but when the lamina has embedded damages the stresses change. This code can be expanded to evaluate and calculate the stress variation at lamina by using a network of FBG sensor to detect delamination or any other damage.

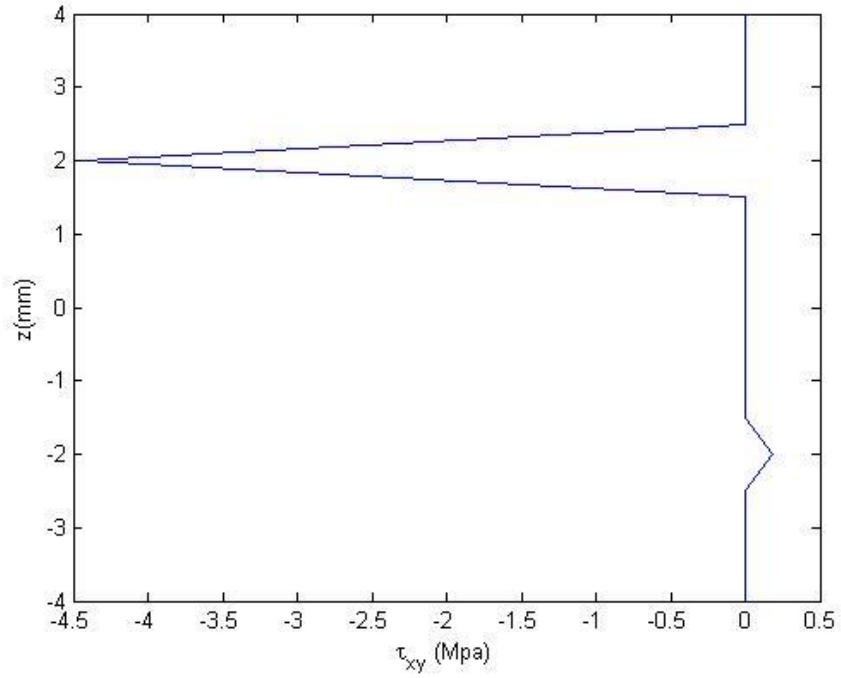

Figure 5-95 The effect of embedded delamination damage on the shear stress in laminated composite materials

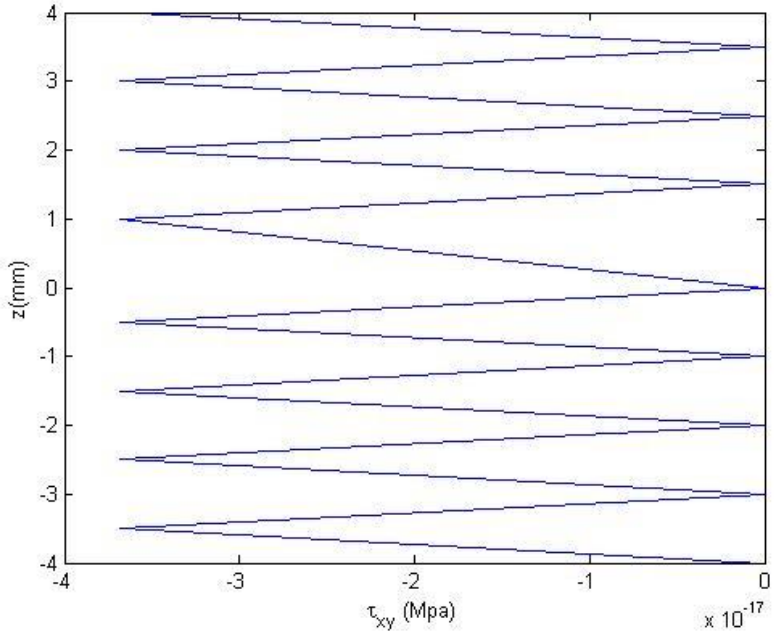

Figure 5-96 Shear stress at the laminated composite material (No damage)

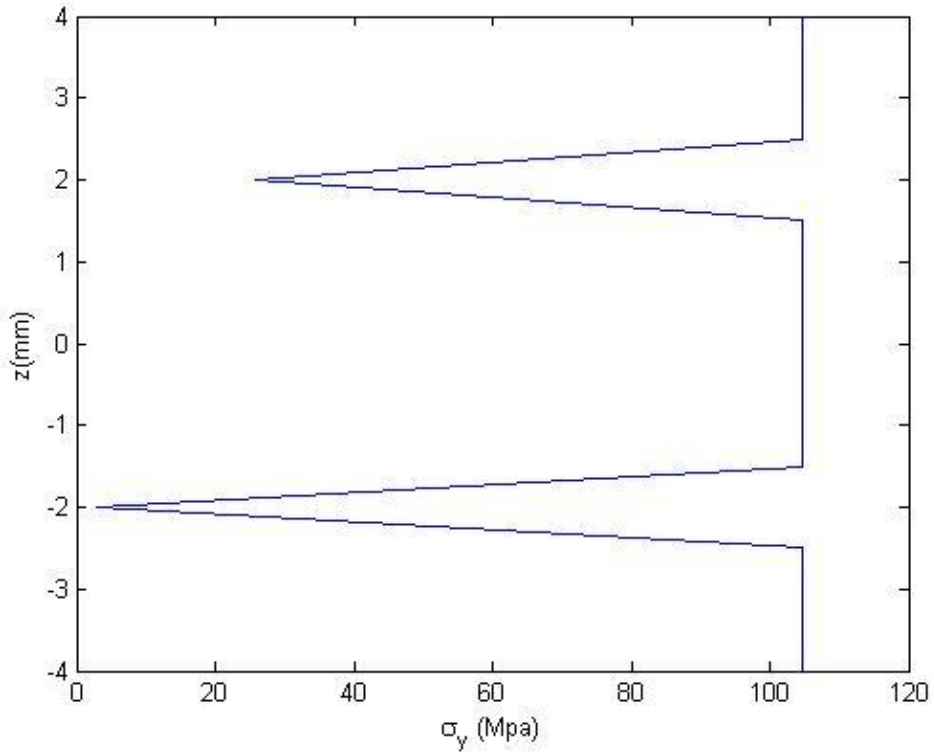

Figure 5-97 The effect of embedded delamination damage on the axial stress in laminated composite material

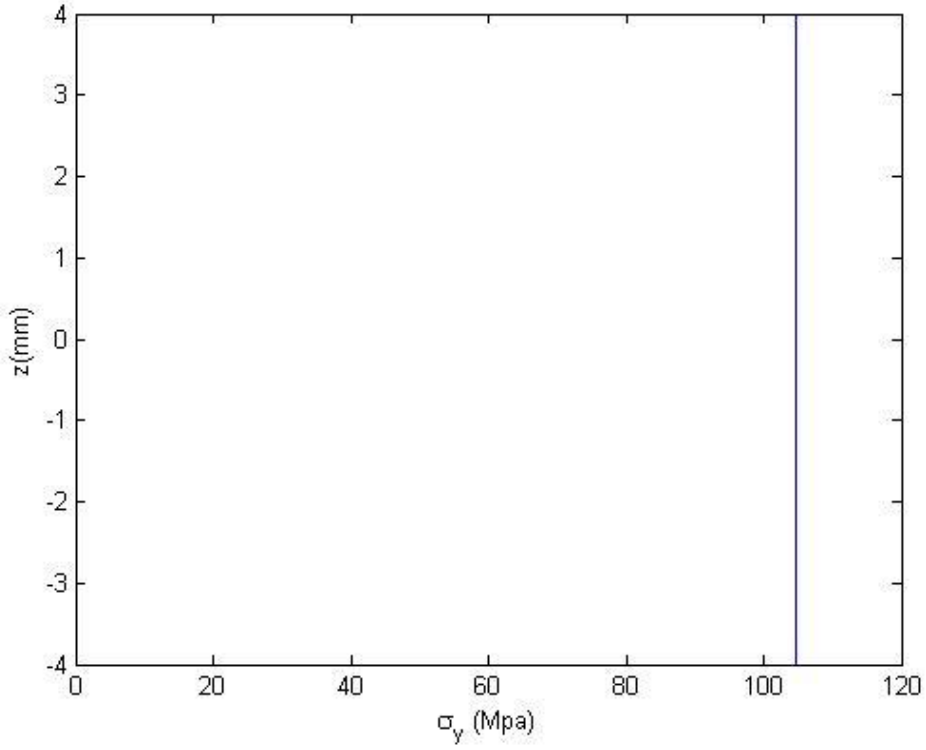

Figure 5-98 Axial stress in laminated composite material (No damage)

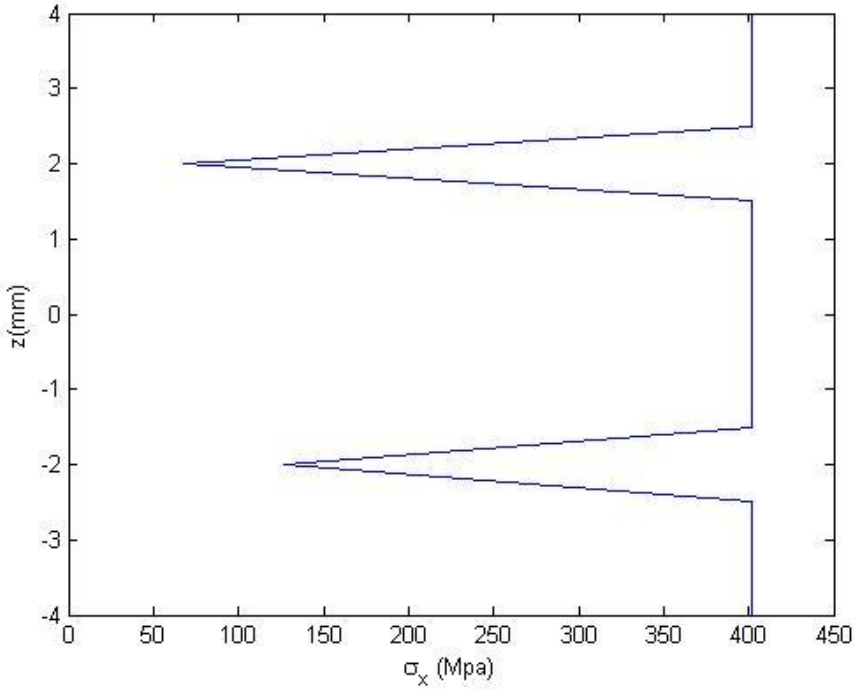

Figure 5-99 The effect of embedded delamination damage on the transverse stress

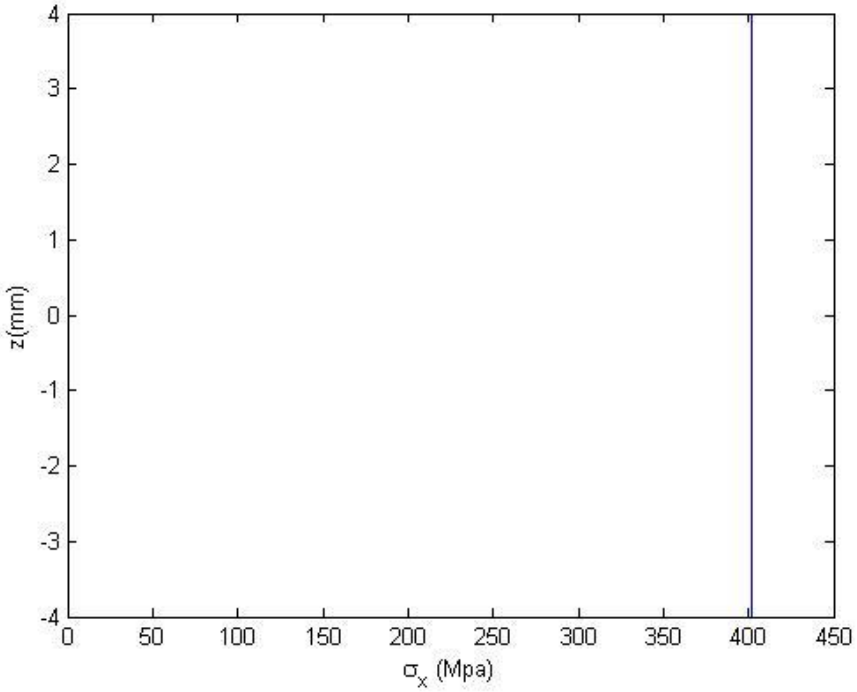

Figure 5-100 Transverse stress in laminated composite material (No damage)

5.8: Summary

Elasto-plastic model has been proposed for estimating delamination damage in laminated composite materials. This model is based on elasto-plastic damage behaviour observations, of an epoxy interface layer in laminated composite materials. Within this model, delamination damage onset prediction is based on the embedded FBG sensor readings. The proposed model was applied on WC/epoxy laminated composite specimens to predict delamination onset and propagation of different delamination damage Modes. The model was applied on Mode I delamination damage. The prediction/results are found to be quite accurate. The proposed Model can also estimate the resistance of delamination crack (R-curve) in woven laminated composite materials. However, the values are slightly different to that estimated using ASTM D5528 standard procedures. The achieved G_{Ic} values were in good agreement with the values estimated with ASTM D5528 standard for all selected laminated composite specimens. Again, the proposed model showed good agreement with ASTM D5528 standard for unidirectional laminated composite materials but slight variations to R-curve values for woven laminated composite specimens. The difference between the two Model is that ASTM D5528 standard procedure was developed from ideal isotropic cantilever beam which may not suitable for calculating R-curve of Woven laminated composite materials. Moreover the ASTM D5528 ignored the effect of woven yarns, orthotropic conditions and damage jumping in woven laminated composite specimens. ENF test was selected for predicting delamination onset and propagation of Mode II. The proposed Model provided G_{IIc} value close to CBT and CCM methods. The main advantage of proposed Model is that it does not need any correction factors. This feature is not seen in other methods. The effect of the factors is visible in DBT method. The proposed Model can easily evaluate the onset delamination damage in Mixed I/II Mode delamination. The proposed Model shows good correlations with two different classical Models. The initiation delamination crack has been evaluated from R-curve, because the initiation of delamination crack cannot be evaluated with classical methods. Another limitation is that, the classical Models cannot evaluate R-curve but the proposed Model has the capability to do so. The advanced feature of proposed Model over classical Models is that it has considered

the internal damage mechanism and elasto-plastic damage by integrating Elasto-plastic model and FBG sensor.

The stress at the delamination crack was evaluated reliant on the embedded FBG sensor strain. Due to the non-uniform strain at the crack tip, the FBG snore cannot calculate the strain at the tip of the crack. As shown the proposed theory (equation 3.8) could not calculate the stress at the crack tip, therefore an interpolations were used to calculate the stress at the tip. Stress calculation at the tip of delamination crack will help to use the accurate damage stress behaviour or cohesive damage stress behaviour value. The proposed model was extended to investigate the effect of embedded damage in GFRP on increasing stress at laminate of composite due to embedded damage under axial tensile loading. The delamination damage in that case is pure Mode II delamination damage because no opening of the tip of delamination crack were detected. The damage extended due to the shear stress around the crack or sliding two faces of the crack. The shear stress at the damaged lamina has increased clearly. In addition some changing of the axial stress (σ_x) and transvers stress (σ_y) has been detected due to embedded damage. It can be concluded that the proposed model detect the damage at the sub-laminate and evaluate the stress at the tip of delamination crack.

This evaluation was extended to investigate the behaviour of delamination through the thickness $\boldsymbol{\mu}$ (h_1/h_2). It has been shown that the applied loading and distance through the thickness has significant influence on the stability of delamination damage extension. At high level of loading the delamination damage showed instability, while the distance to delamination through the thickness $\boldsymbol{\mu}$ ratio did not have an effect on the crack stability. In contrast under lower applied load levels, the distance to delamination through the thickness shows a significant influence on the crack propagation. The outcomes of this study have confirmed that the location of delamination damage along the thickness direction μ has a significant influence on the damage propagation. The study also confirms the relatively high resistance to delamination crack initiation and propagation at deeper locations through the thickness.

Thermoelastic Stress Analysis (TSA) was used to monitor the propagation of delamination. A measurable change in the thermoelastic response indicated the

development of a delamination crack between layers at a relatively low applied strain. Monotonically increasing quasistatic load and a step-cyclic load regime has been applied to a specimen with a purposely created delamination and its thermoelastic response measured using a microbolometer. Subsequently, microscopic analysis is performed on the damaged area of the specimen. The delamination crack length is measured and compared with numerical results.

Chapter 6: CONCLUSION

This thesis has contributed new scientific knowledge to damage mechanics of composite research field by providing an insight into delamination damage in Glass Fibre Reinforced Composite structures. Present work has utilised numerical and experimental techniques to uncover the remaining grey areas and complexities associated with mechanics of delamination damage. There are a number of unresolved areas regarding the mechanics of onset and propagation of delamination under various applied loadings. In particular, the different damage mechanisms associated with the process of delamination due to applied operational loadings have been neglected in the research works to date. Therefore this thesis has made an earnest effort to investigate the shortcomings of existing models to date. The research has also made success in proposing corrective measure to understand and provide answers to some of the questions regarding damage mechanics related to delamination of fibre reinforced composite materials.

6.1: Principle achievement

This thesis has proposed a new Elasto-plastic model and evidently proved its robustness to predict delamination onset and its propagation processes in glass fibre reinforce/epoxy resin composites. The proposed model has considered the elasto-plastic strain at the tip of delamination crack whereas the other models extended the fracture mechanics developed for isotropic materials to explain fibre reinforced composites using additional correction factors. In addition, the currently available standard test methods and damage models are based on crack tip environment i.e. stress/strain at the crack tip. Unfortunately, the strain at crack tip was compensated with the measurement obtained from surface attached strain gauges. This research has taken an innovative step to measure the strain at the crack tip using embedded FBG sensors. The prediction of the proposed model has showed its superior performance. The proposed model has been applied for Mode I, Mode II, and Mixed mode I/II fracture situation with an extreme success. This thesis has evidently proved that the proposed model is superior to the prediction by ASTM D5528 (equation 4.14). Moreover, the proposed elasto-plastic fracture model has been applied to different unidirectional and woven laminated composite (WC/epoxy) materials and evidently proved its robustness of predictions over a wider range of composite configurations. The G_{IIc} value calculated by the proposed

model was closer to the G_{IIc} calculated by to CBT and CCM methods. The main advantage of proposed model is that it does not need any correction factors and it calculates R-curve directly. This study also confirms the relatively high resistance to delamination crack onset and propagation at deeper locations through the thickness.

Addition to the proposed Elasto-plastic model a breakthrough technology for Structural Health Monitoring of composite has been developed by this research. The proposed model prediction and investigation have been evaluated using embedded FBG sensor and TSA stress field mapping techniques. A measurable change in the FBG sensor spectrum response indicates the development of a delamination crack between layers. This distortion of spectrum is caused due to the effect of the non-uniform strain at the tip of delamination crack. The crack tip induces non-uniform strain that promotes non-uniform fringing in the core of the fibre. Further, the calculated DI and PRW parameters show the onset and the stability of delamination crack. The results show that both parameters provide accurate indications for monitoring the status of delamination damage, such as stability and instability of the crack. The comparison of *G/Gc* data has proved the accuracy of the crack status against that provided by the FBG readings. As such FBG sensor show potential for monitoring delamination damage onset. A measurable change in the thermoelastic response indicated the development of a delamination crack between layers at a relatively low applied strain. Monotonically increasing quasistatic load and a step-cyclic load regime has been applied to a specimen with a purposely created delamination and its thermoelastic response measured using a microbolometer. Subsequently, microscopic analysis is performed on the damaged area of the specimen. The delamination crack length is measured and compared with numerical results. A measurable change in the thermoelastic response indicates the development of delamination crack between layers at a relatively low applied strain. A correct way has been utilised to calculate the delamination size exactly modelled around the delamination size at the smallest lap thickness. The results show that the thickness of lap has significant effect on the accuracy of TSA signal. It is seen that the use of TSA techniques has enhanced the accuracy of delamination damage detection. As a consequence, FBG sensor network can be successfully implemented in damage detection of composite

structures. In a comparative study between the experimental and finite element simulation results, the properties of specimens were considered, such as elasticity, cohesiveness and wave geometry of materials. The finite element simulation using cohesive element technique showed similarity with experimental results for P-Δ curve delamination crack propagation and strain in FBG sensor location values. State damage variables (SDVn) in ABAQUS 6.13 FEA software demonstrate the suitability for verification and validation works on delamination test condition. FEA analysis using ABAQUS 6.13 has provided reasonable accurate simulation of damage growth in the considered specimen. The FBG_SiMul V1.0 interface program has been used to simulate the change and distortion in the FBG sensor spectrum. The experimental results are in excellent correlation with the prediction by the combined ABAQUS and FBG_SiMul V1.0 results. An analysis of the delamination process in ABAQUS 6.13 has revealed that a cohesive element model provides reasonable accuracy for the simulation of damage growth in the class of specimen considered. It is shown that local bending in front of the delamination crack tip is the primary cause for propagation of the delamination.

Finally, it can be concluded that the main advantage of the elastoplastic theory is its simple, objective identification of delamination crack and its application with woven yarns. The proposed theory has been integrated with the embedded FBG sensors and strain values measured with externally attached strain gauges. It is a robust model for monitoring onset and propagation of delamination in any composite structures under tensile loading. However, this model needs further research/ refinement to include fracture Modes I, II and III for more robust predictions of structures under multi-axial loading. It can be concluded that "Cohesive Element" in ABAQUS software has proved its ability to simulate a delamination growth in composite materials.

6.2: Future work

The Elasto-plastic model using FBG sensor has been used in this study. In addition TSA technique has been engaged with FBG senor to detect delamination damage. Furthermore Kachanov theory has been extended to use embedded FBG sensor strain measurement to evaluate inclusion and internal damage in laminated composite materials during production and service. There is scope for further research into this topic.

The Elasto-plastic model has been applied for different delamination modes. This theory can be applied on different materials such as CFR composite materials. Furthermore it can be used for Mode III delamination damage.

TSA technique has been used to detect delamination damage but the result show strong diverse response due to woven structures of the laminate. Therefore further work is required to overcome this limitation.

Further research using different composite materials can provide additional collaboration data to support this research.

References

Adams, RD, Cawley, P, Pye, CJ & Stone, BJ 1978, 'A Vibration Technique for Non-Destructively Assessing the Integrity of Structures', *Journal of Mechanical Engineering Science*, vol. 20, no. 2, pp. 93-100.

Ahn, JS & Woo, KS 2015, 'Delamination of laminated composite plates by p-convergent partial discrete-layer elements with VCCT', *Mechanics Research Communications*, vol. 66, pp. 60-9.

Alderliesten, RC, Schijve, J & Zwaag, Svd 2006, 'Application of the energy release rate approach for delamination growth in Glare', *Engineering Fracture Mechanics*, vol. 73, no. 6, pp. 697-709.

Alfredo, G, Antonio, F-L & Soller, BJ 2010, 'Optical Fiber Distributed Sensing - Physical Principles and Applications', *Structural Health Monitoring*, vol. 9, no. 3, pp. 233-45.

Allaoui, A, Bai, S, Cheng, HM & Bai, JB 2002, 'Mechanical and electrical properties of a MWNT/epoxy composite', *Composites Science and Technology*, vol. 62, no. 15, pp. 1993-8.

Andrews, MG & Massabò, R 2007, 'The effects of shear and near tip deformations on energy release rate and mode mixity of edge-cracked orthotropic layers', *Engineering Fracture Mechanics*, vol. 74, no. 17, pp. 2700-20.

Anyfantis, KN & Tsouvalis, NG 2011, 'Experimental and numerical investigation of Mode II fracture in fibrous reinforced composites', *Journal of Reinforced Plastics and Composites*, vol. 30, no. 6, pp. 473-87.

Arrese, A, Carbajal, N, Vargas, G & Mujika, F 2010, 'A new method for determining mode II R-curve by the End-Notched Flexure test', *Engineering Fracture Mechanics*, vol. 77, no. 1, pp. 51-70.

Aslan, Z & Daricik, F 2016, 'Effects of multiple delaminations on the compressive, tensile, flexural, and buckling behaviour of E-glass/epoxy composites', *Composites Part B: Engineering*, vol. 100, pp. 186-96.

B. Pan, K. M. Qian, H. M. Xie & Asundi, A 2009, 'Two-dimensional digital image correlation for in-plane displacement and strain measurement: A review', *Measurement science and Technology*, vol. 20, no. 6, p. 062001.

Barbero, EJ 2011, Introduction to Composite Materials Design, Second Edition edn, CRC Press, USA.

Barbero, EJ & Reddy, JN 1991, 'Modeling of delamination in composite laminates using a layer-wise plate theory', *International Journal of Solids and Structures*, vol. 28, no. 3, pp. 373-88.

Barbero, EJ & Cortes, DH 2010, 'A mechanistic model for transverse damage initiation, evolution, and stiffness reduction in laminated composites', *Composites Part B: Engineering*, vol. 41, no. 2, pp. 124-32.

Barenblatt, G 1962, 'The mathematical theory of equilibrium cracks in brittle fracture', *Advances in Applied Mechanics*, vol. 7, pp. 55-129.

Barenblatt, GI 1962, 'The Mathematical Theory of Equilibrium Cracks in Brittle Fracture', *Advances in Applied Mechanics*, vol. 7, pp. 55-129.

Belytschko, T & Black, T 1999, 'Elastic crack growth in finite elements with minimal remeshing', *International Journal for Numerical Methods in Engineering*, vol. 45, no. 5, pp. 601-20.

Benzeggagh, ML & Kenane, M 1996, 'Measurement of mixed-mode delamination fracture toughness of unidirectional glass/epoxy composites with mixed-mode bending apparatus', *Composites Science and Technology*, vol. 56, no. 4, pp. 439-49.

Bin Mohamed Rehan, MS, Rousseau, J, Fontaine, S & Gong, XJ 2017, 'Experimental study of the influence of ply orientation on DCB mode-I delamination behavior by using multidirectional fully isotropic carbon/epoxy laminates', *Composite Structures*, vol. 161, no. Supplement C, pp. 1-7.

Bolotin, VV 1996, 'Delaminations in composite structures: Its origin, buckling, growth and stability', *Composites Part B: Engineering*, vol. 27, no. 2, pp. 129-45.

Bolotin, VV 2001, 'Mechanics of Delaminations in Laminate Composite Structures', *Mechanics of Composite Materials*, vol. 37, no. 5, pp. 367-80.

Bonhomme, J, Argüelles, A, Viña, J & Viña, I 2009, 'Numerical and experimental validation of computational models for mode I composite fracture failure', *Computational Materials Science*, vol. 45, no. 4, pp. 993-8.

Boyano, A, De Gracia, J, Arrese, A & Mujika, F 2017, 'Equivalent energy release rate and crack stability in the End Notched Flexure with inserted roller mixed mode I/II test', *Theoretical and Applied Fracture Mechanics*, vol. 87, pp. 99-109.

Briscoe, BJ & Williams, DR 1993, 'Interlaminar fracture toughness of aramid/epoxy laminates', *Composites Science and Technology*, vol. 46, no. 3, pp. 277-86.

Briscoe, BJ, Court, RS & Williams, DR 1993, 'The effects of fabric weave and surface texture on the interlaminar fracture toughness of aramid/epoxy laminates', *Composites Science and Technology*, vol. 47, no. 3, pp. 261-70.

Brussat, TR, Chiu, ST & Mostovoy, S 1977a, *Fracture mechanics for structural adhesive bonds*, AFML-TR-77-163, Wright-patterson Air force base, Dayton, OH.

Brussat, TR, Chiu, ST & Mostovoy, S 1977b, *Fracture Mechanics for Structural Adhesive Bonds*, AFNLTR-77-163, Air Force Materials Laboratory, Wright-Patterson AFB, Ohio.

Carlsson, L, Gillespie, J & Pipes, R 1986, 'On the analysis and design of the end notched

flexure (ENF) specimen for mode II testing', *Journal of Composite Materials*, vol. 20, pp. 594-604.

Carlsson, LA, J.W. Gillespie, J & Pipes, RB 1986, 'On the Analysis and Design of the End Notched Flexure (ENF) Specimen for Mode II Testing', *Journal of Composite Materials*, vol. 20, no. 6, pp. 594-604.

Chandra, N, Li, H, Shet, C & Ghonem, H 2002, 'Some issues in the application of cohesive zone models for metal–ceramic interfaces', *International Journal of Solids and Structures*, vol. 39, no. 10, pp. 2827-55.

Chang, F 2003, Strucutral health monitoring, DESTechnol Publications, Lancaster.

Chauffaille, S, Jumel, J & Shanahan, MER 2011, 'Elasto-plastic analysis of the single cantilever beam adhesion test', *Engineering Fracture Mechanics*, vol. 78, no. 13, pp. 2493-504.

Chen, D & El-Hacha, R 2014, 'Cohesive Fracture Study of a Bonded Coarse Silica Sand Aggregate Bond Interface Subjected to Mixed-Mode Bending Conditions', *Polymers & Polymer Composites*, vol. 6, pp. 12-38.

Chen, D & El-Hacha, R 2014, 'Cohesive Fracture Study of a Bonded Coarse Silica Sand Aggregate Bond Interface Subjected to Mixed-Mode Bending Conditions', *Polymers*, vol. 6, no. 1, p. 12.

Cheuk, PT & Tong, L 2002, 'Failure of adhesive bonded composite lap shear joints with embedded precrack', *Composites Science and Technology*, vol. 62, no. 7, pp. 1079-95.

Chiu, WK, Rose, LRF & Nadarajah, N 2017, 'Scattering of the Fundamental Anti-symmetric Lamb Wave by a Mid-plane Edge Delamination in a Fiber-composite Laminate', *Procedia Engineering*, vol. 188, pp. 317-24.

Colombo, C & Vergani, L 2014, 'Influence of delamination on fatigue properties of a fibreglass composite', *Composite Structures*, vol. 107, pp. 325-33.

Colombo, C, Vergani, L & Burman, M 2012, 'Static and fatigue characterisation of new basalt fibre reinforced composites', *Composite Structures*, vol. 94, no. 3, pp. 1165-74.

Crupi, V, Guglielmino, E, Risitano, G & Tavilla, F 2015, 'Experimental analyses of SFRP material under static and fatigue loading by means of thermographic and DIC techniques', *Composites Part B: Engineering*, vol. 77, pp. 268-77.

Curiel Sosa, JL & Karapurath, N 2012, 'Delamination modelling of GLARE using the extended finite element method', *Composites Science and Technology*, vol. 72, no. 7, pp. 788-91.

Daniel, B 2010, 'Introduction to Structural Health Monitoring', in B Daniel, et al. (eds), *Structural Health Monitoring*, John Wiley & Sons.

Davidson, BD & Sun, X 10/2006, 'Geometry and data reduction recommendations for a standardized end notched flexure test for unidirectional composites', *Journal of ASTM International*, vol. 3, no. 9.

Davies, P, Blackman, BRK & Brunner, AJ 1998, 'Standard Test Methods for Delamination Resistance of Composite Materials: Current Status', *Applied Composite Materials*, vol. 5, no. 6, pp. 345-64.

de Morais, AB 2011, 'Novel cohesive beam model for the End-Notched Flexure (ENF) specimen', *Engineering Fracture Mechanics*, vol. 78, no. 17, pp. 3017-29.

de Moura, MFSF & de Morais, AB 2008, 'Equivalent crack based analyses of ENF and ELS tests', *Engineering Fracture Mechanics*, vol. 75, no. 9, pp. 2584-96.

Dugdale, DS 1960, 'Yielding of steel sheets containing slits', *Journal of the Mechanics and Physics of Solids*, vol. 8, no. 2, pp. 100-4.

Fernandes, RL & Campilho, RDSG 2016, 'Numerical evaluation of dissimilar cohesive models to predict the behavior of Double-Cantilever Beam specimens', *Procedia Structural Integrity*, vol. 1, pp. 42-9.

Fraternali, F 1996, 'Energy release rates for delamination of composite beams', *Theoretical and Applied Fracture Mechanics*, vol. 25, no. 3, pp. 225-32.

George, R, Irwin 1956, 'Onset of fast crack propagation and high strength Steel and Aluminum alloys', *Sagamore Research Conference Proceedings*, vol. 2, pp. 289-305.

Geubelle, PH & Baylor, JS 1998, 'Impact-induced delamination of composites: a 2D simulation', *Composites Part B: Engineering*, vol. 29, no. 5, pp. 589-602.

Ghadermazi, K, Khozeimeh, MA, Taheri-Behrooz, F & Safizadeh, MS 2015, 'Delamination detection in glass–epoxy composites using step-phase thermography (SPT)', *Infrared Physics & Technology*, vol. 72, pp. 204-9.

Golewski, GL, Golewski, P & Sadowski, T 2012, 'Numerical modelling crack propagation under Mode II fracture in plain concretes containing siliceous fly-ash additive using XFEM method', *Computational Materials Science*, vol. 62, pp. 75-8.

Greene, R, Patterson, E & Rowlands, R (eds) 2008, *Thermoelastic Stress Analysis*, in In Springer Handbook of Experimental Solid Mechanics, Springer, USA.

Griffith, A 1921, 'The Phenomena of Rupture and Flow in Solids', *Philosophical Transactions of the Royal Society of London. Series A, Containing Papers of a Mathematical or Physical Character*, vol. 221, no. 582-593, pp. 163-98.

Grogan, DM, Leen, SB & Ó Brádaigh, CM 'An XFEM-based methodology for fatigue delamination and permeability of composites', *Composite Structures*, vol. 107, pp. 205-18.

Grogan, DM, Ó Brádaigh, CM & Leen, SB 2015, 'A combined XFEM and cohesive zone model for composite laminate microcracking and permeability', *Composite Structures*, vol. 120, pp. 246-61.

Guillamet, G, Turon, A, Costa, J, Renart, J, Linde, P & Mayugo, JA 2014, 'Damage occurrence at edges of non-crimp-fabric thin-ply laminates under off-axis uniaxial loading', *Composites Science and Technology*, vol. 98, pp. 44-50.

Haj-Ali, R & Elhajjar, R 2014, 'An infrared thermoelastic stress analysis investigation of single lap shear joints in continuous and woven carbon/fiber epoxy composites', *International Journal of Adhesion and Adhesives*, vol. 48, pp. 210-6.

Haj-Ali, R, Wei, B-S, Johnson, S & El-Hajjar, R 2008, 'Thermoelastic and infrared-thermography methods for surface strains in cracked orthotropic composite materials', *Engineering Fracture Mechanics*, vol. 75, no. 1, pp. 58-75.

Harwood, N & Cummings, WM 1991, Thermoelastic stress analysis, Adam Hilger, Bristol, England.

Hashemi, S, Kinloch, AJ & Williams, JG 1989, 'Corrections needed in double-cantilever beam tests for assessing the interlaminar failure of fibre-composites', *Journal of Materials Science Letters*, vol. 8, no. 2, pp. 125-9.

Hawkins, DA & Haque, A 2015, 'Strain Energy Release Rate and Mode-I Delamination Growth in Carbon-Graphene/Epoxy Hybrid Nanocomposites', *Procedia Engineering*, vol. 105, pp. 829-34.

Heidari-Rarani, M & Ghasemi, AR 2017, 'Appropriate shape of cohesive zone model for delamination propagation in ENF specimens with R-curve effects', *Theoretical and Applied Fracture Mechanics*, vol. 90, pp. 174-81.

Heidari-Rarani, M, Shokrieh, MM & Camanho, PP 2013, 'Finite element modeling of mode I delamination growth in laminated DCB specimens with R-curve effects', *Composites Part B: Engineering*, vol. 45, no. 1, pp. 897-903.

Hillerborg, A, Modéer, M & Petersson, PE 1976, 'Analysis of crack formation and crack growth in concrete by means of fracture mechanics and finite elements', *Cement and Concrete Research*, vol. 6, no. 6, pp. 773-81.

Hu, H, Li, S, Wang, J, Wang, Y & Zu, L 2016, 'FBG-based real-time evaluation of transverse cracking in cross-ply laminates', *Composite Structures*, vol. 138, no. Supplement C, pp. 151-60.

Hu, XF, Chen, BY, Tirvaudey, M, Tan, VBC & Tay, TE 2016, 'Integrated XFEM-CE analysis of delamination migration in multi-directional composite laminates', *Composites Part A: Applied Science and Manufacturing*, vol. 90, pp. 161-73.

International, A 1994, *Standard Test Method for Mode I Interlaminar Fracture Toughness of Unidirectional Fiber-Reinforced Polymer Matrix Composites*, ASTM D 5528-13, ASTM International W. Conshohocken, PA, US.

International, A 2014, *Determination of the Mode II Interlaminar Fracture Toughness of Unidirectional Fiber-Reinforced Polymer Matrix Composites*, ASTM D 7905-14, ASTM International W. Conshohocken, PA, US.

IRWIN, GR 1957, 'Analysis of stresses and strains near the end of crack traversing a plate', *Journal of Applied Mechanics*, vol. 24, pp. 361-4.

Jalalvand, M, Fotouhi, M & Wisnom, MR 'Orientation-dispersed pseudo-ductile hybrid composite laminates – A new lay-up concept to avoid free-edge delamination', *Composites Science and Technology*.

Johnson, S 2014, 'Thermoelastic stress analysis for detecting and characterizing static damage initiation in composite lap shear joints', *Composites Part B: Engineering*, vol. 56, pp. 740-8.

Johnson, W 1987, 'Stress Analysis of the Cracked-Lap-Shear Specimen: An ASTM Round-Robin'.

Jokinen, J, Wallin, M & Saarela, O 2015, 'Applicability of VCCT in mode I loading of yielding adhesively bonded joints—a case study', *International Journal of Adhesion and Adhesives*, vol. 62, pp. 85-91.

Jones, R, Kinloch, AJ, Michopoulos, JG, Brunner, AJ & Phan, N 2017, 'Delamination growth in polymer-matrix fibre composites and the use of fracture mechanics data for material characterisation and life prediction', *Composite Structures*, vol. 180, no. Supplement C, pp. 316-33.

Juhász, Z & Szekrényes, A 2017, 'The effect of delamination on the critical buckling force of composite plates: Experiment and simulation', *Composite Structures*, vol. 168, pp. 456-64.

Kachanov, L 1988, Delamination buckling of composite materials, Kluwer Academic publisher, USA.

Kahandawa, GC & Hafizi, ZM, J.Epaarachchi and K.T.Lau 2012, 'Detecting delamination in a composite structure using an embedded FBG – AE hybrid system', in *7th Australasian Congress on Applied Mechanics, ACAM 7*: *Proceedings of the 7th Australasian Congress on Applied Mechanics, ACAM 7* Adelaide, Australia.

Kahandawa, GC, Epaarachchi, JA, Wang, H, Followell, D & Birt, P 2013, 'Use of fixed wavelength Fibre-Bragg Grating (FBG) filters to capture time domain data from the distorted spectrum of an embedded FBG sensor to estimate strain with an Artificial Neural Network', *Sensors and Actuators A: Physical*, vol. 194, pp. 1-7.

Kahandawa, GC, Epaarachchi, J, Wang, H, Canning, J & Lau, KT 2013, 'Extraction and processing of real time strain of embedded FBG sensors using a fixed filter FBG circuit and an artificial neural network', *Measurement*, vol. 46, no. 10, pp. 4045-51.

Kakei, A & Epaarachchi, JA 2018, 'Use of fiber Bragg grating sensors for monitoring delamination damage propagation in glass-fiber reinforced composite structures', *Frontiers of Optoelectronics*, vol. 11, no. 1, pp. 60-8.

Kakei, A, Epaarachchi, JA, Islam, M, Leng, J & Kahandawa, G 1-3 september 2015, 'Integrated FBG sensor response and full field thermoelastic stress approach to monitor damage accumulation in glass fibre reinforced composite plate', in *10th international workshop on structural health monitoring*: *Proceedings of the 10th international workshop on structural health monitoring*, S University (ed.), stanford, CA, USA.

Kakei, A, Epaarachchi, JA, Islam, M & Leng, J 2018, 'Evaluation of delamination crack tip in woven fibre glass reinforced polymer composite using FBG sensor spectra and thermo-elastic response', *Measurement*, vol. 122, pp. 178-85.

Kakei, A, Epaarachchi, JA, Islam, M, Leng, J & Rajic, N 2016, 'Detection and characterisation of delamination damage propagation in Woven Glass Fibre Reinforced Polymer Composite using thermoelastic response mapping', *Composite Structures*, vol. 153, pp. 442-50.

Kakei, A, Epaarachchi, J, Kahandawa, G & Leng, J (eds) 2016, *Development of Fracture and Damage Modeling Concepts for Composite Materials*, in Structural Health Monitoring Technologies and Next-Generation Smart Composite Structures, CRC Press USA.

Kakei, AA, Islam, M, Leng, J & Epaarachchi, JA 2018, 'Use of an elasto-plastic model and strain measurements of embedded fibre Bragg grating sensors to detect Mode I delamination crack propagation in woven cloth (0/90) composite materials', *Structural Health Monitoring*, vol. 17, no. 2, pp. 363-78.

Kanninen, MF & Popelar, CH 1985, *Advanced Fracture Mechanics*, Oxford University Press, 978-0-19-503532-2, <https://app.knovel.com/hotlink/toc/id:kpAFM00007/advanced-fracture-mechanics/advanced-fracture-mechanics>.

Kardos, JL, Duduković, MP & Dave, R 1986, 'Void growth and resin transport during processing of thermosetting — Matrix composites', in K Dušek (ed.), *Epoxy Resins and Composites IV*, Springer Berlin Heidelberg, Berlin, Heidelberg, pp. 101-23.

Kashtalyan, M & Soutis, C 2000, 'The effect of delaminations induced by transverse cracks and splits on stiffness properties of composite laminates', *Composites Part A: Applied Science and Manufacturing*, vol. 31, no. 2, pp. 107-19.

Kashtalyan, M & Soutis, C 2002, 'Analysis of local delaminations in composite laminates with angle-ply matrix cracks', *International Journal of Solids and Structures*, vol. 39, no. 6, pp. 1515-37.

Kelly, A (ed.) 1994, *Concise encyclopedia of composite materials*, PERGAMON, Oxford, UK.

Kessler, MR & White, SR 2001, 'Self-activated healing of delamination damage in woven composites', *Composites Part A: Applied Science and Manufacturing*, vol. 32, no. 5, pp. 683-99.

Kim, H & Kedward, KT 1999, 'A method for modeling the local and global buckling of delaminated composite plates', *Composite Structures*, vol. 44, no. 1, pp. 43-53.

Kim, J-K & Sham, M-L 2000, 'Impact and delamination failure of woven-fabric composites', *Composites Science and Technology*, vol. 60, no. 5, pp. 745-61.

Kollár, L & Springer, G 2003, Mechanics of composite structures, Cambridge university press.

Kuhn, E, Valot, E & Herve, P 2012, 'A comparison between thermosonics and thermography for delamination detection in polymer matrix laminates', *Composite Structures*, vol. 94, no. 3, pp. 1155-64.

Kuhtz, M, Hornig, A, Gude, M & Jäger, H 2017, 'A method to control delaminations in composites for adjusted energy dissipation characteristics', *Materials & Design*, vol. 123, pp. 103-11.

Kushch, VI, Sevostianov, I & Mishnaevsky, L 2009, 'Effect of crack orientation statistics on effective stiffness of mircocracked solid', *International Journal of Solids and Structures*, vol. 46, no. 6, pp. 1574-88.

Kutlu, Z & Chang, F-K 1992, 'Modeling Compression Failure of laminated Composites Containing Multiple Through-the-Width Delaminations', *Journal of Composite Materials*, vol. 26, no. 3, pp. 350-87.

La Rosa, G & Risitano, A 2000, 'Thermographic methodology for rapid determination of the fatigue limit of materials and mechanical components', *International Journal of Fatigue*, vol. 22, no. 1, pp. 65-73.

Lagunegrand, L, Lorriot, T, Harry, R, Wargnier, H & Quenisset, JM 2006, 'Initiation of free-edge delamination in composite laminates', *Composites Science and Technology*, vol. 66, no. 10, pp. 1315-27.

Lambert, J, Chambers, AR, Sinclair, I & Spearing, SM 2012, '3D damage characterisation and the role of voids in the fatigue of wind turbine blade materials', *Composites Science and Technology*, vol. 72, no. 2, pp. 337-43.

Lapidus, L 1999, Numerical solution of partial differential equations in science and engineering, Wiley, New York.

Lekhnitskii, SG 1968, Anisotropic Plates, Gordon and Breach, <https://books.google.com.au/books?id=pp2MAQAACAAJ>.

Li, J, Yan, Y, Zhang, T & Liang, Z 2015, 'Experimental study of adhesively bonded CFRP joints subjected to tensile loads', *International Journal of Adhesion and Adhesives*, vol. 57, no. Supplement C, pp. 95-104.

Li, Q, Li, Y & Zhou, L 2017, 'A micromechanical model of interfacial debonding and elementary fiber pull-out for sisal fiber-reinforced composites', *Composites Science and Technology*, vol. 153, no. Supplement C, pp. 84-94.

Liu, PF & Zheng, JY 2013, 'On the Through-the-Width Multiple Delamination, and Buckling and Postbuckling Behaviors of Symmetric and Unsymmetric Composite Laminates', *Applied Composite Materials*, vol. 20, no. 6, pp. 1147-60.

Liu, Z, Huang, Y, Yin, Z, Bennati, S & Valvo, PS 2014, 'A general solution for the two-dimensional stress analysis of balanced and unbalanced adhesively bonded joints', *International Journal of Adhesion and Adhesives*, vol. 54, pp. 112-23.

Luo, Q & Tong, L 2012, 'Analytic formulas of energy release rates for delamination using a global–local method', *International Journal of Solids and Structures*, vol. 49, no. 23, pp. 3335-44.

M'Membe, B, Gannon, S, Yasaee, M, Hallett, SR & Partridge, IK 2016, 'Mode II delamination resistance of composites reinforced with inclined Z-pins', *Materials & Design*, vol. 94, pp. 565-72.

Ma, L, Wang, X, Feng, X-Q & Yu, S-W 2005, 'Numerical analysis of interaction and coalescence of numerous microcracks', *Engineering Fracture Mechanics*, vol. 72, no. 12, pp. 1841-65.

Ma, ML, Wang, GL, Lian, BY & J, MH 2012, 'FRP STRUCTURE DESIGN METHOD BASED ON THE STIFFNESS EQUIVALENCE: CASE STUDY AND PRACTICE', *Engineering Review*, vol. 32, no. 3, pp. 165-71.

Mall, S & Portner, B 1992, 'Characterization of Fatigue Behavior in Cross-Ply Laminate of SCS-6/Ti-15-3 Metal Matrix Composite at Elevated Temperature', *Journal of Engineering Materials and Technology*, vol. 114, no. 4, pp. 409-15.

Masuelli, MA (ed.) 2013, *Introduction of Fibre-Reinforced Polymers − Polymers and Composites: Concepts, Properties and Processes*, in FIBER REINFORCED POLYMERS - THE TECHNOLOGY APPLIED FOR CONCRETE REPAIR, InTech, Croatia.

Meola, C, Boccardi, S, Carlomagno, GM, Boffa, ND, Monaco, E & Ricci, F 2015, 'Nondestructive evaluation of carbon fibre reinforced composites with infrared thermography and ultrasonics', *Composite Structures*, vol. 134, pp. 845-53.

Michael, J, Jan, Z & Russell, W 2004, Fracture Mechanics, Second Edition edn, Spon Press, Taylor & Francis, 2 Park Square, Milton Park, Abingdon, Oxfordshire, OX14 4RN.

Mohamed, G, Allegri, G, Yasaee, M & Hallett, SR 2017, 'Cohesive element formulation for z-pin delamination bridging in fibre reinforced laminates', *International Journal of Solids and Structures*.

Moya-Sanz, EM, Ivañez, I & Garcia-Castillo, SK 2017, 'Effect of the geometry in the strength of single-lap adhesive joints of composite laminates under uniaxial tensile load', *International Journal of Adhesion and Adhesives*, vol. 72, no. Supplement C, pp. 23-9.

Muskhelishvili, NI 1953, Some Basic Problems of the Mathematical Theory of Elasticity: Fundamental Equations, Plane Theory of Elasticity, Torsion, and Bending, P. Noordhoff, <https://books.google.com.au/books?id=BpDQAAAAMAAJ>.

Nageswara Rao, B & Acharya, AR 1995, 'Evaluation of fracture energy GIC using a double cantilever beam fibre composite specimen', *Engineering Fracture Mechanics*, vol. 51, no. 2, pp. 317-22.

Nageswara Rao, DK, Ramesh Babu, M, Raja Narender Reddy, K & Sunil, D 2010, 'Stress around square and rectangular cutouts in symmetric laminates', *Composite Structures*, vol. 92, no. 12, pp. 2845-59.

Nairn, JA & Hu, S 1992, 'The initiation and growth of delaminations induced by matrix microcracks in laminated composites', *International Journal of Fracture*, vol. 57, no. 1, pp. 1-24.

Nassar, K & Casavant, A 2008, 'Analysis of timed petri nets for reachability in construction applications', *Journal of Civil Engineering and Management*, vol. 14, no. 3, pp. 189-98.

Nick Rajic & Rowlands, D 2013, 'Thermoelastic stress analysis with a compact low-cost microbolometer system ', *Quantitative InfraRed Thermography Journal*, vol. 10, pp. 135-58.

O'brieb, TK 1987, 'analysis of local delaminations and their influance on composite laminate behaviour', in wS Johnson (ed.), *Delamination and debonding of materials*, ASTM, Baltimore, USA.

O'Brien, TK 1998, 'Interlaminar fracture toughness: the long and winding road to standardization', *Composites Part B: Engineering*, vol. 29, no. 1, pp. 57-62.

O.O, O & J. N, R 1992, Finite element analysis of composite laminates, Kluwer Academic Publishers the Netherlands.

Ojo, SO, Ismail, SO, Paggi, M & Dhakal, HN 2017, 'A new analytical critical thrust force model for delamination analysis of laminated composites during drilling operation', *Composites Part B: Engineering*, vol. 124, pp. 207-17.

Okabe, T & Yashiro, S 2012, 'Damage detection in holed composite laminates using an embedded FBG sensor', *Composites Part A: Applied Science and Manufacturing*, vol. 43, no. 3, pp. 388-97.

Panettieri, E, Fanteria, D & Danzi, F 2016, 'Delaminations growth in compression after impact test simulations: Influence of cohesive elements parameters on numerical results', *Composite Structures*, vol. 137, pp. 140-7.

Pankow, M, Salvi, A, Waas, AM, Yen, CF & Ghiorse, S 2011, 'Resistance to delamination of 3D woven textile composites evaluated using End Notch Flexure (ENF) tests: Experimental results', *Composites Part A: Applied Science and Manufacturing*, vol. 42, no. 10, pp. 1463-76.

Pereira, AB & de Morais, AB 2004, 'Mode I interlaminar fracture of carbon/epoxy multidirectional laminates', *Composites Science and Technology*, vol. 64, no. 13, pp. 2261-70.

Pereira, AB, de Morais, AB, Marques, AT & de Castro, PT 2004, 'Mode II interlaminar fracture of carbon/epoxy multidirectional laminates', *Composites Science and Technology*, vol. 64, no. 10, pp. 1653-9.

Pereira, G, McGugan, M & Mikkelsen, LP 2016, 'FBG_SiMul V1.0: Fibre Bragg grating signal simulation tool for finite element method models', *SoftwareX*, vol. 5, pp. 163-70.

R, K 2002, *The virtual crack closure technique: history, approach and applications*, NASA/Contractor Report-2002-211628.

Rajic N., Weinberg S. & D., R 2007, 'Low-cost thermoelastic stress analysis', *Materials Australian Journal of Multi-Disciplinary Engineering*, vol. 20, no. 4, pp. 40-1.

Rebière, JL & Gamby, D 2008, 'A decomposition of the strain energy release rate associated with the initiation of transverse cracking, longitudinal cracking and delamination in cross-ply laminates', *Composite Structures*, vol. 84, no. 2, pp. 186-97.

Rebière, JL, Maâtallah, MN & Gamby, D 2001, 'Initiation and growth of transverse and longitudinal cracks in composite cross-ply laminates', *Composite Structures*, vol. 53, no. 2, pp. 173-87.

Reddy, JN 1993, 'An evaluation of equivalent-single-layer and layerwise theories of composite laminates', *Composite Structures*, vol. 25, no. 1, pp. 21-35.

Reddy, JN 2004, Mechanics of laminated composite plates and shells: theory and analysis, CRC press, USA.

Reifsnider, K 1980, 'Fatigue behavior of composite materials', *International Journal of Fracture*, vol. 16, no. 6, pp. 563-83.

Rhee, KY 1993, 'Parametric studies on the elastic work factor for the CLS specimen', *Composite Structures*, vol. 23, no. 1, pp. 11-6.

Rhee, KY 1994, 'Characterization of delamination behavior of unidirectional graphite/PEEK laminates using cracked lap shear (CLS) specimens', *Composite Structures*, vol. 29, no. 4, pp. 379-82.

Ribeiro, TEA, Campilho, RDSG, da Silva, LFM & Goglio, L 2016, 'Damage analysis of composite–aluminium adhesively-bonded single-lap joints', *Composite Structures*, vol. 136, no. Supplement C, pp. 25-33.

Robinson, P, Javidrad, F & Hitchings, D 1995, 'Finite element modelling of delamination growth in the DCB and edge delaminated DCB specimens', *Composite Structures*, vol. 32, no. 1, pp. 275-85.

Ronald, K April 2002, *The Virtual Crack Closure Technique: History, Approach and Applications*, 2002-10, NASA Langley Research Center, Hampton, Virginia, Operated by Universities Space Research Association, ICASE, Hampton, Virginia, USA.

Russell, AJ & Street, K, N (eds) 1985, *Moisture and temperature effects on the mixed mode delamination fracture of unidirectional graphite/epoxy*, in Delamination and debonding of materials ASTM STP 876, ASTM, Philadephia.

Rybicki, EF & Kanninen, MF 1977, 'A finite element calculation of stress intensity factors by a modified crack closure integral', *Engineering Fracture Mechanics*, vol. 9, no. 4, pp. 931-8.

Saeedifar, M, Fotouhi, M, Ahmadi Najafabadi, M & Hosseini Toudeshky, H 2015, 'Prediction of delamination growth in laminated composites using acoustic emission and Cohesive Zone Modeling techniques', *Composite Structures*, vol. 124, pp. 120-7.

Salpekar, SA, O'Brien, TK & Shivakumar, KN 1996, 'Analysis of Local Delaminations Caused by Angle Ply Matrix Cracks', *Journal of Composite Materials*, vol. 30, no. 4, pp. 418-40.

Samborski, S 2016, 'Numerical analysis of the DCB test configuration applicability to mechanically coupled Fiber Reinforced Laminated Composite beams', *Composite Structures*, vol. 152, pp. 477-87.

Sans, D, Stutz, S, Renart, J, Mayugo, JA & Botsis, J 2012, 'Crack tip identification with long FBG sensors in mixed-mode delamination', *Composite Structures*, vol. 94, no. 9, pp. 2879-87.

Santare, MH, Crocombe, AD & Anlas, G 1995, 'Anisotropic effective moduli of materials with microcracks', *Engineering Fracture Mechanics*, vol. 52, no. 5, pp. 833-42.

Savin, GN 1961, Stress concentration around holes, Pergamon Press, <https://books.google.com.au/books?id=Rc4_AAAAIAAJ>.

Schön, J, Nyman, T, Blom, A & Ansell, H 2000, 'A numerical and experimental investigation of delamination behaviour in the DCB specimen', *Composites Science and Technology*, vol. 60, no. 2, pp. 173-84.

Shanmugam, V, Penmetsa, R, Tuegel, E & Clay, S 2013, 'Stochastic modeling of delamination growth in unidirectional composite DCB specimens using cohesive zone models', *Composite Structures*, vol. 102, pp. 38-60.

Sharma, D 2012, Stress Distribution around Circular/Elliptical/Triangular Holes in Infinite Composite Plate, vol. 20.

Shen, L & Yi, S 2000, 'New solutions for effective elastic moduli of microcracked solids', *International Journal of Solids and Structures*, vol. 37, no. 26, pp. 3525-34.

Shokrieh, MM & Heidari-Rarani, M 2011, 'Effect of stacking sequence on R-curve behavior of glass/epoxy DCB laminates with 0°//0° crack interface', *Materials Science and Engineering: A*, vol. 529, pp. 265-9.

Shokrieh, MM, Heidari-Rarani, M & Ayatollahi, MR 2012, 'Delamination R-curve as a material property of unidirectional glass/epoxy composites', *Materials & Design*, vol. 34, pp. 211-8.

Shokrieh, MM, Heidari-Rarani, M & Rahimi, S 2012, 'Influence of curved delamination front on toughness of multidirectional DCB specimens', *Composite Structures*, vol. 94, no. 4, pp. 1359-65.

Shokrieh, MM, Salamat-talab, M & Heidari-Rarani, M 2014, 'Effect of initial crack length on the measured bridging law of unidirectional E-glass/epoxy double cantilever beam specimens', *Materials & Design*, vol. 55, pp. 605-11.

Shokrieh, MM, Salamat-talab, M & Heidari-Rarani, M 2016, 'Effect of interface fiber angle on the R-curve behavior of E-glass/epoxy DCB specimens', *Theoretical and Applied Fracture Mechanics*, vol. 86, pp. 153-60.

Shokrieh, MM, Rajabpour-Shirazi, H, Heidari-Rarani, M & Haghpanahi, M 2012, 'Simulation of mode I delamination propagation in multidirectional composites with R-curve effects using VCCT method', *Computational Materials Science*, vol. 65, pp. 66-73.

Shor, O & Vaziri, R 2015, 'Adaptive insertion of cohesive elements for simulation of delamination in laminated composite materials', *Engineering Fracture Mechanics*, vol. 146, pp. 121-38.

Singh, CV & Talreja, R 2010, 'Evolution of ply cracks in multidirectional composite laminates', *International Journal of Solids and Structures*, vol. 47, no. 10, pp. 1338-49.

Sorensen, L, Botsis, J, Gmür, T & Cugnoni, J 2007, 'Delamination detection and characterisation of bridging tractions using long FBG optical sensors', *Composites Part A: Applied Science and Manufacturing*, vol. 38, no. 10, pp. 2087-96.

Soto, A, González, EV, Maimí, P, Turon, A, Sainz de Aja, JR & de la Escalera, FM 2016, 'Cohesive zone length of orthotropic materials undergoing delamination', *Engineering Fracture Mechanics*, vol. 159, pp. 174-88.

Sridharan, S 2008, Delamination Behaviour of Composites, Woodhead Publishing, Cambridge England.

Stutz, S, Cugnoni, J & Botsis, J 2011, 'Studies of mode I delamination in monotonic and fatigue loading using FBG wavelength multiplexing and numerical analysis', *Composites Science and Technology*, vol. 71, no. 4, pp. 443-9.

Su, D, Santare, MH & Gazonas, GA 2007, 'The effect of crack face contact on the anisotropic effective moduli of microcrack damaged media', *Engineering Fracture Mechanics*, vol. 74, no. 9, pp. 1436-55.

Suo, Z, Bao, G & Fan, B 1992, 'Delamination R-curve phenomena due to damage', *Journal of the Mechanics and Physics of Solids*, vol. 40, no. 1, pp. 1-16.

Suppakul, P & Bandyopadhyay, S 2002, 'The effect of weave pattern on the mode-I interlaminar fracture energy of E-glass/vinyl ester composites', *Composites Science and Technology*, vol. 62, no. 5, pp. 709-17.

Szekrényes, A 2006, 'Prestressed fracture specimen for delamination testing of composites', *International Journal of Fracture*, vol. 139, no. 2, pp. 213-37.

Tabiei, A & Zhang, W 2017, 'Cohesive element approach for dynamic crack propagation: Artificial compliance and mesh dependency', *Engineering Fracture Mechanics*, vol. 180, pp. 23-42.

Takeda, S, Okabe, Y & Takeda, N 2002, 'Delamination detection in CFRP laminates with embedded small-diameter fiber Bragg grating sensors', *Composites Part A: Applied Science and Manufacturing*, vol. 33, no. 7, pp. 971-80.

Takeda, S, Minakuchi, S, Okabe, Y & Takeda, N 2005, 'Delamination monitoring of laminated composites subjected to low-velocity impact using small-diameter FBG sensors', *Composites Part A: Applied Science and Manufacturing*, vol. 36, no. 7, pp. 903-8.

Tamuzs, V, Tarasovs, S & Vilks, U 2001, 'Progressive delamination and fiber bridging modeling in double cantilever beam composite specimens', *Engineering Fracture Mechanics*, vol. 68, no. 5, pp. 513-25.

Thomson, W 1853, 'On dynamical theory of heat', *Trans. R. Soc. Edinburgh*, vol. 20, pp. 261–83.

Tsukrov, I & Kachanov, M 2000, 'Effective moduli of an anisotropic material with elliptical holes of arbitrary orientational distribution', *International Journal of Solids and Structures*, vol. 37, no. 41, pp. 5919-41.

Tvergaard, V & Hutchinson, JW 1992, 'The relation between crack growth resistance and fracture process parameters in elastic-plastic solids', *Journal of the Mechanics and Physics of Solids*, vol. 40, no. 6, pp. 1377-97.

Ukadgaonker, VG & Rao, DKN 1999, 'Stress distribution around triangular holes in anisotropic plates', *Composite Structures*, vol. 45, no. 3, pp. 171-83.

Ukadgaonker, VG & Rao, DKN 2000, 'A general solution for stresses around holes in symmetric laminates under inplane loading', *Composite Structures*, vol. 49, no. 3, pp. 339-54.

Valvo, PS 2016, 'On the calculation of energy release rate and mode mixity in delaminated laminated beams', *Engineering Fracture Mechanics*, vol. 165, pp. 114-39.

Vasiliev, VV & morozov, EV 2011, Advanced Mechanics of Composite Materials, Second edition edn, ELSEVIER, UK.

Wang, C & Xu, X 2015, 'Cohesive element analysis of fatigue delamination propagation in composite materials with improved crack tip tracking algorism', *Composite Structures*, vol. 134, pp. 176-84.

Wang, Y & Williams, JG 1992, 'Corrections for mode II fracture toughness specimens of composites materials', *Composites Science and Technology*, vol. 43, no. 3, pp. 251-6.

Wang, Z, Yu, T, Bui, TQ, Tanaka, S, Zhang, C, Hirose, S & Curiel-Sosa, JL 2017, '3-D local mesh refinement XFEM with variable-node hexahedron elements for extraction of stress intensity factors of straight and curved planar cracks', *Computer Methods in Applied Mechanics and Engineering*, vol. 313, pp. 375-405.

Ward, IM & Sweeney, J 2004, An Introduction to the mechanical properties of solid polymers, Second Edition edn, John Wiley & Sons, Ltd, England.

Williams, JG 1987, 'Large Displacement and End Block Effects in the 'DCB' Interlaminar Test in Modes I and II', *Journal of Composite Materials*, vol. 21, no. 4, pp. 330-47.

Xiang, Y, Liu, R, Peng, T & Liu, Y 2014, 'A novel subcycle composite delamination growth model under fatigue cyclic loadings', *Composite Structures*, vol. 108, pp. 31-40.

Xie, D & Biggers, SB 2006, 'Strain energy release rate calculation for a moving delamination front of arbitrary shape based on the virtual crack closure technique. Part II: Sensitivity study on modeling details', *Engineering Fracture Mechanics*, vol. 73, no. 6, pp. 786-801.

Yang, B, Wang, Z, Zhou, L, Zhang, J & Liang, W 2015, 'Experimental and numerical investigation of interply hybrid composites based on woven fabrics and PCBT resin subjected to low-velocity impact', *Composite Structures*, vol. 132, pp. 464-76.

Yao, L, Alderliesten, RC, Zhao, M & Benedictus, R 2014, 'Discussion on the use of the strain energy release rate for fatigue delamination characterization', *Composites Part A: Applied Science and Manufacturing*, vol. 66, pp. 65-72.

Yashiro, S, Takeda, N, Okabe, T & Sekine, H 2005, 'A new approach to predicting multiple damage states in composite laminates with embedded FBG sensors', *Composites Science and Technology*, vol. 65, no. 3–4, pp. 659-67.

Yazdani, S, Rust, WJH & Wriggers, P 2016, 'An XFEM approach for modelling delamination in composite laminates', *Composite Structures*, vol. 135, pp. 353-64.

Ying, X, Christopher , L, Zhenglin, Y, Pin, T & Stephen, L 2003, 'A New Fiber Optic Based Method for Delamination Detection in Composites', *Structural Health Monitoring*, vol. 2, no. 3, pp. 205-23.

Yoshihara, H & Satoh, A 2009, 'Shear and crack tip deformation correction for the double cantilever beam and three-point end-notched flexure specimens for mode I and mode II fracture toughness measurement of wood', *Engineering Fracture Mechanics*, vol. 76, no. 3, pp. 335-46.

Yu, F, Wu, Q, Okabe, Y, Kobayashi, S & Saito, K 2016, 'The identification of damage types in carbon fiber–reinforced plastic cross-ply laminates using a novel fiber-optic acoustic emission sensor', *Structural Health Monitoring*, vol. 15, no. 1, pp. 93-103.

Zhang, J & P. Herrmann, K 1999, 'Stiffness degradation induced by multilayer intralaminar cracking in composite laminates', *Composites Part A: Applied Science and Manufacturing*, vol. 30, no. 5, pp. 683-706.

Zhang, J, Fan, J & Herrmann, KP 1999, 'Delaminations induced by constrained transverse cracking in symmetric composite laminates', *International Journal of Solids and Structures*, vol. 36, no. 6, pp. 813-46.

Zhang, L, Gao, Z & Yu, W 2017, 'A string-based cohesive zone model for interlaminar delamination', *Engineering Fracture Mechanics*, vol. 180, pp. 1-22.

Zhigang, S & John, WH 1990, 'Interface crack between two elastic layers', *International Journal of Fracture*, vol. 43, no. 1, pp. 1-18.

Zhou, G & Sim, LM 2002, 'Damage detection and assessment in fibre-reinforced composite structures with embedded fibre optic sensors-review', *SMART MATERIALS AND STRUCTURES*, vol. 11, no. 6, p. 925.

Zhu, H-y, Li, D-h, Zhang, D-x, Wu, B-c & Chen, Y-y 2009, 'Influence of voids on interlaminar shear strength of carbon/epoxy fabric laminates', *Transactions of Nonferrous Metals Society of China*, vol. 19, pp. s470-s5.

Zou, Z & Lee, H 2017, 'A cohesive zone model taking account of the effect of through-thickness compression', *Composites Part A: Applied Science and Manufacturing*, vol. 98, pp. 90-8.

Appendices

Appendix A: Conference Presentations

A.1 Conference Paper I: Integrated FBG Sensor Responses and Full Field Thermo-elastic Stress Approach to Monitor Damage Accumulation in Glass Fibre Reinforced Composite Plates.

Ayad Kakei, Jayantha A Epaarachchi, Nick Rajic, Jinsong Leng, Mainul Islam, Gayan Kahandawa (2015). Integrated FBG Sensor Responses and Full Field Thermo-elastic Stress Approach to Monitor Damage Accumulation in Glass Fibre Reinforced Composite Plates. *Proceeding of the 10th international workshop on Structural Health Monitoring* (IWSHM2017). Stanford, CA, USA1-3 September 2015.

Abstract: Monitoring internal damage status of advanced composite components with distributed sensor network has shown significant success in recent research works. However, application of such a system in a full scale structure is a critically challenging task and maintaining such a system during life time operations is an extremely difficult. An additional non-contactable full field strain measurement system being used to measure outer surface strain field of a composite sample while an embedded FBG sensor closer to an internal void being used to monitor localized strain variation. Recent developments in miniature low-cost microbolometer technology have paved the way to use full field thermo-elastic stress mapping using relatively inexpensive Infra-Red cameras. This paper details a comparison of strain measurements observed from FBG sensors embedded in a composite plate sample at a closer location to a void and full field thermo-elastic stress map. The test coupons were fabricated with a purposely created delamination and sample was loaded by quasi-static and low cycle fatigue uni-axial loads. The FBG responses and IR images were recorded in frequent intervals in order to track the delamination growth. Further the strain variations were studied using a detailed FEA and compared with experimental strain and full field Thermo-elastic stress map.

A.2 Conference Paper II: Elasto-plastic analysis of a delamination damage propagation in a 0/90 Woven Cloth Composite beam.

Ayad Kakei, J. A. Epaarachchi, Mainul Islam, J Leng (2016). Elasto-plastic analysis of a delamination damage propagation in a 0/90 Woven Cloth Composite beam. *Proceeding of 10th Asian-Australasian Conference on Composite Materials* (ACCM-10), Busan, South Korea.

Abstract: Mode I delamination of a 0/90 Glass Woven (WC) composite beam being investigated experimentally using double cantilever test set up. However, due to significantly low yield strength of the matrix material and the infinitesimal thickness of the interface layer the process become partially-plastic process (elasto-plastic). A simple elastic-plastic theory was proposed for the crack propagation modelling to calculate strain energy release rate. A Fibre Bragg Grating (FBG) sensor has embedded closer to the delamination to monitor the progress of delamination. Subsequently a FEA analysis of delaminated composite beam has performed using ABAQUS "Cohesive Elements" to study the delamination behaviour. FEA results has shown a very good correlation with DCB experimental results. FBG spectral response has shown a distortion of spectra due to the progress of delamination along the grating length.

A.3 Conference paper IV: Evaluation of Thermo-Elastic Stress Analysis (TSA) and Digital Image Correlation (DIC) Techniques for Detection of Delamination Crack Propagation of Glass Epoxy Composite Plate under Uni-Axial Cyclic Loading.

Ayad Kakei, J.A. Epaarachchi, Mainul Islam, J. Leng, Anura P. Rathnayake , N.K. Hettiarachchi (2017). Evaluation of Thermo-Elastic Stress Analysis (TSA) and Digital Image Correlation (DIC) Techniques for Detection of Delamination Crack Propagation of Glass Epoxy Composite Plate under Uni-Axial Cyclic Loading. Proceeding of the *21st International Conference on Composite Materials* (ICCM21), Xi'an, 20-25th August 2017.

Abstract: Delamination is the most common failures in composite structures and has harmful effects on the structure integrity. As such, a proper monitoring system of delamination crack propagation is an urgent need for advanced composites structures in various engineering applications. This paper details an investigation performed on the use of Thermal Stress Analysis (TSA) and Digital Image Correlation (DIC) Techniques to monitor delamination crack propagation in a glass fibre reinforced composite sample. Also a finite element analysis using cohesive elements to simulate delamination crack propagation has performed. It has been found that TSA techniques have performed well for monitoring delamination crack. The DIC techniques showed a significant influence of the location of the crack through the thickness direction on its sensitivity. Further FEA results have shown a good correlation with the experimental results.

A.4 Conference paper V: An Investigation of the Performances of Embedded Buckypapers within A 0/90 WC Glass Fibre Reinforced Composite Specimen with a Delamination, Under Tensile Loading.

Ayad Kakei, Jayantha Epaarachchi, Mainul Islam, Zhang Zhichun, Jinsong Leng (2017). An Investigation of the Performances of Embedded Buckypapers within A 0/90 WC Glass Fibre Reinforced Composite Specimen with a Delamination, Under Tensile Loading. Proceeding of the *11th international workshop on Structural Health Monitoring* (IWSHM2017). Stanford, CA, USA12-14 September 2017.

Abstract: Buckypapers (BP) are made from CNT that arrange to produces a thin layer which are bonded to each other by van der Waals forces. One of the sensitive characteristic of a Buckypaper is change of its resistance due to a nano scale change to its geometry. Due to this reason BP has been widely researched for strain measurement of various structures and became a potential candidate for sensing of structural performance under operational loading. Due to compatibility with fibre reinforced composites; BP is becoming an attractive candidate for Structural Health Monitoring (SHM) of composite structures. This paper detailed an investigation conducted on embedded BP strips closer to a purposely created delamination within a glass fibre composite sample under tension loading. In this study, a FBG sensor was also embedded at a location closer to BPs for comparison purpose. The change of electrical resistance of BP under tensile loading was investigated. Interestingly the change of electrical resistance of BPs was following the same trend as FBG sensor strain readings. Further, when the delamination damage approach the locations of BPs, the measured resistance of BP has increased significantly showing strain concentrations around the crack tip.

A.5 Conference paper VI: Use of FBG Sensors for Monitoring Mode I Delamination Damage Propagation.

Jayantha .A. Epaarachchi, ***Ayad*** **Kakei** (2017). Use of FBG Sensors for Monitoring Mode I Delamination Damage Propagation. Proceeding of the *9th Australasian Congress on Applied Mechanics* (ACAM9), *27 - 29 November 2017*, UNSW, Sydney, Australia.

Abstract: Embedded Fibre Braff Grating (FBG) sensors have been widely researched for damage monitoring of advanced fibre composite structures. However, many remaining problems and challenges have caused delays in implementation of FBG based in-situ Structural Health Monitoring (SHM) systems. One of the major problem associated with FBG based SHM system is the unavailability of a reliable damage model for accurate damage prediction. Delamination is the most critical damage in laminated composite structures and cause catastrophic failures without prior warning. Therefore the damage matrix must be robust enough to capture and identify the damage situation. The present work details a study which has been undertaken for identification of Mode I fracture under in-plane and out of plane loading. A novel Elasto-plastic model has proposed to qualitatively & quantitatively analyse delamination damage in Mode I. A double cantilever beam (DCB) experiment was performed for a 0/90 Glass Woven Cloth (WC) sample. A Fibre Bragg Grating (FBG) sensor has embedded closer to purposely created delamination (on the laminae above the delamination) to measure the strain. Strain energy release rate was calculated and compared with the model prediction. Subsequently, a FEA analysis on ABAQUS was performed using "Cohesive Elements" to study the proposed elasto-plastic behaviour. The FEA results have shown a very good correlation with experimental results. The study has concluded that Mode I delamination process of a FRP composite can be monitored successfully using an integral approach of FBG sensors measurements and the prediction of proposed Elasto-plastic model.

A.6 Conference poster VII: Monitoring delamination crack in fibre reinforced polymer (FRP) composite components using Fibre Bragg Grating (FBG) sensors and Thermal Stress Mapping Techniques.

Ayad Kakei, Jayantha A Epaarachchi (2017). Monitoring delamination crack in fibre reinforced polymer (FRP) composite components using Fibre Bragg Grating (FBG) sensors and Thermal Stress Mapping Techniques. Proceeding of the *9th Australasian Congress on Applied Mechanics* (ACAM9)*, 27 - 29 November 2017*, UNSW, Sydney, Australia.

Abstract: Fibre reinforced polymers (FRP) being used in many critical applications in aerospace, automobile, marine and civil infrastructures due to their superior strength to weight ratio. The increased use of fibre reinforced plastic (FRP) composites for critical infrastructures has created urgent need of Structural Health Monitoring (SHM) systems to ensure smooth and safe operation of the critical infrastructures. Damage detection in FRP structures using embedded FBG sensors is a widely researched area in SHM field. However, there are some unresolved problems in the development of accurate SHM systems such as monitoring of continuous crack propagation using minimal number of sensors. As such these grey areas have to be addressed in-depth to produce a reliable SHM system.

A.7 Conference paper VIII: Monitoring Tip of Embedded Mixed Mode Delamination Crack Propagation Using TSA Technique.

Ayad Kakei, Jayantha Epaarachchi (2018). Monitoring Tip of Embedded Mixed Mode Delamination Crack Propagation Using TSA Technique. Proceeding of the *11th Asian-Australasian Conference on Composite Materials* (ACCM11), *Cairns*, 29th July – 1st August, 2018, Australia.

Abstract: The composite material can be used in light-weight structure for aerospace. However the applications of composite are limited by the lack of adequate techniques to monitor internal damage during service. In this work TSA Technique used to monitoring delamination crack tip development and strain distribution due to delamination damage along single shear specimen. The delamination damage was both experimentally and numerically studies at woven laminated composite specimen. The result show that delamination damage propagates due to tensile loading at the single shear specimen. The simulations and measurement showed good agree for the delamination damage monitoring.

Appendix B: A summary of Classical Lamination Theory

A laminate is an organized stack of uni-directional composite plies (uni-directional meaning the plies have a single fibre direction rather than a weave pattern). The stack is defined by the fibre directions of each ply. The ABD matrix is a 6x6 matrix that serves as a connection between the applied loads and the associated strains in the laminate. It essentially defines the elastic properties of the entire laminate. To assemble the ABD matrix, follow these steps:

1. Calculate reduced stiffness matrix Q_{ij} for each material used in the laminate (if a laminate uses only one type of composite material, there will be only 1 stiffness matrix). The stiffness matrix describes the elastic behaviour of the ply in plane loading

$$\boldsymbol{Q}_{ij} = \begin{bmatrix} Q_{11} & Q_{12} & 0 \\ Q_{12} & Q_{22} & 0 \\ 0 & 0 & Q_{66} \end{bmatrix}$$

Where

$$Q_{11} = \frac{E_{11}^2}{(E_{11} - v_{12} \cdot E_{22})}, \quad Q_{12} = \frac{v_{12} E_{11} E_{22}}{E_{11} - v_{12}^2 E_{22}}$$

$$Q_{22} = \frac{E_{11} E_{22}}{E_{11} - v_{12}^2 E_{22}}, \quad Q_{66} = G_{12}$$

2. Calculate the transformed reduced stiffness matrix $\bar{Q}ij$ for each ply based on the reduced stiffness matrix and fibre angle.

$$\begin{aligned}
\overline{Q_{11}} &= Q_{11}\cos(\theta)^4 + 2(Q_{12} + 2Q_{66})\cos(\theta)^2 \cdot \sin(\theta)^2 + Q_{22}\sin(\theta)^4 \\
\overline{Q_{12}} &= \overline{Q_{21}} = Q_{12}(\cos(\theta)^4 + \sin(\theta)^4) + (Q_{11} + Q_{22} - 4Q_{66})\cos(\theta)^2\sin(\theta)^2 \\
\overline{Q_{16}} &= \overline{Q_{61}} = (Q_{11} - Q_{12} - 2Q_{66})\cos(\theta)^3\sin(\theta) - (Q_{22} - Q_{12} - 2Q_{66})\cos(\theta)\sin(\theta)^3 \\
\overline{Q_{22}} &= Q_{11}\sin(\theta)^4 + 2(Q_{12} + 2Q_{66})\cos(\theta)^2\sin(\theta)^2 + Q_{22}\cos(\theta)^4 \\
\overline{Q_{26}} &= \overline{Q_{62}} = (Q_{11} - Q_{12} - 2Q_{66})\cos(\theta)\sin(\theta)^3 - (Q_{22} - Q_{12} - 2Q_{66})\cos(\theta)^3\sin(\theta) \\
\overline{Q_{66}} &= (Q_{11} + Q_{22} - 2Q_{12} - 2Q_{66})\cos(\theta)^2\sin(\theta)^2 + Q_{66}(\cos(\theta)^4 + \sin(\theta)^4)
\end{aligned}$$

$$\overline{\boldsymbol{Q}_{ij}} = \begin{matrix} \overline{Q_{11}} & \overline{Q_{12}} & \overline{Q_{16}} \\ \overline{Q_{12}} & \overline{Q_{22}} & \overline{Q_{26}} \\ \overline{Q_{16}} & \overline{Q_{26}} & \overline{Q_{66}} \end{matrix}$$

3. Calculate the A_{ij}, B_{ij}, D_{ij} matrices using the following equations where z represents the vertical position in the ply from the midplane measured in meters:

$$\boldsymbol{A}_{ij} = \sum_{k=1}^{n} \{Q_{ij}\}_n (z_k - z_{k-1})$$

$$\boldsymbol{B}_{ij} = \frac{1}{2} \sum_{k=1}^{n} \{Q_{ij}\}_n (z_k^2 - z_{k-1}^2)$$

$$\boldsymbol{D}_{ij} = \frac{1}{3} \sum_{k=1}^{n} \{Q_{ij}\}_n (z_k^3 - z_{k-1}^3)$$

4. Assemble ABD:

$$\boldsymbol{ABD} = \begin{bmatrix} A & B \\ B & D \end{bmatrix}$$

5. Calculate inverse of ABD: abd = ABD^{-1}
6. Calculate midplane strains and curvatures induced in the laminate. These represent the deflections of the laminate.

$$\begin{bmatrix} \varepsilon_{xx}^0 \\ \varepsilon_{yy}^0 \\ \varepsilon_{xy}^0 \\ \kappa_{xx} \\ \kappa_{yy} \\ \kappa_{xy} \end{bmatrix} = \begin{bmatrix} a_{11} & a_{12} & a_{16} & b_{11} & b_{12} & b_{16} \\ a_{12} & a_{22} & a_{26} & b_{12} & b_{22} & b_{16} \\ a_{16} & a_{26} & a_{66} & b_{16} & b_{26} & b_{66} \\ b_{11} & b_{12} & b_{16} & d_{11} & d_{12} & d_{16} \\ b_{12} & b_{22} & b_{26} & d_{12} & d_{22} & b_{26} \\ b_{16} & b_{26} & b_{66} & d_{16} & d_{26} & d_{66} \end{bmatrix} \cdot \begin{bmatrix} N_{xx} \\ N_{yy} \\ N_{xy} \\ M_{xx} \\ M_{yy} \\ M_{xy} \end{bmatrix}$$

7. For each ply

a. Calculate ply strains in the x-y coordinate system

$$\begin{Bmatrix} \varepsilon_{xx} \\ \varepsilon_{yy} \\ \gamma_{xy} \end{Bmatrix} = \begin{Bmatrix} \varepsilon_{xx}^0 \\ \varepsilon_{yy}^0 \\ \gamma_{xy}^0 \end{Bmatrix} + z \begin{Bmatrix} \kappa_{xx} \\ \kappa_{yy} \\ \kappa_{xy} \end{Bmatrix}$$

b. Calculate ply stresses in the x-y coordinate system

$$\begin{bmatrix} \boldsymbol{\sigma_{xx}} \\ \boldsymbol{\sigma_{yy}} \\ \boldsymbol{\tau_{xy}} \end{bmatrix} = \begin{bmatrix} \overline{Q_{11}} & \overline{Q_{12}} & \overline{Q_{16}} \\ \overline{Q_{12}} & \overline{Q_{22}} & \overline{Q_{26}} \\ \overline{Q_{16}} & \overline{Q_{26}} & \overline{Q_{66}} \end{bmatrix} \cdot \begin{Bmatrix} \boldsymbol{\varepsilon_{xx}} \\ \boldsymbol{\varepsilon_{yy}} \\ \boldsymbol{\varepsilon_{xy}} \end{Bmatrix}$$

Appendix C: Matlab codes

Code 1: Calculate Transformed reduced Stiffness Matrix (Qbar)

```
function y = Qbar(Q,theta)
%Qbar This function returns the transformed reduced
% stiffness matrix "Qbar" given the reduced
% stiffness matrix Q and the orientation
% angle "theta".
% There are two arguments representing Q and "theta"
% The size of the matrix is 3 x 3.
% The angle "theta" must be given in degrees.
m = cos(theta*pi/180);
n = sin(theta*pi/180);
T = [m*m n*n 2*m*n ; n*n m*m -2*m*n ; -m*n m*n m*m-n*n];
Tinv = [m*m n*n -2*m*n ; n*n m*m 2*m*n ; m*n -m*n m*m-n*n];
y = Tinv*Q*T;
```

Code 2: Calculate transformed reduced compliance matrix (Sbar)

```
function y = Sbar(S,theta)
%Sbar This function returns the transformed reduced
% compliance matrix "Sbar" given the reduced
% compliance matrix S and the orientation
% angle "theta".
% There are two arguments representing S and "theta"
% The size of the matrix is 3 x 3.
% The angle "theta" must be given in degrees.
m = cos(theta*pi/180);
n = sin(theta*pi/180);
T = [m*m n*n 2*m*n ; n*n m*m -2*m*n ; -m*n m*n m*m-n*n];
Tinv = [m*m n*n -2*m*n ; n*n m*m 2*m*n ; m*n -m*n m*m-n*n];
y = Tinv*S*T;
```

Code 3: Calculate the reduced compliance matrix for fibre-reinforced materials.

```
function y = ReducedCompliance(E1,E2,NU12,G12)
%ReducedCompliance This function returns the reduced compliance
% matrix for fibre-reinforced materials.
% There are four arguments representing four
% material constants. The size of the reduced
```

```
% compliance matrix is 3 x 3.
y = [1/E1 -NU12/E1 0 ; -NU12/E1 1/E2 0 ; 0 0 1/G12];
```

Code 4 : Calculate the reduced stiffness matrix for fibre reinforced materials

```
function y = ReducedStiffness(E1,E2,NU12,G12)
%ReducedStiffness This function returns the reduced stiffness
% matrix for fibre-reinforced materials.
% There are four arguments representing four
% material constants. The size of the reduced
% stiffness matrix is 3 x 3.
NU21 = NU12*E2/E1;
y   =   [E1/(1-NU12*NU21)   NU12*E2/(1-NU12*NU21)   0   ;NU12*E2/(1-
NU12*NU21) E2/(1-NU12*NU21) 0 ; 0 0 G12];
```

code 5: calculate the [A] matrix

```
function y = aamatrix(A,Sbar,z1,z2)
%Amatrix This function returns the [A] matrix
% after the layer k with stiffness [Qbar]
% is assembled.
% A - [A] matrix after layer k
% is assembled.
% Qbar - [Qbar] matrix for layer k
% z1 - z(k-1) for layer k
% z2 - z(k) for layer k
for i = 1 : 3
for j = 1 : 3
A(i,j) = A(i,j) + Sbar(i,j)*(z2-z1);
end
end
y = A;
```

Code 6: Calculate cavity compliance tensor of orthotropic matrix

```
function y=Hreduceorthotropy(E1,E2,NU12,G12,theta,a,b,A)
% Hreduceorthotropy this function returns the reduced
% orthotrioc compliance
%    matrix fibre-reinforced material having hole
```

```
% A is referencing area, b&a is hole dimension, and theta is the %
angle, see Figure E-3 (Appendix E).
L=sqrt((1/G12)-(2*NU12/E1)+(2/sqrt(E1*E2)));
H1111=(pi*L/(A*sqrt(E1)))*((b^2-
a^2)*(cos(theta))^2+a^2+(a*b/(L*sqrt(E1))));
H1112=pi*(b^2-a^2)*L*sin(theta)*cos(theta)/(2*A*sqrt(E1));
H1122=-pi*a*b/(A*sqrt(E1*E2));
H1212=pi*L/(4*A*sqrt(E1*E2))*((a^2-b^2)*(sqrt(E2)-
sqrt(E1))*(cos(theta))^2+a^2*sqrt(E1)+a*b*L*sqrt(E1*E2)+b^2*sqrt(
E2));
H1222=pi*(b^2-a^2)*L*sin(theta)*cos(theta)/(2*A*sqrt(E2));
H2222=pi*L/(A*sqrt(E2))*((a^2-
b^2)*(cos(theta))+b^2+a*b/(L*sqrt(E2)));
y=[H1111 H1122 H1112;0 H2222 0; 0 H1222 H1212];
```

Code 7: Calculate the reduced orthotropic compliance matrix fibre reinforced having hole

```
function y= Hreduceisotropic(E1,E2,G12,NU12,a,b,A,alpha1,alpha2)
%           Hreduce this function returns the reduced orthotrioc
%compliance
%              matrix fibre-reinforced material having hole
%              A is referencing area, b&a is hole dimenasion
%              beta1 & alph1µµ are the root of complex equation
beta1=0.5*(((E1/G12)-2*NU12+2*sqrt(E1/E2)+((E1/G12)-2*NU12-
2*sqrt(E1/E2))));
beta2=0.5*(((E1/G12)-2*NU12+2*sqrt(E1/E2)-((E1/G12)-2*NU12-
2*sqrt(E1/E2))));
S11=(pi*b/A)*(1/E1)*(a+b*(beta1-beta2));
S12=(pi*a*b/A)*(1/E1)*(alpha1*alpha2-beta1*beta2);
S22=(pi*a/A)*(1/E2)*(a*(beta1/(alpha1^2+beta1^2)+beta2/(alpha2^2+
beta2^2))+b);
S66=(pi/4*A)*(1/E1)*(a^2*(beta1+beta2)+a*b*((alpha1+alpha2)^2+(be
ta1+beta2)^2)+b^2*(beta1*(alpha2^2+beta2^2)+beta2*(alpha1^2+beta1
^2)));
y=[S11 S12 0;S12 S22 0; 0 0 S66 ];
```

Appendix D: Stress Analysis of the Cracked Lap Shear Specimen An ASTM Round Robin by Johnson (1987), (Johnson, W 1987, 'Stress Analysis of the Cracked-Lap-Shear Specimen: An ASTM Round-Robin').

In this appendix will provide the basic equation for calculating fracture energy (*G*) of cracked lap shear (CLS). Actually this approach was developed to calculate the energy fracture (*G*) of adhesively joint specimen. As shown this approach has been developed to calculate the delamination damage in CLS specimen and applied elasto-plastic concept. The result of this approach was compared with the elasto-plastic method (ELM). However the basic equations of this approach are:

1. Two dimensionless parameters, which are related as follows to the bending rigidities$(El)_2$ and $(EI)_o$ of the strap section and the combined (lap+ strap) section, respectively:

$$\lambda_2 = \sqrt{p/(EI)_2}$$

$$\lambda_o = \sqrt{p/(EI)_o} \qquad \text{D-1}$$

2. The mode I crack opening displacement a distance x from the crack tip is given by

$$y' = \frac{\bar{y}_2 - \bar{y}_o}{1 + (\lambda_2/\lambda_o)} = \left(e^{-\lambda_2 x} + \lambda_2 x - 1\right) \qquad \text{D-2}$$

where $\bar{Y}2$ is the centroid location of the strap section, and $\overline{Yo}$ is the centroid location of the combined section.

3. limiting value of internal bending moment at the crack tip is

$$M_o = \frac{(\bar{y}_2 - \bar{y}_o)P}{1 + (\lambda_2^o/\lambda_o)} \qquad \text{D-3}$$

4. An approximation for the mode I component of strain energy release rate is derived under the following assumption;

a. G_I for CLS specimen in tension is equal to G_I for a CLS specimen subjected to end moments of magnitude M_o

b. G_{II}/G_T=4/7 for the CLS specimen in pure bending. This is the exact beam-theory results for equal thickness adherends and zero-thickness adhesive layer.

c. In according with two these assumptions, G_I is given as;

$$G_I = \frac{2M_o^2}{7b_N(EI)_2}\left[1 - \frac{(EI)_2}{(EI)_o}\right]$$

and

D-4

$$G_{II} = G_T - G_I$$

Appendix E: Tsukrov and Kachanov model

To evaluate the reduction of elasticity properties in anisotropic media, many cases of circular and non-circular hole density in anisotropic media was discussed by Tsukrov and Kachanov (2000) by using the Leknistskii (1987) method. The result showed that randomly oriented ellipses reduce the effective anisotropy and that this effect is more pronounced, at the same porosity p, for narrower ellipses (smaller b/a), as shown in Figure .

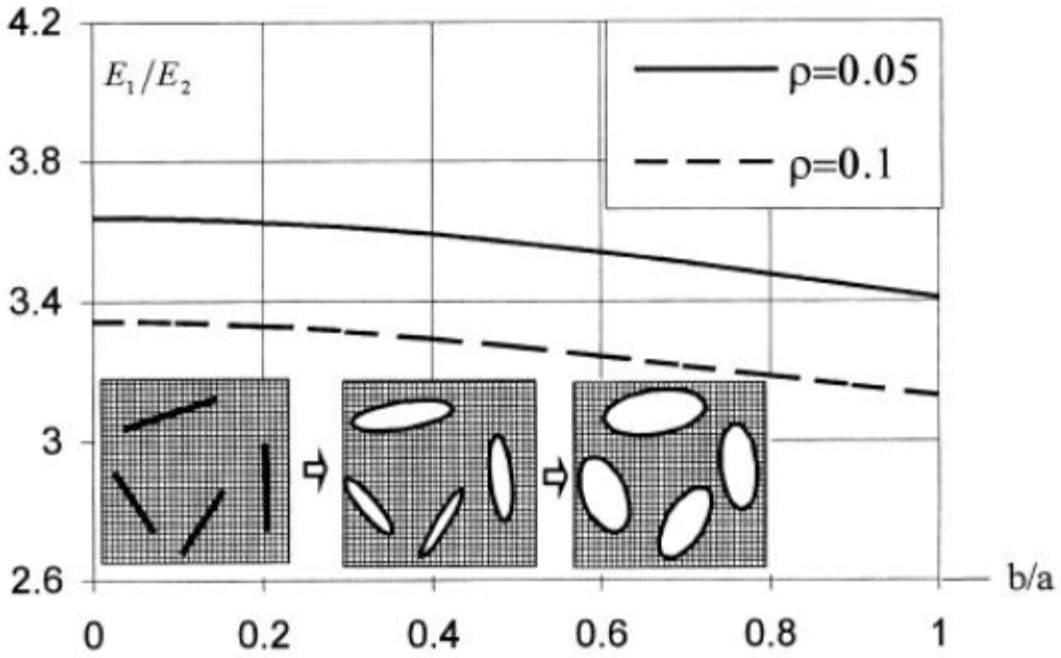

Figure E-1 Ratio E/E2 for the orthotropic matrix with randomly oriented elliptical holes. As function of ellipses ratio b/a. each of the two curves corresponds to keeping the density ρ of cracks constant while b/a increases, (Tsukrov and Kachanov 2000).

Beside shaped cut outs in laminated composite, there is another geometric discontinuity in laminated composite structures. Cavities or inclusions are a common imperfection could be detected in laminated structures. These imperfections may work as discontinuity and raised stress. Stress concentrations occur around the cavity or inclusion. Cavity or inclusion may develop to delamination area. Delamination area works as geometric discontinuity in resin (cohesive) area between two neighbour layers in laminate composite.

Here, in the present work, Kachanove (Tsukrov & Kachanov 2000) will be extended to simulate the effect of elliptical holes on mechanical properties of laminated composite plate. In addition an expectation of delamination propagation form sub-holes will be examined.

Let starting with the analysis of isolated elliptical hole, arbitrarily oriented in an anisotropic matrix. The overall strain (per reference area A) in a material containing a hole with boundary $\boldsymbol{\Gamma}$ having a unit normal $\boldsymbol{n}$ (directed outward to material, i.e. inside the hole) under remotely applied stress $\boldsymbol{\sigma}$ is (Tsukrov & Kachanov 2000)

$$\varepsilon = S^o : \sigma + \Delta\varepsilon \quad \left(or\ \varepsilon_{ij} = S^o_{ijkl} + \Delta\varepsilon_{ij}, in\ indicical\ notations\right) \tag{E.1}$$

Where S^o is the compliance tensor of the matrix and a colon denote contraction over two indices. The strain due to cavity.

$$\Delta\varepsilon = -\frac{1}{2A}\int_{\Gamma} (un + nu)d\Gamma \tag{E.2}$$

where **u** denotes displacements of the points of **Γ** and **un**, **nu** are dyadic (tensor) products of two vectors. Formula (E.2) results from application of the divergence theorem to a solid with a cavity. It is an immediate consequence of a note remark of Hill (1963) and has been used by a number of authors, for example, Vavakin and Salganik (1975). Due to linear elasticity, De is a linear function of s and hence can be written as

$$\Delta\varepsilon = H : \sigma \qquad \ldots \tag{E.3}$$

where fourth rank tensor H is the cavity compliance tensor (possessing the usual symmetries $H_{ijkl} = H_{jilk} = H_{klij}$ implied by symmetries $\varepsilon_{ij} = \varepsilon_{ji}$, $\sigma_{ij} = \sigma_{ji}$ and by the existence of elastic potential). Previously, Tsukrov and Kachanov (1993) and Kachanov et al. (1994) have been found H-tensors for two and three-dimensional shapes of cavities in the isotropic matrix and Mauge and Kachanov (1994), have been found anisotropic matrix with cracks of arbitrary orientations. The present work considers elliptical holes arbitrarily oriented in an anisotropic matrix.

Following Lekhnitski (1963) expression of cavity compliance tensor for an elliptical hole arbitrary oriented in an anisotropic matrix, it will be stated stresses and displacements in a 2D anisotropic elastic solid in terms of two complex stress

functions ϕ (z_1) and $\varphi(z_2)$, where $z_1 = x + \mu_1 y$, $z_2 = x + \mu_2 y$ Complex parameters μ_1 and μ_2 are roots of the characteristic equation

$$S_{1111}\mu^4 - 2S_{1112}\mu^3 + (2S_{1122} + S_{1212})\mu^2 - 2S_{2212}\mu + S_{2222} = 0 \quad \text{(E.4)}$$

where S_{ijkl} are elastic compliances in coordinate system *x, y*. Positive determination of the strain energy implies that μ_1, μ_2 cannot be real. $\mu_k = \alpha_k + i\beta_k$where α_k, β_k are denoted real constants and $\beta_k > 0$. In the case of orthotropy (coordinate axes parallel to the orthotropy axes), Equation (E.5) becomes biquadratic:

$$S_{1111}\mu^4 + (2S_{1122} + S_{1212})\mu^2 + S_{2222} = 0 \quad \text{(E.5)}$$

and has purely imaginary roots $\mu_{1,2}$:

$$\mu_{1,2} = \frac{i}{\sqrt{2S_{1111}}}\left\{(2S_{1122} + S_{1212}) \pm [(2S_{1122} + S_{1212})^2 - 4S_{1111}S_{2222}]^{1/2}\right\}^{1/2} \quad \text{(E.6)}$$

They can be expressed in terms of ``engineering constants" frequently used for the orthotropic materials (Young's moduli E_1, E_2, shear modulus G_{12} and Poisson's ratio $v12$, where x_1 and x_2 are the principal axes of orthotropy) by finding μ_1 and μ_2 Viete's theorem

$$\mu_{1,2} = i\beta_{1,2} = \frac{i}{2}\left[\left(\frac{E_1}{G_{12}} - 2v_{12} + 2\sqrt{\frac{E_1}{E_2}}\right)^{1/2} \pm \left(\frac{E_1}{G_{12}} - 2v_{12} - 2\sqrt{\frac{E_1}{E_2}}\right)^{1/2}\right] \quad \text{(E.7)}$$

where E_i, G_{ij}, and v_{ij} are Young's moduli, shear moduli and Poisson's ratios of the matrix in the case of plane stress. In plane strain, G_{ij} retains its meaning, whereas E_i and v_{ij} are to be understood as $E_1 = \frac{E_1}{(1-v_{13}v_{31})}, E_2 = \frac{E_2}{(1-v_{23}v_{32})}$ and $v_{12} = \frac{(v_{12}+v_{13}v_{32})}{(1-v_{13}v_{31})}, v_{21} = \frac{(v_{21}+v_{23}v_{31})}{(1-v_{23}v_{32})}$.

Calculation cavity compliance tensor of an anisotropic matrix has Elliptical hole arbitrarily oriented

For an elliptical hole in a matrix of arbitrary anisotropy, components of the hole compliance tensor H, in coordinate axes x1, x2 oriented along the ellipses axes *2a* and *2b* (Figure), are as follows (Tsukrov & Kachanov 2000):

$$H_{1111} = \frac{\pi b}{A} S^o_{11111}[a + b(\beta_1 + \beta_2)]$$

$$H_{1112} = \frac{\pi b}{A} S^o_{11111}[a(\alpha_1 + \alpha_2) + b(\alpha_1\beta_2 + \alpha_2\beta_1)] \quad \text{(E.8)}$$

$$H_{1122} = \frac{\pi ab}{A} S^o_{11111}[\alpha_1\alpha_2 - \beta_1\beta_2]$$

$$H_{1212} = \frac{\pi}{4A} S^o_{1111}\{a^2(\beta_1 + \beta_2) + ab[(\alpha_1 + \alpha_2)^2 + (\beta_1 + \beta_2)^2] + b^2[\beta_1(\alpha_2^2 + \beta_2^2) + \beta_2(\alpha_1^2 + \beta_1^2)]\}$$

$$H_{1222} = \frac{\pi a}{2A} S^o_{1111}\{a(\alpha_1\beta_2 + \alpha_2\beta_1) + b[\alpha_1(\alpha_2^2 + \beta_2^2) + \alpha_2(\alpha_1^2 + \beta_1^2)]\}$$

$$H_{2222} = \frac{\pi a}{A} S^o_{2222}\left[a\left(\frac{\beta_1}{\alpha_1^2+\beta_1^2} + \frac{\beta_2}{\alpha_2^2+\beta_2^2}\right) + b\right]$$

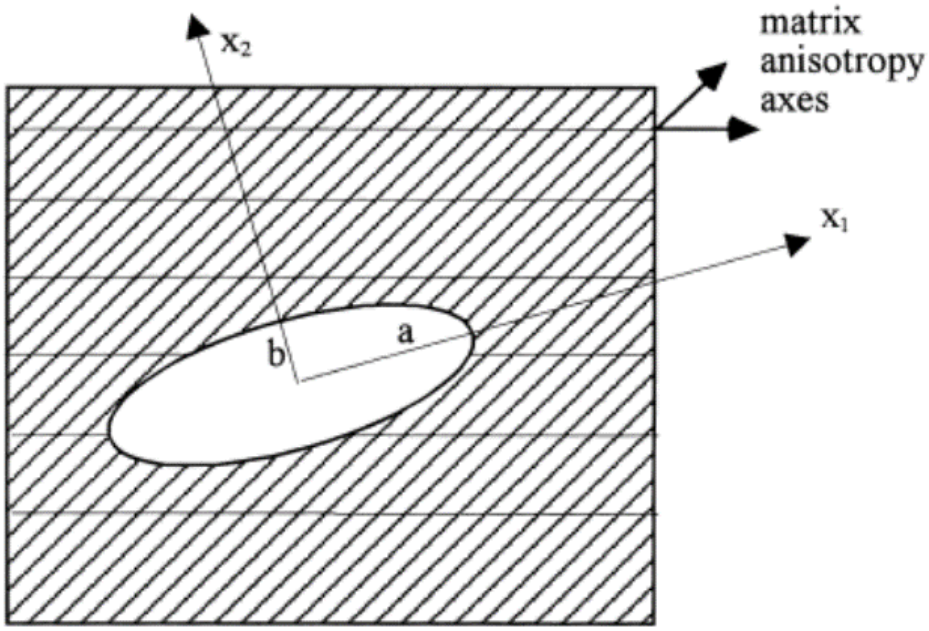

Figure E-2 Elliptical hole arbitrarily oriented with respect to the anisotropy axes of the matrix.

For the important case of the orthotropic matrix, equation (E.8) can be transformed to explicitly reflect the orientation of the hole with respect to the matrix orthotropy axes (Tsukrov & Kachanov 2000). Let, t and n are the unit vectors along 2a and 2b axes of the ellipse and angle φ between t and x_1-direction of the matrix orthotropy as shown in Figure , after some algebra, it can be obtained;

$$H_{tttt} = \frac{\pi b}{A}\left\{\frac{a}{E_t^o} + b[C(1 - D\cos 2\varphi)]\right\}$$

$$H_{tttn} = \frac{\pi b}{4A}\left\{a\left[\frac{1}{E_2^o} - \frac{1}{E_1^o} - F\cos 2\varphi\right] + abCD\right\}\sin 2\varphi$$

$$H_{ttnn} = \frac{\pi ab}{4A}\left(Fsin^2 2 - \frac{4}{\sqrt{E_1^o E_2^o}}\right) \quad \text{(E.9)}$$

$$H_{tntn} = \frac{\pi a^2}{4A}C(1 - D\cos 2\varphi) + \frac{\pi b^2}{4A}C(1 + D\cos 2\varphi) + \frac{\pi ab}{4A}\left[\left(\frac{1}{\sqrt{E_1^o}} + \frac{1}{\sqrt{E_2^o}}\right)^2 - Fcos^2 2\varphi\right]$$

$$H_{tnnn} = \frac{\pi a}{4A}\left\{2aCD + b\left[\frac{1}{E_2^o} - \frac{1}{E_1^o} + Fcos2\varphi\right]\right\} sin2\varphi$$

$$H_{nnnn} = \frac{\pi a}{A}\left\{a[C(1 + Dcos2\varphi] + \frac{b}{E_n^o}\right\}$$

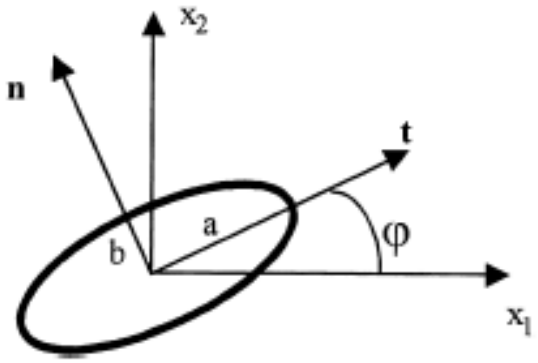

Figure E-3 Elliptical hole in the orthotropic matrix (x_1, x_2 are the orthotropic axes).

where constants C, D and F are expressed in terms of the ``engineering constants" of the matrix, $E_1^o, E_2^o, G_{12}^o \; and \; v_{12}^o$as follows:

$$C = \frac{1}{2}\frac{\sqrt{E_1^o}+\sqrt{E_2^o}}{\sqrt{E_1^o E_2^o}}\sqrt{\frac{1}{G_{12}^o} - \frac{2v_{12}^o}{E_1^o} + \frac{2}{\sqrt{E_1^o E_2^o}}}$$

$$D = \frac{\sqrt{E_1^o}-\sqrt{E_2^o}}{\sqrt{E_1^o}+\sqrt{E_2^o}} \quad \text{(E.10)}$$

$$F = \frac{1+v_{12}^o}{E_1^o} + \frac{1+v_{21}^o}{E_2^o} - \frac{1}{G_{12}^o}$$

Where $E_t^o \; and \; E_n^o$ are Young's moduli of the matrix in t- and n-directions given by

$$\frac{1}{E_t^o} = \frac{cos^4\varphi}{E_1^o} + \left(\frac{1}{G_{12}^o} - \frac{2v_{12}^o}{E_1^o}\right) sin^2\varphi cos^2\varphi + \frac{sin^4\varphi}{E_2^o} \quad \text{(E.11)}$$

and

$$\frac{1}{E_t^o} = \frac{sin^4\varphi}{E_1^o} + \left(\frac{1}{G_{12}^o} - \frac{2v_{12}^o}{E_1^o}\right) sin^2\varphi cos^2\varphi + \frac{sin^4\varphi}{E_2^o} \quad \text{(E.12)}$$

It is also needed components of H-tensor in the principal axes of the matrix orthotropyx_1, x_2. Just this case will be studied in this work because all study cases have orthotropic behaviours. They can be expressed as follows;

$$H_{1111} = \frac{\pi L}{A\sqrt{E_1^o}}\left[(b^2 - a^2)cos^2\varphi + a^2 + \frac{ab}{L\sqrt{E_1^o}}\right]$$

$$H_{1112} = \frac{\pi(b^2-a^2)L}{2A\sqrt{E_1^o}} sin\varphi cos\varphi$$

$$H_{1122} = -\frac{\pi ab}{A\sqrt{E_1^o E_2^o}} \quad \text{(E-13)}$$

$$H_{1212} = \frac{\pi L}{4A\sqrt{E_1^o E_2^o}}\left[(a^2 - b^2)\left(\sqrt{E_2^o} - \sqrt{E_1^o}\right)cos^2\varphi + a^2\sqrt{E_1^o} + abL\sqrt{E_1^o E_2^o} + b^2\sqrt{E_2^o}\right]$$

$$H_{1222} = \frac{\pi(b^2-a^2)L}{2A\sqrt{E_2^o}} sin\varphi cos\varphi$$

$$H_{2222} = \frac{\pi L}{A\sqrt{E_2^o}}\left[(a^2 - b^2)cos^2\varphi + b^2 + \frac{ab}{L\sqrt{E_2^o}}\right]$$

And

$$L = \sqrt{\frac{1}{G_{12}^o} - \frac{2v_{12}^o}{E_1^o} + \frac{2}{\sqrt{E_1^o E_2^o}}}$$

Following Matlab code is built for calculation equation E-13 and Equation 3.82

```
function y=Hreduceorthotropy(E1,E2,NU12,G12,theta,a,b,A)
L=sqrt((1/G12)-(2*NU12/E1)+(2/sqrt(E1*E2)));
H1111=(pi*L/(A*sqrt(E1)))*((b^2-
a^2)*(cos(theta))^2+a^2+(a*b/(L*sqrt(E1))));
H1112=pi*(b^2-a^2)*L*sin(theta)*cos(theta)/(2*A*sqrt(E1));
H1122=-pi*a*b/(A*sqrt(E1*E2));
H1212=pi*L/(4*A*sqrt(E1*E2))*((a^2-b^2)*(sqrt(E2)-
sqrt(E1))*(cos(theta))^2+a^2*sqrt(E1)+a*b*L*sqrt(E1*E2)+b^2*sqrt(
E2));
H1222=pi*(b^2-a^2)*L*sin (theta)*cos(theta)/(2*A*sqrt(E2));
H2222=pi*L/(A*sqrt(E2))*((a^2-
b^2)*(cos(theta))+b^2+a*b/(L*sqrt(E2)));
y=[H1111 H1122 H1112;0 H2222 0; 0 H1222 H1212];
```

```
psilon1=Strains(0.025,0,0,0,0,0,-4);
epsilon2=Strains(0.025,0,0,0,0,0,-3.5);
epsilon3=Strains(0.025,0,0,0,0,0,-3);
epsilon4=Strains(0.025,0,0,0,0,0,-2.5);
epsilon5=Strains(0.025,0,0,0,0,0,-2);
epsilon6=Strains(0.025,0,0,0,0,0,-1.5);
epsilon7=Strains(0.025,0,0,0,0,0,-1);
epsilon8=Strains(0.025,0,0,0,0,0,-0.5);
epsilon9=Strains(0.025,0,0,0,0,0,0);
epsilon10=Strains(0.025,0,0,0,0,0,0.5);
epsilon11=Strains(0.025,0,0,0,0,0,1);
epsilon12=Strains(0.025,0,0,0,0,0,1.5);
epsilon13=Strains(0.025,0,0,0,0,0,2);
epsilon14=Strains(0.025,0,0,0,0,0,2.5);
epsilon15=Strains(0.025,0,0,0,0,0,3);
epsilon16=Strains(0.025,0,0,0,0,0,3.5);
Q=ReducedStiffness(15000,15000,0.26,9500);
H=Hreduceorthotropy(15000,15000,0.126,9500,0.1745,10,5,157.08);
Scrack=S+H;
Qcrack=inv(Scrack);
Qbar1=Qbar(Q,0);
Qbar2=Qbar(Q,90);
Qbar3=Qbar(Q,0);
Qbar4=Qbar(Q,90);
Qbar5=Qbar(Qcrack,0);
Qbar6=Qbar(Q,90);
Qbar7=Qbar(Q,0);
Qbar8=Qbar(Q,90);
Qbar9=Qbar(Q,0);
Qbar10=Qbar(Q,90);
Qbar11=Qbar(Q,0);
Qbar12=Qbar(Qcrack,90);
Qbar13=Qbar(Q,0);
Qbar14=Qbar(Q,90);
Qbar15=Qbar(Q,0);
Qbar16=Qbar(Q,90);
sigma1a=Qbar1*epsilon1;
sigma1b=Qbar1*epsilon2;
sigma2a=Qbar2*epsilon2;
```

```
sigma2b=Qbar2*epsilon3;
sigma3a=Qbar3*epsilon3;
sigma3b=Qbar3*epsilon4;
sigma4a=Qbar4*epsilon4;
sigma4b=Qbar4*epsilon5;
sigma5a=Qbar5*epsilon5;
sigma5b=Qbar5*epsilon6;
sigma6a=Qbar6*epsilon6;
sigma6b=Qbar6*epsilon7;
sigma7a=Qbar7*epsilon7;
sigma7b=Qbar7*epsilon8;
sigma8a=Qbar8*epsilon8;
sigma8b=Qbar8*epsilon9;
sigma9a=Qbar9*epsilon9;
sigma9b=Qbar9*epsilon10;
sigma10a=Qbar10*epsilon10;
sigma10b=Qbar10*epsilon11;
sigma11a=Qbar11*epsilon11;
sigma11b=Qbar11*epsilon12;
sigma12a=Qbar12*epsilon12;
sigma12b=Qbar12*epsilon13;
sigma13a=Qbar13*epsilon13;
sigma13b=Qbar13*epsilon14;
sigma14a=Qbar14*epsilon14;
sigma14b=Qbar14*epsilon15;
sigma15a=Qbar15*epsilon15;
sigma15b=Qbar15*epsilon16;
sigma16a=Qbar16*epsilon16;
sigma16b=Qbar16*epsilon17;
y=[4 4 3.5 3.5 3 3 2.5 2.5 2 2 1.5 1.5 1 1 0 0 -0.5 -0.5 -1 -1 -
1.5 -1.5 -2 -2 -2.5 -2.5 -3 -3 -3.5 -3.5 -4 -4];
x=[sigma16b(1)  sigma16a(1)  sigma15b(1)  sigma15a(1)  sigma14b(1)
sigma14a(1)  sigma13b(1)    sigma13a(1)  sigma12b(1)  sigma12a(1)
sigma11b(1)   sigma11a(1)   sigma10b(1)   sigma10a(1)   sigma9b(1)
sigma9a(1) sigma8b(1) sigma8a(1) sigma7b(1) sigma7a(1) sigma6b(1)
sigma6a(1) sigma5b(1) sigma5a(1) sigma4b(1) sigma4a(1) sigma3b(1)
sigma3a(1) sigma2b(1) sigma2a(1) sigma1b(1) sigma1a(1)];
plot(x,y)
xlabel('\sigma_x (Mpa)')
ylabel('z(mm)')
…….
```

```
plot(x,y)
xlabel('\sigma_y (Mpa)')
ylabel('z(mm)')
……
plot(x,y)
xlabel('\tau_{xy} (Mpa)')
ylabel('z(mm)')
% calculate the compliance of equation 3.82
S=ReducedCompliance(E1,E2,NU12,G12);
H=Hreduceorthotropy(E1,E2,NU12,G12,theta,a,b,A);
Scrack=S+H;
Qcrack=inv(Scrack);
Q=ReducedStiffness(E1,E2,NU12,G12);
Qbar1=Qbar(Q,0);
Qbar2=Qbar(Q,90);
Qbar3=Qbar(Q,0);
Qbar4=Qbar(Q,90);
Qbar5=Qbar(Qcrack,0);
Qbar6=Qbar(Q,90);
Qbar7=Qbar(Q,0);
Qbar8=Qbar(Q,90);
Qbar9=Qbar(Q,0);
Qbar10=Qbar(Q,90);
Qbar11=Qbar(Q,0);
Qbar12=Qbar(Qcrack,90);
Qbar13=Qbar(Q,0);
Qbar14=Qbar(Q,90);
Qbar15=Qbar(Q,0);
Qbar16=Qbar(Q,90);
H=8;
z1=-4;
z2=-3.5;
z3=-3;
z4=-2.5;
z5=-2;
z6=-1.5;
z7=-1;
z8=-0.5;
z9=0;
z10=0.5;
z11=1;
```

```
z12=1.5;
z13=2;
z14=2.5;
z15=3;
z16=3.5;
z17=4;
A=zeros(3:3);
A=Amatrix(A,Qbar1,z1,z2);
A=Amatrix(A,Qbar2,z2,z3);
A=Amatrix(A,Qbar3,z3,z4);
A=Amatrix(A,Qbar4,z4,z5);
A=Amatrix(A,Qbar5,z5,z6);
A=Amatrix(A,Qbar6,z6,z7);
A=Amatrix(A,Qbar7,z7,z8);
A=Amatrix(A,Qbar8,z8,z9);
A=Amatrix(A,Qbar9,z9,z10);
A=Amatrix(A,Qbar10,z10,z11);
A=Amatrix(A,Qbar11,z11,z12);
A=Amatrix(A,Qbar12,z12,z13);
A=Amatrix(A,Qbar13,z13,z14);
A=Amatrix(A,Qbar14,z14,z15);
A=Amatrix(A,Qbar15,z15,z16);
A=Amatrix(A,Qbar16,z16,z17);
% calculating Ex, Ey, Nxy and Gxy
Ex=Ebarx(A,H)
Ey=Ebary(A,H)
NUxy=NUbarxy(A,H)
NUyx=NUbaryx(A,H)
Gxy=Gbarxy(A,H)

%Here in this work the mechanical properties are used as shown in
next Matlab code
S=ReducedCompliance(15000,15000,0.126,9500);
H=Hreduceorthotropy(15000,15000,0.126,9500,0.1745,10,5,157.08);
Q=ReducedStiffness(15000,15000,0.78539,9500);
```